

## Durham E-Theses

---

### *Lipid based sensing of organic vapours: a study combining AFM and QCM*

DUAN, XIAO,XIA

#### How to cite:

---

DUAN, XIAO,XIA (2014) *Lipid based sensing of organic vapours: a study combining AFM and QCM*, Durham theses, Durham University. Available at Durham E-Theses Online:  
<http://etheses.dur.ac.uk/10738/>

#### Use policy

---

The full-text may be used and/or reproduced, and given to third parties in any format or medium, without prior permission or charge, for personal research or study, educational, or not-for-profit purposes provided that:

- a full bibliographic reference is made to the original source
- a [link](#) is made to the metadata record in Durham E-Theses
- the full-text is not changed in any way

The full-text must not be sold in any format or medium without the formal permission of the copyright holders.

Please consult the [full Durham E-Theses policy](#) for further details.

**Lipid based sensing of organic vapours: a  
study combining AFM and QCM**

by

**Xiaoxia Duan**

**School of Engineering and Computing Sciences**

**Durham University**

A Thesis submitted to the Durham University

for the degree of Ph.D.

2014

## **Acknowledgements**

I would like to thank my supervisors, Dr Andrew Gallant and Prof. David Wood, for their outstanding and continued support and encouragement throughout this study. I also would like to thank EPSRC for their additional financial support.

I would like to thank Dr Sherri Johnston for her supervision during the first year of my PhD. No acknowledgement would be complete without a mention for Mr John Gibson and Dr Chris Pearson whose extensive technical assistance was invaluable. I would also like to thank Dr Michael Cooke and Dr Fred Hamlin for their help with sputter coating.

## **Declaration**

I declare that no material in this thesis has previously been submitted for a degree at this or any other university.

The copyright of this thesis rests with the author. No quotation from it should be published in any format, including electronic and the Internet, without the authors' prior written consent. All information derived from this thesis must be acknowledged appropriately.

# Lipid based sensing of organic vapours: a study combining AFM and QCM

## Abstract

This thesis investigates the development of a vapour sensor that is useful in fields such as environmental protection, or healthcare. A summary review of vapour sensing techniques is given, leading to the choice of exploiting a simple, low cost, high-resolution mass sensing technique-Quartz Crystal Microbalance (QCM) to fabricate a lipid based vapour sensor. Both hydrophilic and hydrophobic vapours have been introduced in the sensing experiment.

Three types of lipids based sensors, which were 1, 2-dilauroyl-*sn*-glycero-3-phosphocholine (DLPC), 1, 2-dioctadecanoyl-*sn*-glycero-3-phosphocholine (DSPC), cholesterol and their mixtures, were fabricated on AT cut quartz crystal based substrates by spin coating. Atomic Force Microscopy (AFM) was used for topography analysis; QCM was used for quantitative analysis. Film thickness data suggests that a bilayer DLPC is 4.3 nm and a bilayer DSPC is 5.8 nm thick. The average film thickness is approximately proportional to the coating concentration with a constant of proportionality of 4.3 nm/mM and 5.8 nm/mM for DLPC and DSPC, respectively. The results from the AFM and QCM trials have led to the development of a controllable process for the fabrication of a repeatable amount of lipid membrane based vapour sensors.

The response of each film when exposed to ethanol, methanol, toluene and cyclohexane vapours was recorded. The results show that hydrophilic compounds could be recognised efficiently by lipids having shorter alkyl chains. Frequency changes caused by adsorption of test vapours could be enhanced when cholesterol was co-immobilised in the lipid layer. The best sensing behaviour (that is, excellent response, reversibility and negligible baseline drift) and sensitivity was achieved in a sensor coated with DLPC/DSPC/cholesterol mixed film (50 mg/ml DLPC/DSPC/cholesterol-1:1:8 in volume ratio). The limit of detection of this sensor is 400 ppm to ethanol, 800 ppm to methanol, 1300 ppm to toluene and 2300 ppm to cyclohexane, separately.

# Table of Contents

<b>Chapter 1</b>	<b>Introduction</b>	<b>1</b>
1.1	Senses and daily life	1
1.2	Biotechnology, biomimetic sensors and applications	2
1.3	Aims of this study	4
<b>Chapter 2</b>	<b>Review: materials and techniques</b>	<b>6</b>
2.1	Sensing material	6
2.1.1	Polymers	7
2.1.2	Carbon nanotubes	9
2.1.3	Lipids	9
2.2	Review of gas and vapour sensing techniques	11
2.2.1	Techniques based on variation of electrical properties	11
2.2.2	Techniques based on variation of thermodynamic properties	14
2.2.3	Techniques based on variation of optical properties	15
2.2.4	Techniques based on variation of ultrasonic properties	18
2.3	Summary	21
<b>Chapter 3</b>	<b>Lipid based QCM vapour sensor</b>	<b>25</b>
3.1	Lipids	25
3.1.1	DSPC, DLPC and cholesterol	25
3.1.2	Vesicles and vesicle fusion	27
3.1.3	Monolayer, bilayer and cell membrane	30
3.1.4	Multilamellar films	32

3.2	Quartz crystal microbalance .....	33
3.2.1	Background .....	33
3.2.2	The piezoelectric effect .....	34
3.2.3	Quartz crystal .....	36
3.2.4	Stable baseline .....	39
3.2.5	Calculation theory.....	44
3.3	Summary .....	48
<b>Chapter 4</b>	<b>Lipid film fabrication .....</b>	<b>49</b>
4.1	Substrate preparation and cleaning .....	49
4.1.1	Substrate properties and contact angle measurement .....	49
4.1.2	Hydrophilic surface preparation.....	51
4.1.3	Hydrophobic surface preparation .....	56
4.2	Review of sensing material fabrication technology.....	58
4.3	Lipid bilayer preparation.....	63
4.3.1	Vesicle preparation .....	63
4.3.2	Bilayer preparation by drop coating for AFM mapping .....	65
4.3.3	Bilayer preparation by flow injection for QCM weighing.....	65
4.4	Ultrathin lipid layers and lipid multilayer (sensor) fabrication .....	66
4.4.1	Spin coating theory .....	66
4.4.2	Thin lipid layer and multilayer fabrication .....	69
4.4.3	Multilayer (sensor) fabrication.....	70
4.5	Summary .....	71

<b>Chapter 5</b>	<b>Results and discussion: lipid film characterisation .....</b>	<b>72</b>
5.1	Lipid film characterisation methods .....	72
5.1.1	Atomic force microscopy.....	73
5.1.2	QCM weighing .....	76
5.2	Lipid layer mapping.....	77
5.2.1	Mapping of lipid film formed by spin coating .....	77
5.2.2	Mapping of lipid films formed via vesicle fusion .....	80
5.3	Lipid layer weighing .....	92
5.3.1	Quantitative analysis of bilayer formed by vesicle fusion.....	92
5.3.2	Quantitative analysis of lipid layer formed by spin coating .....	100
5.4	Summary .....	106
<b>Chapter 6</b>	<b>Vapour sampling methods.....</b>	<b>108</b>
6.1	Design of a vapour generation system.....	108
6.2	Design of a vapour sensing system.....	111
6.3	Calibration of the vapour sensing system .....	113
6.3.1	Saturated vapour pressure .....	113
6.3.2	Calibration of the vapour generation system .....	115
6.3.3	Calibration of the flow rate .....	116
6.4	Summary .....	118
<b>Chapter 7</b>	<b>Results and discussion: bare gold based vapour sensing.....</b>	<b>119</b>
7.1	Sensor fabrication .....	119
7.1.1	Effect of subphase on sensor response .....	119

7.1.2	Repeatability study on sensor response .....	120
7.1.3	Correspondence of sensor response to film thickness on quartz crystal.....	121
7.1.4	Fabricated sensors.....	123
7.2	Sensor response .....	124
7.2.1	Measurement setup and procedure .....	124
7.2.2	Sensor responses.....	124
7.2.3	Interaction mechanism.....	128
7.3	Evaluation of sensor sensitivity and selectivity .....	131
7.3.1	Sensor selectivity.....	131
7.3.2	Sensor sensitivity.....	136
7.3.3	Adsorption behaviour .....	140
7.4	Evaluation of sensor useful life .....	141
7.5	Summary .....	143
<b>Chapter 8</b>	<b>Results and discussion: increase of sensitivity .....</b>	<b>145</b>
8.1	Improving sensitivity .....	145
8.2	Optimization of film thickness .....	146
8.2.1	Testing of high concentration DLPC and DSPC lipid sensors .....	146
8.2.2	Correspondence of sensor response to film thickness on quartz crystal.....	148
8.2.3	Typical response of high concentration DLPC and DSPC single phase sensors .....	150
8.3	Sensor sensitivity improvement by increase film thickness .....	156
8.3.1	Sample sensor preparation .....	156

8.3.2	Evaluation of sensors' sensitivity and selectivity.....	157
8.3.3	Sensor selectivity: effect of acyl chain length on sensor response.....	161
8.4	Optimization of DSPC/cholesterol film flexibility.....	162
8.4.1	Effect of cholesterol on DSPC sensor response .....	162
8.4.2	Typical response of cholesterol and cholesterol modified DSPC sensors.....	163
8.4.3	Evaluation of sensors sensitivity and selectivity .....	165
8.5	Optimization of DSPC/DLPC/cholesterol film flexibility.....	167
8.5.1	Effect of cholesterol on DSPC/DLPC sensor response .....	168
8.5.2	Sensor sensitivity and selectivity.....	169
8.5.3	Mechanism of sensitivity improvement and interaction mechanism .....	174
8.6	Sensors' useful life .....	185
8.7	Oil vapour sensing .....	186
8.8	Summary .....	187
<b>Chapter 9</b>	<b>Conclusions and future work .....</b>	<b>189</b>
9.1	Initial aims.....	189
9.2	Results.....	189
9.3	Limitations and future work.....	192
	References.....	194

## Nomenclature

Symbol	Description	Unit
$A$	the total electrode area of the quartz crystal used in QCM device (equation 3-4)	$\text{cm}^2$
$A$	absorbance described in Beer-Lambert law equation (equation 2-1)	n/a
$C$	a constant of integration (equation 6-1)	n/a
$C_0$	parasitic capacitance (section 3.2.5 b)	F
$C_f$	sensitivity factor of the quartz crystal (equation 5-1 and 5-2)	$\text{Hz}/\text{ng}/\text{cm}^2$
$\Delta C$	test vapour concentration difference (equation 7-2)	ppm
$D$	diameter of lipid domains (Table 5-3)	nm
$I$	rms current of the impedimetric gas/vapour sensors (section 2.2.1 c)	A
$L$	length of the cantilevers used for AFM (Table 5-1)	$\mu\text{m}$
$K$	spring constant of the cantilevers used for AFM (Table 5-1)	N/m
$K_p$	partition coefficient in the equation of frequency shift calculation for surface acoustic wave device (equation 2-6)	$\text{sec}^{-1}$
$L$	length of the diffusion tube used for diffusion vapour generation system (Figure 6-2)	cm
$L$	inductance of the QCM circuit (equation 3-9)	H
LODs	Limit of detection (equation 7-3)	ppm
$\Delta M$	change in mass of the sensing film (equation 3-4)	g
$\Delta m$	areal mass difference of the sensing membrane on quartz crystal (equation 2-7, 3-4 and 3-5)	$\text{g}/\text{cm}^2$
$N$	an integer in the piezoelectric effect calculation equation (equation 3-2)	n/a
$N_q$	frequency constant for AT cut quartz crystal (equation 3-6)	$\text{Hz} \cdot \text{cm}$
$R$	gas constant = 8.3144 (equation 6-1)	J/K/mol
$R$	resistance of the quartz crystal (equation 3-9)	$\Omega$

$R_q$	root mean squared surface roughness of the AFM height or phase image of the sample surface (section 5.2.1 a)	nm or °
$R^2$	correlation coefficient, used for linear fit evaluation	n/a
$R_z$	Z-factor of the film material, i.e. the acoustic impedance ratio (equation 3-7)	n/a
$\Delta R$	dynamic resistance shift of the quartz crystal (section 5.3.1 b)	$\Omega$
$\Delta R_{final}$	peak value of the QCM quartz crystal resistance shift (section 5.3.1 b)	$\Omega$
$\Delta R_{max}$	equilibrating data level of the QCM quartz crystal resistance shift (section 5.3.1 b)	$\Omega$
S	sensitivity of sensors (equation 7-2 and 7-3)	Hz/ppm
T	temperature of the system in Clausius-Clapeyron equation (equation 6-1)	K
$TK_f$	thickness of the film loaded on crystal (equation 3-8 and 5-4)	cm
V	rms voltage of the impedimetric gas/vapour sensors (section 2.2.1 c)	v
W	width of the cantilever used for AFM (Table 5-1)	$\mu\text{m}$
c	concentration of solution described in Beer-Lambert law equation (equation 2-1)	$\text{mol}/\text{cm}^3$
$c_{coat}$	concentration of sample solution used for spin coating (equation 5-1)	mg/ml or mM
$c_v$	vapour concentration in the equation of frequency shift calculation for surface acoustic wave device (equation 2-6)	mol/L
d	inner diameter of the diffusion tube used for diffusion vapour generation system (Figure 6-2)	cm
d	half-length of a round trip in the piezoelectric effect calculation equation, i.e. the distance between the crystal sides (equation 3-1)	m
f	resonant frequency of the loaded quartz crystal (equation 3-2, 3-3, 3-4, 3-5 and 3-6)	Hz
$f_0$	characteristic frequency of surface acoustic wave device	Hz

(equation 2-5), the oscillation frequency of bare crystal used in QCM device (equation 8-2 and 8-3)

$f_q$	resonant frequency of an unloaded crystal (equation 3-5)	Hz
$f_r$	the ratio of the resonant frequency shift (equation 7-1)	%
$f_x$	frequency shift corresponding to each lipid (equation 7-1)	Hz
$f_{xmax}$	maximum frequency shift for each compound (equation 7-1)	Hz
$\Delta f$	frequency shift of the piezoelectric device caused by sorption of substance (equation 2-6, 2-7, 3-4, 5-1, 7-2 and 8-2)	Hz
$\Delta f_n$	the nominal frequency shift, $\Delta f_n = \Delta f / C$ , where C is the concentration of the vapour (section 7.3.1)	Hz/ppm
$\Delta f_p$	frequency shift caused by the membrane in surface acoustic device (equation 2-6)	Hz
$\Delta f_{as}$	asymptotic values of the frequency shifts in flow injection QCM measurements (section 5.3.1 a)	Hz
$f_{final}$	final frequency of flow injection QCM measurements (section 5.3.1 a)	Hz
$\Delta f_{norm}$	changes in normalised frequency with n being the harmonic number (= $\Delta f_n / n$ , section 5.3.1 c)	Hz
h	tip (used for AFM) height (Table 5-2)	$\mu\text{m}$
l	distance between the input and output transducer of surface acoustic wave device (equation 2-4), length of solution the light passes through (equation 2-1)	m
$l_{23}$	latent heat of transformation in Clausius-Clapeyron equation (equation 6-1)	J
$\Delta m$	change in mass per unit area (equation 2-7, 5-1 and 5-2)	$\text{g}/\text{cm}^2$
n	number of the harmonic, n= 1, 3, 5, 7 etc. (equation 5-2)	n/a
$r_{sp}$	set-point amplitude ratio, which is relevant to the tapping type in tapping mode AFM (section 5.1.1 c)	n/a
t	thickness of the cantilever (Figure 5-2)	$\mu\text{m}$
$t_d$	delay time between the electrical input and the output signal of	sec

	surface acoustic wave device (equation 2-4)	
$t_{as}$	the time after which the QCM quartz crystal frequency shifts reach asymptotic value (Table 5-5)	sec or min
$\alpha$	weight fraction of DSPC	%
$\alpha_X$	coating constant of substance X (equation 5-1, Table 5-7)	Hz/mM, Hz/(mg/ml), nmol/mM, nmol/(mg/ml), nm/mM, nm/(mg/ml)
$\gamma$	the velocity of the wave in crystal (equation 3-2 and 3-3)	m/sec
$\gamma_{LG}$	liquid-vapour interfacial energy (equation 4-1)	J
$\gamma_{SG}$	solid-vapour interfacial energy (equation 4-1)	J
$\gamma_{SL}$	solid-liquid interfacial energy (equation 4-1)	J
$\gamma_{lipid}$	thickness constant of the lipid film (Table 5-5)	nm/Hz
$\delta$	decay length of the shear wave (equation 8-3)	cm
$\varepsilon$	molar absorptivity (equation 2-1)	cm <sup>2</sup> /mol
$\eta_L$	absolute viscosity of the liquid (equation 8-2 and 8-3)	N·sec/m <sup>2</sup>
$\theta$	contact angle of any surface (equation 4-1)	°
$\lambda$	wavelength of the electrical signal in the piezoelectric effect calculation equation (equation 3-1 and 3-2)	m
$\lambda_0$	wavelength of the electrical signal of surface acoustic device (equation 2-5)	m
$\mu_q$	effective piezoelectrically stiffened shear modulus of quartz (equation 3-4, 3-6, 3-7, 5-2, 5-3 and 8-2)	g/cm/sec <sup>2</sup>
$\mu_f$	shear modulus of film material (equation 3-7)	g/cm/sec
$\omega_s$	angular frequency at series resonance (equation 3-9)	rad
$\rho$	vapour pressure in Clausius-Clapeyron equation (equation 6-1)	Pa
$\rho_L$	absolute density of the liquid (equation 8-2 and 8-3)	kg/m <sup>3</sup>
$\rho_p$	density of the sensing membrane in the equation of frequency shift calculation for surface acoustic wave device (equation 2-6)	mol/L

$\rho_q$	density of quartz crystal used for QCM device (equation 3-4,3-6, 3-7, 5-2, 5-3 and 8- 2)	$\text{g/cm}^3$
$\rho_f$	density of the coating material on quartz crystal (equation3-7)	$\text{g/cm}^3$
$\sigma$	noise level of the QCM system (equation 7-3)	Hz
$\tau_q$	period of the unloaded crystal (equation 3-8)	sec
$\tau$	period of the loaded crystal (equation 3-8)	sec
$\nu$	speed of the wave in surface acoustic wave device (equation 2-4 and 2-5)	m/sec

# Chapter 1 Introduction

As a result of concerns regarding environmental pollution, there is now an increasing need for sensitive pollution detectors, such as biomimetic sensors, in our daily life. A brief introduction to biotechnology and existing research in the sensor field can be found in this chapter. The main aim of this study will be introduced at the end of the chapter.

## 1.1 Senses and daily life

Sight, hearing, touch, smell and taste are together known as five important senses of humans. We act after receiving information from the outside world via these senses [1]. Mimetic technologies aim to replicate these biological functions artificially.

With the continuous growth of industry and agricultural production, unpleasant odours, environmentally dangerous gases such as  $\text{NO}_x$ , health threatening vapours such as toluene, and a variety of other emissions from industrial and agricultural sources are seen as the main factors contributing to environmental pollution problems, especially in densely populated areas over the last few decades. Due to these increased levels of pollution, environmental protection, healthcare and regulation of the food industry have become increasingly significantly parts of modern life. Many people are exposed to a variety of substances such as chemicals, fumes, and dusts at work which can, in certain circumstances, have a harmful effect on their health. If exposure to hazardous substances is not properly controlled, it may cause ill health in a number of ways. It is very important to know in advance how to protect the health of people working with hazardous substances [2].

In UK, the Health and Safety Executive (HSE) has set occupational exposure limits (OELs) for hazardous substances at work which are updated annually. OELs recommend a maximum long term limit of 8 hours continuous exposure and short term limit of

15 minutes exposure for acetone, chloroform, ethanol, methanol, benzene, cyclohexane, hexane, and toluene vapours as shown in Table 1-1 [2]. The risk assessments relating to health effects of certain chemicals also note that benzene can cause cancer and poses a danger of serious damage to health if prolonged exposure occurs [2].

Table 1-1 Safe exposure limits in parts per million (ppm) and milligram per cubic metre ( $\text{mg}/\text{m}^3$ ) for toxic gases [2]

Substance	Long-term exposure limit (8-hour time weighted average(TWA) reference period)			Short-term exposure limit (15-minute reference period)		
	ppm	$\text{mg}/\text{m}^3$	mmol/L	ppm	$\text{mg}/\text{m}^3$	mmol/L
Acetone	500	1210	0.021	1500	3620	0.062
Chloroform	2	9.9	0.00016	-	-	-
Ethanol	1000	1920	0.042	-	-	-
Methanol	200	266	0.0083	250	333	0.01
Benzene	1	-	-	-	-	-
Cyclohexane	100	350	0.0042	300	1050	0.012
n-hexane	20	72	0.00084	-	-	-
Toluene	50	191	0.0021	150	574	0.0062

As we know, human sensory evaluations are often affected by physical and mental conditions. Normally, humans have poorer sensitivity to odour by a factor of  $10^{11}$ - $10^{13}$  than dogs (e.g.  $5.0 \times 10^{13}$  molecules per ml water thresholds for acetic acid in humans and  $5.0 \times 10^5$  molecules per ml water thresholds for acetic acid in dogs) [3]. As a result, research dedicated to the development of reliable and highly sensitive vapour sensors, such as those used in the detection of volatile organic compounds (VOCs) has become a task whose challenging nature is matched by its ever increasing demand.

## 1.2 Biotechnology, biomimetic sensors and applications

As mentioned above, to solve the problem of low detection of VOCs by humans, the fabrication of a more reliable and sensitive biomimetic vapour sensor will become of great importance. Biotechnology provides a viable approach to the development of such a device.

Biotechnology involves making use of living systems and organisms to develop useful products such as biosensors, programmed drug delivery, and the production of catalytic interfaces [4-6]. Biomimetic sensor technology makes use of artificial system to simulate biological systems in order to reproduce the five human senses or even to surpass them in their ability to overcome severe conditions and improve upon limited sensory ranges. Many sensors have been developed to measure the taste of foods [7], control the quality of foods [8], suppress bitterness [9] and so on. The sensor plays the role of recognition as well as reception, which artificially reproduces the sense of sight (optical sensor), hearing (pressure sensor), touch (pressure sensor and temperature sensor), smell (vapour or odour sensor), and taste (ion sensor or taste sensor). Overall, we can simply classify sensor types according to the subject of their measurements and the sensing materials used in their manufacture [10].

Normally sensors of sight, hearing and touch use readily available materials to receive only one physical quantity: light, sound and pressure respectively. The sensors, corresponding to the receptor parts of sight, hearing and touch (also called physical sensors), have been developed for many years in an active area of research. For smell and taste, many chemical substances must be assessed at once to be transformed into meaningful quantities to represent these senses. By comparison, the sensors which stimulate the senses of smell (also called chemical sensors) such as odour sensing [11-13] and taste [14-16] have been proposed relatively recently. For example, a biosensor, such as an enzyme and tissue sensor, is a kind of a chemical sensor made by immobilising biomaterials and related materials in combination with an electrochemical device to a sensing membrane that measures chemical substances.

In our daily life, the sense of smell (odour) is identified by the reception of the vapour followed by its perception in living systems. Similarly, the sense of taste involves receiving chemical substances. The sense of smell is powerful in detecting the smell of an enemy or prey in the dark of a forest. The sense of taste is used to judge whether anything to be taken into the mouth is beneficial or poisonous for the body. If we consider a situation where we need to measure two or more factors, it seems good to combine various effects simulated in sensors and different materials used for sensors. If we can visualise taste and smell quantitatively, a new world will be opened up [1]. In recent years, most odour sensors using several nonspecific receptors have one striking property. Different to

this type of sensor, a novel sensor has also been developed for high sensitivity detection of one molecule, such as using a receptor molecule in an artificial odour sensing system by extracting it from the biological membrane [1].

### **1.3 Aims of this study**

The main aim of this work is to produce an artificial membrane based reliable and sensitive vapour sensor for the detection of organic vapours which have a harmful effect on human health. Here, the lipid membranes are the sensing material. A quartz crystal microbalance (QCM) is used as the sensing transducer. The idea is to coat the lipid sensing film on quartz oscillators to produce the vapour sensor. On exposure to the target vapour, the sensing film will attract the vapour molecules and result in a crystal frequency shift. By detection the change of frequency then the vapour can be identified by analysing the output pattern.

Although a number of papers dealing with sensing behaviour optimisation or comparison of the lipid coated vapour sensors have been published [11] [17-18], there is a significant gap with regards to the study of reliable lipid sensing coating techniques and investigations of the relationship between lipid phase and sensitivity of the sensor. In this work, we use a quartz crystal microbalance (QCM), in combination with Atomic Force Microscopy (AFM) to study the reliability of spin-coated lipid films and to evaluate the effect of the lipid phase on the sensors' sensitivity.

The study will be structured as follows:

➤ Chapter 2:

Review of existing vapour sensing materials and techniques leading to the comparison of the existing method and technique used in this work, evaluation rules for vapour sensor

➤ Chapter 3:

Outline the theory of mass based lipids vapour sensor used in this work, including the biological function of lipids and introduction of sensing devices

➤ Chapter 4 and 5:

Description of experimental procedures and results for sensing film fabrication and characterisation

➤ Chapter 6

Design of vapour sensing system

➤ 7 and 8:

Results of vapour sensing and discussion of sensor property aspects including sensitivity improvement, including an example application for oil vapour sensing

➤ Chapter 9:

Conclusions and suggestions for future work

# Chapter 2 Review: materials and techniques

In the past decade, many devices and methods have been introduced for biomimetic odour and vapour sensing. A sensitive, reliable gas/vapour sensor should exhibit a stable and reproducible signal over a long period of time. There are several performance figures of merit for sensors, including sensitivity, selectivity, response time, reversibility, adsorptive capacity and the fabrication cost. To fabricate a reliable vapour sensor, we should consider two distinct elements: sensing material and transducer. A summary of relevant sensing materials, techniques and devices can be found in this chapter. In the first part, possible sensing materials are described. This is followed by a review of vapour sensing techniques and devices. Finally, the conclusions lead to the design of the lipid based vapour sensor described in this work.

## 2.1 Sensing material

Existing vapour sensors are classified into two types based on materials involved. One is a biomimetic material, the other one is a non-biomimetic material. There is also an alternative way to subdivide the vapour sensing material: inorganic compounds, such as metal oxides; and organic compounds such as lipids and polymers. Lipids are one of the organic materials used for sensing, and so this section reviews several recently used organic materials and the structures to which they can be applied.

Generally, sensors based on metal oxide semiconductor (MOS) structures exhibit significantly greater sensitivity to inorganic gases such as ammonia and a few types of VOCs such as alcohol. Whereas, some other VOCs which could cause health effects cannot be efficiently detected by MOS based sensors [19]. Compared to MOS sensors, organic sensing material based sensors are most frequently used to detect a wide range of

VOCs which can occur at room temperature. A brief summary of organic sensing materials will be given in this section.

### 2.1.1 Polymers

Upon adsorption, physical properties such as mass and dielectric properties will change when polymers are exposed to VOC vapours. There are various physical adsorption mechanisms by which VOCs molecules interact with polymer molecules, such as induced dipole/induced dipole interactions (also named London dispersion), dipole/induced dipole interactions, dipole/dipole interactions and hydrogen bonds (Lewis acidity/basicity-concept) [20]. Polymers for vapour sensing can be further classified into two types including conducting polymers and non-conducting polymers.

#### (a) Conducting polymer

Organic conducting polymers show reversible changes in conductance when chemical substances such as methanol, ethanol and toluene adsorb and desorb from the film surface. The organic conducting polymers used for vapour and odour sensors are derived from aromatic or heterocyclic compounds [21] (see examples in Figure 2-1).

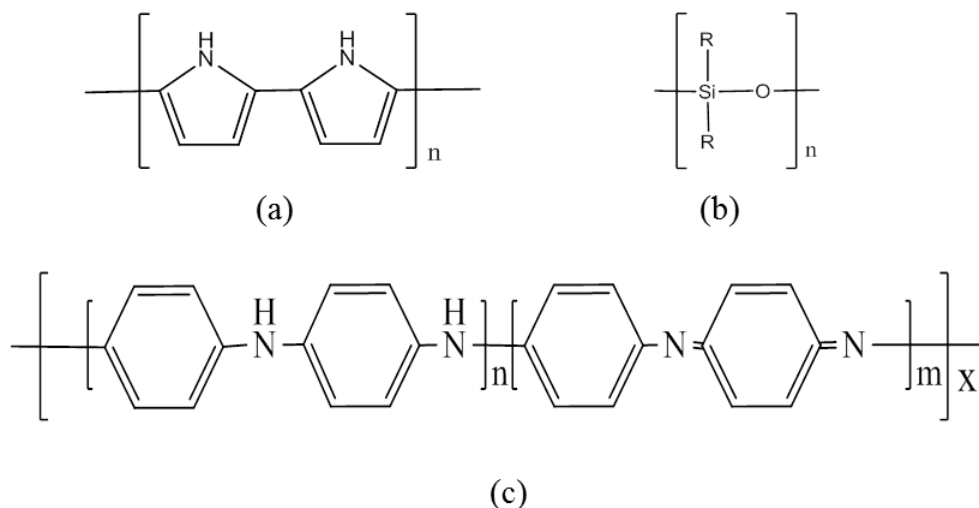


Figure 2-1 Chemical structure of (a) polypyrrole (b) polysiloxane (R is a wild card, standing for any hydrocarbon group) (c) polyaniline.

So far, a number of groups of conducting polymers have been investigated [22-23]. A variety of types of polymeric materials are commercially available. Polypyrrole (PPy) was first prepared by electrochemical growth across electrodes in 1968 [21] and has been

extensively studied [24]. Research into the chemical synthesis of other special polymers has been undertaken to optimise the selectivity and sensitivity, such as polysiloxane [25] and polyaniline (PTh) [26]. Studies also show the low conductivity of pure polymers can be improved through processes of doping by redox or protonation [19]. Mabrook et al, for example, report on the use of inkjet printed PEDOT-PSS doped poly(3,4-ethylene dioxathiophene) for alcohol sensing [27].

**(b) Non-conducting polymers**

Non-conducting polymers have been also widely used as vapour sensors. Depending on the different properties or physical adsorption mechanisms, polymers can be coated onto respective transducers. As a non-conducting polymer, polyimide (PI) has also been used on MOS vapour sensors as molecular sieves to enhance the selectivity of the sensor [19] (see Figure 2-2).

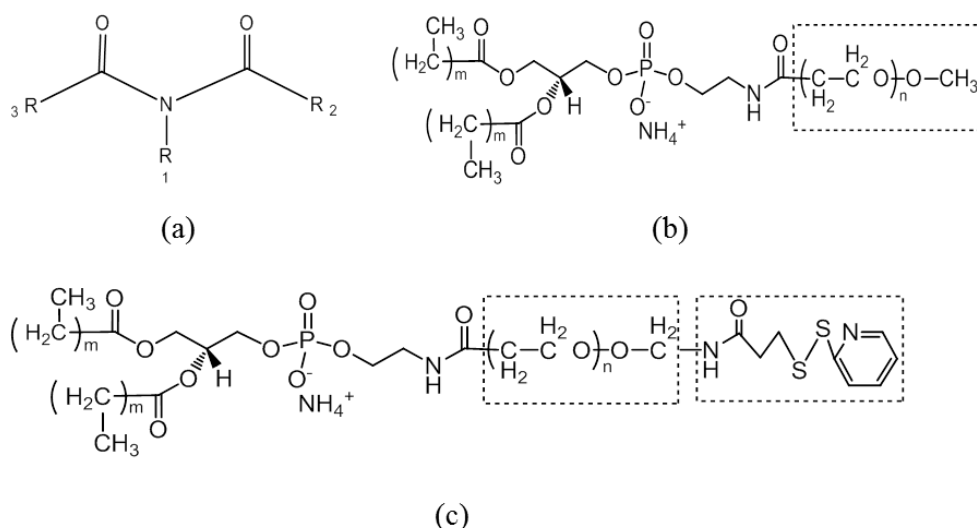


Figure 2-2 Chemical structure of (a) Polyimide (R is a wild card, standing for any hydrocarbon group) (PI) and PEGylated lipopolymers (b) terminated with ether groups (c) terminated with PDP. The n values are 22, 57, 57 and 113 for PEG 1000, PEG 3000 and PEG 5000 respectively.

Besides conducting and non-conducting polymers, a series of papers have been published recently on PEGylated lipopolymers for vapour sensing. One group has studied chemisorbed PEGylated lipopolymers used as a vapour sensing film [11], and PDP terminated PEGylated lipopolymers used as a subphase to improve the sensitivity of polymer or lipid vapour sensor [28]. Another one makes use of (pyridyldithio)propionate

(PDP) terminated PEGylated lipopolymers to stabilise the coating of gas chromatography (GC) materials based vapour sensors [29].

### 2.1.2 Carbon nanotubes

Due to their unique properties, carbon nanotubes (CNTs) have attracted attention in the gas sensing field (see Figure 2-3). The mechanism of CNT gas sensing is based on changes to the permittivity and conductivity when reacting with the gas. CNT based gas sensors have a good sensitivity at room temperature [19]. Although like other gas sensing materials, the response time and property of CNTs vary with different sensing gases.

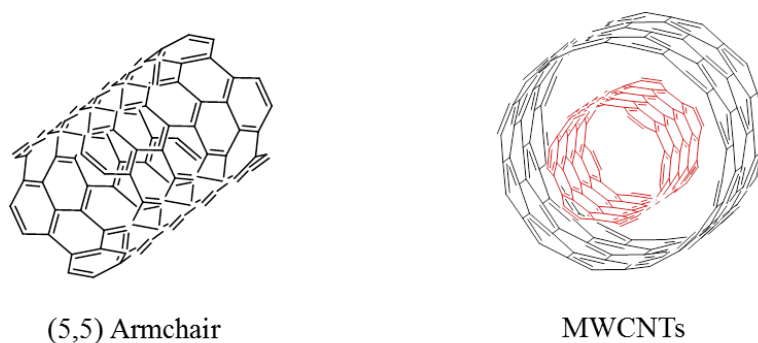


Figure 2-3 Schematic structure of SWCNTs (left) and MWCNTs (right).

Normally, CNTs can be classified into two types: single-walled carbon nanotubes (SWCNTs) and multiwall carbon nanotubes (MWCNTs). SWCNTs have been employed in Radio-Frequency Identification (RFID) tag antennas for toxic gas sensing [30], while MWCNTs are usually used for remote detection of inorganic gases such as carbon dioxide ( $\text{CO}_2$ ), oxygen ( $\text{O}_2$ ) and ammonia ( $\text{NH}_3$ ). CNTs are frequently decorated with other materials to improve the sensitivity and selectivity to certain gases [31]; e.g. in the detection of a partial discharge generated by the decomposition of sulphur hexafluoride ( $\text{SF}_6$ ) by CNTs based gas sensors [32].

### 2.1.3 Lipids

As the main component of cell membranes within human body, lipids play an outstanding role in biological chemoreception schemes [33]. The mechanical properties of lipids are expected to contribute to the complex function of a cell. Normally, lipids possess remarkable chemical-sensing properties, and are used for the detection of odorants by



organic solvents. Lipid molecules contain a large hydrocarbon portion and not many polar functional groups. The amount of these compounds account for their solubility behaviour.

In summary, the materials described so far respond to both water vapour and flammable gases. Among them, the ease of tailoring the molecule and improved sensitivity and selectivity makes organic materials often offer advantages over inorganic compounds. As a popular structure with which to model cell membranes, lipid formed membranes show promise for applications in biomimetics and diagnostic devices [37-39]. Although several studies have already been reported which use lipids as vapour sensors in the past decade, the sensing mechanism and response properties of different lipids is only partially understood [11] [17-18]. Thus, in this thesis, a lipid is chosen as the vapour sensing material.

## **2.2 Review of gas and vapour sensing techniques**

When the sensing gas/vapour is applied to the sensor, gas/vapour molecules interact with solid-state sensors by adsorption and chemical reaction with sensing films. The second distinct element of a vapour sensor, the transducer, detects the physical and/or chemical changes incurred by these processes and these changes are measured as an output signal (e.g. an electrical voltage). Based on different detection principles, vapour sensors can be classified into several different types. The four most common types of devices used as a transducer are summarised and compared in this section.

### **2.2.1 Techniques based on variation of electrical properties**

The main principle here is the detection of the electrical changes incurred during the gas/vapour interaction process. This method can be further catalogued by measurements of current, potential or impedance. These types of sensors are also known as electrochemical sensors.

#### ***(a) Amperometric gas/vapour sensors***

The working principle of amperometric gas/vapour sensors is detecting the current induced by the reaction (either oxidised or reduced) of a sensing material and gas/vapour over a scanned potential range. The current is induced by the adding or withdrawing of electrons from the electrode by the ambient gas/vapour. The amperometric gas/vapour

sensors are similar to other amperometric sensors with semi-permeable membranes that are used for gas/vapour diffusion.

A good example is a thin film microelectrode device with three coplanar electrodes deposited on a SiO<sub>2</sub>/Si wafer substrate used to detect concentrations of CO<sub>2</sub> in pure nitrogen [40].

**(b) Potentiometric gas/vapour sensors**

A potentiometric sensor is a type of chemical sensor that is used to detect the potential difference between the membrane coated working electrode and the reference electrode with zero current flow, and then to determine the analytical concentration of some components of the gas/vapour. The working electrode's potential depends on the concentration of the gas/vapour. The reference electrode is needed to provide a defined reference potential. The potential change is obtained from the interaction of electrically neutral gas/vapour molecules with the sensor. Based on the absorption of a gas/vapour into an electrolyte (solid or liquid) via the porous metal electrode, either ions or electrons at the interface within the sensor are then generated which results in a potential difference at the sensor head.

As potentiometric gas/vapour sensors, a suspended gate field effect transistor (SGFET) has been used to detect nitrobenzene, nitrotoluene and methanol gases/vapours [41]. Another example is metal-oxide-semiconductor field-effect transistor (MOSFET) based gas/vapour sensors [42-44]. A typical structure of a MOSFET-based sensor is shown in Figure 2-5 [42].

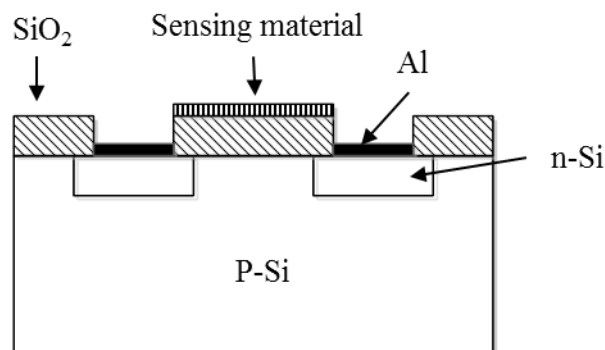


Figure 2-5 Structure of MOSFET gas/vapour sensor with gas/vapour sensitive membrane deposited on top of SiO<sub>2</sub> (reproduced from [42]).

(c) *Impedimetric gas/vapour sensors*

If alternating current (ac) is applied to a material, the ratio  $V/I$  is known as the impedance, where  $V$  is rms voltage and  $I$  is rms current. In many materials, especially those which are not generally regarded as conductors of electricity, the impedance varies as the frequency of the applied voltage changes, due to the conductivity properties of the sensing material. If a measurement of impedance over a suitable frequency range is made, it is possible to relate the results to the physical and chemical properties of the material. This is known as Electrochemical Impedance Spectroscopy (EIS).

Impedimetric sensors (also known as chemiresistors), comprise two electrodes coated with a gas/vapour sensitive layer on the surface, and measure the impedance change induced by changes in the concentration of mobile charges in conducting materials when reacting with gas/vapour. The reason for the change can be explained as when a voltage is applied to the electrodes, conduction electrons and holes are able to travel through the thin film from one electrode to the other. On exposure to a gas/vapour, a reaction, either increasing or decreasing the number of available charge carriers, takes place. A number of materials have been used as the active sensing layer including metal oxides [45-51] and conducting polymers [43] [45] [52-54]. A typical structure of an impedimetric sensor is shown in Figure 2-6.

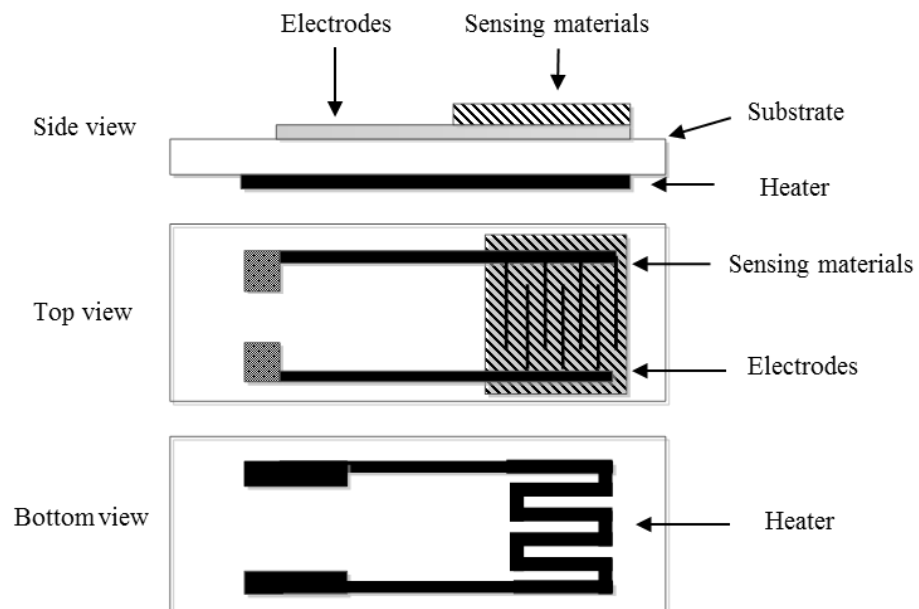


Figure 2-6 Typical structure of a conductivity sensor (reproduced from [54]).

## 2.2.2 Techniques based on variation of thermodynamic properties

The first law of thermodynamics states that any process involving a change in internal energy also absorbs or generates heat or work. The main principle of thermal gas/vapour sensing is detecting the heat evolved (i.e. temperature variation more directly) when the sensing materials interacts with a gas/vapour.

Specifically, there are two main types of thermal sensors. One is pyroelectric sensors and the other one is pellistor sensors. The pellistor, known as calorimetric in nature, can be further classified into thermal conductivity (TC) sensors and catalytic sensors.

### (a) *Pyroelectric sensors*

Pyroelectricity describes a property of certain materials that generate a temporary voltage by acquiring different charges on opposite faces when they are heated or cooled [55]. Materials which have the property include certain crystals, ceramics and polymeric materials. This type of sensor consists of pyroelectric materials with two evaporated electrodes as metal contacts. One of the electrodes has a layer of the sensitive material; the second is used as a reference electrode. When a heat changes (loss or gain of heat) is induced by the interaction between the gas/vapour and sensing material, the voltage will be generated by the pyroelectric materials. By detecting the electrical response of the device, the sensing gas/vapour can be detected [56].

### (b) *Pellistor sensors*

Pellistor sensors are used to detect either combustible gases or those having a significant difference in thermal conductivity compared to that of air [57]. Such sensors measure the temperature variation created by the gas/vapour combustion enthalpy or thermal conductivity separately by a platinum resistance temperature detector or a thermistor.

#### (i) **Thermal conductivity sensors**

The working principle of TC sensors is based on the detection of the heat dissipation into the target gas/vapour which is linked to their thermal conductivity. When the target gas/vapour is pumped into the gas/vapour chamber, the heater/calorimeter (e.g. platinum, tungsten wire, thermistor) in the centre is then heated to a specific temperature. The

gas/vapour is then identified by the thermal conductivity worked out from the resistance of the heater [58-59].

TC sensors have large detection ranges, good stability, and reliability. They require comparatively simple measurement equipment. But accuracy and sensitivity needs to be enhanced further.

### (ii) Catalytic gas sensors

Catalytic gas sensors (pellistors), designed specifically for the detection of flammable gases within air, detect the heat evolution from catalytic oxidation of the gas analyte. The heat evolved is achieved by burning the target gas to generate a specific combustion enthalpy. Figure 2-7 is the schematic diagram of a catalytic sensor.

This type of sensor consists of a high surface area catalytic layer coated on a ceramic bead, and a platinum coil in the bead acts as the heater. When the platinum coil is heated until the catalytic layer reaches a certain designated temperature, the combustible gas will burn on the catalytic layer surface. The generated heat will change the resistance of the coil, and then the heat can be measured by simple circuits [19].

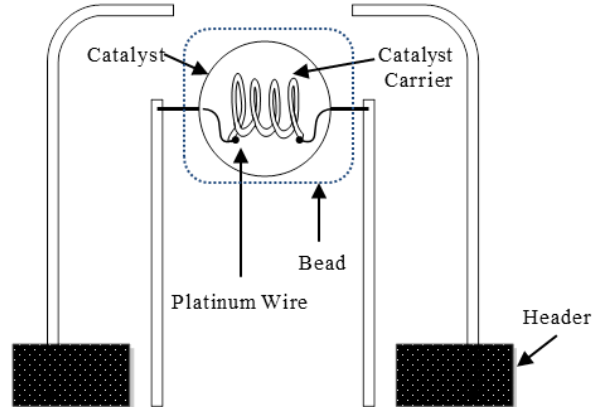


Figure 2-7 Schematic diagram of catalytic sensor configuration of a ceramic bead (reproduced from [19]).

### 2.2.3 Techniques based on variation of optical properties

The main principle of optical gas/vapour sensing is detecting the optical property change of the sensing materials when it interacts with gas/vapour. Normally optical methods can achieve higher sensitivity, selectivity and stability than non-optical methods. The relatively short response time of this method enables real time detection. However, their applications

on gas/vapour sensors are restricted by relatively high cost. Optical methods for gas/vapour sensing are mostly based on spectroscopy involving techniques based on adsorption and emission spectrometry [19].

**(a) Adsorption spectrometry based gas/vapour sensors**

Based on the Beer-Lambert law (see equation 2-1), adsorption spectrometry is the concentration dependent adsorption of the photons at specific wavelengths [60]. The precise wavelengths for specific gases can be found in a high-resolution transmission molecular absorption (HITRAN) database [61]. There are many types of adsorption spectrometry including Differential Optical Adsorption Spectroscopy (DOAS) [62], Tunable Diode Laser Adsorption Spectroscopy (TDLAS) [63], Intra-Cavity Adsorption Spectrometry (ICAS) [64], etc. The relevant gas/vapour sensors such as infrared (IR)-source adsorption gas/vapour sensors and optical fibre gas/vapour sensors have been used widely [19] [65].

$$A = \epsilon lc \quad (2-1)$$

$A$  = absorbance

$\epsilon$  = molar absorptivity [ $\text{cm}^2/\text{mol}$ ]

$l$  = length of solution the light passes through [cm]

$c$  = concentration [ $\text{mol}/\text{cm}^3$ ]

**(b) Emission spectrometry based sensors**

Emission spectrometry makes use of the phenomenon that excited atoms emit photons and go back to the ground state to make any relevant analysis. Emission spectrometry based gas/vapour sensors detect the transfer of energy caused by boundary conditions between sensing materials and gas/vapour. Laser-Induced Breakdown Spectroscopy (LIBS) is one type of spectroscopy based on emission spectrometry [66]. Fourier Transform Infrared Spectroscopy (FTIR) can be used as both adsorption and emission spectrometry [67].

**(c) Other optical gas/vapour sensors**

There are also many other types of optical gas/vapour sensors which are difficult to classify. They can be separate from their working mechanisms. To explain the working principle of some modern optical gas/vapour sensors, more specifically, we take fibre

optical gas/vapour sensors and Surface Plasmon Resonance based gas/vapour sensor as examples.

**(i) Fibre optic gas/vapour sensor**

The sides or tips of optic fibres (core) are coated with a lower refractive index sensing material (cladding). Because of the adsorption of light at a range of frequencies, only part of the light beam will be transmitted to the end of the fibre by total internal reflection at the interface of core and cladding. When the sensor is surrounded by the sensing gas/vapour the optical property changes in the cladding involving intensity change, spectrum change, life time change or wavelength shift in fluorescence [45] [68] will make a further change in the amount of light transmitted down the fibre. Figure 2-8 illustrates the principle of a gas/vapour optical fibre sensor. It represents how the vapour interacts with the material and causes a shift in the wavelength of the propagating light wave.

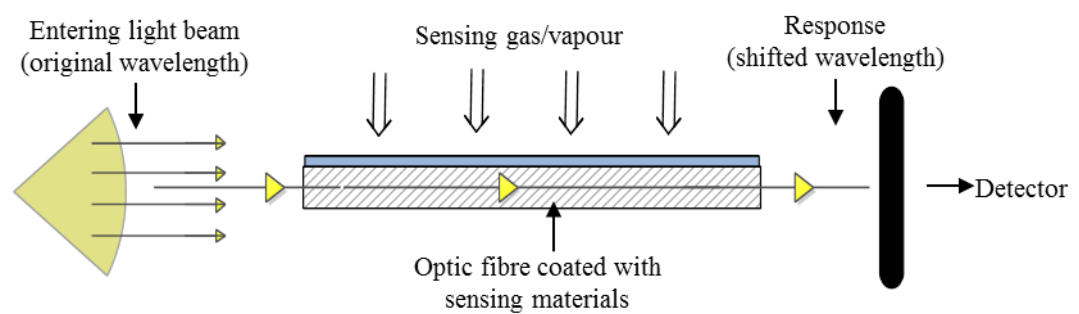


Figure 2-8 The working principle of a gas optical fibre sensor.

**(ii) Surface plasmon resonance based gas/vapour sensor**

Surface plasmon resonance (SPR) is the phenomenon when the frequency of incident light on a metal surface matches the natural frequency of surface electrons oscillating against the restoring force of positive nuclei. Thus, the resonance condition is established by collective oscillation of valence electrons emission in a solid stimulated by incident light. A SPR system based gas sensing device, also known as a Kretschmann configuration, consists of a laser beam, prism and a photodiode detector used to record the reflected intensity of the beam (see Figure 2-9).

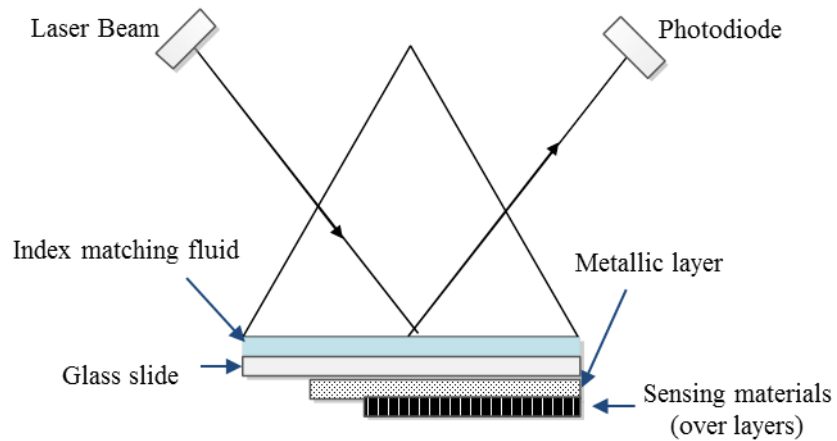


Figure 2-9 Kretschmann configuration of SPR investigation.

When lasers illuminate the sensing surface (metallic layer and over layers) via a prism at a certain angle, the parallel component of the light wave vector will match that of the surface plasmon of the metallic film at the opposite surface of prism and be attenuated. A minimum reflected intensity is reached at this point (also called the SPR minimum). By scanning the laser through a range of angles, the intensity of the reflected light against incident angle can be plotted. The transfer of energy from the evanescent wave to the surface plasmon will change when the metallic layer is loaded (deposition on the metallic layer or any interaction between the metallic layer, over layer and any external compounds). Exploiting the surface plasmon sensitivity to the boundary conditions, it is possible to use the SPR technique for detecting different gases.

#### 2.2.4 Techniques based on variation of ultrasonic properties

Gas sensors based on chemical principles experience some intrinsic weakness, such as short lifetime and secondary pollution, which are difficult to overcome. Sensors based on the ultrasonic method (mass gas sensing devices) can avoid those weaknesses. The main working principle of mass gas sensing is based on the piezoelectric effect (details will be described in chapter 5). Piezoelectricity, similar to pyroelectricity, is a property of certain materials which will generate a temporary voltage by acquiring different charges on opposite faces when they are applied to an outer force. These materials include crystals and certain ceramics etc. This type of sensor detects the physical total mass change when a sensor interacts with a gas.

**(a) Surface acoustic wave (SAW) gas/vapour sensors**

A surface acoustic wave (Rayleigh wave) is electrically excited in a piezoelectric single-crystal plate substrate by use of a metallic interdigitated transducer (IDT) structure. One IDT works as transmitter, the other IDT works as receiver. The delay time  $t_d$  between the electrical input and the output signal is determined by equation 2-4.

$$t_d = \frac{l}{v} \quad (2-4)$$

$t_d$  = delay time between the electrical input and the output signal [s]

$l$  = distance between input and output transducer [m]

$v$  = speed [m/sec]

The maximum acoustic-electric interaction occurs at a characteristic frequency  $f_0$  defined by equation 2-5.

$$f_0 = \frac{v}{\lambda_0} \quad (2-5)$$

$f_0$  = characteristic frequency [Hz]

$v$  = speed [m/sec]

$\lambda_0$  = wavelength [m]

The typical structure of SAW sensor is shown in Figure 2-10. It is composed of a piezoelectric substrate with an input and output interdigitated transducer deposited on the top of the substrate, and the gas sensing material deposited between the two transducers [69].

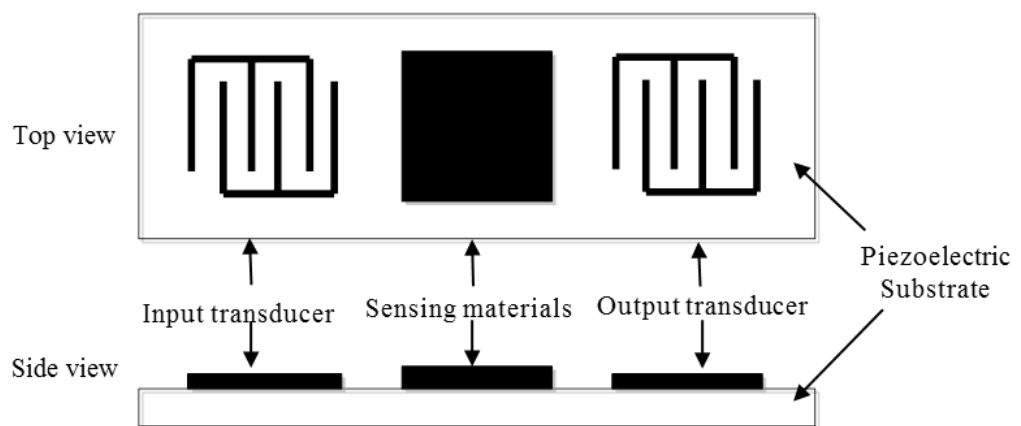


Figure 2-10 SAW sensor.

When an ac signal is applied, the Rayleigh wave is generated and propagates along the crystal at a depth of one wavelength at operating frequencies between 100 to 400 MHz [45]. The frequency of this wave will change when the mass of the sensing material changes caused by adsorption of gas/vapour, given by equation 2-6 [43] [45] [68].

$$\Delta f = \Delta f_p c_v K_p / \rho_p \quad (2-6)$$

$\Delta f_p$  = change in frequency caused by the membrane [Hz]

$c_v$  = vapour concentration [mol/L]

$K_p$  = partition coefficient [ $s^{-1}$ ]

$\rho_p$  = density of the sensing membrane [mol/L]

**(b) Quartz crystal microbalance (QCM) gas/vapour sensors**

As another piezoelectric property based sensing device, the interest in QCM has increased with much of the research focused on polymer, ionic liquids, lipid films, and oxidised metal sensing of gas/vapour over recent years. QCM sensors operate using the same principle as SAW sensors. The advantages of this approach are low cost, compact volume, ease of portability, high sensitivity and a quick response.

The sensing membrane is deposited onto the surface of the quartz crystals. By using QCM, the sensing membrane mass change incurred by adsorption of gas/vapour can be monitored (see Figure 2-11).

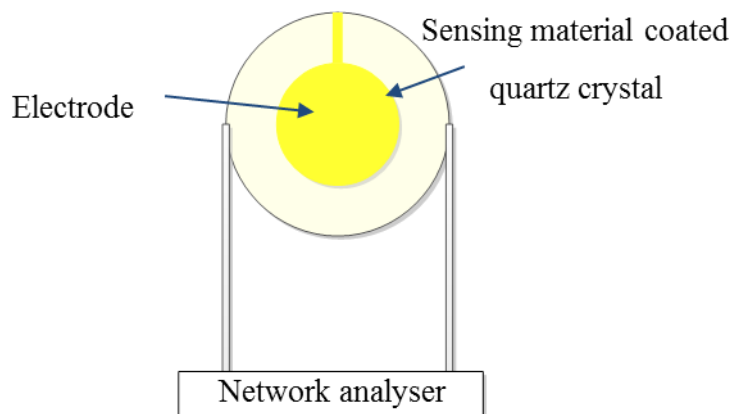


Figure 2-11 QCM with sensing membrane coating.

The linear relationship between the mass adsorbed to a QCM device and the resonance frequency is described by the Sauerbrey equation (equation 2-7) [70] (details will be further discussed in section 3.5). The main output to be measured is the shifting of quartz

oscillation frequency which allows the total /mass adsorption to be determined. Ultimately, this information will be invaluable to the manufacture of a bio-inspired membrane based sensor which can provide tailored sensitivity to particular vapour chemistry.

A number of studies have been published, aiming at the fabrication of QCM sensor. This includes pegylated lipid coated odour sensors [11], liquid GC material coated odour sensors [29], ionic liquid coated vapour sensor [71], siloxane polymer coated vapour sensors [25], olive oil coated gas sensor [72]. The QCM sensor benefits from various sensing film coating techniques, including spin coating [17], drop coating [18], self-assembly [73], Langmuir-Blodgett [74] which will be further discussed in chapter 4.

$$\Delta f = -C_f \times \Delta m \quad (2-7)$$

$\Delta f$  = shifting of quartz crystal frequency [Hz]

$C_f$  = constant related to the property of the crystal and driving mode [Hz/ng/cm<sup>2</sup>]

$\Delta m$  = change in mass per unit area [g/cm<sup>2</sup>]

To sum up, conducting polymer, carbon nanotubes and metal oxide conductivity gas/vapour sensors, thermal gas/vapour sensors, optical gas/vapour sensors, SAW and QCM piezoelectric gas/vapour sensors have been reviewed in this section. The sensing principles and the typical characteristics of the various types of sensors have been reviewed. These systems offer excellent discrimination and lead the way for a generation of smart sensors which will mould the future commercial markets for gas/vapour sensors. The comparison of the principle of operation, advantages, disadvantages and applications of each sensor have been more clearly compared and outlined in Table 2-1.

### 2.3 Summary

A review of gas/vapour sensing materials and sensing devices has been summarised in this chapter. Overall, all the described sensor types have their own advantages and disadvantages depending on the operating environment. The electrical sensors show a good response to a wide range of analytes and have fast response and recovery times, but they are normally limited to certain materials (depends on the conductivity). Thermal sensors, which require high temperatures, are also not suitable for lipids. Possible sensing techniques could be optical gas sensors and mass change gas sensors. Comparing the two vapour sensing techniques, the relevant devices of optical gas sensors are usually

expensive. Mass change based gas sensors have the advantage that they have a diverse range of coating methods and relatively low cost. Whilst the SAW sensors are highly sensitive mass sensors, the requirement of reproducibility will make processing complex. QCM, known as a simple and low cost ultra-sensitive device based on the piezoelectric effect, can not only be used to study the coating of lipid membranes, but can also be used as a transducer of lipids based vapour sensor. The quartz crystal substrates can also be modified by diverse methods to provide a suitable hydrophilic or hydrophobic interface for the amphiphilic lipid deposition. Various methods can be used for modifying the crystal surface including spin coating, self-assembled monolayers (SAM), or physical vapour deposition (PVD) applied by sputtering or thermal evaporation, which will be further discussed in chapter 4. For these reasons, QCM is the most promising solution for the intended application. Thus, lipids and Quartz Crystal Microbalance (QCM) have been chosen to work as the sensing material and the transducer of the vapour sensor, respectively. Furthermore, QCM is also used for sensing film characterisation. The sensing technique used in this work in quartz crystal microbalance which has been briefly introduced in section 2.2.4 (b) and will be described in detail in section 3.2.

The coming chapter will further discuss the sensing material (lipid) structures and the operation theory of the transducer (QCM) leading to a better understanding of the sensing film structure and sensing mechanism.

Table 2-1 Summary of the properties of each sensor type reviewed part-I

Sensor devices	Sensor type	Physical changes	Target Gases and Application Fields	Advantages	Disadvantages	References
Electrical gas sensors	Metal oxide semiconductor gas sensor (MOSFET)	<ul style="list-style-type: none"> <li>• Conductivity</li> <li>• Work function</li> <li>• Threshold voltage change</li> </ul>	<ul style="list-style-type: none"> <li>• Industrial applications and civil use</li> </ul>	<ul style="list-style-type: none"> <li>• Low cost</li> <li>• Short response time and fast recovery time</li> <li>• Integrable and reproducible</li> </ul>	<ul style="list-style-type: none"> <li>• High energy consumption</li> <li>• Relatively low sensitivity and selectivity</li> <li>• Sensitive to environmental factors</li> <li>• Limited range of coatings</li> </ul>	[19] [45] [68] [75-77]
	Polymer conductivity gas sensor	<ul style="list-style-type: none"> <li>• Conductivity</li> </ul>	<ul style="list-style-type: none"> <li>• Indoor air monitoring</li> <li>• Storage place of synthetic products as paints, wax or fuels</li> <li>• Workplaces like chemical industries</li> </ul>	<ul style="list-style-type: none"> <li>• Low cost of fabrication</li> <li>• Short response time and recovery time, high sensitivity</li> <li>• Simple and portable structure</li> <li>• Low energy consumption</li> <li>• Diverse range of coatings</li> </ul>	<ul style="list-style-type: none"> <li>• Poor selectivity</li> <li>• Long-time instability and irreversibility</li> <li>• Sensitive to environmental factors</li> </ul>	[68] [78]
	Carbon nanotubes gas sensor	<ul style="list-style-type: none"> <li>• Conductivity</li> </ul>	<ul style="list-style-type: none"> <li>• Detection of partial discharge (PD)</li> </ul>	<ul style="list-style-type: none"> <li>• Ultra-sensitive and quick response time</li> <li>• Great adsorptive capacity</li> <li>• Large surface-area-to-volume ratio</li> <li>• Low weight.</li> </ul>	<ul style="list-style-type: none"> <li>• High cost</li> <li>• Difficulties in fabrication and repeatability</li> </ul>	[79]

Table 2-1 Summary of the properties of each sensor type reviewed part-II

Sensor devices	Sensor type	Physical changes	Target Gases and Application Fields	Advantages	Disadvantages	References
Thermal gas sensors	<ul style="list-style-type: none"> <li>Pyroelectric gas sensors</li> <li>Pellistor gas sensor</li> </ul>	<ul style="list-style-type: none"> <li>temperature</li> </ul>	<ul style="list-style-type: none"> <li>Most combustible gases under industrial environment</li> <li>Petrochemical plants</li> <li>Mine tunnels</li> <li>Kitchens</li> <li>Remote air quality monitoring</li> </ul>	<ul style="list-style-type: none"> <li>Low cost</li> <li>Adequate sensitivity for industrial detection (parts-per-thousand range)</li> <li>Stable at ambient temperature</li> </ul>	<ul style="list-style-type: none"> <li>Intrinsic deficiencies in selectivity</li> <li>Risk of catalyst poisoning and explosion</li> </ul>	[80-81]
	Optic gas sensors	<ul style="list-style-type: none"> <li>Spectroscopy gas sensor</li> <li>Other types e.g. SPR gas sensor</li> </ul>	<ul style="list-style-type: none"> <li>Intensity</li> <li>Spectrum</li> </ul>	<ul style="list-style-type: none"> <li>Gas leak detection systems with high accuracy and safety</li> <li>High-end market applications</li> </ul>	<ul style="list-style-type: none"> <li>High sensitivity, selectivity and stability</li> <li>Long lifetime</li> <li>Insensitive to environment change.</li> </ul>	<ul style="list-style-type: none"> <li>High cost</li> <li>Difficulty in miniaturisation</li> </ul>
Mass gas sensors	SAW gas sensor	<ul style="list-style-type: none"> <li>Mass</li> </ul>	<ul style="list-style-type: none"> <li>VOCs and pollution gas check</li> </ul>	<ul style="list-style-type: none"> <li>High sensitivity and good response time</li> <li>Diverse range of coating</li> <li>Long lifetime</li> <li>Avoiding secondary pollution</li> <li>Integrated circuit (IC) intergratable</li> </ul>	<ul style="list-style-type: none"> <li>Sensitive to environmental change</li> <li>Difficult to reproduce</li> </ul>	[45] [48] [68]
	QCM gas sensor	<ul style="list-style-type: none"> <li>Mass</li> </ul>	<ul style="list-style-type: none"> <li>VOCs and pollution gas check</li> </ul>	<ul style="list-style-type: none"> <li>Diverse range of coatings</li> <li>Good batch to batch reproducibility</li> </ul>	<ul style="list-style-type: none"> <li>Sensitive to environmental change</li> <li>Complex circuitry</li> </ul>	[68] [76]

# Chapter 3 Lipid based QCM vapour sensor

As mentioned in earlier chapters, the aim of this work is to fabricate a lipid based QCM vapour sensor. To design a vapour sensor with good operational stability, it is crucial to fully understand the properties and structure of the materials and the operating principle of the measurement system.

Detailed descriptions of the lipids, lipids structure and vapour sensing device (transducer) used in this work are contained in this chapter.

## 3.1 Lipids

Lipids, used as sensing material in this work, are expected to exhibit mechanical properties that contribute to the complex function of a cell. Several structures of lipids that may be applicable are reviewed in this section, leading to a brief introduction to the experimental plan of sensor fabrication. The two phospholipids and cholesterol used in this study are also introduced next.

### 3.1.1 DSPC, DLPC and cholesterol

Lipids typically contain a hydrophilic head group that is soluble in water and a hydrophobic part normally containing one or two alkyl tails, which are insoluble in water. As such they have a tendency to self-organise and form bilayers and vesicle type structures by gathering the hydrophobic chains inside and facing the hydrophilic group to the water [1]. At a given temperature, a lipid and its bilayer will exist in either liquid or a gel (solid) phase. Normally, at higher temperatures, the lipids exist as a liquid disordered phase, have a high mobility and ‘wander’ around the surface; their tails are disordered and wiggle

around. At lower temperature, lipids tails all go straight, line up and lock in place. The two phases of a lipid can transition between each other when the temperature changes. The characteristic temperature at which the phase transition happens is called the transition temperature. A schematic diagram of the lipid molecules and lipid phase is shown in Figure 3-1.

The phase behaviour of a lipid bilayer is largely determined by the strength of the attractive Van der Waals interactions between adjacent lipid molecules. Longer tailed lipids have more area over which to interact, increasing the strength of this interaction and consequently decreasing the lipid mobility. Thus, at a given temperature, a shorter tailed lipid will be more fluid than a long-tailed lipid [83].

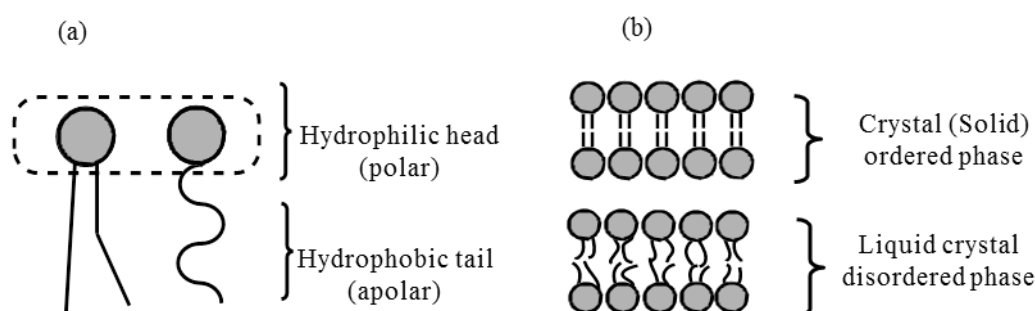


Figure 3-1 The schematic diagram of the (a) the structure of a normal lipid molecules (b) the structure of lipid phases.

Two saturated fatty acid phospholipid lipids with a similar structure were chosen to prepare the biological structure used in this thesis. 1,2-dilauroyl-*sn*-glycero-3-phosphocholine (DLPC) and 1,2-dioctadecanoyl-*sn*-glycero-3-phosphocholine (DSPC) were purchased as powder from Avanti Polar Lipids (Alabaster Inc. AL, USA) without further purification. The chemical structure and properties of the two lipids and cholesterol are shown in Figure 3-2 and Table 3-1.

Two phospholipids are zwitterionic lipids, with exactly the same hydrophilic head and glycerol linker. The only difference is the length of the hydrophobic alkyl tails. As mentioned before, at room temperature (25 °C), DSPC will exhibit a gel phase and DLPC will exhibit a relatively higher mobility fluid phase.

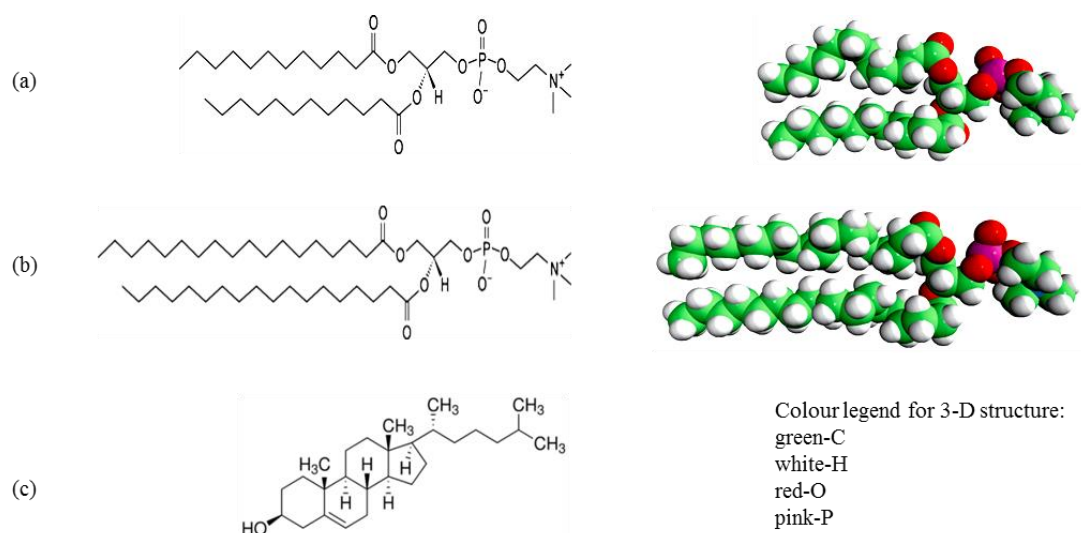


Figure 3-2 Chemical and 3-Dimensional structures of (a) DLPC, (b) DSPC and (c) chemical structure of cholesterol (reproduced from [204]).

Table 3-1 Properties of DLPC and DSPC

Name	Synonyms	Molecular Formula	Molecular Weight	Exact mass	Storage Temperature (°C)	Transition Temperature (°C)
DLPC	1, 2-dilauroyl- <i>sn</i> -glycero-3-phosphocholine	C <sub>32</sub> H <sub>68</sub> NO <sub>8</sub> P	621.826	621.437	-20	-1
DSPC	1, 2-distearoyl- <i>sn</i> -glycero-3-phosphocholine	C <sub>44</sub> H <sub>88</sub> NO <sub>8</sub> P	790.145	789.625	-20	55
Cholesterol	3β-hydroxy-5-cholestene 5-cholesten-3β-ol	C <sub>27</sub> H <sub>46</sub> O	386.65	n/a	-20	147-149

The percentage composition of DLPC is C 61.81% H 10.37% N 2.25% O 20.58% P 4.98%

The percentage composition of DSPC is C 66.88% H 11.23% N 1.77% O 16.20% P 3.92%

### 3.1.2 Vesicles and vesicle fusion

Vesicles, also known as liposomes, are formed from thin liquid crystalline bilayers when they are hydrated, become fluid and swell. More technically, a vesicle (liposome) is a small membrane enclosing aqueous core. A typical structure of vesicle is shown in Figure 3-3. The method to prepare vesicles in the lab will be described in section 4.3.

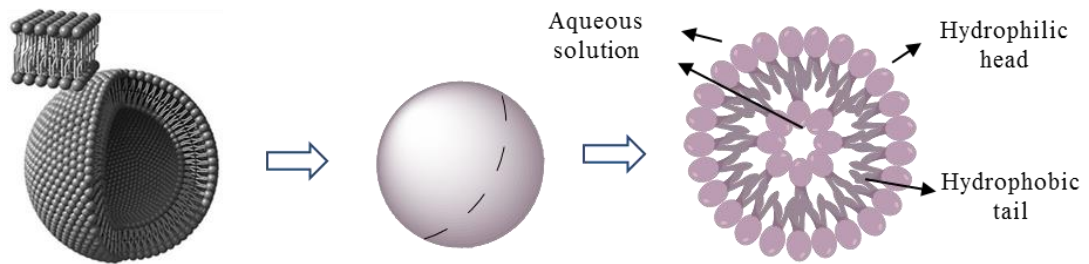


Figure 3-3 Cross-sectional scheme of how a simple vesicle exists in a hydrophilic solution (part reproduced from [87]).

Vesicles are spherical membranes, which can be also visualised as a bubble of liquid within another liquid. They often remain isolated in the cytoplasm and occur in most cells but are especially abundant in smooth endoplasmic reticulum [84]. Vesicles can form naturally because of the properties of lipid and lipid membranes [85-86]. Most vesicles have specialised functions depending on what materials they contain.

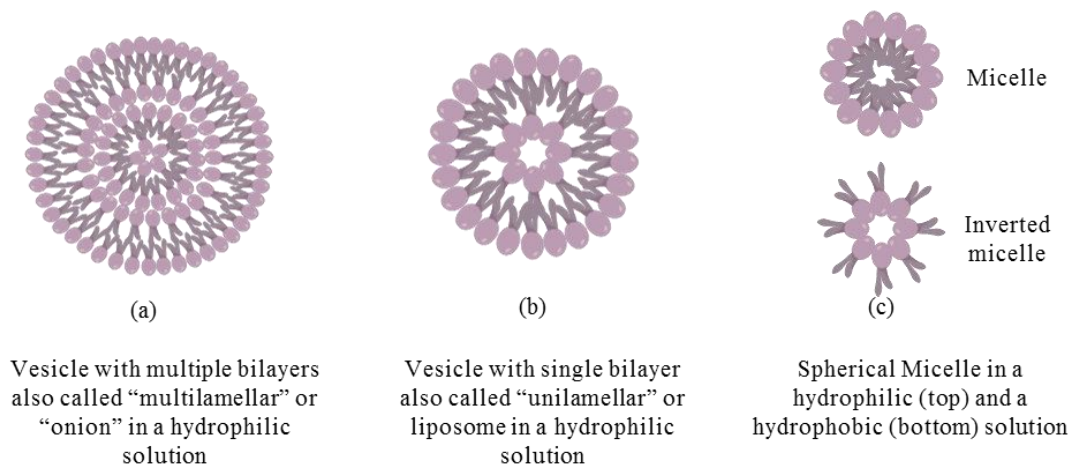


Figure 3-4 Three different cross-sectional structures of phospholipids.

Table 3-2 Types of vesicles

Classification	Number of Layers	Label	Size
<b>Small</b>	Unilamellar	SUV	30-100 nm
<b>Large</b>	Unilamellar	LUV	100-5000 nm
<b>Giant</b>	Unilamellar	GUV	5-100 microns
<b>Small</b>	Multilamellar	SMV	30-100 nm
<b>Large</b>	Multilamellar	LMV	n/a

There are different types of vesicles as shown in Table 3-1 and Figure 3-4. Vesicles can be classified by the number of layers and the size of the liposome. Normal vesicles consist of a single bilayer, also called unilamellar vesicles. Vesicles with a multi-bilayer are called multilamellar vesicles or an “onion”. Lipids will form single layers (also called micelles) spontaneously during hydration. Small vesicles are defined as mean vesicles with diameters of less than 100 nm. Large vesicles have diameters in the 100-5000 nm range. Giant vesicles usually mean those with a diameter from 5 microns up to 100 microns.

The thermal fusion of lipid vesicles on a solid substrate is the most simple and widely used method for preparing supported lipid bilayers (SLBs). This method has been used in this research and will be described further below and in section 4.3. A schematic showing the mechanism of vesicle fusion is in Figure 3-5.

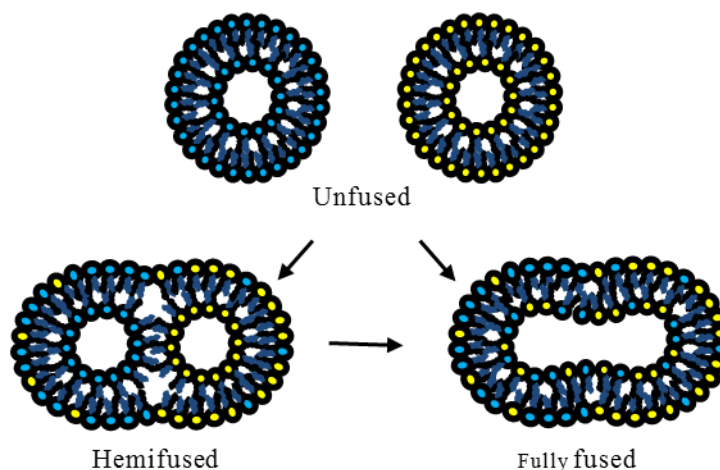


Figure 3-5 Illustration of lipid vesicles fusion showing two possible outcomes: hemi-fusion and full fusion.

After vesicles are formed (preparation procedures will be described in section 4.3), the fusion step is achieved by three main steps. Firstly, after the vesicle suspension is deposited on a solid substrate, isolated adsorbed vesicles rupture spontaneously. Secondly, adjacent adsorbed vesicles fuse and rupture to form a bilayer. Thirdly, the edge of a bilayer patch induces the rupture of neighbouring vesicles to produce planar membranes. There are several parameters that govern SLB formation including vesicles curvature energy, lipid suspension composition, temperature, critical vesicular coverage, electrostatic interactions, presence of calcium ions, pH of the solvent and the roughness of solid support [87-89].

### 3.1.3 Monolayer, bilayer and cell membrane

A monolayer is a single closely packed layer of lipids. A bilayer is a double layer of closely packed lipids. SLBs are always a single unilamellar bilayer on a hydrophilic solid substrate with a thin layer of water between. The schematic diagram of a monolayer, bilayer and the supported lipid bilayer sheet, formed on a glass substrate, is shown in Figure 3-6.

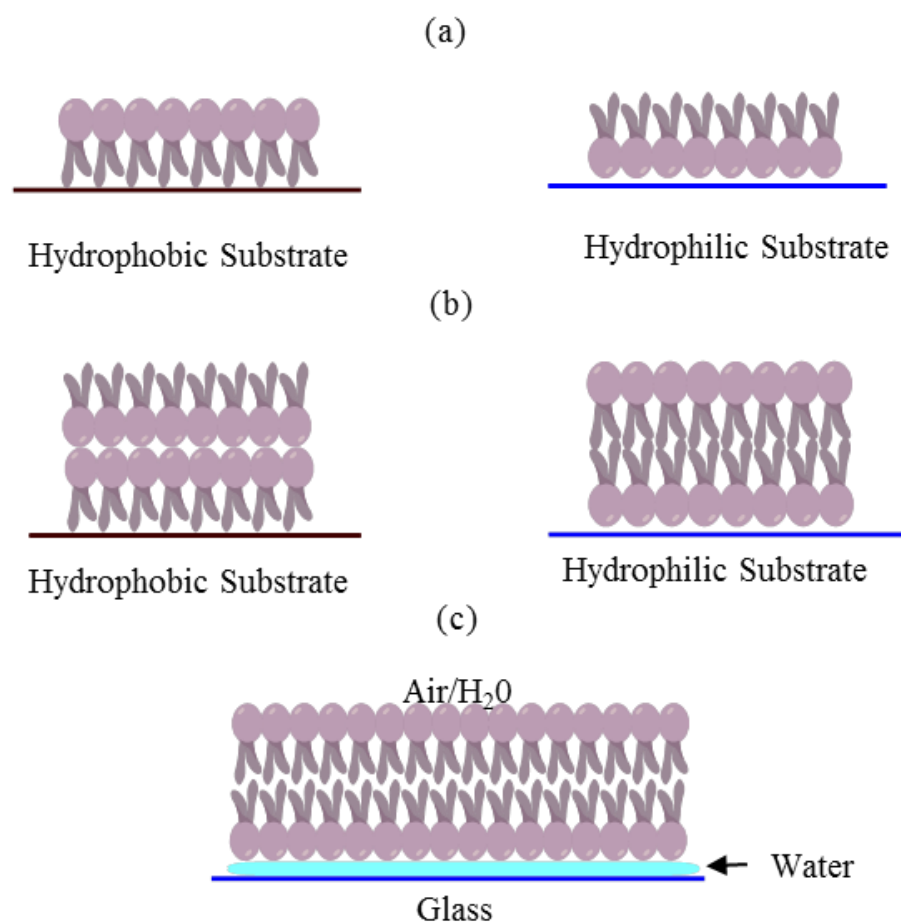


Figure 3-6 Schematic diagram of (a) monolayer on a hydrophobic and hydrophilic substrate (b) inverted bilayer on a hydrophobic substrate and bilayer on a hydrophilic substrate (c) the SLB on glass.

The hydrophilic support could be, for example thiolated gold [90-94], silicon, dimethyldichlorosilane modified quartz [74] [95], LD2K-PDP lipopolymer modified gold [28]. The hydrophilic support is usually quartz, glass, mica, oxidised silicon, or silicon. For SLBs, between the two layers, with aqueous solution above, and ultra-thin aqueous layer

below, there will be around 1 nm space full with liquid. These are useful structures for modelling membrane properties as they have a defined geometry. However, the dynamics are restricted. Methods of preparing the structures used in this study include spin coating and drop coating via vesicle fusion, which will be further disused in chapter 4.

As mentioned in section 3.1.1, at a given temperature, a majority of phospholipid formed lipid bilayers can exist in two distinct phases, gel and fluid, according to their phase transition temperature. The acyl chains are extended and parallel to each other. Intra and intermolecular motions are slow as compared to the fluid, liquid disordered phase where the acyl chains are highly mobile and the molecules undergo fast rotational and lateral diffusion. In a real cell membrane and also our lab mimic SLBs both lipid phases will exist. Lipid bilayer phases then have several important phase behaviours: in both phases, the lipids molecules are prevented from flip-flopping across the bilayer; liquid phase lipid formed bilayers will exchange their locations (random walk) with a neighbour millions of times a second, which allows the lipid to diffuse and thus wander across the surface membrane; gel (solid) phase lipid formed bilayers are locked in place [96].

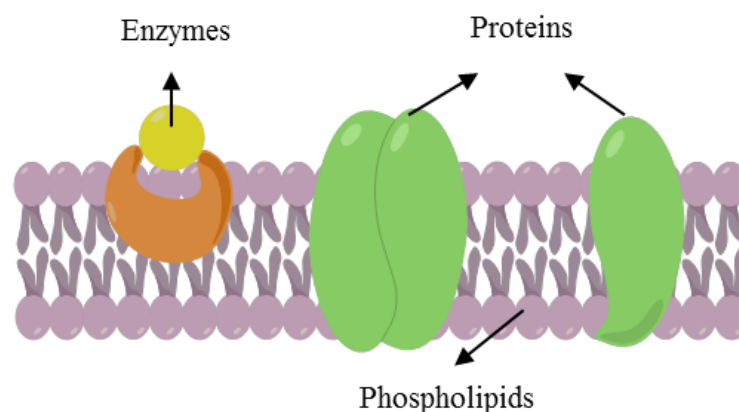


Figure 3-7 Structure of a cell membrane.

The cell membrane is a biological membrane that separates the interior of all cells from the outside environment. It is one of the most important constituents in living organisms, acting as a selective barrier enclosing or separating contents between two phases within or around a cell. The cell membrane consists of the phospholipid bilayer with embedded proteins [97]. As previously reported, a cell membrane does not exist as homogeneous lipid matrix [98], but certain lipids may phase separate into micro-domains or rafts [85]

[99-101]. Two dimensional domain growths may be involved in many phenomena observed in cell membranes [86]. As a result, cell membranes consisting of phospholipid bilayers exhibit complex properties because of their structural diversity [83] (see Figure 3-7).

### 3.1.4 Multilamellar films

As a potentially useful structure for vapour sensing, multilamellar films can be fabricated by certain techniques (details will be described in section 4.2). Just as its name implies, multilamellar films are stacks of unilamellar bilayers. A schematic illustration of the lipid structure of dry (a) and hydrated (b) lipid films and the slab models (c) used for modelling and the construction of multilamellar films is shown in Figure 3-8.

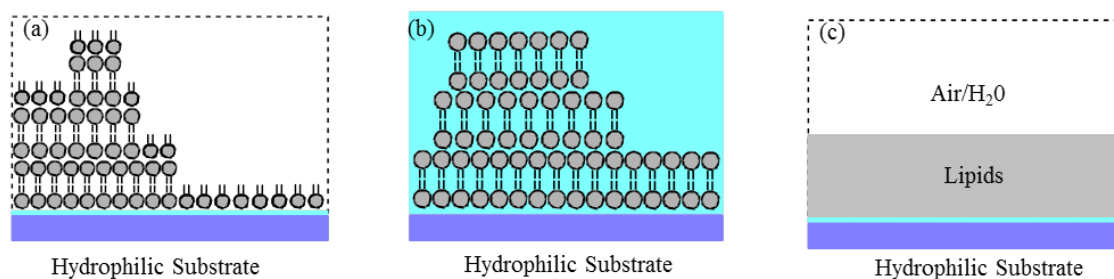


Figure 3-8 A schematic illustration of the lipid structure of dry (a) and hydrated (b) lipid films and the slab models (c) used for modelling and construction of multilamellar films.

Generally, it is assumed that the hydrophobic alkyl chains of lipids would be in contact with a hydrophobic solid surface with hydrophilic heads residing on top, whereas hydrophilic heads will be in contact with a hydrophilic solid substrate with hydrophobic alkyl chains residing on top. When the coated films are stored in air, the surface of the membranes will end with a final monolayer with its hydrophobic alkyl chains on top of the remaining layers [102].

In this section, the structures of lipids which may be formed have been reviewed. Based on the reaction mechanism of vapours and lipids, the better the quality of the deposited film, the better the sensitivity of the sensor will be. Multilamellar films may be the best

forming structure for the vapour sensor because more materials will be involved in the sensing interaction. It would be very interesting to mix the two lipids with a different molar ratio to use as the vapour sensing film. Results for three types of lipids based sensors with DLPC, DSPC, and their mixture are discussed later in chapter 4. Cholesterol will be used to change the phase of the two phospholipid formed layers and improve the sensing behaviour (refer to chapter 8).

The film characterisation equipment and sensing transducer, QCM will be introduced in the following section, including operational theory, quartz crystal information and calculation theory.

## **3.2 Quartz crystal microbalance**

All the information which is relevant to the microbalance work can be found in this section. This information such as working theory, calculation theory and establishment of a stable baseline will be useful for sensing system setup as well as for understanding the sensing mechanism.

### **3.2.1 Background**

As a well-established ultrasensitive weighing device, the piezoelectric quartz crystal microbalance (QCM) has been applied at a solid-air interface in vapour sensing for several decades. QCM normally consists of the quartz resonator and a flow system.

The Research Quartz Crystal Microbalance (RQCM, Maxtek<sup>®</sup> Inc.) is designed for many types of research applications where QCM measurement is desired. It consists of a quartz resonator, a flow system, a high performance phase locked oscillator (PLO) circuit which provides measurement stability over a wide frequency range (3.9 to 6.06 MHz, or 5.1 to 10 MHz), software, and the oscillator circuit (see Figure 3-9). The frequency range used in this work is within 3.9 to 6.06 MHz and usually much less than this range. The software uses the crystal frequency, accurately measured by the system to derive various physical parameters of the deposited film in a liquid or a gaseous environment at the surface of the crystal. The whole flow system, shown schematically in Figure 3-10, includes a CHK-100 Kynar<sup>®</sup> crystal holder and FC-500 Kynar<sup>®</sup> flow cell, creates a flow chamber of approximately 0.1 ml. The cell has two stainless steel inlet and outlet tubes

compatible with inlet and outlet tubing. A Viton<sup>®</sup> O-ring provides sealing between the cell and the front face of the sensor crystal in such a way that an electrode on the rear side of the sensor is connected to the electronic unit of the instrument while only the front side of the sensor is exposed to the vapours or fluids. Plastic tweezers were used to insert the crystal with the front side exposed into the crystal holder cavity. The flow cell and holder need to be rinsed with deionised water and thoroughly blow dried using filtered air after each experiment.

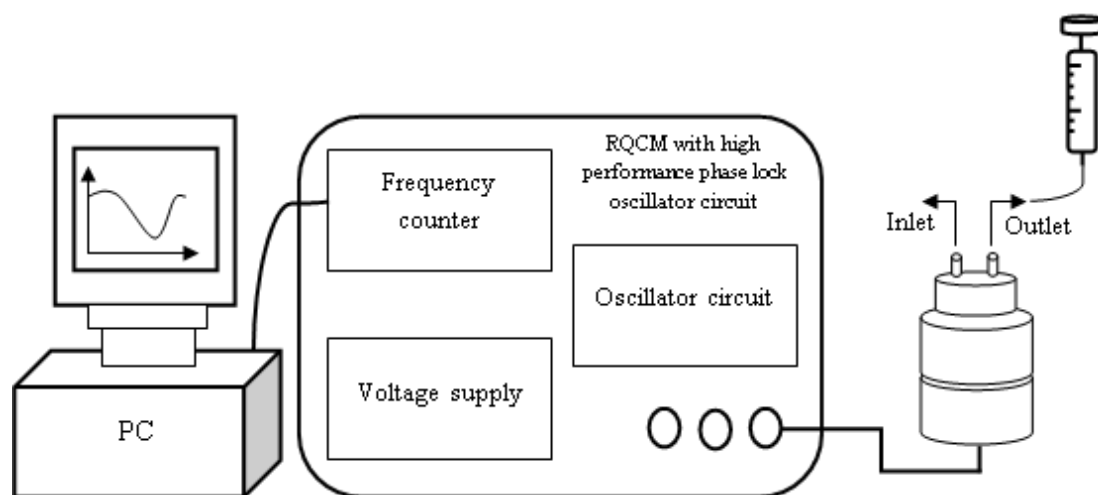


Figure 3-9 Experimental set up of QCM based on the flow system.

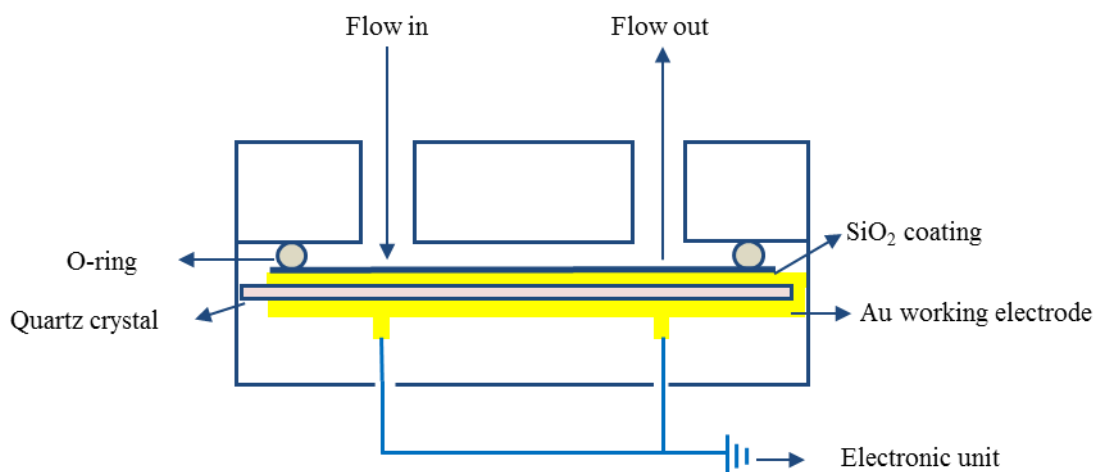


Figure 3-10 Schematic representation of the QCM flow cell.

### 3.2.2 The piezoelectric effect

The direct piezoelectric effect was first demonstrated by the brothers Pierre and Jacques Curie in 1880 [103]. As a unique property of certain substances, the direct piezoelectric effect is where an electric field will be generated if subjected to physical stress.

Conversely, a mechanical deformation (i.e. the substances shrink or expand) is also produced when an electric field is applied. The reversible effect was mathematically deduced from fundamental thermodynamic principles by Gabriel Lippmann [104] and confirmed experimentally by the Curies shortly after a demonstration of the direct piezoelectric effect [105]. The piezoelectric effect was found in some solid material such as crystals, certain ceramics, bone, DNA and various proteins [106]. Piezoelectricity is not only employed in applications such as the detection of sound, generation of high voltages, or microbalances, but also used in scientific instrumental techniques with atomic resolution such as scanning tunnelling microscope STM and atomic force microscopy (AFM).

Normally, only crystals (both natural and synthetic) with no centre of symmetric structures will exhibit piezoelectric effects, such as quartz, zinc oxide and sodium niobate. To explain the formation of piezoelectricity, we need to take look at each molecule of the crystal. Although a solid may be electrically neutral because of the cancellation of individual polarisation, each molecule has a polarisation also known as a dipole. This is a result of the atoms that make up the molecule and the way the molecules are shaped, where one end of each molecule is more negatively charged and the other end is positively charged. By applying a force or electric field, the charged atoms are displaced and will develop a net dipole. Figure 3-11 represents the direct piezoelectric effect, the converse piezoelectric effect and polarisation of a crystal to generate the piezoelectric effect.

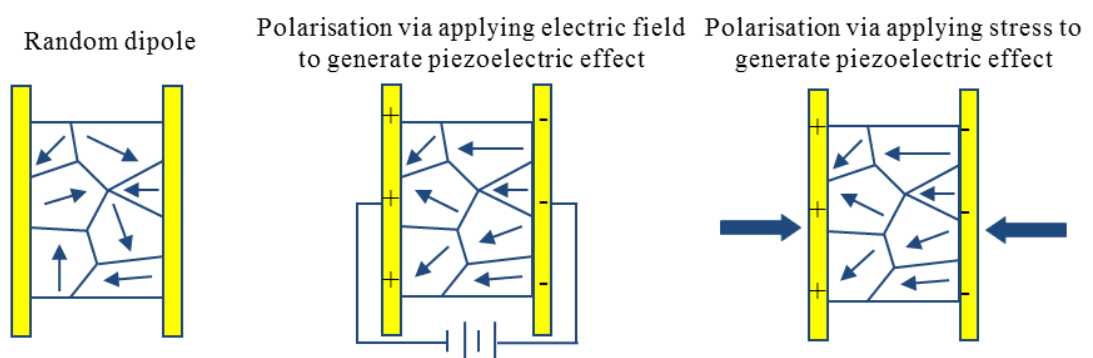


Figure 3-11 Representing the direct piezoelectric effect, the converse piezoelectric effect and polarisation of crystal to generate piezoelectric effect.

The quartz crystal resonator in the QCM utilises the converse piezoelectric effect of a quartz crystal. By applying an electric field, shear motions will occur in one direction. The sensitivity of the quartz crystal resonators is determined by the oscillating frequency. The thickness of the crystal will directly influence the frequency oscillation of the quartz crystal. The relationship of the thickness and frequency is shown in equation 3-1, 3-2 and 3-3. The resonant frequencies are integer multiples of the first or fundamental, resonant frequency.

$$2d = N\lambda \quad (3-1)$$

$$f = \gamma/\lambda \quad (3-2)$$

$$f = \frac{N\gamma}{2d} \quad (3-3)$$

$2d$  = length of a round trip [m]

$N$  = an integer

$\lambda$  = wavelength [m]

$\gamma$  = velocity of a wave [m/s]

$f$  = resonant frequency [Hz]

### 3.2.3 Quartz crystal

#### (a) *Crystal Orientation*

Synthetic quartz is grown hydrothermally using an autoclave [107]. However piezoelectric quartz in its natural form has many different modes of vibration [108]. Accurate substrate orientations allow exploitation of different piezoelectric properties, such as the temperature dependence of the quartz in certain directions. Its frequency stability characteristics are a result of how the quartz bars are cut in a certain pre-oriented angle into crystal wafers. Quartz crystal orientation is specified by the initial surface normal orientation in terms of x, y, or z axis followed by a rotation around another axis as illustrated in Figure 3-12.

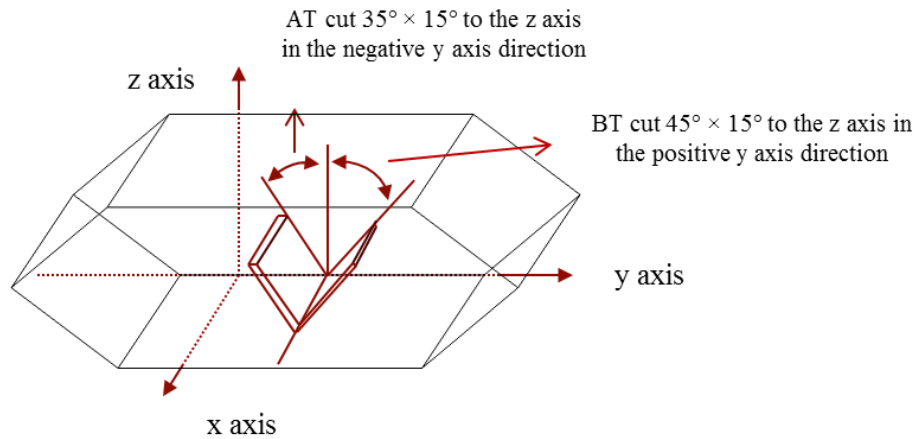


Figure 3-12 Quartz bars orientation is specified by the initial surface normal orientation in terms of x, y, or z axis (AT cut and BT cut angles).

**(b) Crystal Manufacture**

To make use of a quartz crystal as the basic resonator device of QCM, it should be properly cut. The X-cut quartz crystal microbalance was first described in 1921. AT cut quartz crystal with a near zero temperature dependence at room temperature was introduced in 1934. Two of the most common orientations for quartz have a cutting angle varying between  $30^\circ$  and  $45^\circ$  to the z-axis in the negative y-axis direction: the AT cut ( $35^\circ$  negative from z bar), SC cut ( $42.75^\circ$  negative from z axis). As a comparison, BT cut is also given here which has a cutting angle of  $45^\circ$  to the z-axis and positive to the y-axis. The AT cut quartz is a temperature-compensated cut crystal; careful control of temperature and stress has been carried out in the operation. SC cut quartz is stress-compensated crystal [109]. Compare to AT cut quartz, higher frequencies can be achieved using BT cut. AT cut quartz has been widely used because of the straightforward manufacturing process and lower cost.

The well developed AT cut quartz crystal resonators, as used for QCM, normally consist of a thin piezoelectric quartz piece with electrodes deposited on both sides. The electrode is connected to the oscillator circuit via silver wires which were fixed on the electrodes by a conductive adhesive. A photograph of AT cut quartz crystal metallised with gold is shown in Figure 3-13. Grown crystals are cut and polished into hair-thin discs which support a thickness shear resonance in the 1-30 MHz range.



Grey=quartz, yellow=metallic gold electrodes. Front side (left), Back side (right)

Figure 3-13 Front side (left) and back side (right) of Quartz Crystal.

*(c) Crystals choice*

Normally, to choose a suitable quartz crystal for target work, two parameters need to be considered. One is the working temperature, and the other one is the required sensitivity. Based on the system at Durham, crystals (INFICON<sup>®</sup> 1 inch) are optimised for two operating temperatures, namely 90 °C and 25 °C, with 5 MHz fundamental frequencies.

Firstly, comparing 90 °C and 25 °C AT cut crystal (see Figure 3-14), the two crystals have very good temperature stability when operating close to their specified temperature. The 25 °C crystal is then better suited for this work because of the more stable frequency between 20-50 °C which was the working temperature of vapour sensing. Whereas there will be a large frequency shifting on the 90 °C AT cut crystal itself which will result in a thermal interference in the results.

Secondly, we compare the two different fundamental frequency crystals. It can be seen from the Sauerbrey Equation (refer to equation 3-4 in section 3.2.5 a) that the sensitivity (indicates how much the sensor's output changes when the measured quantity changes) increases linearly with the square of the fundamental frequency. The higher the fundamental frequency of the quartz crystal, the higher the sensitivity of the sensors will be. On the other hand, crystals with high resonant frequencies are usually thin, more fragile and more expensive.

In this work, AT cut 25 °C 5 MHz crystals (INFICON<sup>®</sup> 1 inch diameter) were used. Polished 1 inch (25.4 mm) diameter AT cut quartz crystals with a fundamental frequency of 5 MHz were purchased from INFICON (made by MAXTEK, USA). A gold sensing

electrode (front electrode with 0.5 inch diameter on adhesion layer of chromium) was deposited on both sides of the crystal.

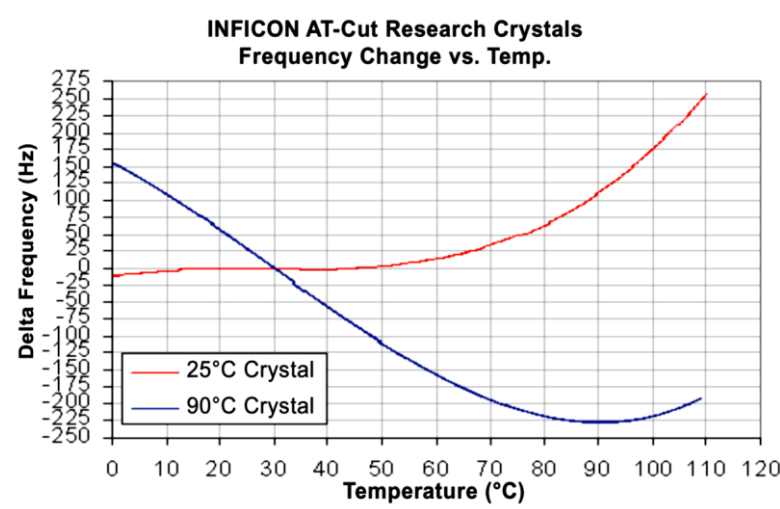


Figure 3-14 Comparison of frequency vs. temperature of INFICON 1" AT cut crystal for 25 °C and 90 °C (reproduced from RQCM operation and service manual).

### 3.2.4 Stable baseline

For an accurate real-time QCM frequency shift response due to adsorption, a stable baseline needs to be set up before doing any measurements. There are several reasons that may cause the frequency shift without any loading, including leaks of tubes, gas bubbles in buffer, temperature changes, and surface reactions, pressure changes, mounting stresses change, backside reactions, poor electrical contact and O-ring swelling. Guidelines for temperature and flow rate control are now discussed to minimise errors in the measurements due to the environment of the sensor crystal.

#### (a) *Temperature equilibrium*

For a crystal operating in air, the intrinsic dependence of resonance frequency on temperature is generally small when operating at or near the crystal's turn around point (the temperature at which the crystal frequency is most stable). For crystal operating in liquid, due to the coupling of the shear mode oscillation with a temperature dependent

viscosity and density of the fluid, the frequency change due to temperature is magnified. For our experiments, sensor crystals were mostly operated in gas phase conditions in which frequency was to be monitored over a long period of time; hence, strict temperature control is then especially important. Although AT cut crystals used in this work are designed to minimise the change in frequency due to temperature, the effect of temperature may be significant when attempting to resolve small frequency changes over long periods of time. Thus, the resonance frequency stability was checked in a certain temperature range over a long period of time. As a result, the experiments in this work were often carried out with temperature controlled baths and jacketed cells. During all the measurements, the flow cell with crystal inside was always left in the water tank for about 30 minutes for temperature equilibrium to be achieved to obtain a stable baseline before any accurate measurement. The measurement of crystal frequency change versus temperature was carried out (illustrated in Figure 3-15).

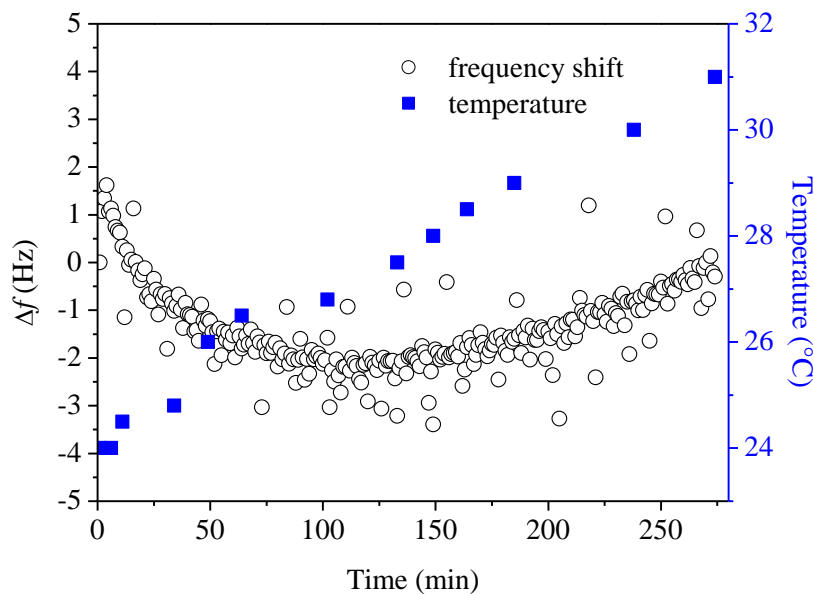


Figure 3-15 Experimental result of Maxtek® 1 inch 25 °C AT cut polished crystal oscillation frequency change vs. temperature change.

After the crystal was mounted in the flow cell, the chamber was placed in a water tank. When the measurement started with a starting temperature of 24 °C, the water tank heating system temperature was set to 33 °C. The starting frequency was reset to zero. During this period, the crystal oscillation frequency shifted within  $\pm 1.5$  Hz but was stable at around the

mean frequency, and a standard deviation of  $\pm 0.9$  Hz could be measured. These values could be used to check and calibrate the crystal oscillation sensor system, by comparing the experimental figures to those obtained from RQCM manual, the frequency shift due to adsorption of mixed lipids and vapour sensing. The data derived from the 25 °C AT cut polished crystal indicated that the experimental system of the QCM works and was stable at temperatures between 24 °C and 31 °C.

**(b) Line pressure equilibrium**

The line pressure may change when the fluid volume reduces in the reservoir. There are normally two ways to carry out QCM measurements with constant pressure. One is to pump liquid or gas with a continuous constant flow rate, known as flow mode (kinetic mode). Another one is to fully exchange the inner volume of content within a short time (usually 1 or 2 seconds), known as exchange mode (static mode).

In the liquid flow mode experiments, the whole liquid flow system includes a volume of 2.5 ml glass gastight syringe, and a syringe pump (Cole-Parmer<sup>®</sup>) used to pump liquid through the quartz chamber. A FC-550 flow cell (Kynar<sup>®</sup>) was installed in the crystal holder which creates a flow chamber of approximately 0.1 ml inner volume. Two stainless steel inlet and outlet pipes on the flow cell allowed for a continuous flow syringe pump which was connected by Teflon tubing. A three way stopcock was also employed in the inlet route. The valve could be used to stop the flow when making any exchanges, and also to avoid any dead volume flow into the flow cell (refers to Figure 3-16).

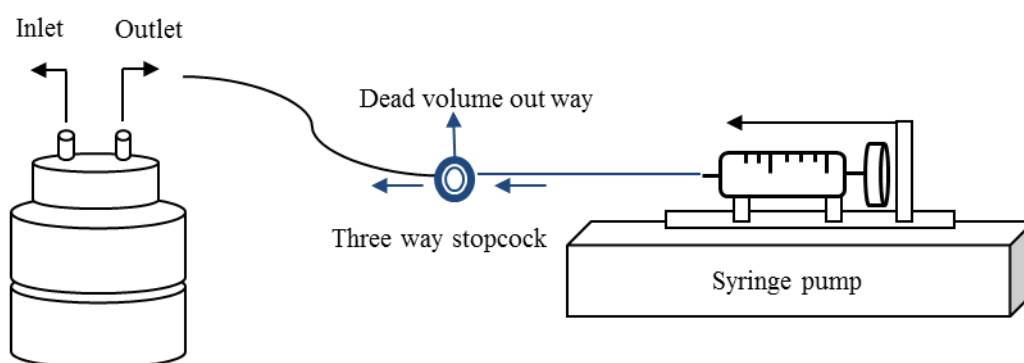


Figure 3-16 Design of flow injection system for flow mode.

Using a pumping system will minimise pulsation and maintain a constant line pressure throughout the experiment. Syringe pumps which provide pulse-less flow, or a peristaltic

pump which pulls the liquid through the flow cell and gravity flow are all good methods for flowing fluid through the flow cell, chamber without pulsation effects. When the system enters equilibrium, i.e. when a stable baseline has been achieved, further actions can be carried out. Similar designs have been developed for vapour sensing, which will be further discussed in chapter 5.

Exchange mode is normally used as the second way to introduce a sample for measurement in hydrated condition. A simple system setup for exchange mode with an axial flow cell, sample reservoir and single valve is illustrated in Figure 3-17.

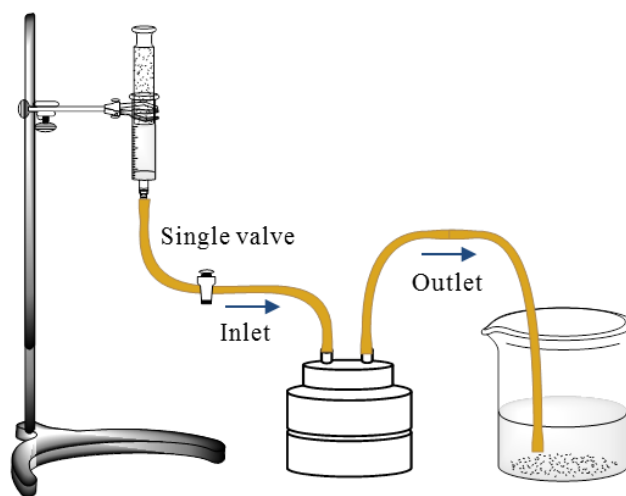


Figure 3-17 Design of flow injection system for exchange mode.

In this case, the sample reservoir, loaded with more than 2 ml of the sample, was connected to the inlet port. The outlet port tube was immersed in a beaker of the same solution. Exchange of the fluid in the cell was accomplished by gravity feed from the reservoir directly above the cell. The exchange was controlled by a single valve. After the measurement system was tuned to the resonant frequency of the crystal, the buffer was exchanged at least twice to check for contamination and to ensure that the measurements began from the same stable baseline. Exchange mode is exchanging the inner solution (buffer for buffer, or buffer for sample) by pumping in enough exchange liquid within 1-2 seconds. Figure 3-18 shows a stable baseline of the bare crystal achieved after three exchanges with 1 ml deionised water.

Usually signal distortion (a frequency spike) will be found upon flushing and will be recovered within a few seconds. The stable baseline was achieved by exchanging at least twice, each time by allowing a certain amount (10 times the inner chamber volume) of

buffer to flow through the chamber [88]. After checking for contamination and ensuring that the measurements were started from a stable baseline, further actions could be carried out. In this mode, the content in the measurement chamber is generally still. “Stand by” condition will be in most of the experiment time. The measurement started at Point A with the bare crystal mounted in a chamber immersed in a water tank without buffer inside (Figure 3-18). From points B to C, the first baseline is achieved after the equilibrium of the system temperature. 1 ml deionised water for the first exchange has been carried out at point C which resulted in a rapid decrease of frequency. A stable baseline 2 has been achieved from D to E. Second and third exchanges were carried out at point E and G separately. A recovery curve within several seconds can be seen followed by a stable baseline after each exchange. At least two buffer for buffer exchanges to get the similar frequency was essential to ensure that the inner buffer was full exchanged and perfectly degassed.

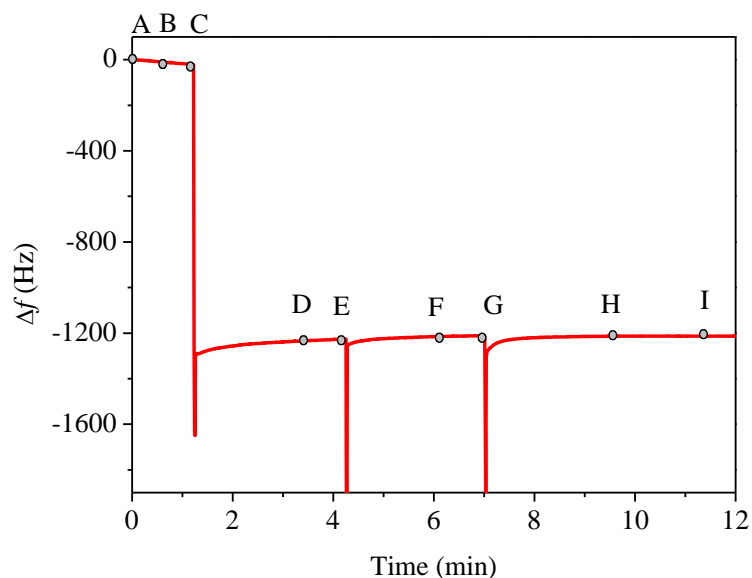


Figure 3-18 Stable baseline achieved after three times exchange with 1 ml deionised water.

Comparing the two modes, exchange mode is quick, convenient and easy to start with. Whereas flow mode requires a more complex experimental set up. But for vapour sensing, flow mode is more suitable which will offer a constant flow rate and provide a constant pressure which can reduce the hidden chance of frequency shifts and the possibility of crystal failure.

During all the measurements in this work, the crystal and the oscillator circuit were placed in a temperature controlled water tank set to the turn-around-point of AT cut crystal we used (i.e. 25 °C). A combination of flow mode and exchange mode was considered for the lipid bilayer flow injection coating (see section 4.3.3 and 5.3.1). A flow mode with constant flow rate was always used for vapour sensing (see chapter 6).

### 3.2.5 Calculation theory

Normally the change of frequency in QCM is likely to be due to two opposing effects, namely, the mass-increase in the sensing film resulting in a decrease in the frequency and the viscosity decrease resulting in an increase in QCM frequency [71] [110]. The mass increase causing a frequency decrease can be calculated via the Sauerbrey Equation and will be discussed here. The viscosity causing a frequency increase will be further discussed in chapter 7 and 8.

#### (a) *Sauerbrey Equation and thickness calculation*

Sauerbrey was the first to recognise the ability of the QCM to measure very small mass changes on the crystal surface. The linear relationship between the mass adsorbed to a QCM device and the resonance frequency can be described by equation 3-4 which will be discussed further in chapter 6 [70].

$$\Delta f = - \frac{2nf^2}{\sqrt{\mu_q \times \rho_q}} \frac{\Delta M}{A} \quad (3-4)$$

$f$  = resonance frequency of crystal [Hz]

$\rho_q$  = density of quartz = 2.648 [g/cm<sup>3</sup>]

$\mu_q$  = effective piezoelectrically stiffened shear modulus of quartz  
= 2.947 × 10<sup>11</sup> [g/cm/sec<sup>2</sup>]

$A$  = total the electrode area [cm<sup>2</sup>]

$\Delta M$  = change in mass of the sensing film [g]

The equation has been demonstrated to be valid within 5% error for lipid bilayers or adsorbed non-ruptured small unilamellar vesicles on rigid sensor coatings with a thickness ranging from several nanometres [111-112] to several micrometres such as glued mica sheets [113]. We can also see from this equation, in a QCM system there will be several different modes of vibration corresponding to the sensitivity needs of different

experiments. Sensitivity increases linearly with harmonics and the square of the fundamental frequency.

Lu and Lewis also introduced another term, the ratio of the acoustic impedance of quartz to the acoustic impedance of the deposited film, to analyse the loaded crystal as a one-dimensional composite resonator of the quartz and the deposited film [114]. The acoustic impedance is associated with the transmission of a shear wave in the deposited mass. The Lu and Lewis equation, also called Z-Match equation is shown below.

$$\Delta m = \left( \frac{N_q \cdot \rho_q}{\pi \cdot R_z \cdot f} \right) \cdot \tan^{-1} \left[ R_z \cdot \tan \left[ \pi \cdot \left( \frac{f_q - f}{f} \right) \right] \right] \quad (3-5)$$

$$N_q = \frac{\sqrt{\rho_q \mu_q}}{2 \rho_q} \quad (3-6)$$

$$R_z = \frac{\sqrt{\rho_q \mu_q}}{\sqrt{\rho_f \mu_f}} \quad (3-7)$$

$\Delta m$  = change in mass per unit area [ $\text{g}/\text{cm}^3$ ]

$N_q$  = frequency constant for AT cut quartz crystal =  $1.668 \times 10^5$  [ $\text{Hz} \cdot \text{cm}$ ]

$\rho_q$  = density of quartz =  $2.648$  [ $\text{g}/\text{cm}^3$ ]

$f_q$  = resonant frequency of an unloaded crystal [ $\text{Hz}$ ]

$f$  = resonant frequency of loaded crystal [ $\text{Hz}$ ]

$R_z$  = Z-factor of the film material, i.e. acoustic impedance ratio

$\rho_f$  = density of material [ $\text{g}/\text{cm}^3$ ]

$\mu_q$  = shear modulus of the quartz =  $2.947 \times 10^{11}$  [ $\text{g}/\text{cm}/\text{s}^2$ ]

$\mu_f$  = shear modulus of film material in [ $\text{g}/\text{cm}/\text{s}^2$ ]

We can notice that if the acoustic impedance ratio is equal to one (i.e. quartz on quartz), then the Z-match equation reduces to Sauerbrey's equation. The Lu and Lewis equation is generally considered to be a good match for the experimental results for a frequency change up to 40% compared to the unloaded crystal [115-116]. The thickness of the film is also an interesting parameter which can be calculated from the equation 3-8 shown below.

$$TK_f = \frac{\Delta m}{\rho_f} = \left( \frac{\rho_q}{\rho_f} \right) \cdot N_q \cdot \left( \frac{\tau}{\pi R_z} \right) \cdot \tan^{-1} \left[ R_z \cdot \tan \pi \cdot \left( \frac{\tau - \tau_q}{\tau} \right) \right] \quad (3-8)$$

$TK_f$  = thickness of the film [ $\text{cm}$ ]

$\tau_q$  = period of the unloaded crystal [ $\text{sec}$ ]

$\tau$  = period of the loaded crystal [ $\text{sec}$ ]

The thickness adsorbed on quartz is calculated by dividing the film mass by the material density. The QCM measures the period of oscillation rather than the frequency to calculate the thickness of the film.

**(b) Capacitance cancellation and dissipation method**

QCM not only allows an observation of the change in resonance frequency due to adsorption but also the change in the dynamic resistance  $\Delta R$  as a result of changes of viscoelastic properties. Figure 3-19 shows the equivalent circuit of the QCM quartz crystal.

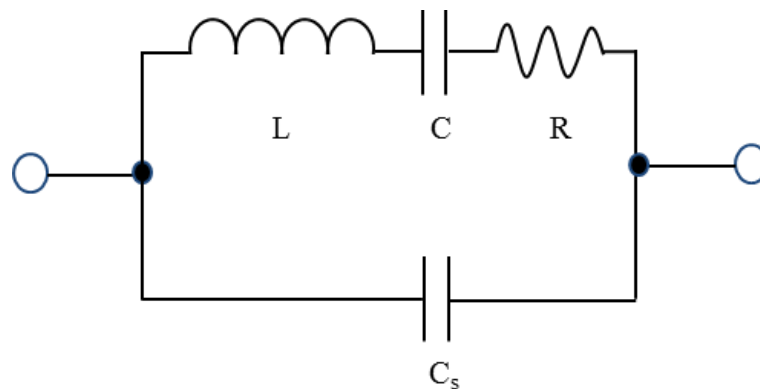


Figure 3-19 The electrical equivalent circuit of the QCM quartz crystal.

The circuit has two branches: the motional branch and the shunt branch. The motional branch contains the L, R and C which is modified by mass and viscous loading of crystal. The shunt branch contains the lone  $C_s$  element which represents the shunt sum capacitance of the crystal electrodes, any cable and fixture R (resistor) corresponds to the dissipation of the oscillation energy from mounting structures and from the medium in contact with the crystal (i.e. losses induced by a viscous solution). C (capacitor) corresponds to the stored energy in the oscillation and is related to the elasticity of the quartz and the surrounding medium. L (inductor) corresponds to the inertial component of the oscillation, which is related to the mass displaced during the vibration. Typical values for a 1 inch diameter, 5 MHz crystal used in the QCM system with good fine adjustment (discussed in section 3.5.6), and the resistance should be between 5-15  $\Omega$  (for a dry crystal). Resistance should increase to 364  $\Omega$  for a crystal with one face in water. In a QCM application the motional inductance, L, is increased when mass is added to the crystal electrode. The frequency shift of the series resonance is a sensitive indicator of the added mass. Films of less than 1  $\text{ng}/\text{cm}^2$  can easily be resolved by the QCM. The motional resistance, R, can also provide

important information about a process since soft films and viscous liquids will increase motional losses and increase the value of  $R$ .

An alternative method for studying the properties of the loaded QCM sensor, called the dissipation method has been used in gaseous as well as in liquid environments. In this case, the crystal is driven at its resonant frequency by an oscillator that can be intermittently disconnected causing the crystal oscillation amplitude to decay exponentially. From the recorded decay curve, the absolute Q-factor (inversely proportional to  $R$ ) and the frequency of the oscillator are simultaneously obtained. The dissipation (damping) is the sum of all energy losses in the system per oscillation cycle. It is defined as  $1/Q$ , i.e. the energy dissipated per oscillation divided by the total energy stored in the system.

$$D = \frac{1}{Q} = \frac{R}{\omega_s \cdot L} \quad (3-9)$$

$Q$  = the quality factor

$\omega_s$  = the angular frequency at series resonance [rad]

$L$  = inductance [H]

$R$  = resistance [ $\Omega$ ]

The frequency response of a quartz crystal represents the change of total mass. This mass always includes a certain amount of water. However, the amount of water may vary between 10% and 90% depending on the type of molecule and the way it adsorbs to the surface (an elongated protein that adsorbs flat to the surface gives low dissipation while the very same molecule standing up on the surface gives high dissipation). By measuring the dissipation, it is possible to determine if a soft film (water rich) or a rigid film (less water) has formed on the surface. Only when the film is fairly rigid does the Sauerbrey relation give a good estimation of adsorbed mass. Measuring the dissipation means that it is possible to determine whether the Sauerbrey relation is valid. The dissipation factor gives additional "structural" information, compared to an ordinary QCM measurement, in that one can measure the conformational change of the film, e.g., crosslinking (collapse) and swelling [117].

Independent studies have shown that as long as the effect of the parasitic capacitance ( $C_0$ ) is properly cancelled, the results provided by the QCM system should be in good agreement with those obtained by dissipation method. Thus, adjustment of the capacitance cancellation was essential for accurate measurements of liquids and soft films before

further action carried out. The cancellation adjustment was performed with the crystal holder and crystal in the water tank which was our measurement environment. After cancellation had been properly carried out, the QCM provided a mechanism for cancelling out the imaginary current. The frequency measured is the frequency at which the inductive and capacitive impedances in the motional branch cancel out and the crystal looks like a pure resistance of value  $R$ . The resistance change was used for some of the measurements and will be discussed in chapter 5.

*(c) Activation area*

The sensitivity of the quartz crystal sensor is highest in its centre, and decreases towards the sensor edge. When calculating mass and viscoelastic properties of an adsorbed layer, the QCM measurement system assumes that the surface has been homogeneously coated, and so the result is always an average of, for instance, mass per unit area. In other words, it is not applicable to talk about sensitivity or results of specific regions of the sensor surface, and any approach to partially cover the sensor is thus not recommended. The activation area will be mentioned again later when different substrates were considered for sensor fabrication.

### **3.3 Summary**

Lipids (sensing material) and QCM (the transducer and film weighing equipment) were introduced in this chapter. As mentioned earlier in chapter 1, the idea of this work is to fabricate multilayer lipids onto a gold electrode surface which can be used for vapour sensing. The potential structures of lipids and relevant information have been detailed in this chapter. The working principle and relevant information of QCM that will be used in this work have also been detailed in this chapter. These will lead to a better understanding of both the film property and the sensing mechanism.

The forthcoming chapter will talk about all the film fabrication procedures based on the theory mentioned in this chapter.

## Chapter 4 Lipid film fabrication

The sensitivity of a lipid-based vapour sensor is highly dependent on the affinity of the lipids to vapour as well as on the successful production of the lipid films. To compare the response between different sensors to the same vapour, a controllable process for the lipid fabrication should be developed. To achieve this, the lipid film deposition and characterisation are detailed here and in chapter 4.

This chapter introduces the experimental procedures involved with lipid inverted bilayer deposition and lipid sensing film deposition. In the first part, substrates prepared for film deposition are described. This is followed by a review of methods available for film deposition. The summary and comparison of these methods leads to the choice of suitable fabrication methods for both the study of bilayers and multilayer films for vapour sensing.

### 4.1 Substrate preparation and cleaning

A QCM will respond to anything that has mass. Thus, it is imperative to develop a substrate surface where lipids can form specific structures of interest. In this work, surface modification was used for the preparation of surfaces with either hydrophilic or hydrophobic properties. The relevant structures of lipids formed on various substrate types have already been explained in section 3.1. Preparation and cleaning procedures for hydrophilic mica, silicon dioxide sputtered crystals (for bilayer study), hydrophilic gold electrodes and hydrophobic thiolated gold substrates (for multilayer sensor fabrication), template stripped gold substrates (for multilayer film study) are detailed in this section.

#### 4.1.1 Substrate properties and contact angle measurement

Wetting is an important phenomenon for lipid based sensors, since the wettability of the substrate by the solution will significantly influence the film structure and uniformity. The

definition of wetting is described as the ability of a liquid to maintain contact with a solid surface, resulting from intermolecular interactions when the two are brought together. The wettability (degree of wetting) of a solid interface is an important property determined by the properties of the fluid (surface energy) and the solid surface (geometric microstructure) [118-121]. If a liquid has a high surface tension, the cohesive forces are stronger than the adhesive forces, and the wetting will not occur. Instead, the liquid will form beads on the surface. Whereas, if the liquid has stronger adhesive forces but lower surface tension, then the solution will spread out and wet the surface.

As important solid surface wettability quantification, the contact angle  $\theta$ , is given by the angle between the interfaces of the droplet and the surface (see Figure 4-1). The relationship between contact angle, the surface energy and the wettability properties of the substrate is given in Table 4-1.

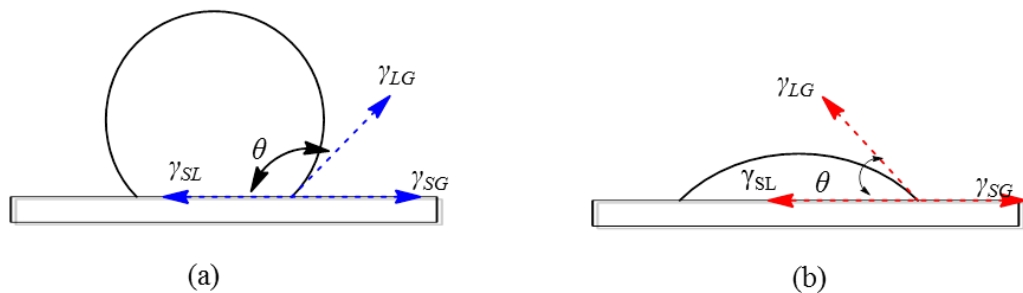


Figure 4-1 Dewetting of a hydrophobic surface with  $\theta > \pi/2$  (a); and wetting of hydrophilic substrate surface with contact angle  $\theta < \pi/2$  (b).

Table 4-1 The relationship between contact angle, surface energy and wettability property of the substrates

Contact angle ( $\theta$ )	Degree of wetting	Strength	
		Solid/liquid interactions	Liquid/liquid interactions
$0^\circ$	Completely wetted (CW)	Strong	Weak
$0^\circ$ - $90^\circ$	Hydrophilic Highly wetted (HW)	Strong	Strong
$90^\circ$ - $180^\circ$	Hydrophobic Partially wetted (PW)	Weak	Weak
$180^\circ$	Non wetted (NW)	Weak	Strong

The shape of a droplet is determined by the Young–Laplace equation (equation 4-1), with the contact angle playing the role of a boundary [122]. The theoretical description of contact arises from the consideration of a thermodynamic equilibrium between the three phases: the liquid phase ( $L$ ), the solid phase ( $S$ ), and the gas/vapour phase ( $G$ ).

$$\gamma_{SG} = \gamma_{SL} + \gamma_{LG} \cos \theta \quad (4-1)$$

$\gamma_{SG}$  = solid–vapor interfacial energy [J]

$\gamma_{SL}$  = solid–liquid interfacial energy [J]

$\gamma_{LG}$  = liquid–vapor interfacial energy, i.e. surface tension [J]

$\theta$  = equilibrium contact angle [°]

As mentioned previously in chapter 3, the wettability property of the substrate will influence the lipid structure formed. Thus, the contact angle of the substrate was always checked after the substrate was prepared. All the substrates prepared and used in this study will be described in the next section including substrate preparation, contact angle measuring and substrate cleaning.

### 4.1.2 Hydrophilic surface preparation

As mentioned previously in section 3.2.3, polished 1 inch AT cut quartz crystals with a fundamental frequency of 5 MHz were purchased from INFICON and used as vapour sensing substrates. As the most sensitive region of the QCM crystals, the gold electrode which is coated on the front side was evaluated as the main working substrate and used for the vapour sensors in this study. Crystals were modified into four types used as a lipid film deposition subphase including hydrophilic oxidised gold substrates, SiO<sub>2</sub> sputtered quartz, platinum evaporated quartz (refer to section 4.1.2 a-c) and hydrophobic thiolated gold substrates (refer to section 4.1.3). The preparation of hydrophilic mica and template stripped gold are also detailed in this section (refer to section 4.1.2 d-e).

General cleaning for new crystals were always carried out by following steps before any further treatments, if not otherwise stated. An ultrasonic cleaning method was used to clean the crystals in a solution of non-basic detergent (Decon<sup>®</sup> 90, purchased from Decon laboratories) in deionised water for 15 minutes. This was followed by a rinse with deionised water and drying under a gentle flow of filtered nitrogen gas [123].

#### (a) *Wettable gold electrode modification*

The gold electrodes on the QCM crystals were prepared for oxidation by treating the crystals with 75 °C NH<sub>4</sub>OH-H<sub>2</sub>O<sub>2</sub>-H<sub>2</sub>O solution for 5-10 minutes [124-125] to remove trace organics that are not covalently bonded to the surfaces, followed by rinsing with water and drying under N<sub>2</sub>. Then the crystals were exposed to 100 W oxygen plasma

(YES<sup>®</sup> Etcher) for 10 minutes, rinsing with water, and drying under filtered N<sub>2</sub> gas. By this treatment, the surface was cleaned from films of various organic contaminants and rendered hydrophilic [111]. Cleaned, modified crystals were stored in air in a clean room and dried in an air-filtered convection vacuum oven for a whole night to remove traces of surface bound water. Immediately before coating, crystals were rinsed in at least two cycles with acetone, isopropanol and trace chloroform in sequence until no change of oscillation frequency was found by the QCM. After being absorbed with lipids, the crystals were cleaned by immersing into a 1:1:5 solution of hydrogen peroxide (30%) ammonia (25%) and deionised water bath, heated to a temperature of about 75 °C for 5 minutes.

The observation of the crystal cleaning procedure was carried out by using optical microscopy imaging, contact angle measurement and AFM imaging. Pictures under an optical microscope were taken after each cleaning step. The oscillation frequency of crystals after each cleaning step was checked by QCM. Surface features and surface roughness were acquired by AFM and optical microscope indicating the integrity of the surface. The contact angle for a fresh unmodified gold electrode is about 85°, with a modified gold electrode immediately after plasma treatment measuring about 30°. After drying for the whole night it had a contact angle of about 45°, i.e. hydrophilic (see Figure 4-2). The surface roughness of the gold electrode is 4.8 nm (see Figure 4-4 a).

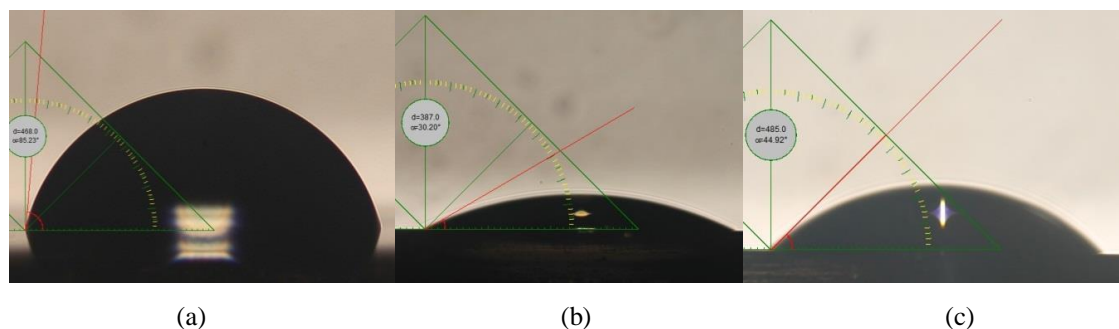


Figure 4-2 Fresh gold electrode (a)  $\theta = 85^\circ$ , plasma treated gold electrode (b)  $\theta = 30^\circ$ , gold electrode dried whole night (c)  $\theta = 45^\circ$ . The red line indicates the contact angle.

### **(b) Silicon dioxide sputtering**

Gold electrode QCM crystals with an additional SiO<sub>2</sub> sputter coated outer layer to create a hydrophilic surface were considered as substrates for bilayer deposition. Quartz crystals were cleaned by briefly etching in an oxygen plasma before sputter coating with 50 nm or

100 nm SiO<sub>2</sub> onto the adhesion layer of titanium. The contact angle measurement gives a SiO<sub>2</sub> sputtered crystal's contact angle of about 10° (i.e. hydrophilic, image not shown here). After use, SiO<sub>2</sub> sputtered quartz crystals were cleaned by etching in an oxygen plasma for 10 minutes, and then immersing the crystals into 2% sodium dodecyl sulphate (SDS, purchased as powder from Sigma Aldrich) solution at room temperature for 30 minutes, rinsing generously with deionised water and blowing dry with filtered nitrogen gas (see Figure 4-3, optical microscopy image of crystals before and after cleaning). As shown in Figure 4-3, lipids adsorbed on the crystals appear to be removed after being treated. After using the cleaning procedure described above, nearly all the unwanted substances have been removed from the sputter coated crystal surface. Immediately prior to each measurement, the crystal was treated with at least 10 minutes in an oxygen plasma.

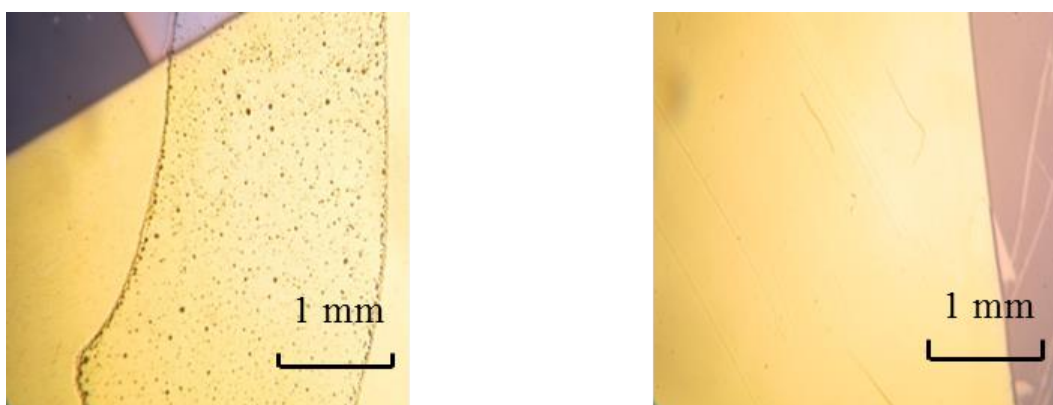


Figure 4-3 Crystal surface appearance comparison of quartz coated with lipids before (left) and after (right) cleaning. Image size: 2.5 mm × 2.5mm; magnitude: × 5.

The topography of a bare crystal sensor and sputter coated crystal surface is illustrated in Figure 4-4. The root mean squared surface roughness ( $R_q$ ) of each sample is indicated on the corner of each image. The topography of the polished crystal (Figure 4-4 b) is smoother than surface (a), (c) and (d) as indicated by the root mean square roughness which is provided in the top right corner of each image. However, some characteristic polishing tracks which are several nanometres deep and up to several microns in length can be found in all of the scanning areas. The bare gold electrode surface appears to be homogeneous

and looks similar to the topography of 100 nm SiO<sub>2</sub> sputter coated crystal. All images exhibit globular features that are arranged unevenly.

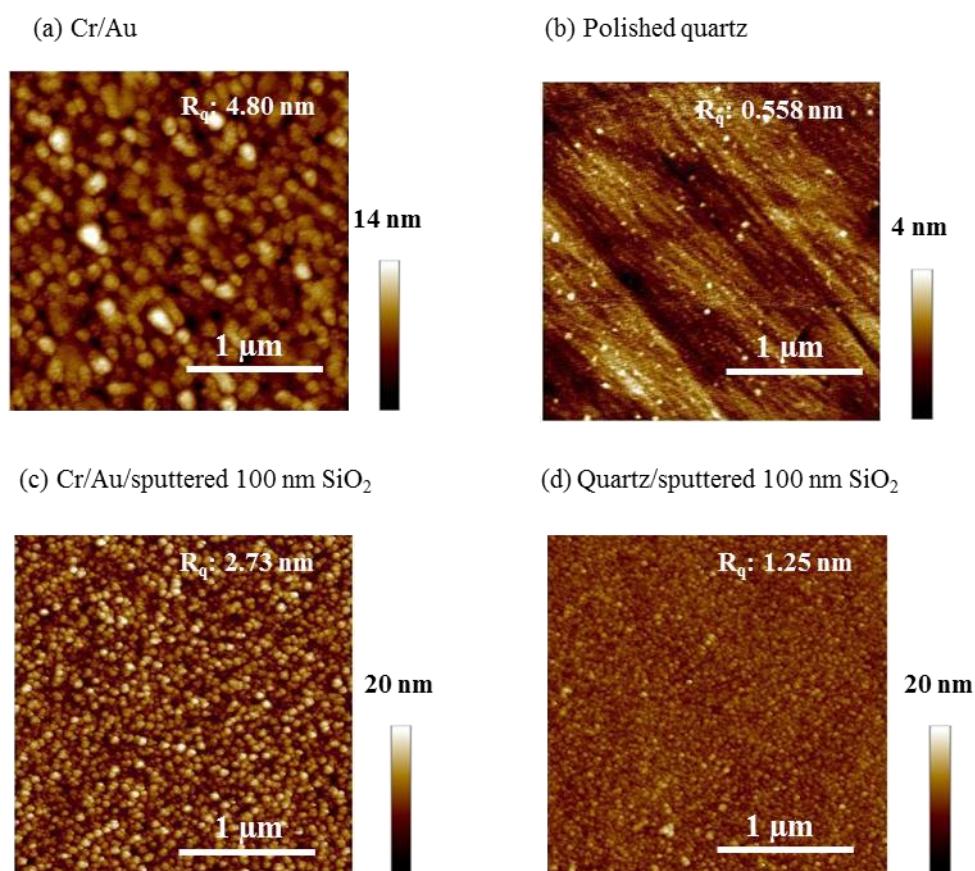


Figure 4-4 Tapping-mode AFM images ( $2.5 \times 2.5 \mu\text{m}^2$ ) with 1 Hz scan rate showing the topography of the different surfaces. The height scales vary as shown on the right of each image. The surface roughness is indicated on the top right corner of each image. (a) bare gold electrode part with chromium as its seed layer on the crystal; (b) the bare quartz part on the crystal; (c) the gold electrode part sputtered with 100 nm SiO<sub>2</sub>; (d) the quartz part sputtered 100 nm SiO<sub>2</sub>. Scale bar: 1  $\mu\text{m}$ ; Z scale is indicated on the right of each image.

**(c) *Platinum evaporated quartz***

A platinum evaporated quartz substrate was prepared for a sensor coating repeatability study. Chromium (5 nm) and platinum (100 nm) were evaporated on the crystal surfaces to give a contact angle of about 60° (i.e. hydrophilic). Chromium was deposited to obtain good adhesion between the gold and crystal surfaces. Before and after use, the crystals were washed by sonification in chloroform and received an oxygen plasma treatment.

**(d) Mica**

Mica, as a sheet silicate (phyllosilicate), is monoclinic with a tendency towards pseudo hexagonal crystals that are similar in chemical composition. The manufactured muscovite mica (potassium aluminosilicate) sheets were purchased from Goodfellow<sup>®</sup> directly. Prior to deposition, freshly cleaved mica substrates were prepared by peeling away the external layers of mica using scotch tape. During this procedure, care was taken not to contaminate the freshly exposed mica surfaces. The freshly cleaved mica substrates had a contact angle of about 45° (i.e. hydrophilic). Freshly cleaved mica was always used for film deposition without further cleaning or reuse. Hydrophilic mica was considered for inverted lipid bilayer preparation. However, it is designed for one use only.

The contact mode AFM mapping of freshly cleaved mica is shown in Figure 4-5. It is quite clear that bare mica is extremely smooth with a root mean square roughness of 0.049 nm. It indicates that mica is an ideal substrate for thin lipid layer deposition and AFM investigation.

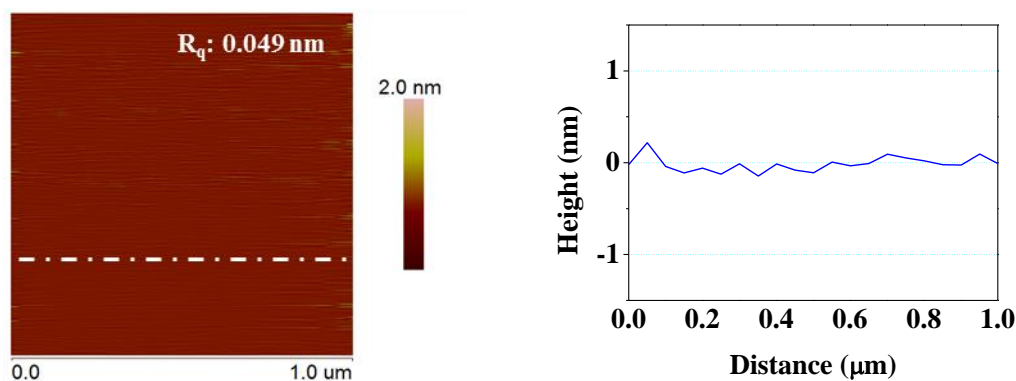


Figure 4-5 Contact mode AFM height image ( $1 \times 1 \mu\text{m}^2$ ) and cross-sectional analysis. The dashed lines denote the location of the sections. Z scale: 2 nm.

**(e) Template stripped gold**

To produce a smooth surface for lipid film topography investigation, the template stripped gold was prepared and used instead of a gold electrode for AFM study. The template stripped gold was prepared by evaporating a layer of gold on the clean silicon surface without a seed layer. A droplet of glue was deposited in the centre of the glass substrate. The evaporated gold on silicon was placed concentrically on top of the droplet with the gold facing the glue. Capillary forces ensured spreading of the glue along the

interface without entrapment of bubbles. Before use, any excess of glue was scratched off around the glass sheet. The tape was peeled off, uncovering a surface of freshly cleaved gold.

The comparison tapping mode AFM image of gold electrode and smooth gold is shown in Figure 4-6 with the roughness of each indicated on the right top corner of each image. It is very clear that the template stripped gold surface is significantly smoother than the normal gold electrode surface on the quartz crystal. The contact angle measurements give a fresh smooth gold contact angle of about  $45^\circ$  (i.e. hydrophilic).

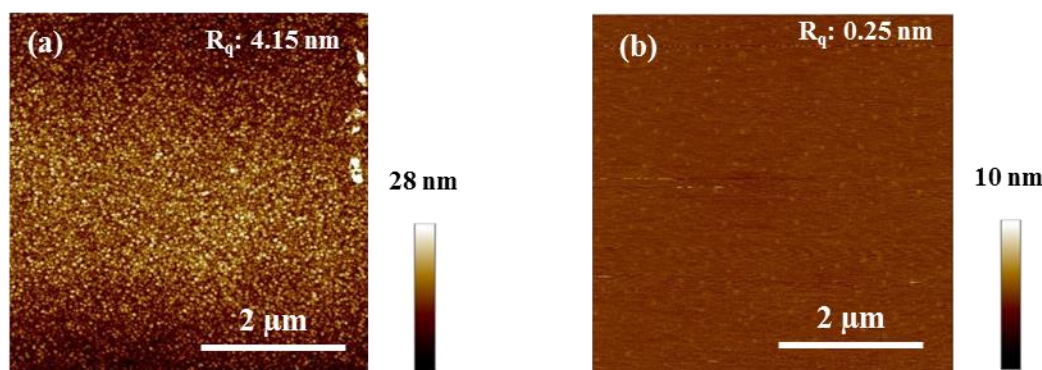


Figure 4-6 (a) A  $5 \times 5 \mu\text{m}^2$  tapping mode AFM image of a gold electrode surface and (b) a  $5 \times 5 \mu\text{m}^2$  tapping mode AFM image of a smooth gold surface. The surface roughness is indicated on the top right corner of each image. Scale bar: 2  $\mu\text{m}$ ; z scale is indicated on the right side of each image.

### 4.1.3 Hydrophobic surface preparation

Modification of the bare quartz crystal via chemical bonding was used to create hydrophobic gold electrode surfaces. One of the relatively well known and simple techniques for modifying the substrate to be hydrophobic via chemical bonding is formation of self-assembled monolayers (SAM).

Several groups reported the formation of a SAM on gold surfaces using either thiol or material terminated with thiol groups (see Figure 4-7 a) [90] [111] [126-127]. Since the thiol termination was on the side of the chemical, the resulting monolayer was organised in such a way that the hydrophobic chains were extending on top of the hydrophilic substrate via the head-surface chemical bonding. An alternative way to form hydrophobic surfaces

via chemical bonding is the formation of SAMs on the target surface (including  $\text{SiO}_2$ , quartz, glass, aluminium, etc.) using silane [74] [95] (see Figure 4-7 b). With a similar working principle to the thiols, aliphatic hydrocarbon substituents or fluorinated hydrocarbon substituents are the hydrophobic entities that enable silanes to induce surface hydrophobicity.

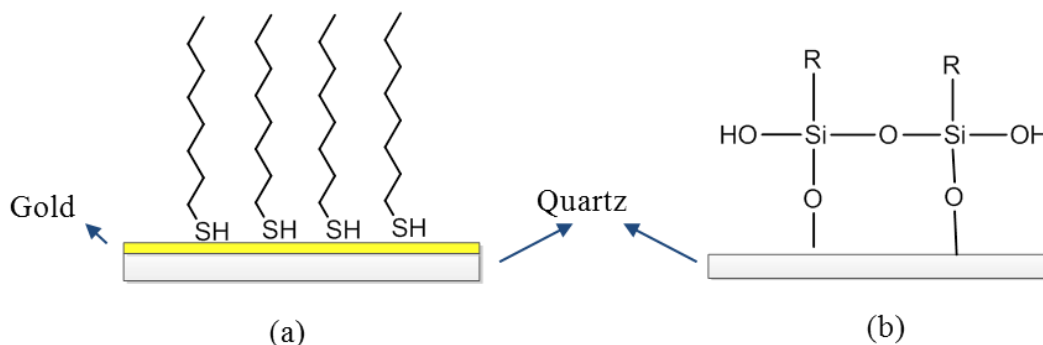


Figure 4-7 (a) chemical bonding of gold by thiolisation (b) chemical bonding of quartz by silanisation.

Modifying the gold electrode with thiol is considered to create a hydrophobic subphase for a lipid spin coating repeatability study. Crystals were prepared for thiolation using the same cleaning procedure as outlined for oxidation (refer to section 4.1.2 a). In this work, 1 mM 1-dodecanethiol in hexane solution was used to form a SAM on gold surface. After cleaning, the crystals were immediately immersed in a 1 mM 1-dodecanethiol (99+% (GC) 1-dodecanethiol was purchased from Acros) in hexane (95+% HPLC grade hexane was purchased from Aldrich) bath and left overnight. The thiolated gold created a surface with a contact angle of about  $110^\circ$  (see Figure 4-8, i.e. hydrophobic). Immediately before use, crystals were removed from the thiol bath, rinsed several times with hexane, ethanol and water in succession and dried under filtered  $\text{N}_2$  gas until the oscillation frequency remained stable. After coating with lipids, crystals were also cleaned, as described earlier for oxidised gold, to remove all the lipids and thiolated compounds [128].

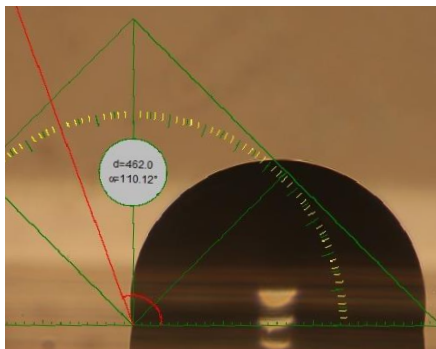


Figure 4-8 Thiolated gold with  $\theta = 110^\circ$ . The red line indicates the contact angle.

In summary, six different substrate preparation procedures have been described in this section. Mica and sputtered quartz were prepared for bilayer deposition via drop coating. Smooth gold substrates were used for thin lipid film deposition via spin coating. Modified gold electrodes (hydrophilic and hydrophobic) were used as multilayer lipids substrate for vapour sensing. All the substrates prepared were either used for lipid film AFM or QCM study before vapour sensing (i.e. film characterisation). Furthermore, before fabricating any vapour sensors, all the substrates for vapour sensing were exposed to sensing vapours to check the subphase response. These results which were also used for sensor calibrations will be discussed in detail in chapter 7.

## 4.2 Review of sensing material fabrication technology

In the past decade, many methods have been introduced for fabricating the sensing material. The response properties of the sensor are determined by the structure of the sensing film, which in turn is strongly dependent on its deposition method. It is important to choose a material deposition technique combination which is both consistent and likely to lead to a high sensitivity to a target vapour.

Many methods have been introduced for lipids sensing material fabrication. The most prevalent methods available to form lipid layers on quartz sensors are: the spin-coating technique (see Figure 4-9) [17], Langmuir-Blodgett (LB) or Langmuir-Schaefer (LS) techniques (see Figure 4-10) [74], drop coating (see Figure 4-11) [18] [129] and spray coating via a spray gun or ultrasonic atomiser (see Figure 4-12) [11] [28] [130]. Among them, the LB technique usually requires expensive equipment and complex procedures, while the other methods are simpler and cheaper. Films coated by the LB technique are

highly ordered with consecutive lipid monolayers [131-135]. However, besides the complex procedure limitations, the choice of the solution makes the preparation time even longer. Drop coating is simple and quick, and is a widely used method for not only lipids but also other sensing film fabrication [18] [129] [136]. Only simple equipment is required during the film deposition procedure; however, the film thickness and uniformity is less controllable [74] [137]. Spray coating and spin coating methods have better controllability, but they were reported to have a lack of sensor response reproducibility, which is dependent on the uniformity, structure and thickness of the sensing film [130]. Moreover, as one of the spray coating techniques, a novel method for depositing sensing films on QCM using an ultrasonic atomiser was developed with an improvement of the surface stability and the reproducibility of sensor responses [130]. However, it is difficult to coat a range of film thicknesses reliably.

Spin coating, which is well known as a low running cost, simple and quick fabrication method for thin, uniform films [102], has also been reported for lipids and also many other sensing films [72] [138-139]. Spin-coated lipid films are known to have a highly organised multilamellar structure when characterised topographically with AFM [140-141], and showed better uniformity compared to spray coating. The membranes were much more controllable and reproducible compared to air brushing, and allowed gases or vapours to diffuse in and out of the layer, making it more responsive [137].

A summary of the properties of each deposition method reviewed is given in Table 4-2. The suitable sensing material, advantages and disadvantages for each deposition method are listed in the table.

To choose a suitable deposition method, the cost of fabrication, property of sensing materials, as well as property of substrate together should be carefully considered. Any of the factors will influence one other. Finally, drop coating was used for lipid bilayer preparation and the spin coating technique was chosen here and used throughout the sensor fabrication in this work.

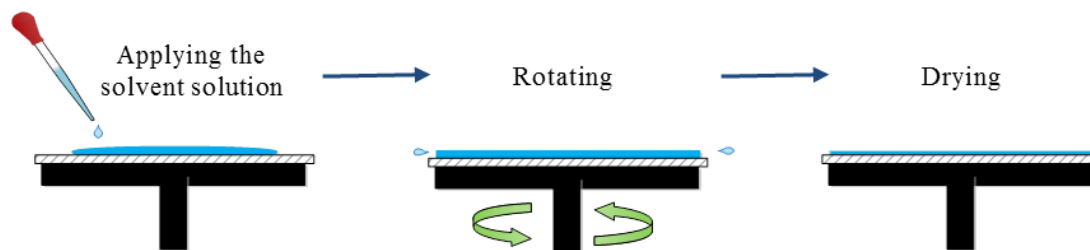


Figure 4-9 Main procedures of spin-coating.

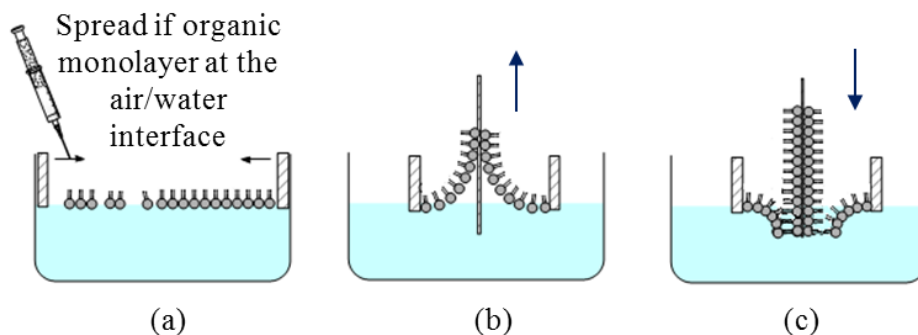


Figure 4-10 Main procedures of Langmuir-Blodgett. a) compressing the film whilst maintaining a constant surface pressure with a teflon barrier; b) the LB film transferred by attaching the surface substrate vertically or c) by dipping the interface horizontally.

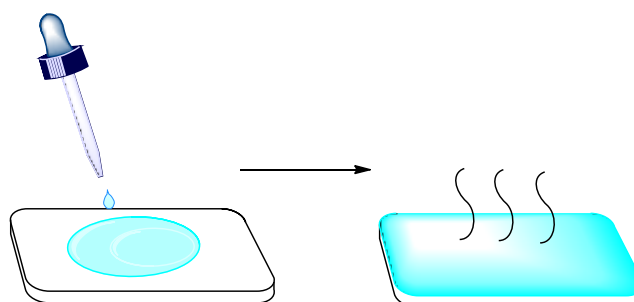


Figure 4-11 Preparation of a drop coating film, including apply the solvent (left) and dry (right).

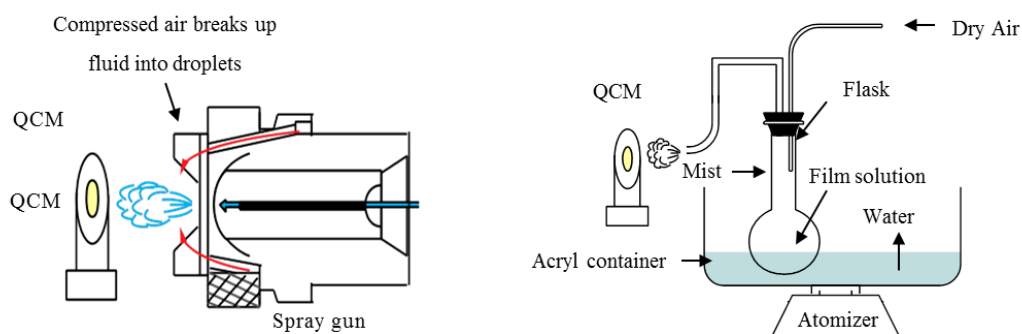


Figure 4-12 The normal spray coating (left) and Ultrasonic Atomiser deposition (right).

Table 4-2 Summary of the properties of each deposition method reviewed-part-I

Fabrication method	Sensing materials	Advantages	Disadvantages	References
<b>Dip coating</b>	<ul style="list-style-type: none"> <li>Polymer</li> <li>Self-assembled materials</li> </ul>	<ul style="list-style-type: none"> <li>Relatively inexpensive equipment used</li> <li>Light or heavy coatings may applied on complex shapes</li> <li>Best uniformity of self-assembled film</li> </ul>	<ul style="list-style-type: none"> <li>Dip withdrawal rate may need to be controlled</li> <li>Large amount of material solution may be needed for large substrate</li> <li>Limitation thickness of self-assembling film</li> </ul>	[130] [142-143]
	Amphiphilic materials	<ul style="list-style-type: none"> <li>Uniform film can be deposited</li> <li>Good controllability of film thickness</li> </ul>	<ul style="list-style-type: none"> <li>Quite sophisticated and expensive equipment required</li> <li>Slow and complex procedures</li> <li>Limit range of deposition materials</li> </ul>	[130] [144]
<b>Spin coating</b>	<ul style="list-style-type: none"> <li>Organic compounds</li> <li>Metal Oxide films</li> </ul>	<ul style="list-style-type: none"> <li>Better controllability</li> <li>low-running costs, simple and quick</li> <li>Good sensor response compare to drop and spray coating</li> </ul>	<ul style="list-style-type: none"> <li>Lack of sensor reproducibility compare to LB technique and self-assembling</li> <li>Better immobilisation</li> </ul>	[130] [140-141] [145-146]
<b>Casting</b>	<ul style="list-style-type: none"> <li>Soluble Organic compounds</li> </ul>	<ul style="list-style-type: none"> <li>Possible to deposit thicker film</li> <li>low-running costs, simple and quick</li> </ul>	<ul style="list-style-type: none"> <li>Poor control on the amount and uniformity of deposited material</li> <li>Poor immobilisation</li> </ul>	[130] [137]

Table 4-2 Summary of the properties of each deposition method reviewed-part-II

Fabrication method	Sensing materials	Advantages	Disadvantages	References	
<b>Air brushing</b>	<b>Spray coating</b>	<ul style="list-style-type: none"> <li>• Soluble organic compounds</li> </ul>	<ul style="list-style-type: none"> <li>• Better controllability</li> <li>• simple quick and economical</li> <li>• Adaptable to various sizes</li> </ul>	<ul style="list-style-type: none"> <li>• Lack of sensor response reproducibility</li> <li>• Hard to control coating thickness</li> <li>• Overspray and surface defects maybe a problem</li> <li>• Poor sensing film structure may form for materials with dewetting phenomenon</li> </ul>	[137] [147]
	<b>Ultrasonic Atomiser</b>	<ul style="list-style-type: none"> <li>• Soluble organic compounds</li> </ul>	<ul style="list-style-type: none"> <li>• Improvement of the surface stability and the reproducibility of sensor response</li> </ul>	<ul style="list-style-type: none"> <li>• Factors influence the amount of mist produced not yet clear defined</li> </ul>	[130]
<b>PVD</b>	<b>Evaporation</b>	<ul style="list-style-type: none"> <li>• Inorganic conducting materials</li> </ul>	<ul style="list-style-type: none"> <li>• Highest purity (good for Schottky contacts) due to low pressures</li> </ul>	<ul style="list-style-type: none"> <li>• Quite sophisticated and expensive equipment required</li> <li>• Poor step coverage, forming alloys can be difficult</li> <li>• lower throughput due to low vacuum</li> </ul>	[75] [148-149]
	<b>Sputtering</b>	<ul style="list-style-type: none"> <li>• Inorganic conducting materials</li> <li>• Metal oxide alloys</li> </ul>	<ul style="list-style-type: none"> <li>• Better step coverage</li> <li>• less radiation damage than E-beam evaporation</li> <li>• easier to deposit</li> </ul>	<ul style="list-style-type: none"> <li>• Quite sophisticated and expensive equipment required</li> <li>• Some plasma damage including implanted argon</li> </ul>	[148-150]

### 4.3 Lipid bilayer preparation

In our work, two zwitterionic lipids DSPC and DLPC purchased from Avanti Polar Lipids were used for vapour sensing (details see section 3.1.1). A mixture of them was also planned to be deposited as a sensing film. For better understanding of multilayers of mixed lipids structures and their stability, it is good to start with mapping a lipid bilayer on a flat substrate other than on a rough quartz crystal surface. Drop coating and flow injection via vesicle fusion techniques were used as lipid bilayer fabrication methods. Mica and sputtered quartz were used as film substrates. The bilayer prepared from vesicle via vesicle fusion method will be detailed in this section and the preparation procedure of these resulting structures for AFM mapping and QCM weighing will also be described.

#### 4.3.1 Vesicle preparation

The glassware for all lipid sample preparation was cleaned by placing it in non-phosphate detergent hot soapy water, using appropriate brushes or sponges to clean both inside and outside of the glassware. Then it was rinsed, first with deionised water and then methanol (Fisher Scientific UK) at least twice until all excess water was removed. Deionised water, having a minimum resistivity of 18 M $\Omega$ ·cm and 5.8 pH from Elga Process Water System, was used in all the experiments. The cleaned glassware was stored in a container filled with methanol.

Nanometre unilamellar vesicles were prepared with mixed lipid composition. First two lipid powders were dissolved in chloroform separately to make a concentration of 10 mg/ml suspension. The lipid in chloroform suspension was stored at -20 °C when not in use. Vesicles were prepared from DLPC/DSPC mixed lipids with a fixed final concentration of 0.5 mg/ml in deionised water. Three different samples were prepared with increasing the amount of DSPC and decreasing the amount of DLPC. For all samples, the initial solution in chloroform was mixed and purified by evaporating the mixed organic solvent using a dry nitrogen stream until the lipids were completely dry. The sample was further dried in a desiccator connected to a rotary vacuum pump for at least 1 hour. Lipids were re-suspended by stirring them in buffer solution (2 mM CaCl<sub>2</sub> in deionised water) above all the lipids' transition temperatures, at a final concentration of 0.5 mg/ml. The buffer solution was used for all lipid preparation, if not otherwise stated. Finally, the

resulting suspension was kept in a water bath with a temperature between 65 °C and 70 °C (above all lipids' transition temperatures) for 5 minutes with vortexing periods of 15 seconds. At this stage, the resulting milky large multilamellar vesicles (LMVs) suspension was ready for further treatments. The main procedures of vesicle preparation are illustrated in Figure 4-13.

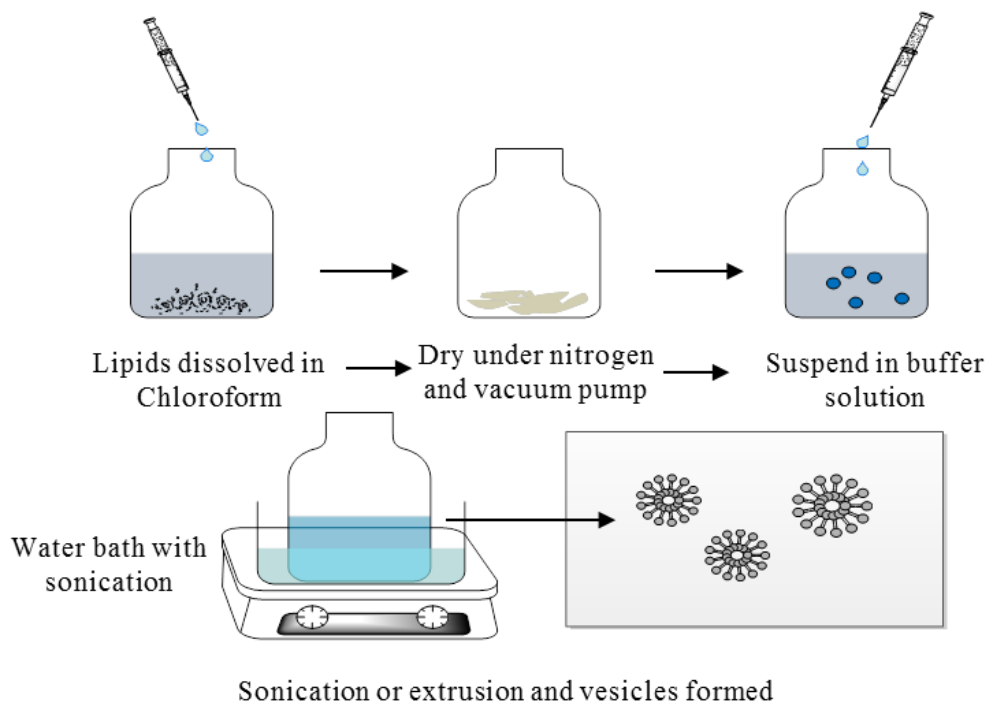


Figure 4-13 Main procedures of vesicle preparation.

Small unilamellar vesicles (SUVs) were prepared by sonication above their transition temperature. It can be used to speed up dissolution, by breaking intermolecular interactions. It has been implemented in this project using an ultrasonic bath to “stir” the lipid solutions twice for 30 seconds, with a 20 seconds pause typically to form SUVs with diameters in the range of 15-50 nm [151]. The product of hydration with sonication was mixture of LMVs analogous in structure to an onion and SUVs. A mini extruder was introduced to produce the vesicle suspension with a particular mean diameter. This was used to push the vesicle suspension 21 times through the polycarbonate filter with 100 nm pores at 65 °C to 70 °C to yield particles having a diameter near the pore size of the filter. Extrusion through filters with 100 nm pores typically yields large, unilamellar vesicles (LUV) with a mean diameter of 120-140 nm. After extrusion, the final formed vesicles with a diameter ranging from 100-200 nm were ready for deposition.

Five different samples were prepared for comparison, and are listed in Table 4-3. The fraction of mixed lipids was weight fraction ( $\alpha$ ) of DSPC in our experiments if not otherwise stated.

Table 4-3 List of five different samples

Sample number	Weight percentage of DSPC (%)	Weight percentage of DLPC (%)	Total Concentration (mg/ml)
1	25%	75%	0.5
2	50%	50%	0.5
3	75%	25%	0.5
4	100%	0%	0.5
5	0%	100%	0.5

### 4.3.2 Bilayer preparation by drop coating for AFM mapping

Bilayers prepared for mapping on mica were formed by drop coating via vesicle fusion. Freshly cleaved mica was mounted onto a stainless steel disc using a sticky tab (Digital Instruments) for AFM mapping. Immediately after the vesicles were prepared by the procedures described in section 4.3.1, the vesicle droplet was allowed to incubate for about 30 minutes and then rinsed in deionised water 10 times with a final liquid volume of 200  $\mu$ l to remove excess lipid vesicles. An additional 120 minutes was required to ensure phase separation of two lipids was complete before acquiring data [86]. During this period, samples were kept in the covered petri dishes in air conditions. After the first scans were taken, all samples were removed from the AFM, and kept in a fridge at about 5 °C in air for subsequent days of scanning. Vesicle fusion happens when the mixed lipid suspension is immediately transferred from a 65 °C water bath to mica to make a SLB and cooled to room temperature. In the surface image study, SUV suspensions were used, formation of SLBs occurred during a thermal quench from slightly above the transition temperature of DSPC to room temperature 25 °C. This is also called the quenched vesicle fusion method [152].

### 4.3.3 Bilayer preparation by flow injection for QCM weighing

Immediately after the vesicles were prepared by the procedures described in section 4.3.1, the suspensions were cooled to room temperature. Bilayers deposited on sputtered crystals were carried out in the QCM in flow mode if not otherwise stated, i.e. the buffer or

mixed lipid solution was continuously delivered to the chamber of the flow cell with the aid of a syringe pump (flow rate 6 ml/h). Occasionally exchange mode was employed to rinse deionised water to fully fill the chamber before measurements and to check the stability of the bilayer after the adsorption of lipids was completed. The SiO<sub>2</sub> coated QCM sensors were modified by adsorption of SLBs via the vesicle adsorption-rupture-fusion. Measurements of crystal resonance frequency change were performed during the deposition to track the bilayer mass and formation kinetics.

In conclusion, the preparation of vesicles (for lipid bilayer formation) and lipid bilayer (for AFM mapping and QCM weighing) have been detailed in this section. The information from the bilayer study will help with understanding of the lipid multilayer properties. The following section will describe the preparation procedures for sensor fabrication. The sensor fabrication technique involves spin coating. Ultrathin lipid layers were also fabricated on smooth gold to help provide insight into the sensing film phase and stability, results which will be further discussed in chapters 5 and 8.

## **4.4 Ultrathin lipid layers and lipid multilayer (sensor) fabrication**

As discussed in section 4.2, the spin coating method was used to coat the adsorbent on the surface of gold electrode forming multilayer lipids for vapour sensing. The relevant spin coating parameters, which will influence the film properties, are discussed in the first section. Each sub-section of this will also give a brief discussion and conclusion of the parameters that were used for the target film fabrication. The detailed fabrication procedures are described afterwards.

### **4.4.1 Spin coating theory**

A typical process of spin coating involves depositing enough lipid solution onto the centre of a substrate and then spinning the substrate at high speed (typically around 3000 rpm). Centripetal acceleration will cause the solution to spread to, and eventually off, the edge of the substrate leaving a thin film on the surface. A final drying step is applied to eliminate excess solvents from the resulting film.

The parameters chosen for the spin process factors such as final rotational speed, acceleration, and fume exhaust contribute to how the properties of coated films are

defined. One of the most important factors in spin coating is repeatability. Subtle variations in the parameters that define the spin process can result in drastic variations in the coated film. The following is an explanation of some of the effects of these variations.

**(a) *Spin methods***

Two common methods of dispense are static dispense, and dynamic dispense. Static dispense is simply depositing fluid on or near the centre of the substrate. The deposition amount depends on the viscosity of the fluid and the size of the substrate to be coated. Dynamic dispense is the process of dispensing while the substrate is turning at low speed (about 500 rpm). After the dispense step it is common to accelerate to a relatively high speed (typical from 1500-6000 rpm) to thin the fluid to near its final desired thickness. Dynamic dispense is a particularly advantageous method when the fluid or substrate itself has poor wetting abilities and can result in less waste of coating material.

The solutions used in this work are chloroform and chloroform/hexane. They are organic solvents that evaporate easily. It is then usually better to choose static dispense and avoid the first pre-coating step, or the film will dry during the first step of dynamic and static dispense.

**(b) *Spin time and speed***

The combination of spin speed and time in addition to the viscosity of solution will define the final film thickness. In general, higher spin speeds and longer spin times create thinner films.

The spin speed of the substrate (revolutions per minute-rpm) affects the degree of radial (centrifugal) force applied to the liquid as well as the velocity and characteristic turbulence of the air immediately above it. Film thickness is largely a balance between the force applied to shear the fluid towards the edge of the substrate and the drying rate which affects the viscosity of the solvent. As the solvent dries, the viscosity increases until the radial force of the spin process can no longer appreciably move the materials over the surface. At this point, the film thickness will not decrease significantly with increased spin time. As we can see, the spin coating process involves a large number of variables that tend to cancel and average out during the spin process and it is best to allow sufficient time for

this to occur. The general trends for the various process parameters and film thickness in spin coating are represented in Figure 4-14 [153].

For most coating materials, the final film thickness will be inversely proportional to the spin speed and spin time. Final thickness and film uniformity will also be proportional to the exhaust volume. If the exhaust flow is too high turbulence will cause non uniform drying of the film during the spin process. In this work, a fixed coating speed and time was used without pre-coating because of the quick evaporation of chloroform, i.e. the film thickness was not determined by the coating speed and time but the concentration of the sample solvent, which will be discussed in section 5.3.2.

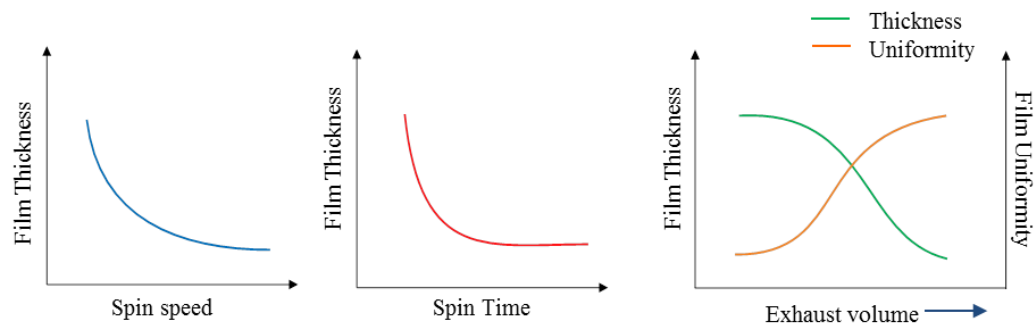


Figure 4-14 The general trends for the various process parameters and quality of the film.

### (c) *Nature of the solution*

Film thickness and other properties will also depend on the nature of the material solution, including viscosity, drying rate, concentration, surface tension, etc.

Above all, a suitable solvent should be chosen and used throughout all the fabrication procedures. Two important factors of solution choice for spin coating are: solubility (solute to solvent) and wettability (solvent to substrate). A popular aphorism used for predicting solubility is "*like dissolves like*". This statement indicates that a solute will dissolve best in a solvent that has a similar chemical structure to itself. The two lipids, DSPC and DLPC, used in this work are polar phospholipids. At a certain temperature and pressure, they are more soluble in polar solvents than in non-polar solvents [154]. Moreover, a successful coating relies on whether the substrate could be properly wetted. The substrate used for the final sensor fabrication was the gold electrode on the bare AT cut quartz crystals. The

whole substrate consisted of a partially wetted (PW) gold electrode in the centre and completely wetted (CW) polished quartz at the edge. As an un-polar, but relatively high dielectric constant (4.81) with 1.04 dipole moment solvent [155], chloroform was used throughout the spin coating. When applying the chloroform on the substrate, the PW gold electrode can be properly wetted compared to the CW quartz substrate. Both DSPC and DLPC can be well dissolved in chloroform even at a high concentration, and an additional polar solvent is then not essential. When a hydrophobic substrate is used, chloroform cannot properly wet the surface, and hexane is introduced, which will be further discussed in section 4.4.3. Trace analysis chloroform was used as the sample solution and laboratory grade chloroform was used for any cleaning if needed, if not otherwise stated.

The drying rate of the fluid during the spin process and afterwards is defined by the volatility of the solvent used as well as by the ambient conditions surrounding the substrate during the spin process. It is well known that such factors as air temperature and humidity play a large role in determining coated film properties. It is also very important to minimise the air flow and associated turbulence above the substrate during the spin process to slow the drying rate, which offers the advantage of increased film thickness uniformity across the substrates. The fluid dries out as it moves toward the edge of the substrate during the spin process. Even the organic solvent used is a readily volatile liquid, and a separate drying step is added after the high speed spin step to further dry the film without substantially thinning it. This can be advantageous for thick films since long drying times may be necessary to increase the physical stability of the film before handling.

In this work, the viscosity and drying rate were the main factors determining the film thickness. The concentration effect on thickness was quantified by QCM and AFM analysis, and will be further discussed in chapter 5.

#### **4.4.2 Thin lipid layer and multilayer fabrication**

Air-stable lipid layers were prepared by spin-coating in this work. Lipid samples were dissolved in chloroform at a concentration of 0.5 mg/ml. As mentioned in section 4.4.1, for fast evaporating solutions such as chloroform, it has been proven useful to not use a low speed spreading step but instead to start the rotation with the final rpm [145]. 100-200  $\mu$ l of mixture were dispensed onto the surface of the substrates by using a digital micropipette (Transferpette<sup>®</sup> electronic). Immediately after the solution of lipids was applied to the

quartz crystal substrates and spun on a WS-400B-6NPP/LITE model spin-coater (Laurell Technologies Corporation) at 1500 rpm for 60 seconds, the solvent dried quickly leaving a thin film of adsorbent on the surface of quartz crystals. Next, the samples were scanned under AFM directly and then placed under vacuum in a desiccator until the next measurement.

The samples fabricated on smooth gold used by spin coating for AFM mapping are listed in Table 4-4.

Table 4-4 Lists of fabricated ultrathin lipid layer samples

Sample number	Weight fraction ( $\alpha$ ) of DSPC	Substrates	Amount ( $\mu$ l) and concentration (mg/ml)	
1	0	Template stripped gold	180	0.5
2	0.5	Template stripped gold	180	0.5
3	1	Template stripped gold	180	0.5
4	0.5	Template stripped gold	180	5

### 4.4.3 Multilayer (sensor) fabrication

Highly aligned membranes were prepared by spin coating whereby lipids and lipid-lipid mixtures were pipetted from a solution onto the substrates. All lipids were co-dissolved in the desired ratio in a suitable organic solvent. The solvent should simultaneously meet the requirements of solvation and wettability of the substrate [155]. Chloroform is a suitable stock solution for DLPC, DSPC and their mixtures. In our case, the use of methanol is not essential because of the good solubility of the lipids in chloroform. For the first period of study, the lipids initially dissolved in chloroform at a concentration of 10 mg/ml. Before use, lipids were diluted with chloroform or hexane/chloroform solution to the desired concentration. Additional hexane was used when thiolated gold was used as the coating substrate to meet the requirement of surface wettability. The standard spin coating procedures have been mentioned previously in section 4.4.2. After the spin coated film formed, the excess coating material on the edge of the quartz wafer outside the gold electrode region (for oxidised gold and thiolated gold substrates) were wiped off by using a chloroform-soaked tissue. An appropriate film thickness was obtained by controlling the concentration of the lipid samples (details will be discussed in section 5.3). For substrates rendered hydrophilic in an etching process (i.e. oxidised gold, sputtered SiO<sub>2</sub>, evaporated platinum) chloroform was used as the coating solution, while for hydrophobic surface (i.e. thiolated gold) hexane was used as the coating solution, and additional chloroform was

used to give solubility of the lipids. Table 4-5 gives an overview about all lipid and lipid-lipid mixtures solutions examined. The spin coating parameters for all samples were 1500 rpm and 60 seconds. Prior to deposition, the crystals were carefully cleaned with the procedures described in section 4.1. The fabricated sensors were placed in a vacuum storage box dried at least for 48 hours to allow the maximum evaporation of solution.

Table 4-5 List of fabricated sensors

Sensor number	Weight fraction ( $\alpha$ ) of DSPC	Solvent	Substrates	Amount ( $\mu$ l)	Concentration (mg/ml)
0	0	Chloroform	Hydrophilic gold	100	1-10
1	0.25	Chloroform	Hydrophilic gold	100	1-10
2	0.5	Chloroform	Hydrophilic gold	100	1-10
3	0.75	Chloroform	Hydrophilic gold	100	1-10
6	1	Chloroform	Hydrophilic gold	100	1-10
7	0	Chloroform/Hexane (86.40% hexane)	Thiolated gold	100	1
8	0	Chloroform	Sputtered SiO <sub>2</sub>	200	1
9	0	Chloroform	Evaporate platinum	200	1

## 4.5 Summary

Film depositions were undertaken using the spin coating and drop coating techniques on specified substrates. Different substrates for film deposition have been detailed in this section, as well as procedures for different film deposition. Bilayers were formed on mica and a SiO<sub>2</sub> sputter coated crystal via vesicle fusion for AFM mapping and QCM weighing, separately. An ultrathin lipid film was formed on smooth gold via spin coating for AFM mapping as well. All these results will help to understand complex multilayer lipid formed on quartz crystal for vapour sensing. Furthermore, DLPC lipids were spin coated on hydrophilic gold, thiolated gold, sputtered SiO<sub>2</sub> and evaporated platinum at different concentrations for spin coating and a sensor repeatability study, which will be further discussed in section 5.3.2 and 7.1. The next chapter will discuss all the AFM mapping and QCM weighing results used for film characterisation.

# Chapter 5 Results and discussion: lipid film characterisation

Lipid film characterisation has been carried out by both Atomic Force Microscopy (AFM) and Quartz Crystal Microbalance (QCM). In this chapter, AFM is introduced for topography analysis, whereas QCM is introduced for quantitative analysis. The results from the AFM and QCM trials will lead to the development of a controllable process for the fabrication of the lipid membranes based vapour sensors. This chapter contains a brief introduction to the working principle of AFM and relevant film characterisation results. The results presented in this chapter, obtained from AFM and QCM investigate in detail the properties of the bilayer, an air-stable ultrathin lipid layer, and then the sensing films. Bilayers were deposited on mica and sputtered silicon dioxide substrates as well as a water-wettable smooth gold surface for mapping and weighing. The stability of domains formed by mixed lipids was checked over time. This data provides understanding of the multilayer lipid structure.

## 5.1 Lipid film characterisation methods

Over several decades, a diverse range of equipment including Surface Plasmon Resonance (SPR) [156-157], Quartz Crystal Microbalances (QCM) [88] [111] [157], Impedance Spectroscopy [158], Atomic Force Microscopy (AFM) [87-88], and Fluorescence Microscopy [159-160] has been used to investigate lipid membrane formation, structure and properties. For example, a combination of QCM, Ellipsometry, AFM and SPR has been reported for the characterisation of the dry mass of absorbed lipids and different phase absorption [157]. Recently published work has also demonstrated that in situ measurements on mica [87] [113] [161], silicon dioxide [88] [111] [162-163] and modified gold [90] [111] [127] substrates can be performed with QCM in a reproducible

manner. AFM scanning techniques and QCM weighing techniques for film characterisation are introduced in this section.

### 5.1.1 Atomic force microscopy

In order to measure the topography of lipid samples (e.g. to characterise domains, SLBs and multilayers), a Nanoscope<sup>®</sup> Multimode Atomic Force Microscope from Digital Instruments was used. The laser beam and initial data were calibrated following the standard procedures manual provided by Digital Instruments. Observations were made with respect to domain size, stability, perimeter, area friction of the gel (solid) phase domains, maximum height, minimum height and average height of the features in AFM images of the samples.

#### (a) *Basic theory of AFM*

AFM is a particularly well-suited to the characterisation of biological surfaces. The AFM can be operated in situ, under buffer and real time at nanometre length scale. It can also provide a direct method to measure mechanical properties of adsorbed vesicles and the surface image of vesicles or membranes [152] [164-165]. Thus, significant effort has been made to make use of AFM to study biological problems. Briefly, AFM consists of a cantilever with a sharp tip (probe) which is used to scan the sample surface. When the tip is brought close enough to a sample surface, the force (including mechanical contact force, Van der Waals forces, capillary forces, chemical bonding, electrostatic forces, magnetic forces etc.) leads to a deflection of the cantilever according in accordance with Hooke's law. A feedback system is set up such that the tip is kept at a constant height from the sample surface while scanning. Typically, the cantilever deflection due to the change of the force is measured with using a laser beam spot focussed on the top surface of the cantilever and reflected into a photo-detector array [166]. The experimental AFM set-up used to investigate sample surfaces is illustrated in Figure 5-1.

AFM is a very sensitive approach. Various environmental factors, such as environmental noise (e.g. from building vibration or sound) can drastically affect the quality of the scanning results obtained. Even in a clean room on an air table, the noise (including noise from fans used to cool the computer system or from air conditioning units etc.) is hard to

avoid [167]. So a fraction of the roughness show in a cross-sectional image AFM can be attributed to environmentally induced noise (0.1 nm in this work).

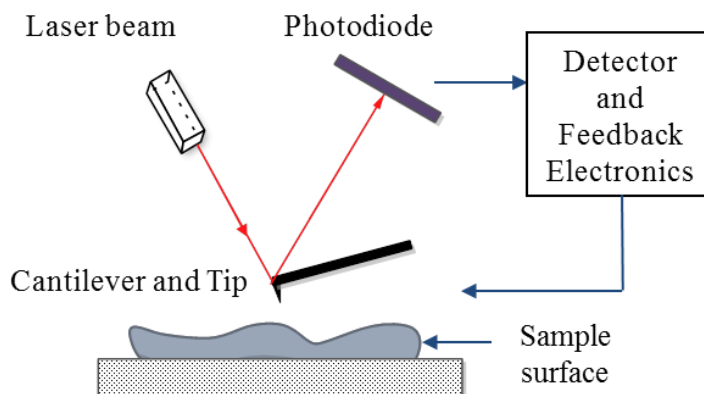


Figure 5-1 AFM works by measuring the forces between the sharp tip and the sample surface.

**(b) AFM tip**

The cantilever is typically silicon or silicon nitride with a tip diameter of curvature of the order of nanometres. Normally, the longer cantilever with smaller spring constant is more suitable for hard surface scanning such as on a metal surface, while the shorter cantilever with a higher spring constant is more suitable for the scanning of soft surfaces such as lipids. The ORT8-35 AFM probes were purchased from Veeco Instruments. Two cantilevers with different sizes are available on each probe substrate. The parameters of two cantilevers are listed in Table 5-1.

Table 5-1 Parameters of two cantilevers on one tip holder

Shape	Length ( $L$ ) ( $\mu\text{m}$ )			Width ( $W$ ) ( $\mu\text{m}$ )			FREQ (KHz)			$K$ (N/m)		
	Nom.	Min.	Max.	Nom.	Min.	Max.	Nom.	Min.	Max.	Nom.	Min.	Max.
<b>A triangular*</b>	100	90	110	15	13	16	73	45	95	0.57	0.28	1.14
<b>B triangular**</b>	200	180	220	30	28	32	24	16	32	0.15	0.07	0.3

A triangular\*: shorter cantilever

B triangular\*\*: longer cantilever

The cantilever with a gold reflective coating was made from silicon nitride which has a thickness ( $t$ ) ranging from 0.7  $\mu\text{m}$  to 0.9  $\mu\text{m}$ . The back side of the cantilever was coated with chromium (Cr–2 nm) and gold (Au–20 nm). The specification of this AFM probe tip used in this work is given in Table 5-2 and Figure 5-2.

Table 5-2 Probe tip specification

Geometry	Cast
Tip Height (h)	2.5-3.5 $\mu\text{m}$
Front Angle (FA)	$36 \pm 2^\circ$
Back Angle (BA)	$36 \pm 2^\circ$
Side Angle (SA)	$36 \pm 2^\circ$
Tip Radius (Nom)	15 nm
Tip Radius (Max)	20 nm
Tip SetBack (TSB) (Nom):	4 $\mu\text{m}$
Tip SetBack (TSB) (RNG):	3-5.5 $\mu\text{m}$

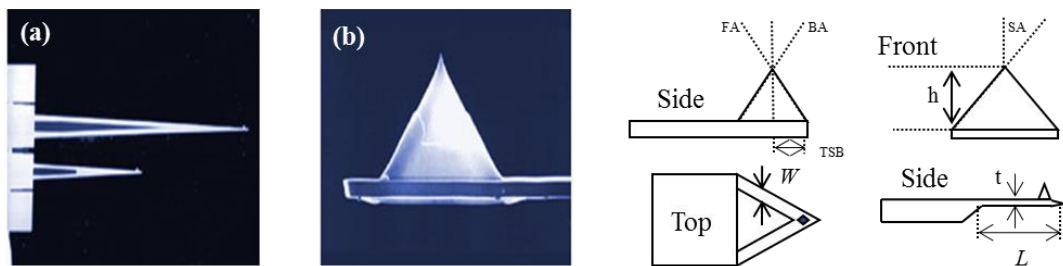


Figure 5-2 Scanning electron microscope images of (a) cantilevers and (b) probe tip, where  $t$  is the thickness of the tip [reproduced from MultiMode™ SPM Veeco probes web page].

### (c) *AFM mode and phase image*

In general, imaging modes are divided into static (also called contact) modes and a variety of dynamic (or non-contact) modes, where the cantilever is vibrated. Here, contact mode and tapping mode were used and will be introduced below.

In contact mode, the sample surfaces are imaged directly using the deflection of the cantilever. The force between the tip and the surface is kept constant during scanning by maintaining a constant deflection. While scanning, the cantilever is "dragged" across the sample surface. In this mode, the AFM probes are close to the sample surface, and the strong attractive forces may cause the tip to snap into the surface or displace a molecule on the surface away from its original location.

Another mode is tapping mode, also called intermittent contact mode. Tapping mode will drive the cantilever to oscillate up and down near to its resonance frequency. The

oscillation amplitude is used as a feedback signal to measure topographic variations of the sample. Compared to contact mode, tapping mode moves the probe tip just close enough to the sample for short-range forces to become detectable whilst preventing the tip from sticking to the surface [168]. As a powerful extension of tapping mode AFM, phase image can also be captured when samples are investigated. In phase imaging, the phase lag of the cantilever oscillation will be monitored which relates to variations in material properties such as adhesion and viscoelasticity. As a result, the phase image will give a hint of how “soft” the sample is compared to the subphase.

Furthermore, for different tapping type, the phase shifts will give different information of the sample surface. The tapping types are relevant to the value of  $r_{sp}$  (i.e. the set-point amplitude ratio). The phase shifts are larger on the harder than on the softer part of the sample surface at moderate tapping ( $r_{sp} = 0.4-0.7$ ). While at hard tapping ( $r_{sp} < 0.4-0.7$ ), the phase shift of the softer part becomes larger than that of the harder part. At light tapping ( $r_{sp} = 0.8-0.9$ ) the hard and soft parts show similar phase shifts close to zero. In a Durham tapping mode AFM image, the phase shift of the harder part becomes larger than that of the softer part (i.e. moderate tapping) [169].

In summary, all the details of AFM that are relevant to this work have been detailed.. For the measurements, the smaller tip with a larger spring constant was always used for contact mode scanning. Both contact mode and tapping mode were carried out to map the surfaces of the samples. Tapping mode phase imaging was also used for the phase study which was important for understanding the sensing mechanism of lipids and will be further discussed in chapter 8. The AFM operational parameters can be found at the beginning of section 5.2.

### 5.1.2 QCM weighing

QCM was not only used as a vapour sensing transducer but also for sensing film characterisation. The detailed working principle of QCM has already been described in Chapter 4. The deposition mass of different samples such as domains, thin dry lipid films and multilayer produced measurements were carried out by the Research Quartz Crystal Microbalance from Maxtek<sup>®</sup> Inc.

It is worth mentioning the activation area again here (refer to section 3.2.4 c). The idea to track bilayer formation via the flow injection method is to create a condition that an exact bilayer was formed and fully covered the substrate. After a hydrated membrane is dried in air for a long time, de-wetting patterns will form without a change in the average lipid density. If that is the case, the real-time measurement can obtain more accurate data of the frequency shift caused by bilayer deposition compared to the frequency shift caused by spin coating based on 5 MHz crystals. The weighing operation details for lipid films formed via drop coating and flow injection coating can be found in the next section.

## 5.2 Lipid layer mapping

The AFM technique was used for lipid film mapping. The relative humidity during AFM measurements was 35-55%. All AFM measurements were carried out at room temperature (25 °C). Images were either recorded in contact mode with E scan mode, using standard silicon nitride ( $\text{Si}_3\text{N}_4$ ) cantilevers with nominal spring constants between 0.01 N/m and 0.06 N/m. For tapping mode measurements on lipid films in air, we used standard silicon nitride cantilevers with nominal force constants of 40 N/m and a resonance frequency in air of 300 kHz for all scans [152]. Normally, the contact mode scanning set points ranged between 0.1 V and 0.25 V with a typical scan rate of 1 Hz. The tapping mode amplitude set point was 1 mV.

### 5.2.1 Mapping of lipid film formed by spin coating

Spin-coated lipid films are known to have a highly organised multilamellar structure when characterised topographically with AFM [102] [140-141]. The topography of lipid films formed by spin coating techniques can be found in this section. Two substrates were used for spin coating, including a hydrophilic gold electrode on a crystal and smooth gold.

#### (a) *Mapping lipids formed on QCM gold substrates*

Figure 5-3 illustrates the topography measured in air of a bare gold electrode (a) and DSPC/DLPC ( $\alpha = 0.5$ , 1 mg/ml) spin-coated on bare gold electrode substrate (c). Figure 5-3 (b) and (d) are the corresponding phase images. The root mean squared surface roughness ( $R_q$ ) of each sample is indicated on the corner of each image.

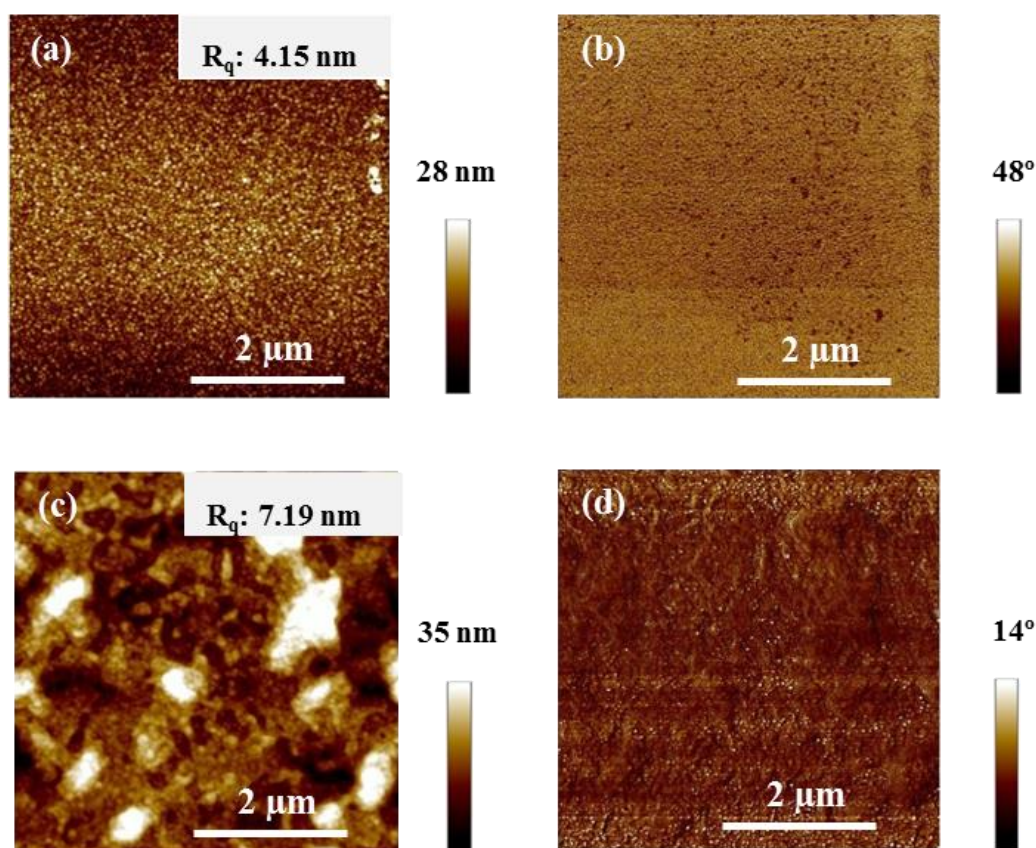


Figure 5-3 Comparison of tapping mode AFM mapping and phase imaging ( $5 \times 5 \mu\text{m}^2$ ) of bare gold electrodes (a and b); a mixed lipid coated substrate (c and d). The surface roughness and the z scale are indicated on the top right hand corner of the height AFM image. Scale bar:  $2 \mu\text{m}$ .

It is very clear that the lipids have been successfully coated on the quartz crystal substrate by spin coating. However, due to the rough surface of quartz crystal gold electrode, it is hard to obtain reliable, quantitative measurements of the lipid structures from the AFM images. To overcome this, a template stripped gold substrate was prepared in order to provide a highly smooth gold surface for the lipid spin coating.

***(b) Mapping of lipids formed on template stripped gold***

As mentioned section 5.2.1 (a), the quartz crystal substrates were too rough to obtain any accurate quantitative details of lipid films. Thus, lipid films were prepared and investigated on substrates of template stripped gold. The films were prepared by the spin coating method with the sample coating parameters set to the same as those used to prepare the vapour sensors (details can be found in section 4.4.1).

AFM tapping mode images of single phase DLPC, mixed DSPC/DLPC ( $\alpha = 0.5$ ) and single phase DSPC spin coated on smooth gold are shown in Figure 5-4 including images from samples investigated on the first and fifth day after preparation. Samples in Figure 5-4 a were prepared from 0.5 mg/ml solution. Sample details can be found in Table 4-4 number 1, 2 and 3. Sample in Figure 5-4 b were prepared from 5 mg/ml solution. Sample details can be found in Table 4-4 number 4.

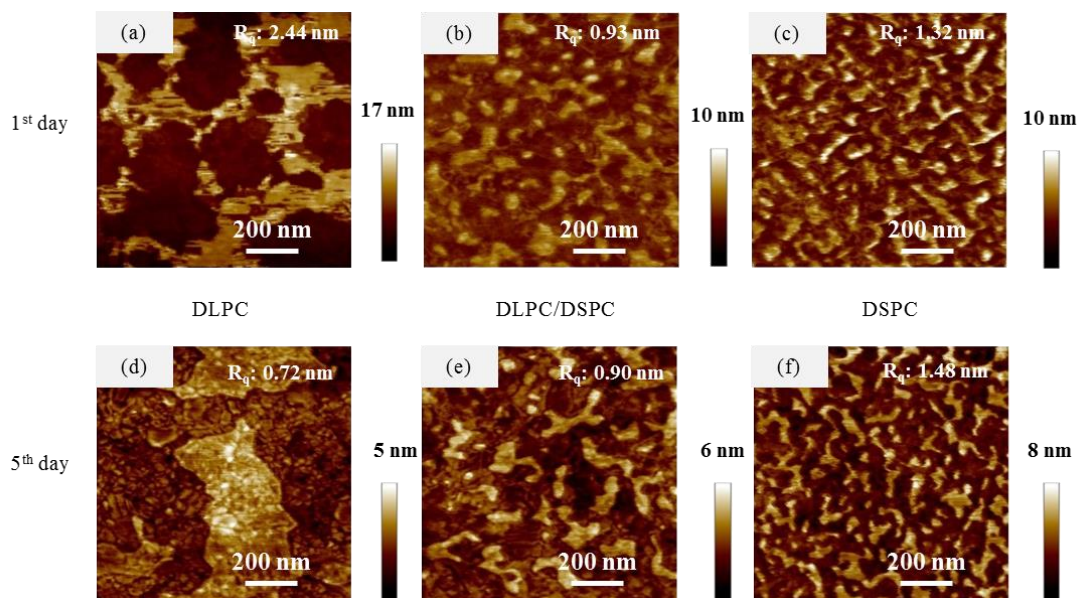


Figure 5-4 a Tapping mode AFM topography images of spin-coated sample of single phase DLPC ( $1 \times 1 \mu\text{m}^2$ , 0.5 mg/ml) prepared on the first day (a) and fifth day (d); DSPC/DLPC mixed lipids ( $1 \times 1 \mu\text{m}^2$ ,  $\alpha = 0.5$ , 0.5 mg/ml) prepared on the first day (b) and fifth day (e); single phase DSPC ( $1 \times 1 \mu\text{m}^2$ , 0.5 mg/ml) prepared on the first day (c) and fifth day (f). The  $R_q$  and z scale are indicated on the right of each image; scale bar: 200 nm.

It is very clear that all samples were successfully spin coated on the smooth gold substrates. All of the sample structures showed apparent changes after five days. Comparing the roughness, all of the films became smoother compared to the freshly coated film structure. Further discussion of lipid film stability can be found in section 8.5.3. However, it is difficult to model the membranes because of the complex multilayer structure formed by the spin coating. This is probably because the structures are of mixed shapes and sizes in the coating solution. By comparison, the film prepared from 5 mg/ml 1:1 DSPC/DLPC solution is shown in Figure 5-4 (b).

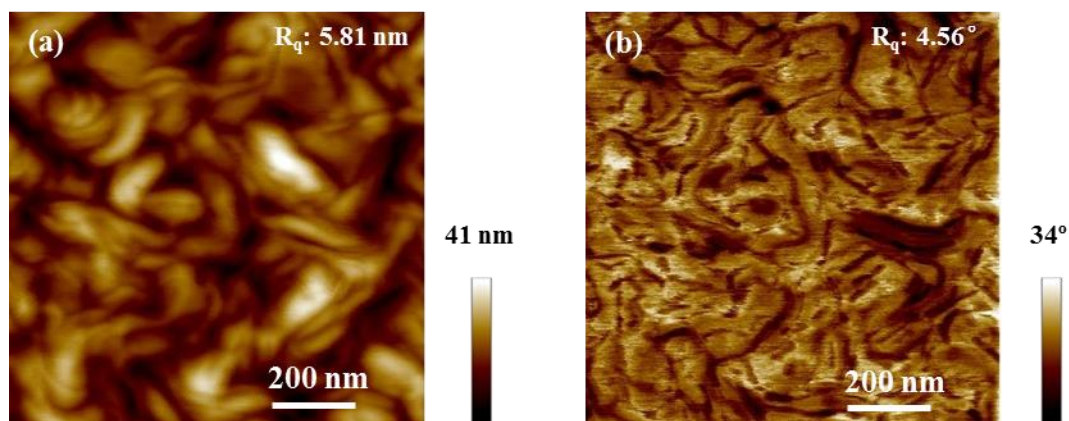


Figure 5-4 b Tapping mode AFM topography images of spin-coated sample of DSPC/DLPC mixed lipids ( $1 \times 1 \mu\text{m}^2$ ,  $\alpha = 0.5$ , 5 mg/ml) (a) and corresponding phase image (b). The  $R_q$  of each sample is indicated on to top right corner of each image.

It is clear that the 5 mg/ml 1:1 DSPC/DLPC solution was successfully spin coated on the smooth gold and form a complex multilayer films. The topography is rougher than the films prepared from the 0.5 mg/ml solution. Thus, it is more difficult to model the structures of these films. As a result, the vesicle fusion method was introduced to try to understand the film structures and will be discussed in the following section.

### 5.2.2 Mapping of lipid films formed via vesicle fusion

As a commonly reported method for hydrated lipid bilayer preparation, vesicle fusion was used to prepare mixed lipid films in order to achieve clear phase separation. As a result, when compared to spin coating, the monolayer lipid thickness and proposed model structure of the de-wetting lipid film could be better investigated from a sample prepared by this method. Mica, an extremely smooth (roughness: 0.049 nm) and hydrophilic (contact angle:  $45^\circ$ ) material, was used as substrates for films prepared by vesicle fusion.

As mentioned in section 4.3.1 and section 4.3.2, the vesicles were sized by sonication (Ultra 6000 Maplin Electronics) followed by mini-extrusion to form SUVs. Quenched vesicle fusion methods were used to prepare mixed lipids for AFM measurements. Both contact and tapping mode AFM scanning were carried out on the same sample for investigation. Freshly cleaved mica was mounted onto a stainless steel disk using a sticky pad (Digital Instruments) [86]. The vesicle droplet was allowed to incubate for about 30 minutes and then rinsed in deionised water 10 times with a final liquid volume of 200  $\mu\text{l}$

to remove excess lipid vesicles. An additional 120 minutes was required to ensure the phase separation of two lipids was complete before acquiring data [86]. During this period, samples were kept in covered petri dishes in air conditions. After the first scans were taken, all samples were removed from the AFM, and kept in a fridge at about 5 °C in air for scanning on subsequent days.

No evidence of DLPC layers can be observed in the AFM images when samples were prepared from DLPC single lipids using the vesicle fusion method. This is probably because this method is not suitable for DLPC film preparation. During the drying and deionised water rinsing procedure, all the DLPC lipids may be flushed off the substrate because of the weak bonding between the lipids and the mica. For DSPC single lipids, a thick film (up to 300 nm thickness) was measured. This is due to the phase of the two lipids: either liquid-crystalline state DLPC or gel state DSPC at room temperature (25 °C). This suggests that the liquid-crystalline state DLPC was difficult to form as layers with this technique and its deposition conditions. Gel state DSPC will have a strong inner bonding between the lipids which are somewhat flattened on the substrate, keeping their solid-like molecular rigidity to form thick multilayer films. Finally, the two lipids were mixed to create a “matrix” for comparison. This “matrix” was measured and demonstrated by AFM scanning.

**(a) Lipid phase separation and domains**

Figure 5-5 shows a contact mode (a) and tapping mode (b) AFM 2-dimensional scanning and cross-sectional analysis images. The sample was produced from 50% DLPC and 50% DSPC mixed lipids, drop coated on mica and dried in air conditions at room temperature for five days.

During the AFM scanning, bare mica (see Figure 4-2) did not show any obvious surface characteristics when compared to the mixed lipids (Figure 5-5 a and b). A comparison of the results from bare mica and those from mixed DLPC/DSPC lipids suggests that both fluid phase DLPC and mixed lipid systems, after transfer to the mica/water interface, form a flattened bilayer on the substrate. In mixed lipid systems, the gel phase DSPC flattened on the mica, keeping a solid-like molecular rigidity, which causes the formation of the lipid-ordered DSPC domain “rafts” in DLPC. In AFM contact mode measurement, the measured domain heights extended either 4.4 nm or 5.9 nm above the surrounding

DSPC/DLPC fluid-gel phase monolayer matrix. In AFM tapping mode measurement, the measured domain heights extended either 4.3 nm or 5.8 nm above the surrounding DSPC/DLPC fluid-gel phase monolayer matrix. Furthermore, contact mode AFM scanning showed a surface roughness of 1.63 nm with a main measured membrane height of 0.9 nm, 4.4 nm, 4.8 nm and 5.9 nm. While tapping mode scanning showed 1.32 nm of surface roughness with a main measured membrane height of 0.8 nm, 4.3 nm, 4.9 nm and 5.6 nm. The predicted model structure will be further discussed later.

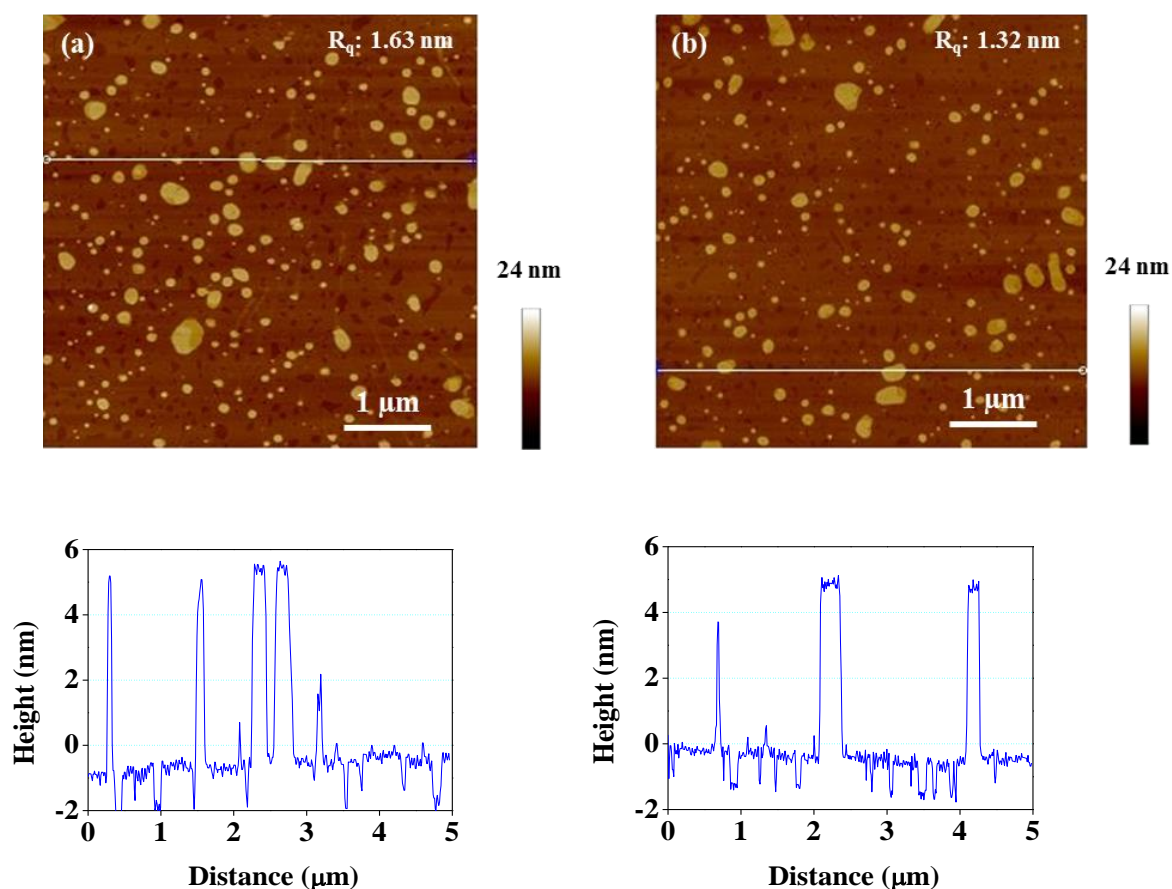


Figure 5-5 AFM images and section analyses of phase separated de-wetting lipid films. (a) Contact mode image ( $5 \times 5 \mu\text{m}^2$ ) and (b) Tapping mode image ( $5 \times 5 \mu\text{m}^2$ ) of phase separated films. The white lines denote the location of the sections; The  $R_q$  and  $z$  scale are indicated on the right of each image; scale bar:  $1 \mu\text{m}$ .

From previous reports in the literature, we know that at room temperature DSPC is supposed to exhibit a gel-phase and DLPC should exhibit a fluid-phase [83]. Thermal

quenching has caused phase separation of the gel and fluid phases with the majority of gel-phase lipid domains areas ranging from 200 nm to 360 nm in diameter. The diameter corresponds to the width of the peak at the base of the AFM cross-sectional height analysis image.

Two points we should also note are: firstly, the height value measured in contact mode was similar to the height value measured in tapping mode. Second, the feature width value measured by contact mode was slightly larger than the value measured by tapping mode. This might be because of the tip convolution and the effect of the tip being "dragged" across the sample surface while scanning. Soft lipids can flatten on the substrate during contact mode scanning which will result in "compression" followed by a small region of molecular movement and therefore a smaller measured sample height and larger lateral sample size [164-165] [170]. While tapping mode causes less movement by intermittently contacting the surface, it is true that, in ambient conditions, a capillary layer of water will form between the tip and the surface. This will, in effect, "pull" the AFM tip onto the surface, usually applying an even stronger force than the force applied (via the set-point) by the operator. Our experience suggests that both contact mode and tapping modes were successfully employed to effectively scan mixed lipids. Although contact mode has reported disadvantages when used for imaging very soft samples, many types of soft biological material have been successfully imaged by contact mode AFM including the ones in this investigation [167]. If we consider in contact mode, the tip has already contacted the sample surface, resulting in a slight decrease in the lipid's thickness. The height measured here was the height difference between the fluid DLPC layer and gel phase DSPC layer. Although, the fluid phase DLPC is more likely to be compressed by the AFM tip during scanning, we must also take into account that the matrix formed by mixed lipids will give a "support" from phase to phase. From this point of view, and the comparison of contact mode and tapping mode AFM scanning results, we consider the thickness was almost likely to be accurate.

***(b) Membrane model structure and de-wetting***

The membrane formed via the vesicle fusion method in hydrated condition has been previously reported by several groups [87] [152] [165] [171]. In these papers, the thickness

of DSPC bilayer was found to be about 5.8 nm while the DLPC bilayer was found to be about 4.8 nm in fully hydrated conditions measured with AFM contact mode [152].

In contrast with the experiments carried out under hydrated conditions, lipid films deposited onto hydrophilic mica substrates via the quenched vesicle fusion method have been investigated with tapping mode AFM (Figure 5-6). This DSPC/DLPC mixed lipid ( $\alpha = 0.5$ ) sample was prepared and deposited on mica substrate via the quenched vesicle fusion method as described in section 4.3. The tapping mode AFM image was obtained under our lab conditions (25 °C in air, dry 2 hours in air after coated) just after the sample was prepared. The phase image of this sample was also monitored by moderate tapping. During each AFM scan, four typical structures were investigated in the same sample. To clearly show the details of structures, the image was cropped and split. Two white boxes and numbers denote the location of the crop and split. The zoomed in images are shown in Figure 5-6 (a)-(1) and (a)-(2) separately. The phase image corresponding to Figure 5-6 (a) is shown in Figure 5-6 (b).

Combining the height analysis in Figure 5-7 with the phase image in Figure 5-6, the onset of the phase image is clearly seen where there are three different phases including a few of the darkest areas (named phase 1) with the thickest section layers, a large lighter areas (named phase 2 and 3) with nearly no clear contrast except at the boundary lines of the lipid layers. The height difference of these layers is 0.8 nm in thickness. As mentioned previously in section 5.1.1, the phase shift of the harder part becomes larger than that of the softer part. The difference in the stiffness of each area can be deduced from the phase angle of the phase image. Considering the two different lipids, a hard gel-phase DSPC and soft fluid DLPC will have a different stiffness and viscoelastic response to the cantilever motion which will give rise to a contrast difference in the phase image [172-173]. Phase 1 corresponds to areas where the complex multilayers were allocated. The height difference of phases 2 and 3 and their similar phase shift are clear signs that the substrate is completely covered by lipids and none of the holes in the lipid layers extend all the way to the substrate in this scanning area. As a result, phases 2 and 3 may have thinner lipid layers underneath.

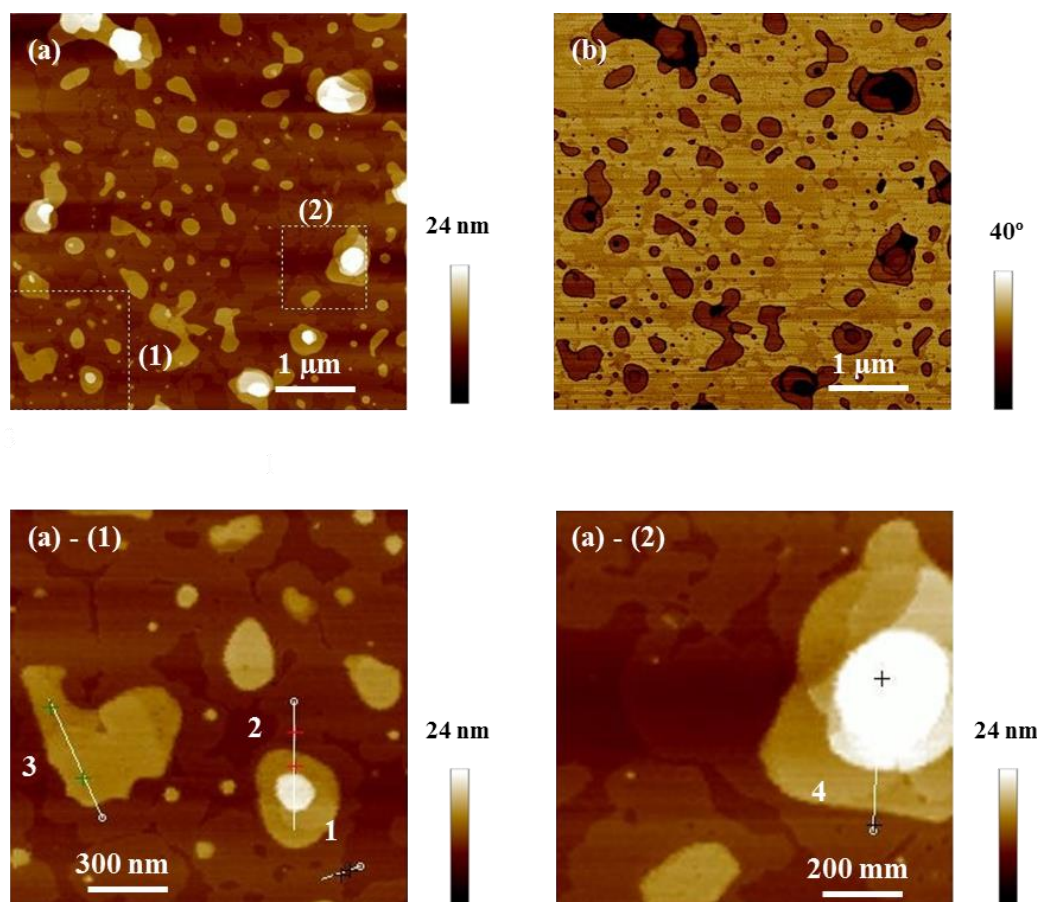


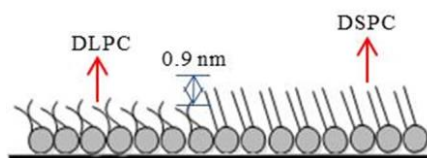
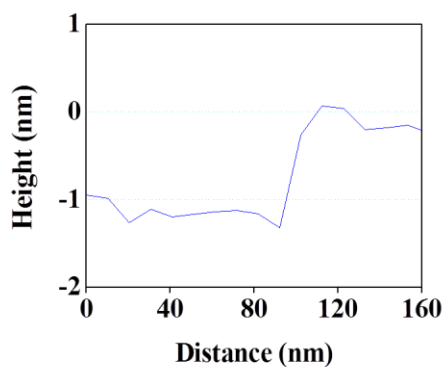
Figure 5-6  $5 \times 5 \mu\text{m}^2$  tapping mode AFM height-deflection (a) and phase (b) image of DLPC/DSPC membranes; (c)  $1.5 \times 1.5 \mu\text{m}^2$  crop and split image of (a) in location(1); (d)  $1 \times 1 \mu\text{m}^2$  crop and split image of (a) in location (2).

In the model structure of the lipid membrane in air mentioned previously in section 3.1.4, the lipid head groups will, in this case, be oriented toward the hydrophilic mica substrate while the acyl chains are directly outward to the air. By combining the heights reported previously by other groups, the theory of the model structure of lipids in air, and the height analysis of this sample and the phase image presented here, it is then possible to suggest the possible model structure of each area.

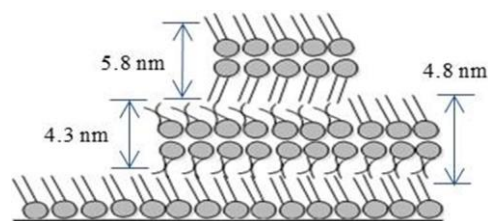
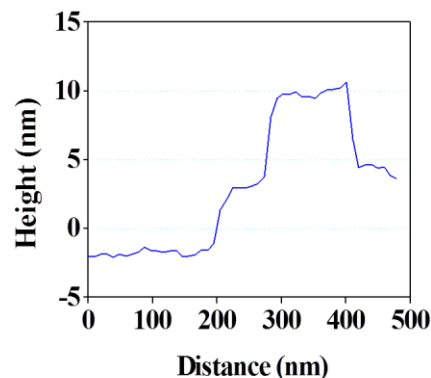
Four typical structures in this sample were investigated and shown as the section analysis images in Figure 5-7 (a) (b) (c) (d). The lines in Figure 5-6 (a)-(1) and (a)-(2) with numbers denote the location of the four sections. The proposed model structures of each section are shown below each section analysis image in Figure 5-7 (a) (b) (c) (d) separately. The lipid with the disordered fluid phase shown in the model structure of

Figure 5-7 is DLPC, while the lipid with ordered gel phase shown in the model structure of Figure 5-7 is DSPC (see marks in Figure 5-7 a).

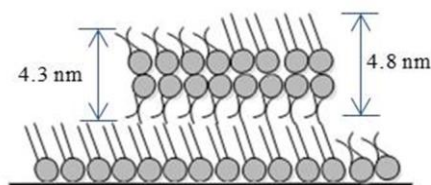
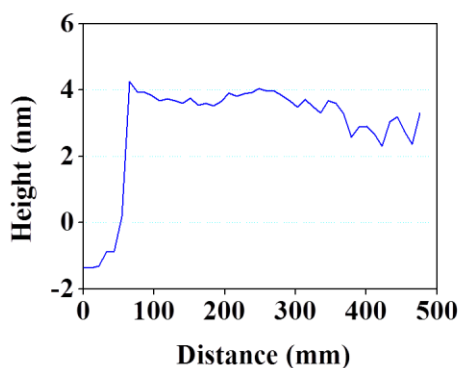
(a) Section 1 in figure 5-6 (a)-(1): DSPC/DLPC monolayer



(b) Section 2 in figure 5-6 (a)-(1): inverted DSPC/DLPC asymmetric/symmetric domains



(c) Section 3 in figure 5-6 (a)-(1): inverted DSPC/DLPC asymmetric domains



(d) Section 4 in figure 5-6 (a)-(2): complex DSPC/DLPC multilayers

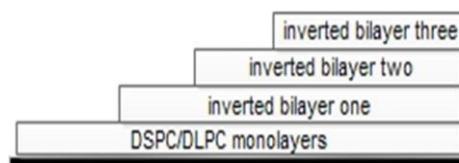
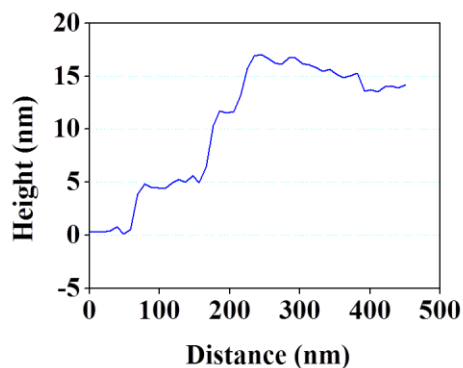


Figure 5-7 Tapping mode AFM section analysis images (a, b, c and d) of DLPC/DSPC membranes. The corresponding various types of membranes model structures are given at the bottom.

The patterns shown in phases 1 and 2 with 0.8 nm in thickness are most likely initiated by the de-wetting of the DSPC/DLPC lipid bilayer films during phase separation in dry conditions and finally formed DSPC monolayers surrounding by DLPC monolayer “pools”. There are also several structures that can be viewed above the monolayer “pools”. According to the height from the cross-sectional analysis, these structures are inverted bilayers. As shown in Figure 5-7 (b) and (c), both inverted symmetric domains and inverted asymmetric domains existed. In this study, the thickness of the inverted DSPC bilayer is most likely to be 5.8 nm, while the thickness of the inverted DLPC bilayer is most likely to be 4.3 nm. The thickness of the DLPC inverted bilayer is slightly lower than existing results (4.8 nm). However, this may be because of the lipid layers in our measurement environment do not “stand upwards” as they do in fully hydrated conditions.

It is very clear that the mixed lipids formed vesicles will lead to two distinct conditions for the formation of the DLPC/DSPC membranes. We believe that symmetric domains consisted of an even distribution of either gel phase DSPC or fluid phase DLPC in both leaflets (Figure 5-8 a and b), whereas asymmetric domains consisted of a single leaflet of gel phase DSPC (Figure 5-8 c).

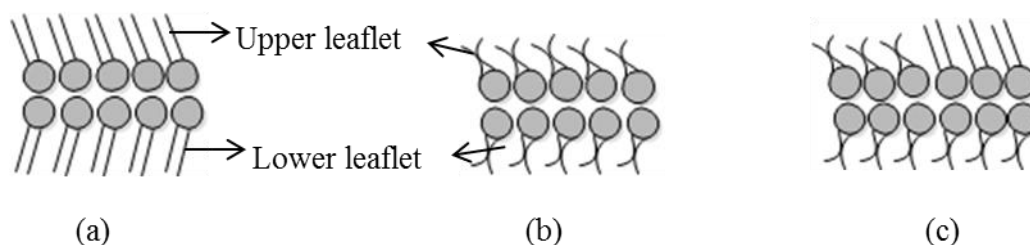


Figure 5-8 Model structures (a) DSPC inverted symmetric domains (b) DLPC inverted symmetric domains and (c) DSPC/DLPC inverted asymmetric domains.

Domain stability quantified in hydrated conditions over several hours has been reported before [171]. In this study, the structure of membranes in air formed by the quenched vesicle fusion method remained unchanged for a 2 hour observation period, while we observed that the structures were unstable after several days. AFM contact mode quick scan (7.18 Hz) measurements were carried out on the DLPC/DSPC (1:1) mixture lipids on the first, second and third day after preparation in order to check the membrane stability. Figure 5-9 illustrates the change in membrane structure as a function of time, investigated

by contact mode AFM quick scan. These images were fast scanned with low resolution, which although not good enough to compare the details of changing thickness, is sufficient to study the stability of these structures.

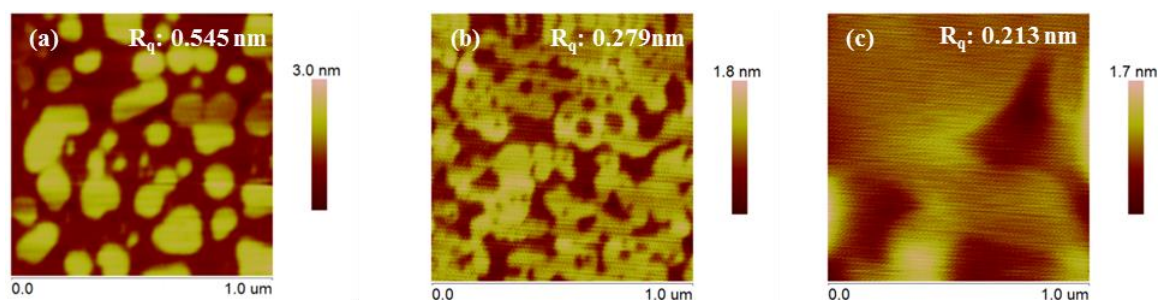


Figure 5-9 AFM 2-dimensional flattened image ( $1 \times 1 \mu\text{m}^2$ ) of mixed 50% DSPC and 50% DLPC formed by quenching vesicle fusion method coated on bare mica surface captured on the a) 1<sup>st</sup> day b) 2<sup>nd</sup> day c) 3<sup>rd</sup> day of preparation.

During the three day observation of the films, the surface roughness of the membranes was found to decrease. During the changes, the decreasing of number of multilayer areas is likely to have resulted from lipid molecules transferring and flipping from the two upper leaflets to the lower leaflets thus making each leaflet more “continuous”. The detailed structure tapping mode AFM scanning was carried out on the first, the third and the fifth day after sample preparation (50% DSPC 50% DLPC, 1 mg/ml quenched vesicle fusion method coated on mica dry in air) which is shown in Figure 5-10.

Figure 5-10 illustrates the change in membrane structures as a function of time for a DSPC/DLPC lipid layers prepared by quenched vesicle fusion method. We found during the conversion, the roughness of the sample kept decreasing as the sample was drying out and the number of multilayers was decreasing. This phenomenon was not observed in the sample of single phase DSPC multilayers which was found to be relatively more stable. The structure seen on the first day has been discussed previously: with features including inverted bilayer asymmetric, inverted bilayer symmetric/asymmetric and monolayer “pools”. It has been reported that: “the mechanical coupling observed for asymmetric DSPC domains in the model membrane system suggests that rafts or ordered phase domains in one leaflet are able to locally decrease the membrane undulation and lead to a strong adhesion and close contact between the other leaflet and a substrate, which can be a

cytoskeleton or another membrane” [171]. From this point of view, if we consider that the monolayer “pools” were formed after the vesicles were ruptured, with the driving force of this mechanism the de-wetting phenomenon, then after the vesicles ruptured on mica, or even after more vesicles ruptured above the existing bilayer, DSPC/DLPC leaflets in the upper layer have a tendency to move up to a location above the upper leaflet of the DSPC/DLPC symmetric/asymmetric domains, which try to form one and three monolayer de-wetting patterns.

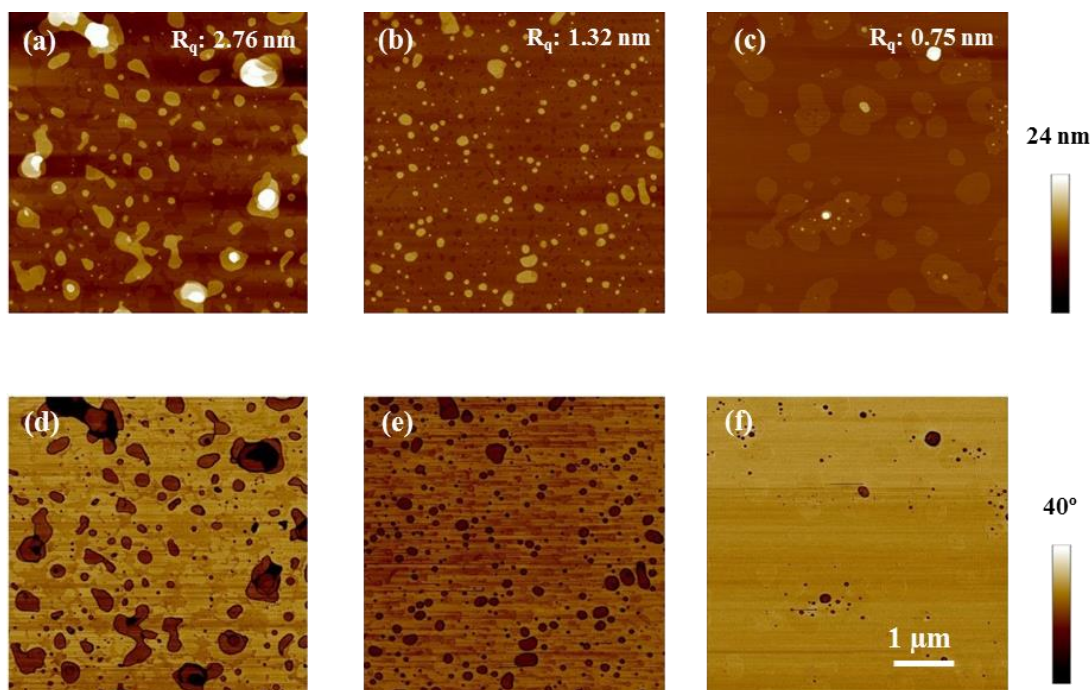


Figure 5-10 Tapping mode AFM imaging of DSPC/DLPC ( $\alpha = 0.5$ ) membranes prepared by vesicle fusion method in air on the first day (a), the third (b) and the fifth day (c) with all images covering  $5 \times 5 \mu\text{m}^2$ . Images (a), (b) and (c) are topographical maps whereas parts (d), (e) and (f) show the corresponding phase images. Scale bar:  $1 \mu\text{m}$ ; z scale for height image: 24 nm; z scale for phase image:  $40^\circ$ .

During the five days, the total amount of the lipids remained roughly constant (this will be further discussed in section 7.4). It seems that the existence of the fluid phase DLPC, gel phase DSPC matrix and DLPC matrix were then able to be transferred or flipped from upper leaflet to the proximal leaflet; in effect, trying to fill in the “holes” of each leaflet and form a continuous monolayer covering the whole subphase underneath. On the third day of scanning, nearly all of the complex multilayers had disappeared; the remaining structures included monolayer “pools” and asymmetric inverted domains which give a hint that the thick multilayers and trans symmetric/asymmetric domains were relatively

unstable. On the fifth day of scanning, even though there were still some surface features similar to those seen in Figure 5-10 (b), the majority of the scans showed smooth, uniform domains with 0.75 nm roughness and 0.7 nm height difference. The phase image corresponding to Figure 5-10 (c) is shown in Figure 5-10 (f). Apart from a few dark multilayer regions, this image contains essentially no contrast except at the boundary lines of the lipid layers. The AFM imaging revealed that the membranes prepared in this manner after drying for about 5 days consisted of immobile DSPC monolayer domains extending only 0.7 nm above the surrounding DLPC matrix. However, there may be more structures underneath.

It is worth mentioning that the measured relative phase shift is highly dependent on the physical property of each cantilever. Therefore, while it is possible to compare the phase shifts within one image, it is impossible to compare them for different days of scanning, even though they are the same sample.

*(c) gel-phase mean molecular area*

Three samples with increasing proportion of DSPC in the DLPC/DSPC mixture lipids were prepared on mica for comparison using quenched vesicle fusion method. Figure 5-11 shows quick scan, contact mode AFM images of three different samples coated on mica substrates after drying for 5 days.

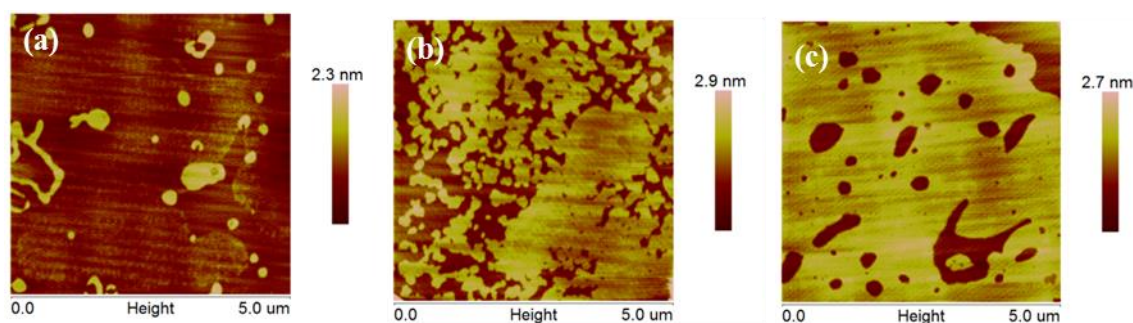


Figure 5-11 AFM ( $5 \times 5 \mu\text{m}^2$ ) height deflection images of mica-supported DSPC/DLPC bilayers by increasing composition of DSPC while decreasing the composition of DLPC dried for 5 days. (a)  $\alpha = 0.25$  (b)  $\alpha = 0.5$  (c)  $\alpha = 0.75$ , where  $\alpha$  is the weight fraction of DSPC.

The main objective was to find out the proportion of gel-phase lipid that was enclosed and coated as a function of the DSPC/DLPC weight fractions. As a result of the complex

structure formed on the first day, it easier to use the ratio of each mixture on the fifth day after the samples were prepared. Therefore, the data was always acquired after the relatively stable structures were formed, i.e. where the monolayer DSPC matrix is surrounded by monolayer DLPC “pools” (see Figure 5-11).

We observe that by increasing the weight fraction ( $\alpha$ ) of DSPC gel-phase lipid, the total gel-phase area and the number of domains was increased and DLPC total fluid-phase was decreased. Some aggregation of gel-phase DSPC was present all three samples, but high aggregation of gel-phase DSPC was found when the weight fraction of DSPC increased to 75%, and no individual domain “rafts” in DLPC bilayer could be observed under AFM.

Different domain sizes can be found in the each sample scanned. The domain diameters ranged from several nanometres up to hundreds of nanometres. As we know the domains were formed by the vesicle fusion method. When the vesicle fusion has just occurred on the substrate, the domain sizes mainly depend on the size of vesicles. During preparation, the vesicle suspensions could be mixtures of SUV with diameters in the range of 15-50 nm, LUV and LMV analogous in structure to an onion. After rinsing with deionised water, the excess vesicles, which have weak bonding to the substrate, will be washed off; resulting in domains of various sizes. Table 5-3 below shows different fractions of domain coverage area contained within different samples.

Table 5-3 Relationship between the weight percentage of total DSPC and total gel-phase DSPC domain area

Weight percentage of DSPC (%)	Total concentration (mg/ml)	Diameter of main domain (D)	Calculated gel-phase area (%)	Total gel-Phase area enclosed (%)
25%	0.5	130-240 nm	20.76%	18.44%
50%	0.5	120-250 nm	44.05%	41.76%
75%	0.5	N/A	70.24%	63.23%

In conclusion, the quenched vesicle fusion method has been successfully carried out to obtain two types, i.e. asymmetric and asymmetric/symmetric, of domains in the DSPC/DLPC monolayer matrix. Both contact mode and tapping mode AFM has been used to image the domain surface coated on the bare mica. Initial results suggest that phase separation occurred in DLPC/DSPC bilayers. Fewer changes are found in asymmetric individual domains over 3 days observation, where inverted symmetric/asymmetric

domains were noticeably unstable and converted by flipping to the relatively stable trans asymmetric domains, thus filling up the “holes” of each leaflet. Further scanning was carried out on the samples prepared from different composition of mixed lipids. By increasing the composition of DSPC gel-phase lipid, the total gel-phase coverage area was increased and DLPC total fluid-phase was decreased. When the weight fraction of DSPC increased to 75%, the domains could not be observed by AFM due to the highly aggregated gel-phase DSPC. The amount of gel phase successfully coated on mica was in good agreement with the possible prediction results showed in table 5-3.

Overall, single phase DLPC, DSPC and mixed lipids can be successfully coated on gold electrodes and smooth gold by the spin coating method during this period of study. Only mixed lipid bilayers were successfully coated on mica by the vesicle fusion method. The detailed topography of different methods to form lipid layers and the model structure of them has been discussed in this section. Moreover, fluid phase DLPC was relatively unstable when compared to mixed DSPC/DLPC and single phase DSPC lipids. With the existence of DLPC, gel phase DSPC was able to flip-flop over the leaflet of the lipid membrane. Mixed films were more like to form a fine uniform structure finally. This might be a possible way to improve the sensing film properties and will be further discussed in chapter 8.

### **5.3 Lipid layer weighing**

The lipid film weighing was carried out by QCM. The weighing was completed by two main steps. The first step was to weigh the bilayer formed on sputtered SiO<sub>2</sub>, in order to find out the average film density of the lipid bilayer. The second step was to weigh the spin coated vapour sensor, which is required to complete the first step of the film coating repeatability study to be further discussed in section 5.3.2 and 7.1.2.

#### **5.3.1 Quantitative analysis of bilayer formed by vesicle fusion**

As described in section 4.2.3, after assembly in the QCM instrument, deionised water was injected into the flow cell and the system was allowed to reach equilibrium. The flow rate of the deionised water was fixed at 6 ml/h. A vesicle suspension was then injected at the same flow rate after the stable baseline in deionised water flow had been achieved. In brief, upon interaction of vesicles with the surface of a sensor crystal, changes in the

resonance frequency related to the attached mass are measured. Measurements in a liquid environment were performed at a working temperature of  $25 \pm 0.2$  °C [162]. The frequency stability was monitored for 5 minutes before addition of lipids (or buffer). Measurements for different lipids were performed under fixed conditions-usually the same buffer, liposome preparation procedures, lipid concentration, temperature and repeat procedures to reduce statistical errors. A rinse with a buffer was carried out for each measurement to wash off excess lipids and check the stability of lipids adsorption.

*(a) Hydrated membrane adsorption*

Supported lipid bilayers (SLB) and supported vesicular layer (SVL) formation were performed using lipid vesicles prepared from phospholipids. We studied the formation of DLPC, DSPC and DSPC/DLPC mixtures on the 100 nm thick 5 MHz quartz crystals which had been sputter coated with silicon dioxide. Six measurements were carried out with the same measurement procedures which are listed in Table 5-4. As mentioned in the preparation section 4.3, the weight fractions ( $\alpha$ ) of DSPC were set at 0, 0.25, 0.5, 0.75 and 1. All measurements were carried out at room temperature (25 °C) with an injection flow rate of 6 ml/h.

Table 5-4 Six different measurements

Measurement number	Sample details	Concentration (mg/ml)
1	$\alpha = 0$	0.5
2	$\alpha = 0.25$	0.5
3	$\alpha = 0.5$	0.5
4	$\alpha = 0.75$	0.5
5	$\alpha = 1$	0.5
6	DI water	n/a

The QCM system was first stabilised in a buffer flow for at least 5 minutes (not shown here), and then 2 ml liposome dispersions were injected into the flow cell under the same fixed flow rate of 6 ml/h. For each measurement, the solution is pumped through the chamber for approximately 20 minutes. The response of a quartz crystal to the liposome adsorption was monitored until the frequency became stable for at least 5 minutes. To ensure fully complete vesicle fusion, another 40 minutes (“stand by” conditions) observation was applied before starting to rinse with a buffer. Figure 5-12 shows the QCM response when the DLPC, DSPC and DLPC/DSPC liposomes flowed in the QCM flow cell. For better clarity, all frequency-time traces were shifted to the time at which the frequency started to decrease.

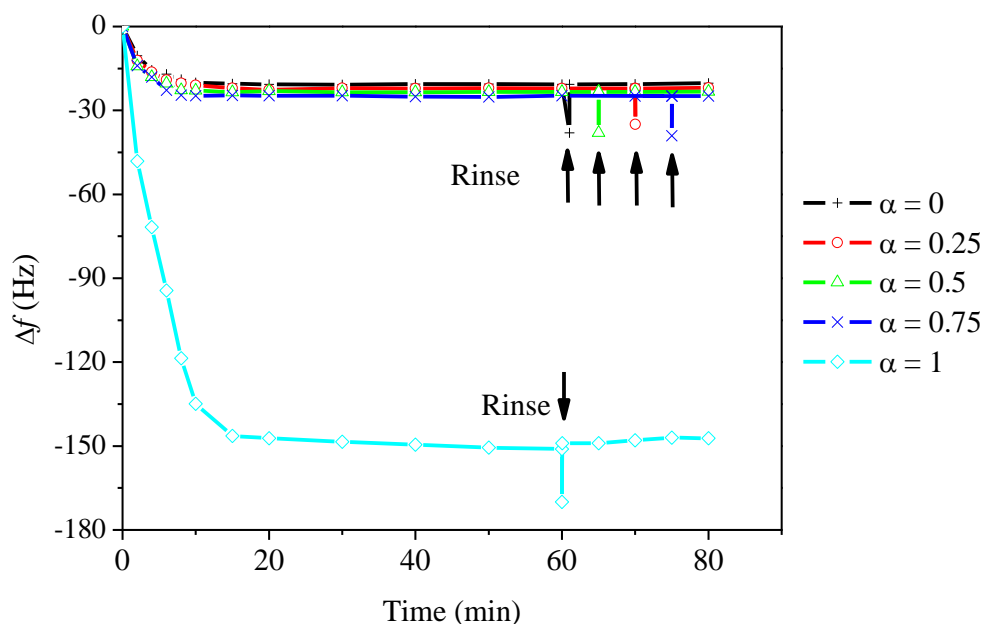


Figure 5-12 Frequency shift as function of time upon formation of a)  $\alpha = 0$  (black plus), b)  $\alpha = 0.25$  (magenta cricle), c)  $\alpha = 0.5$  (green triangle) d)  $\alpha = 0.75$  (blue cross) e)  $\alpha = 1$  (cyan rhombus) on top of a silicon dioxide sputtered coated crystal.

Generally, after injection of liposome at time  $t = 0$  min, the frequency decreased which indicates that lipid adsorption was taking place. After a certain time ( $t_{as}$ ), the frequency shifts reach asymptotic values ( $\Delta f_{as}$ ). After a rinse with a buffer, the final frequency ( $f_{final}$ ) was recorded (see Table 5-5). The first trends (case a) were seen at  $\alpha = 0, 0.25, 0.5$  and  $0.75$ , where a decreased frequency and increased resistance were observed within about 10-15 minutes after the injection of vesicle suspension; thereafter, the values became constant. The increased  $\alpha$  resulted in the greater changes in frequency and resistance observed at each plateau region. The second trend (case b) was seen at  $\alpha = 1$  (i.e. DSPC single phase), where significant rapid shifts were observed in both the frequency and resistance data just after the sample dispersion reaches the silicon dioxide sensor.

DSPC has a higher molecular weight than DLPC. If we presume that the SLBs were fully covering the quartz crystal surface, increasing the weight fraction of DSPC will result in a total increase of mass in the lipids' mixture and, consequently, will result in a higher mass adsorption onto the same surface area of sputter coated quartz crystal. The results shown in Figure 5-12 support the hypothesis that the increase of DSPC in mixed lipids results in a greater decrease of frequency. Based on the whole experimental procedure we

assume that all of the liposome suspensions were successfully adsorbed on the sputtered silicon dioxide surface. A rinse with water indicates that the resulting structures were stable.

The observed difference clearly reflects the different pathways in adsorption and subsequent structural transformations of different samples that occur at the sputtered silicon dioxide interface. Further discussion will be given in the following sections.

**(b) Pathways of vesicle deposition**

The two basic types of QCM responses when (a)  $\alpha = 0.5$  (50% DSPC), (b)  $\alpha = 1$  (100% DSPC) liposome dispersions flow in the QCM sensor cell are shown in Figure 5-13. Figure 5-13 (a) shows the formation of a continuous SLB (case a). Upon adsorption, the frequency decreases. Hence, during injection, a decrease of frequency was observed and then the value reached equilibrium level and kept constant during all “stand by” conditions. The resistance increases spontaneously and soon reaches equilibrating data level of about  $\Delta R_{final} = 1.1 \Omega$ . This type of trend was also observed at  $\alpha = 0, 0.25$  and  $0.75$  which suggests that the onset of bilayer formation occurs for low surface coverage, i.e. either adsorbed liposomes rupture spontaneously under flow injection, and (or) only a few contacts between adsorbed vesicles were necessary to induce the formation of bilayer.

Changes in the QCM resonant frequency versus time for the adsorption of DSPC liposomes on the crystal sensor (case b) is shown in Figure 5-13 (b). Upon adsorption of SUVs made of DSPC, there was a large shift in resonant frequency accompanied by a large shift in the resistance. The large resistance shift indicated that the structure of the adsorbed lipids was fundamentally different from either an adsorbed monolayer or an adsorbed bilayer. After about 20 minutes, the frequency equilibrates. The resistance shift shows a peak of  $\Delta R_{max} = 6.3 \Omega$ , soon after the onset of adsorption before equilibrating data level of about  $\Delta R_{final} = 6.0 \Omega$ . The resistance increased and equilibrates an elevated level of  $\Delta R = 6.0 \pm 0.3 \Omega$ . From the  $\Delta f$  and  $\Delta R$  values, we attribute this to the formation of a flexible layer of lipids vesicles. The frequency and resistance both remain stable upon rising with buffer, indicating that the vesicles were adsorbed in a stable manner at the timescales investigated here.

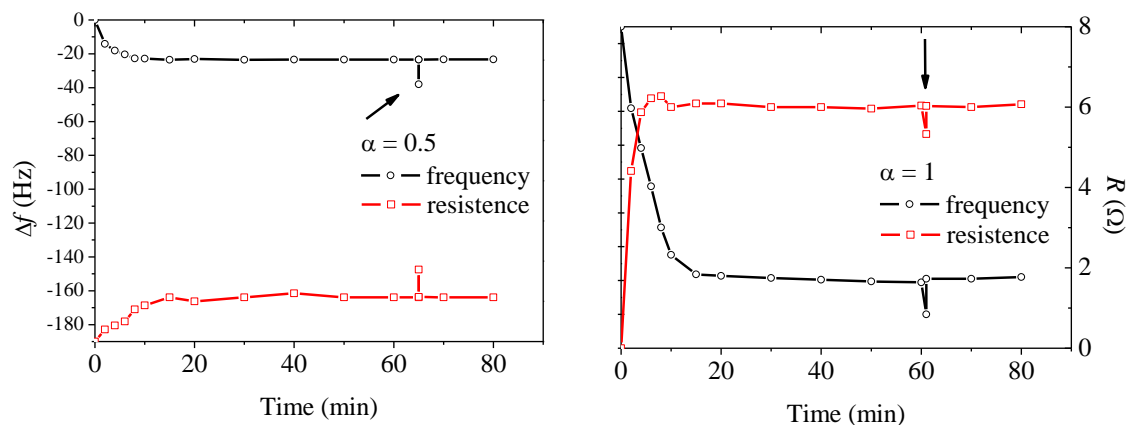


Figure 5-13 QCM response for (a) deposition of 50% DSPC, example of SLB formation (case a) triggered at low vesicular coverage; and (b) 100% DSPC, example of SVL formation (case b). Lipids exposure started at 0 minutes; rinsed with buffer was indicated by arrows.

Immediately after the flow injection was complete, the resulting modified crystals were carefully taken out and observed under an AFM. No features of DLPC and DLPC/DSPC were observed, which indicate that the SLBs were relatively weakly bonded physically and may be damaged when they were carried out in this working condition. Adsorbed DSPC LUVs were resolved as objects with a minimum height of about 15 nm. AFM measurements were carried out after all the vesicle fusion was complete, but no clear shapes were observed for single phase DLPC and three mixed lipids which showed that the bilayer formed under hydrated condition was relatively unstable and may be damaged during the handling procedure (from a flow cell in hydrated condition to AFM in air). Only clear evidence of non-ruptured DSPC coated on a gold electrode was investigated under AFM and shown in Figure 5-14.

Because of the rough substrate, the shape and maximum thickness was difficult to identify. From AFM mapping and phase imaging, it is very clear DSPC layers were successfully coated on the sputtered  $\text{SiO}_2$  substrate via the vesicle fusion flow injection method with a minimum thickness of 15 nm. Combining the QCM and AFM results, it could be concluded that the large frequency shift ( $149 \pm 1.5$  Hz) corresponds to that expected for the adsorption of lipid vesicles. The structure formed in case b was completely different from the structure formed in sensor fabrication. The frequency shift used later in the multilayer study was then estimated from the other 4 sample data which will be further discussed in section 5.3.2.

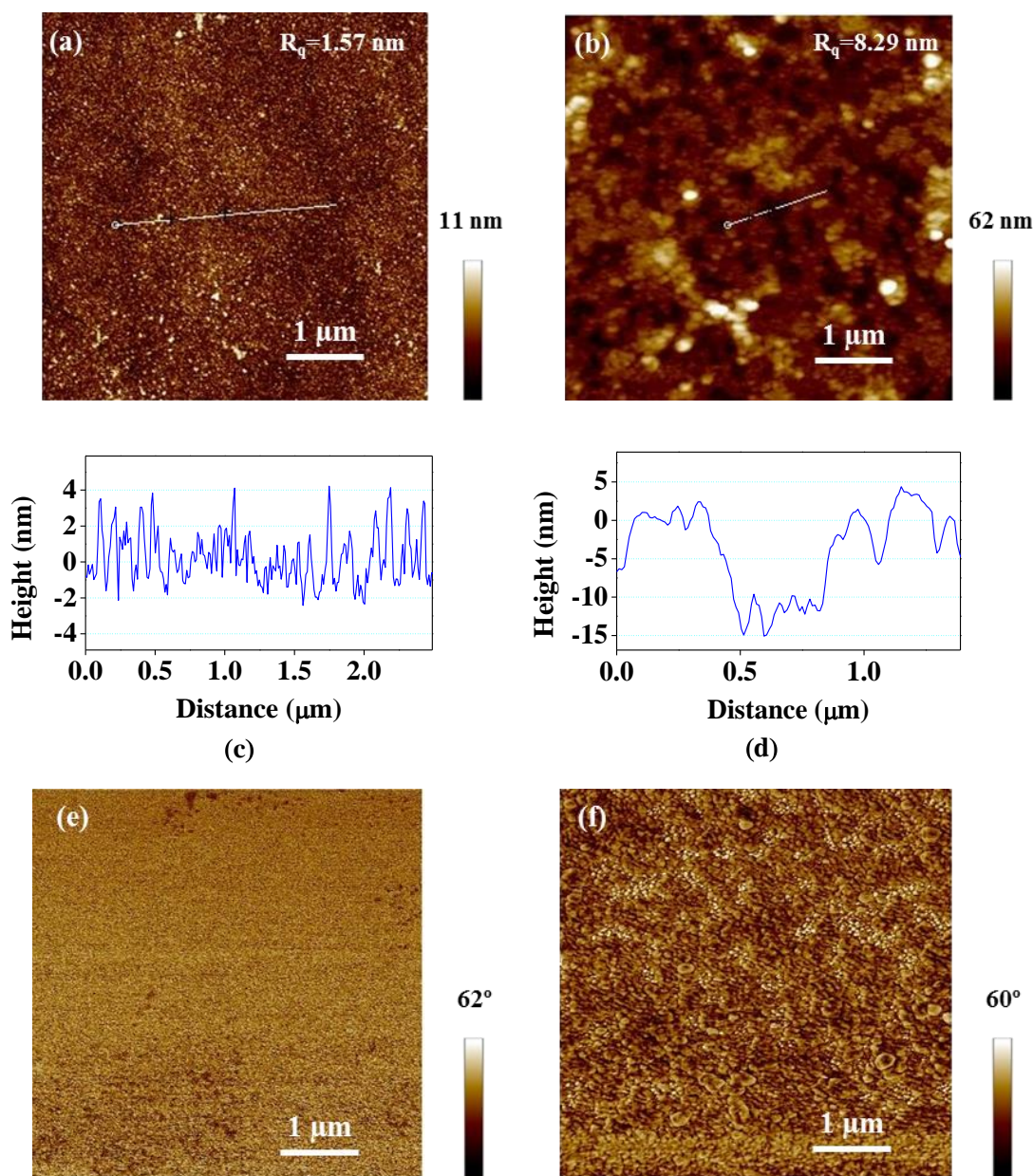


Figure 5-14 Comparison of tapping mode AFM mapping (a and b); cross sectional analysis (c and d) and phase imaging (e and f) before (bare sputtered SiO<sub>2</sub> crystal surface) and after coating with DSPC (via flow injection mode). The surface roughness is indicated on the top right corner of the AFM height image.

**(c) Lipids adsorption kinetics and quantitative analysis**

Further analysis on the basis of QCM data could be made using the adsorbed mass values. The experimental change of frequency was obtained by final frequency minus the frequency just before the inlet sample. The Sauerbrey equation could be simplified as equation 5-1.

$$\Delta f = -C_f \times \Delta m \quad (5-1)$$

$\Delta f$  = frequency change [Hz]

$C_f$  = sensitivity factor of the crystal [Hz/ng/cm<sup>2</sup>]

$\Delta m$  = change in mass per unit area [ng/cm<sup>2</sup>]

The Sauerbrey equation also assumes that the film deposited on crystal has the same acoustic-elastic properties as quartz. This assumption results in a sensitivity factor  $C_f$ , which is a fundamental property of QCM crystal which has been shown in equation 5-2.

$$C_f = \frac{2n \times f^2}{\sqrt{\rho_q \times \mu_q}} \quad (5-2)$$

$C_f$  = sensitivity factor of the crystal [Hz/ng/cm<sup>2</sup>]

$n$  = number of the harmonic at which the crystal is driven

$f$  = resonant frequency of the fundamental mode of the crystal [Hz]

$\rho_q$  = density of quartz = 2.648 [g/cm<sup>3</sup>]

$\mu_q$  = effective piezoelectrically stiffened shear modulus of quartz =  $2.947 \times 10^{11}$  [g/cm/sec<sup>2</sup>]

Combining equations 5-1 and 5-2, we can write equation 5-3 for calculate  $\Delta m$ . The thickness of the film can be calculated from the known density  $\rho_f$ , or vice versa, via equation 5-4.

$$\Delta m = \frac{(f_q - f) \sqrt{\rho_q \times \mu_q}}{2n \times f^2} \quad (5-3)$$

$$TK_f = \frac{\Delta m}{\rho_f} \quad (5-4)$$

$f_q$  = resonant frequency of the unloaded crystal [Hz]

$f$  = resonant frequency of loaded crystal [Hz]

$TK_f$  = thickness of the coated film [cm]

$\Delta m$  = change in mass per unit area [ng/cm<sup>2</sup>]

$\rho_f$  = density of the film [ng/cm<sup>3</sup>]

For our study, unless otherwise stated, changes in normalised frequency ( $\Delta f_{norm} = \Delta f_n / n$ , with  $n$  being the harmonic number) of the first overtone were presented, i.e. the fundamental mode. For the 5 MHz crystals used in this work, the sensitivity factor is 0.0566 Hz/ng/cm<sup>2</sup>. Adsorbed masses,  $\Delta m$  were then calculated according to the Sauerbrey equation,  $\Delta m = -C \times \Delta f_{norm}$  with  $C = 17.66$  ng/cm<sup>2</sup>/Hz, i.e. in this study, a frequency shift of 1 Hz corresponded to an adsorbed mass per unit area of 17.66 ng/cm<sup>2</sup>.

In previous work, the thickness of DLPC and DLPC monolayers has been studied. On the basis of the AFM and QCM data, it is possible to calculate the film density under the bilayer assumption. Table 5-5 summarises the characteristic parameters describing the kinetics of SLB and LUV formation for all studied combination of lipid compositions, film thickness, film density and surface treatment.

Table 5-5 Parameters investigated by experimental

Weight fraction of DSPC	Experimental $\Delta f$ [Hz]	$\Delta m$ [ng/cm <sup>2</sup> ]	Average $TK_f$ of bilayer* [nm]	Thickness constant $\gamma_{lipid}^{**}$ [nm/Hz]	Density		$t_{as}$ (min)
					nmol/cm <sup>2</sup>	ng/cm <sup>3</sup>	
$\alpha = 0$	$-20.0 \pm 0.7$	353	4.3	0.22	0.57	76.8	$10 \pm 1$
$\alpha = 0.25$	$-22.0 \pm 0.5$	389	4.6	0.21	0.59	80.1	$12 \pm 1$
$\alpha = 0.5$	$23.5 \pm 0.5$	415	5.0	0.21	0.59	80.9	$9 \pm 1$
$\alpha = 0.75$	$24.8 \pm 0.3$	438	5.4	0.22	0.59	80.5	$8 \pm 1$
$\alpha = 1$	$149.0 \pm 1.5$	2631	5.8	0.23	3.33	453.7	$15 \pm 3$
Deionised water	0	0	n/a	n/a	n/a	n/a	n/a

Average  $TK_f$  of bilayer \*: Results from AFM

Thickness constant  $\gamma_{lipid}^{**}$ : Results combine AFM and QCM

Frequency shifts of DSPC were calculated from mole weight ratio of DLPC and DSPC including QCM results of DLPC (i.e. 25.4 Hz if DSPC bilayer formed)

The frequency shift and adsorption time were measured by QCM. The adsorbed mass was calculated from the Sauerbrey equation 5-1. Combining the QCM and AFM results, the density can be calculated from equation 5-4.

Repeated measurements of adsorption on QCM show some variability in the time required to complete the adsorption of a complete bilayer, whereas the time for completing the adsorption were similar as existing work [88] [111] [162-163]. We have yet to determine the source of these variations.

In conclusion, QCM has been shown to be a versatile tool for time-resolved monitoring of SLB formation of different lipid compositions directly onto a single crystal surface. The results have demonstrated that neutral SLBs can be formed on the sputter coated hydrophilic crystals. The combination of QCM and AFM data demonstrates that liposomes formed by the gel-state DSPC (in the absence of DLPC) are somewhat flattened on silicon dioxide by keeping their solid-like molecular rigidity. This results in a large resistance shift as well as large frequency response. In contrast, for DLPC single system and DLPC/DSPC

mixed systems, a liquid-crystalline bilayer is instantaneously formed at the SiO<sub>2</sub>/buffer interface. Moreover, similar number of molecules can be coated based on formation of SLBs upon fully covered crystals surface. These data will be further discussed and used for sensing film quantity study mentioned in the next section.

### 5.3.2 Quantitative analysis of lipid layer formed by spin coating

#### (a) *Spin coating repeatability study*

One of the most important factors in spin coating is repeatability. Subtle variations in the parameters that define the spin process can result in considerable variations in the coated film. The repeatability study of the spin coating technique based on our sensor sample fabrication was carried out before any further actions. The repeatability analysis was done by two steps. First, the quantity of spin coated films was measured by checking the oscillating frequency shifts of each sensor before and after lipid coating in the dry state (which will be discussed in this section referring to Table 5-6). Second, the sensor to sensor reproducibility of spin coated films was evaluated by exposing the fabricated sensors to the same vapour pressure of ethanol (which will be further discussed in section 7.1).

The substrate surface property is one of the important factors which influences the coated film amount. Prior to the first step of the repeatability study, the substrates contact angles were checked after plasma treatment. Figure 5-15 shows the QCM frequency shifts of bare quartz crystals coated with DLPC versus different condition of treatments.

As shown in Figure 5-15, after the crystals were cleaned by oxygen plasma, the contact angle changed as the trace water dried out. However, the gold electrode became hydrophilic after the essential cleaning treatments (including O<sub>2</sub> plasma and RCA cleaning) required for reusing these crystals. Noble metals, such as gold, tend to be hydrophobic but this is not an intrinsic property of the metal surface. Instead, it is simply due to contamination. Au evaporated in a vacuum system has been reported as hydrophilic because of trapped trace water, but it becomes hydrophobic when exposed to air in the laboratory [144] [174-175]. It has been previously reported that a thin oxide layer was invariably present on the metal surface after the treatments [92] [94], thus changing the wettability of the gold. The significant change of wettability of the substrates influenced

the amount of lipids (when other parameters such as solution, spin coating speed, lipids concentrations etc. remain unchanged) coated on the substrates via spin coating. Most lipids could be coated on fresh untreated crystals which showed a contact angle of about  $85^\circ$ . More lipids could be coated as the crystals were drying out. The coating amount was hard to predict with an existence of trace water. This is because the water will influence the surface wettability when an organic solvent such as chloroform is applied. What we are concerned about is the physical property, i.e. the wettability of the surface prior to lipid deposition. As a result, crystal cleaning treatments were always carried out before spin coating to make sure all the sensing substrates have a similar wettability. Furthermore, after being treated with plasma, crystals were always dried in a vacuum oven the whole night and rinsed for at least two cycles with acetone, isopropanol and trace chloroform in sequence.

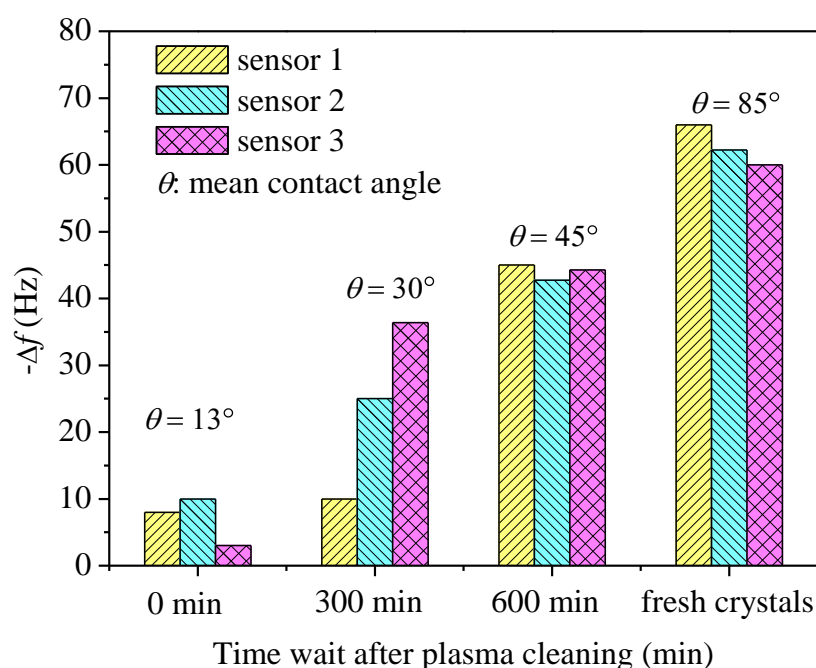


Figure 5-15 Surface property influence on the spin coated film.

The adsorbent DLPC, due to its low viscosity (ease of handling, DLPC liquid phase adsorption is more unstable compared to the DSPC gel phase adsorption), was chosen to study the sensor fabrication process repeatability. Therefore, a QCM vapour sensor with only DLPC adsorbent as a sensing film was prepared three times a day during three consecutive days, i.e.  $100 \mu\text{l}$  of a  $1 \text{ mg/ml}$  solution of adsorbent, DLPC was deposited onto the quartz crystal nine times on each substrates (three times  $\times$  3 days) [72] [139]. Four

sensor types (DLPC coated on four different substrates, i.e. oxidised gold, sputtered coated SiO<sub>2</sub>, evaporated platinum and thiolated gold) were used for the first step sensor fabrication repeatability study. The quartz crystal frequency shift caused by film deposition is shown in Table 5-6.

Table 5-6 Repeatability measurements of sensor construction process

Day	Substrates	Sensor 1 (Hz)	Sensor 2 (Hz)	Sensor 3 (Hz)	Mean (Hz)	STD (Hz)	RSD (%)
1	Oxidised Au	44.4	41.5	37.2	41.0	3.0	7%
	SiO <sub>2</sub> Sputtered	49.5	39.0	34.5	41.0	6.3	15%
	Evaporated platinum	45.4	42.0	39.0	42.1	2.6	6%
	Thiolated Au	40.5	41.1	50.0	43.9	4.3	10%
2	Oxidised Au	45.4	32.7	41.1	39.8	5.3	13%
	SiO <sub>2</sub> Sputtered	33.8	48.0	45.0	42.3	6.1	14%
	Evaporated platinum	38.0	44.4	41.2	41.2	2.6	6%
	Thiolated Au	45.0	40.1	48.0	44.4	3.3	7%
3	Oxidised Au	41.0	33.9	46.9	40.6	5.3	13%
	SiO <sub>2</sub> Sputtered	42.0	44.3	45.8	44.0	1.5	4%
	Evaporated platinum	46.4	39.5	40.1	42.0	3.1	7%
	Thiolated Au	47.0	49.0	42.1	46.0	2.9	6%

STD is the standard deviation. The relative standard deviation (% RSD) can be used to analyse the precision of the sensor construction process and the repeatability RSD is defined as the ratio between the standard deviation and the mean [72] [139].

In Table 5-6, the RSD of the frequency shift caused by film coating is calculated from the results of an intraday study. For the same substrate, a similar film thickness was coated based on the same coating concentration. The results indicate, once the solution can properly dissolve the lipids and properly wet the substrates, the average thickness of lipid film coated by spin-coating exhibits a good repeatability. The relative standard deviation values of sensor response showed a maximum error of approximately 15%. The results were not as good as previous studies on polymers [72] [176], but still good enough to recognise the sensors spin coated at a specific concentration. These results express that the sensing films coating process used here was good and guaranteed to apply a reproducible amount of coating material onto the quartz crystal resonator under a fixed condition.

**(b) Qualification of different sensors**

The film thickness on the surface of a quartz crystal has an important effect on the sensor performance. In order to compare different sensor's affinity to the same vapour based on the same vapour pressure, an equal amount of lipid molecules should be coated. Quantitative analysis on the basis of QCM data of different lipids has been made using the adsorbed mass values. First of all, different concentrations of DLPC solutions were prepared for spin coating. Frequency shifts due to lipid adsorptions were measured each time after coating. The DLPC film growth can conveniently be characterised in terms of the global film thickness obtained as an average from the frequency shifts. Figure 5-16 shows the mean oscillation frequency shift  $-\Delta f_{lipid}$  plotted versus the coating concentration  $C_{coat}$ .

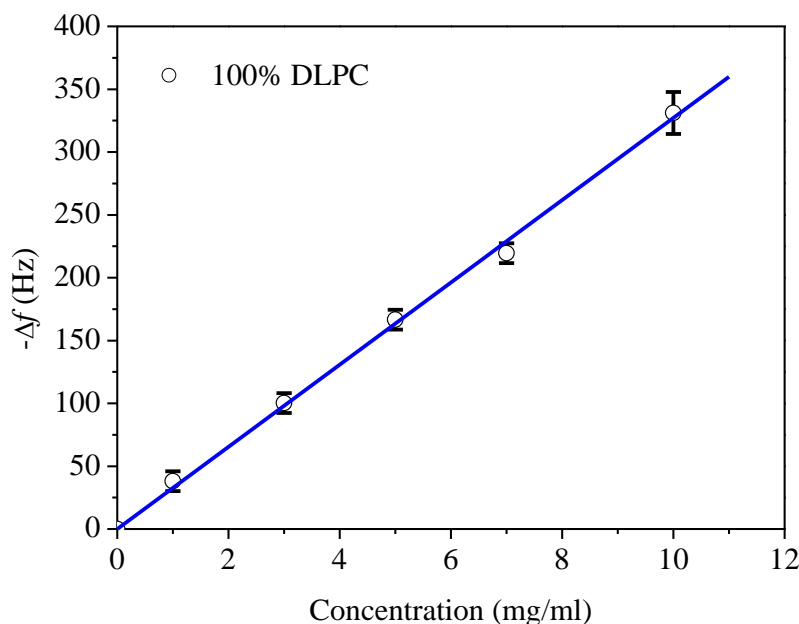


Figure 5-16 Concentration plots of the mean of the frequency shift generated from QCM measurements. Data displayed for dry DLPC films. The line is the linear fit of the data ( $R^2 = 0.99$ ).

The error for concentration 1-7 mg/ml was the precision error of 7.9 Hz (standard deviation was lower). The error for a concentration 10 mg/ml was 16.6 Hz, a measure of the sensor-to-sensor response due to coating reproducibility (i.e. the standard deviation). For DLPC, an approximately proportional relationship was found to be:

$$-\Delta f_{lipid} = \alpha_{lipid} \times c_{coat} \quad (5-5)$$

$\Delta f_{lipid}$  = mean oscillation frequency shift [Hz]

$\alpha_{lipid}$  = constant of proportionality [Hz/(mg/ml)]

$c_{coat}$  = coating concentration [mg/ml]

This relationship is in agreement with previous results of fluorescence microscopy [177] X-ray diffraction [145] [178] and AFM mapping [140] from other groups. The DLPC constant of proportionality (coating constant) was found to be 20 Hz/mM (33 Hz/(mg/ml)) in this work. Assuming that the density (molecule number/unit area per layer) of monolayer in the multilayer lipids was the same as the density of monolayer in a bilayer formed via vesicle fusion, e.g. for DLPC single system, a 20 Hz shift in oscillation frequency corresponding to 4.3 nm mean film thicknesses, the constant of proportionality (coating constant) to be  $\alpha_{DLPC} = 4.3 \text{ nm/mM}$ .

To confirm this relationship, the same measurements were carried out on DSPC and DSPC/DLPC mixtures. The concentrations used were 1 mg/ml, 3 mg/ml, 5 mg/ml, 7 mg/ml and 10 mg/ml separately. Each concentration sample has been deposited with at least three repeats. Figure 5-17 shows the mean frequency shifts  $-\Delta f_{lipid}$  plotted versus the coating concentration  $c_{coat}$ .

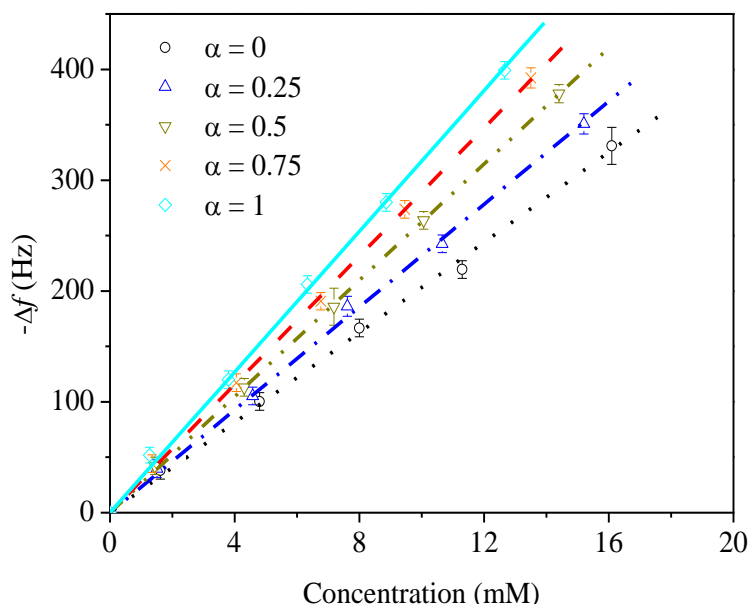


Figure 5-17 Concentration plots of the mean of the frequency shift generated from QCM measurements. Data displayed for dry DLPC, DLPC/DSPC and DSPC films. The lines are linear fits ( $R^2 = 0.99$ ).

From the results compared, for all samples, an approximately proportional relationship (see equation 5-5) was found. The only difference is the constant of proportionality.

If the same amount of lipid molecules were coated and we assume that the coated molar ratio of the mixed lipids remains unchanged, the rough approximation frequency shift ratio caused by film adsorption and coated film thickness can be calculated using the Sauerbrey equation, AFM imaging results, predicted molar ratio of mixed lipids and the molar weight. Table 5-7 shows the comparison of the proportionality constant of different samples based on different units.

Comparing the proportionality constant in Table 5-7, it was found when a fixed concentration in mg/ml of different lipids was used, a repeatable amount of lipids could be coated under this experimental condition. The reason why the concentration influences the amount of lipids being coated has not yet been determined. This might be influenced by the sample viscosity and the lipids' structure which could be formed in the solution. If we presume the individual DLPC and DSPC micelles formed in solution contain the same number of molecules, DSPC with a longer tail then will form larger inverted micelles in a hydrophobic solution. If the structure before a multilayer is formed was the individual micelles, then the amount of DLPC molecules coated on the same sized substrate should be more than DSPC. On the other hand, the low viscosity of DLPC may cause less aggregation of these micelles compared to DSPC, and the centrifugal force might cause more DLPC to be rejected from the substrates. The opposite multi-influence could be expected to determine the amount of lipids that could be coated. The size of substrates, the viscosity of each sample and the spin coating parameter was fixed in this work. Thus the amount that could be coated was also fixed.

In conclusion, the sensor construction process repeatability studies on DLPC showed a good repeatable coating process and guaranteed a reproducible amount of coating material was applied onto a quartz crystal resonator. Five different DLPC/DSPC mixture ratios have been successfully coated on the quartz crystals and measured by QCM. The average thickness, density (mass per cubic metre) and total mass were increasing proportionally to the concentration of the coating solution with nearly the same amount of coated molecules when same concentration in mg/ml was used. The five different sensors were finally fabricated at the same concentration of 5 mg/ml and will be discussed again in chapter 7.

## 5.4 Summary

The film characterisation results from the AFM and QCM trials have led to the development of a controllable process for the fabrication of the lipid membranes with similar amount of molecules coated on the vapour sensors. The sensing film structure, density and stability have been investigated and discussed in this chapter. The film characterisation in this chapter has guaranteed a reliable and controllable vapour sensor fabrication process.

The vapour sensing system setup will be discussed in the coming chapter before vapour sensing (chapter 7 and 8).

Table 5-7 Proportionality constant of different sample lipids in various units

Weight fraction of DSPC	Calculated Mole percentage of DSPC (%)	$\alpha_{lipid}^*$ [Hz/(mg·ml <sup>-1</sup> )]	$\alpha_{lipid}$ (Hz/mM)	$\alpha_{lipid}^{**}$ [nmol/(mg·ml <sup>-1</sup> )]	$\alpha_{lipid}^{***}$ [nmol/mM]	$\alpha_{lipid}^{****}$ [nm/mM]	$\alpha_{lipid}^{*****}$ [nm/(mg·ml <sup>-1</sup> )]
$\alpha = 0$	0	-32.7	-20.3	0.93	0.57	4.3	7.1
$\alpha = 0.25$	21	-34.3	-23.2	0.92	0.62	4.9	7.1
$\alpha = 0.5$	44	-37.7	-26.2	0.95	0.66	5.5	8.1
$\alpha = 0.75$	70	-39.1	-28.9	0.93	0.69	6.3	8.5
$\alpha = 1$	100	-40.2	-31.7	0.90	0.71	7.3	9.1

$\alpha_{lipid}$  and  $\alpha_{lipid}^*$  were worked out from linear fit of real experiment data points

$\alpha_{lipid}^{****}$  and  $\alpha_{lipid}^{*****}$  were worked out from thickness constant  $\gamma_{lipid}$  (refer to Table 5-5)

## Chapter 6 Vapour sampling methods

In this chapter, a vapour generation system is designed to form test vapours from pure liquids, for example, volatile organic compounds (VOCs). In order to characterise the vapour sensor, it is important to obtain good control of the test vapour quality (e.g. concentration and flow rate). The background theory of the vapour generation system and details of the design are presented here. Test vapours of ethanol, acetone, toluene and cyclohexane were produced using an evaporation technique. At the core of the vapour sensing system is a piezoelectric resonator (QCM) which is used as a detector. This chapter also deals with the practical operation of the vapour sensing system and system calibration.

### 6.1 Design of a vapour generation system

Various methods to test vapour generation have been reported in the literature. They can be divided into two types: static and dynamic methods [179]. The functional principle of all static methods involves the injection of liquid into, and its subsequent evaporation from, an enclosed container using a defined volume of diluting vapour. Dynamic methods are based on continuously diluting the vapour flow through the generation system and the mixture with the vapour at a known generation rate [180]. Comparing the static method with dynamic methods, static methods do not require complex apparatus and are, therefore, relatively simple and inexpensive. In contrast, dynamic methods are more complex to implement and expensive. However, there are three crucial drawbacks of static methods which make them unsuitable for highly controlled and calibrated vapour generation. One is the appearance of adsorption and condensation on the wall of the container. Therefore, the concentration of the test vapour cannot be reliably controlled at higher concentrations [180]. Another drawback is that only a finite amount of test vapour can be generated in one experimental run. Furthermore, leakages and pressure changes exert an effect on output. Dynamic methods show important advantages such as a negligible effect of the adsorption

and condensation on the state of equilibrium, a continuous dilution which provides a wide concentration range, and ready control of test vapour temperature, relative humidity and flow rate. As a result, dynamic methods were used in this work.

Dynamic methods can be further classified into those based on injection [72] [136], permeation [181-182], diffusion [183-185] evaporation [18] [179], electrolytic [179] and chemical means [179]. Each method has unique advantages and disadvantages. Thus, a short overview is presented in Table 6-1.

Table 6-1 Comparison of test gas generated based on different methods

Technique	Accuracy	Advantages	Disadvantages
<b>Injection</b>	5-9% (v/v)	A well-known concentration can be prepared; variable concentrations may be obtained	Require atomizers, heaters and expanded mixing chamber; limited volume of the syringe; need to refill
<b>Permeation</b>	2-5% (v/v)	Commercially available (calibrator); effective and accurate way of preparing low concentration test gas	Require precise temperature control; long initial time for reaching permeation equilibrium; relatively high costs; continuous output from the source without possibility to stop
<b>Diffusion</b>	3-5% (v/v)	Wide applicability; suitable for many compounds	Need good temperature control; impossible for preparation of a multicomponent mixture in one diffusion vessel
<b>Evaporation</b>	5-15% (v/v)	Inexpensive; has a short stabilisation period for the test gas generation	Used to humidify air; may require re-cooling using a heat exchanger
<b>Electrolytic</b>	Low ppm concentrations	Ideal method for low gas concentration	Requires good current and voltage control, not well investigated
<b>Chemical</b>	N/A	Produces gases which are commercially unavailable; prohibitively expensive	The reactant feed mechanisms required are normally more complex; require temperature control, if is hard to control reaction rate; unwanted products may be produced

In this study, two methods have been set up and calibrated. The experimental design of the bubbler system employed in this study is illustrated in Figure 6-1. The sample liquid was placed in a reservoir which had a glass seal containing inlet and outlet glass pipes. Dilutant gas flowed into the reservoir via the inlet pipe. The reservoir, where dilutant gas and vapour were mixed, was immersed in a temperature controlled water bath [179]. The temperature controlled bath determined the operating temperature and hence the

concentration of the vapour in addition to the flow rate of carrier gas. In our study, pure nitrogen gas was chosen as a dilutant in order to avoid the introduction of any contaminant compounds, for example, water vapour and particles which may be contained in compressed air. The flow regulator sets a constant inlet pressure of 1 bar, thus providing a steady flow.

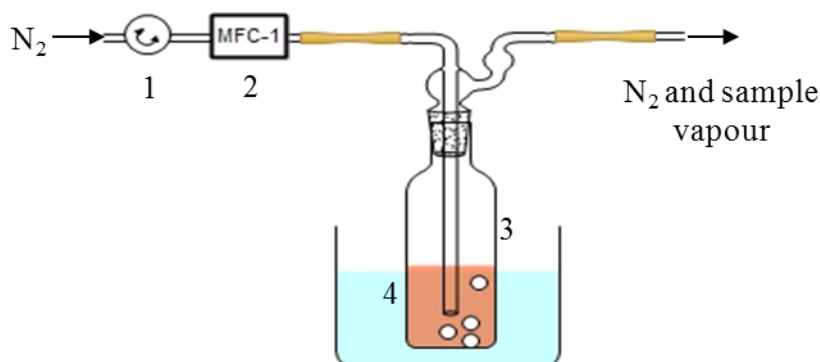


Figure 6-1 Schematic of bubbler system for the generation of test gas: (1) flow regulator, (2) mass flow controller (3) Impinger gas scrubber, (4) water bath.

The experimental design of the diffusion system used is illustrated in Figure 6-2 below. The sample liquid was placed in a reservoir and immersed in a temperature controlled water bath. The mixing chamber, where nitrogen and the generated vapour were mixed, was connected with the liquid reservoir via a diffusion tube [186]. The concentration of the vapour was determined by the flow rate of diluting gas and the vapour generation temperature.

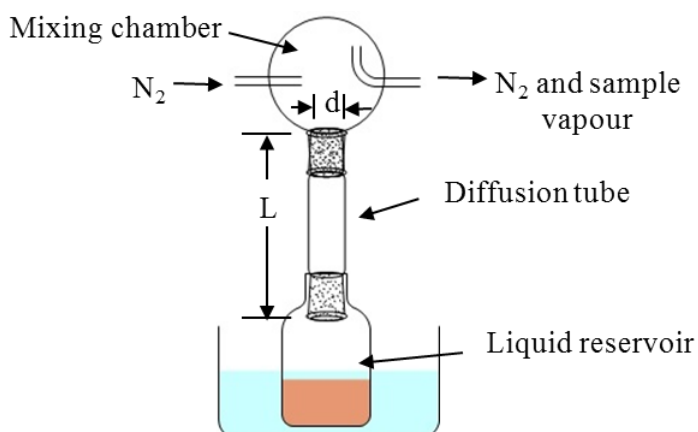


Figure 6-2 Schematic of diffusion system for the generation of the test gas.  $L$  is the length of the diffusion tube,  $d$  is the inner width of the diffusion tube.

During the test sensing experiment, the concentration of the vapour generated by the diffusion method was detected by the vapour sensors. For example, the maximum ethanol vapour concentration generated by diffusion system at 25 °C was measured to be about 400 ppm. Thus, during the course of this work, vapours were generated using evaporation methods (bubbling). Four vapours were generated including ethanol, methanol, toluene and cyclohexane. Due to different chemical and physical properties, each vapour had a different saturated vapour pressure at a different temperature and will be discussed in section 6.3.1. The properties of the four vapours are shown in Table 6-2.

Table 6-2 Chemical and physical properties of used in this work

	Vapour	Molecular Formula	Boiling point (°C)	Molecular weight (g/mol)
Hydrophilic vapours	ethanol	C <sub>2</sub> H <sub>6</sub> O	78.37	46.07
	methanol	CH <sub>4</sub> O	64.70	32.04
Hydrophobic vapours	toluene	C <sub>7</sub> H <sub>8</sub>	111.00	92.14
	cyclohexane	C <sub>6</sub> H <sub>12</sub>	86.74	84.16

## 6.2 Design of a vapour sensing system

The vapour sensing system, shown in Figure 6-3, was used to expose sensors to a range of concentrations of ethanol, methanol, toluene and cyclohexane vapour.

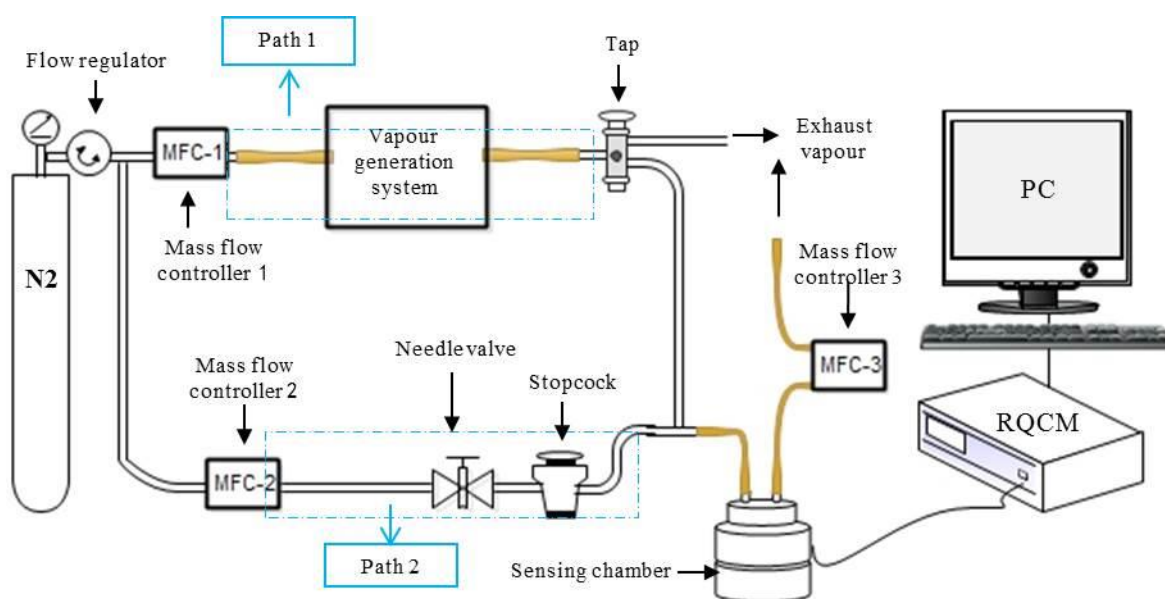


Figure 6-3 Schematic of vapour sensing system design.

The vapour sensing was carried out after the measured resonant frequency of the QCM had stabilised for a given flow rate of nitrogen carrier gas – this will be referred to as achieving a stable baseline. To reduce the possibility of the adsorption of sample vapour onto the tube walls, the length of the vapour path to the QCM chamber was minimised [187]. The sensing system was designed to include two paths with two separate mass flow controllers to control the flow rate of each route. During operation, first the nitrogen gas was flowed to the sensor (with no vapour present) in order to determine the stable baseline of the oscillator (path 2). After this, the flow of the nitrogen gas was switched to the vapour generation path by using a tap without any dead volume (path 2). The precise flow rate of nitrogen or mixed gas/vapours introduced into the sensor chamber was kept constant and was indicated by the mass flow controller 3 (Platon<sup>®</sup>).

Both the sensor chamber and the vapour reservoir were placed in two separate temperature controlled water baths. The sensor chamber was maintained at a working temperature of 25 °C, while the vapour reservoir was kept at a constant working temperature within 1 °C. The bubbling gas (N<sub>2</sub>, i.e. the carrier gas) was introduced at a constant flow rate. The vapour operating temperature and bubbling gas flow rate combine to determine the initial vapour concentration. The N<sub>2</sub> gas introduced via path 2 was used for both achieving a stable baseline calibration and also as a diluting gas. The quartz crystal chamber electrical output was connected to a QCM with the data transferred to the computer. As can be seen from Figure 6-3, by controlling the bubbling gas flow rate and the working temperature of the vapour generation system, a constant flow of the homogeneous vapour was maintained throughout the experiment to avoid any variations in concentration, even when the QCM sensor was exposed to nitrogen gas for calibration.

Overall, the vapours were produced in two stages, including the vapour initial generation (via path 1) and vapour dilution stages. In the first step, nitrogen at a flow rate of 100 ml/min was passed over the vapour generation system containing a known quality of liquid; the initial vapour concentration (C<sub>0</sub>) in the stream of nitrogen with a fixed flow rate was calculated using equation 6-1 and 6-2. Where the diffusion rate (D) is been measured by the experimental method described in section 6.3.3.

$$C_0 = \frac{D\rho}{F_1} \quad (6-1)$$

C<sub>0</sub> = initial vapour concentration [part per million = ppm]

$D$  = diffusion rate [g/min]

$\rho$  = reciprocal vapour density, depend mainly on the molecular weight of the organic vapours [ml/mg]

$F_1$  = Nitrogen flow rate via path 1 [ml/min]

$$\rho = \frac{24.5 \times 10^6}{M} \quad (6-2)$$

$M$  = molecular weight of the liquid [g/mol]

In the second stage, the diluted gas concentration was given by 6-3.

$$C = C_0 \frac{F_1}{F_2 + F_1} \quad (6-3)$$

$C_0$  = initial vapour concentration [ppm]

$C$  = concentration of the measured gas [ppm]

$F_2$  = Dilute nitrogen flow rate via path 2 [ml/min]

### 6.3 Calibration of the vapour sensing system

Four vapours were generated and used in the sensing experiments including ethanol, methanol, toluene and cyclohexane vapour. The chemical structure of ethanol, methanol, toluene and cyclohexane are shown in Figure 6-4.

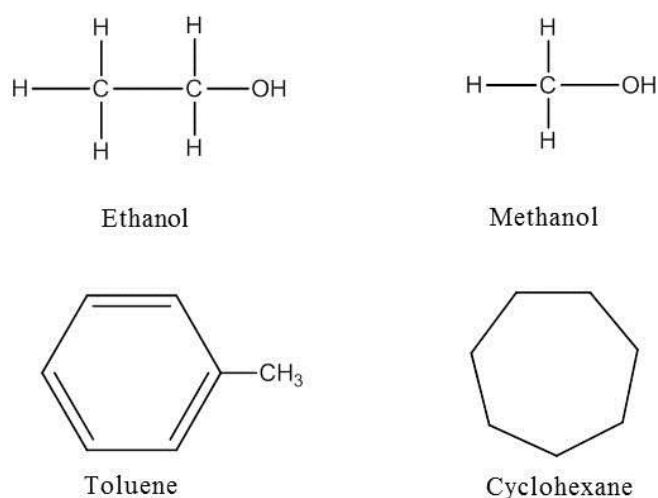


Figure 6-4 Chemical structures of four vapour molecules.

#### 6.3.1 Saturated vapour pressure

The Clausius-Clapeyron equation (equation 6-1 [188]) is an important relationship that describes how pressure of two phase system varies with temperature [189-190]. The two

phase system in question is one in which a liquid and its vapour are in equilibrium (saturated). This equation is a vapour pressure equation and describes the relationship between vapour pressure and temperature for pure components.

$$\ln p = \frac{-l_{23}}{RT} + \ln C \quad (6-1)$$

$p$  = vapour pressure [Pa]

$l_{23}$  = latent heat of transformation [J]

$R$  = gas constant = 8.31 [kPa·d<sup>3</sup>/mol/K]

$T$  = temperature of the system [K]

$C$  = a constant of integration

The saturated vapour pressure of the compound could be obtained from the literature by applying equation 6-1 [191]. Six data points for the vapour pressure of ethanol, methanol, toluene and cyclohexane were obtained from literature and plotted in Figure 6-5.

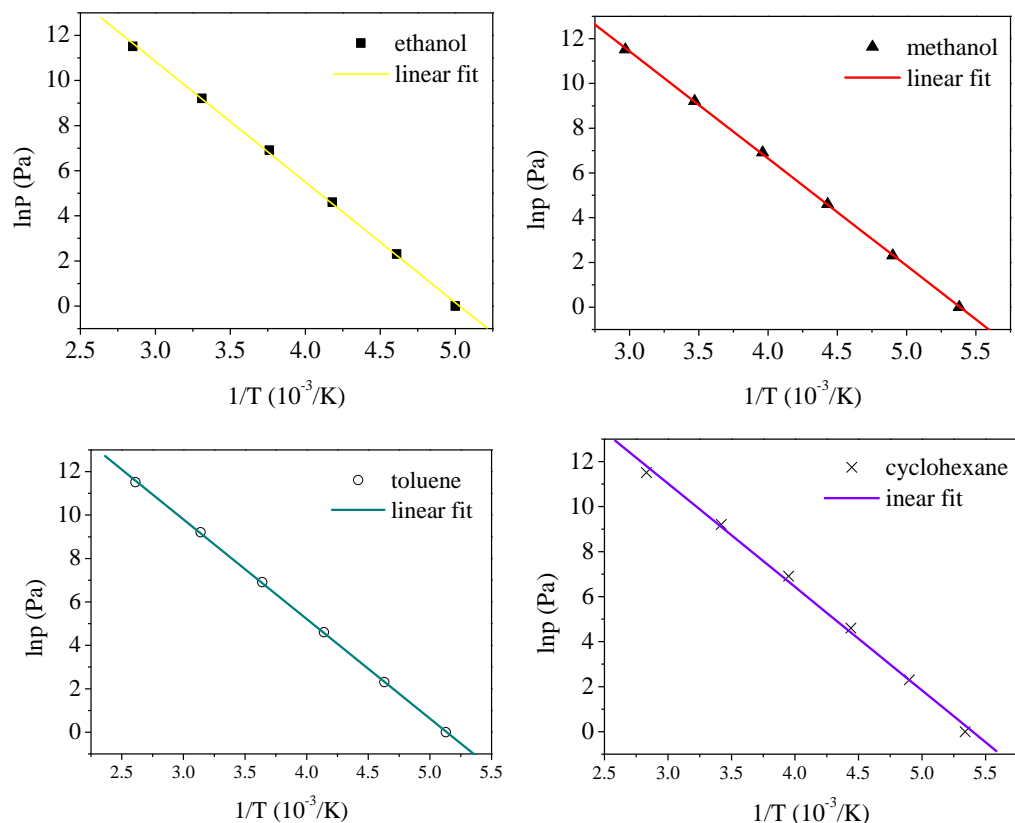


Figure 6-5 Calibration of saturated vapour pressure from [188].

The saturated vapour pressure of the compound was obtained from the literature by applying the Clausius-Clapeyron equation, i.e. from the best fit line of the saturated vapour

pressure graph. Furthermore, the saturation concentration of the compound in the gaseous mixture was calculated based on the ideal gas law.

### 6.3.2 Calibration of the vapour generation system

The concentration of the vapour was calibrated using the weight loss of the reservoir liquid caused by a long exposure to the nitrogen flow [187]. For each vapour generated, the reservoir (and its liquid) was weighed regularly over a 4 day period. The diffusion rate (g/min) for the vapour was worked out by calculating the ratio of the weight difference (before and after the vapour exposure) and the exposure time. The final diffusion rate used is a mean value of the experimental data. This experiment was repeated for each vapour (and required calibration temperature). It is possible to predict the diffusion rate of a solvent and thereby the concentration of vapour produced at a constant flow rate.

Figures 6-6 and 6-7 show the measured results for ethanol, methanol, toluene and cyclohexane. The flow rate and water bath temperature of the vapour generation system is set to be 100 ml/min, 20 °C and 100 ml/min, 25 °C, respectively. A pair of samples is taken and analysed. The mean values and the standard deviations are also presented. The dotted lines in the figures indicate the ideal saturated vapour pressure of each vapour.

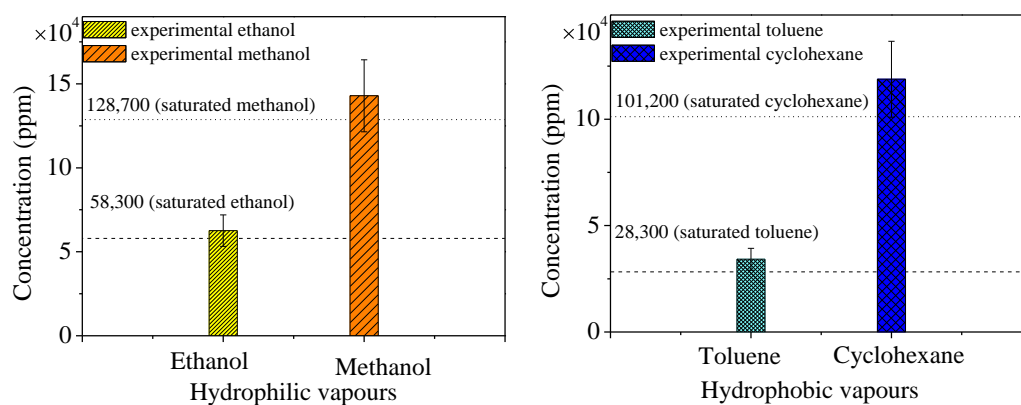


Figure 6-6 Comparison of hydrophilic test vapour (left) and hydrophobic test vapour (right) sampled from the bubbler system and calculated concentrations at 20 °C.

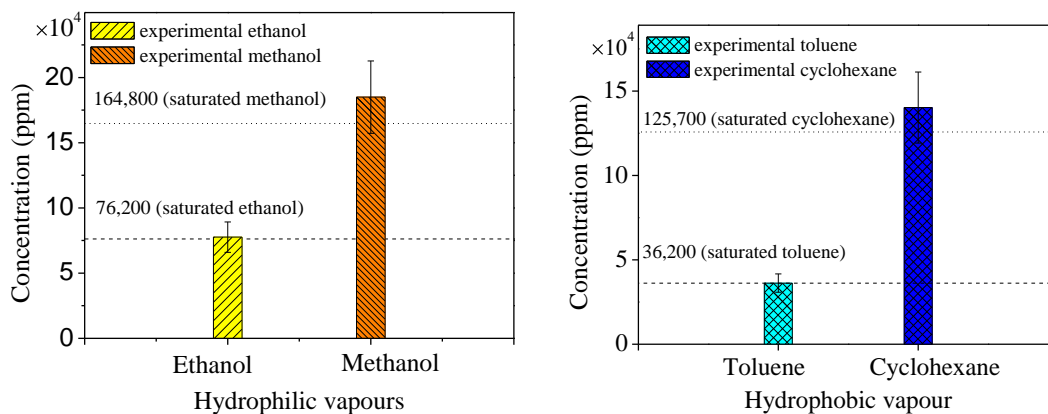


Figure 6-7 Comparison of hydrophilic test vapour (left) and hydrophobic test vapour (right) sampled from the bubbler system and calculated concentrations at 25 °C.

It can be seen that the concentrations of each vapour are different for a given vapour generation condition. Within the literature [179], the assumption is that the test vapour concentrations generated via the evaporation method are close to the saturated vapour pressure. Here, the experimentally measured concentrations are in good agreement with this assumption. A standard deviation of up to 15% is caused by run-to-run changes in the amount of evaporant. Furthermore, the evaporated amount of liquid will depend on the bubble size, the rate of ascent, the temperature of the liquid, and the height of the liquid column, as well as its boiling point, vapour pressure and viscosity. This vapour generation method was designed to generate a high initial concentration of each vapour, which was used to meet the requirement of using a 5 MHz quartz crystal based vapour sensor.

### 6.3.3 Calibration of the flow rate

The vapour sensing system was designed to balance the flow rate of the gas/vapours from two different paths by using a mass flow controller. Under real conditions, there will be a small pressure difference at the sensing chamber when gas/vapours were passed through different paths. Figure 6-8 shows the evaluation of frequency shifts difference for the nitrogen gas passed through the crystal sensor via the two different paths. The crystal sensor was conditioned in a flow cell which was fully filled with deionised water and immersed in a 25 °C water tank at least 30 minutes prior to the exposure measurements.

As shown in Figure 6-8, the nitrogen gas was allowed to flow through the crystal sensor with a different flow rate. When no lipids were coated, the line pressure difference in the

sensor chamber was relatively low for the bare sensor (i.e. a small frequency shift difference between the two paths), while the frequency shift difference slightly increased to about 10 Hz because of the sensitivity of the sensor as the line pressure increased with the lipids on. The calibration was always carried out on different thickness lipids coated sensors. It was found that the frequency shift difference increased while the thickness of the lipid membranes increased. These values can be used to check and calibrate the stable baseline of the sensor system by comparing the same nitrogen gas flow rate to the measured frequency shift via different paths. This behaviour is typical of that seen in the system. Comparing the relationship between measured frequency and the gas flow rate, a higher flow rate will result in a lower frequency once stable. Comparing the measured frequency different paths, at the same flow rate, the average frequency is lower when gas flows via path 1 than when it flows via path 2, again once stability was achieved. When the flow rate is greater, the difference will also be greater. Considering the frequency shifts after the injection of the mixed lipids and also the injection of sample vapour; this difference is much smaller, and so the stable frequency flow through two different paths can be ignored, i.e. we treat the stable baseline to be the same via two different paths at the same flow rate of nitrogen gas.

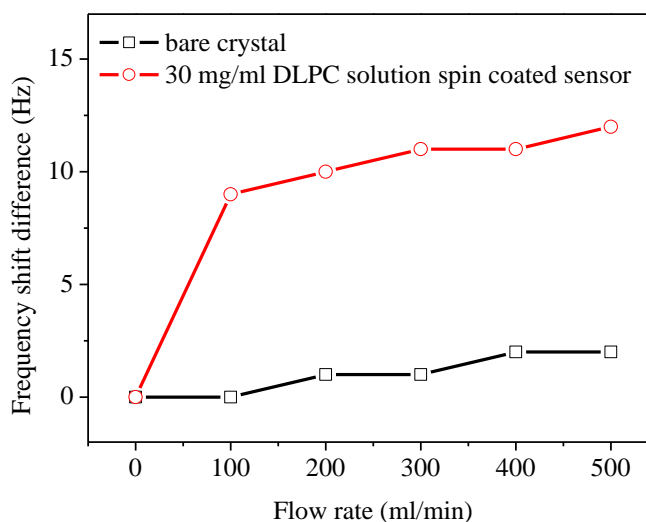


Figure 6-8 Crystal oscillation frequency shift difference when gas/vapour was passed through two paths into the sensor chamber as a function of flow rate.

## **6.4 Summary**

This chapter deals with the design, operation and calibration of the vapour generation and sensing equipment used throughout this work. Concentrations of ethanol, methanol, toluene and cyclohexane vapours were generated using bubbling. The relevant working concentrations of vapours were also estimated. This work prepared the system for vapour sensor performance evaluation, which will be discussed further in the coming chapters.

## Chapter 7 Results and discussion: bare gold based vapour sensing

Chapters 7 and 8 present the results obtained from vapour sensing systems described in chapter 6, with a discussion of the significance of the results on our understanding of how the vapour interacts with the lipid membranes. This chapter is primarily concerned with the vapour sensor response patterns and sensing mechanism; including the working subphase chosen, sensor repeatability and key performance parameters such as selectivity, sensitivity and lifetime.

### 7.1 Sensor fabrication

#### 7.1.1 Effect of subphase on sensor response

Different types of substrates have been prepared for film coating and vapour sensing. The response of different bare substrates to ethanol are summarised in Figure 7-1. The standard error is a measure of the sensor-to-sensor response reproducibility.

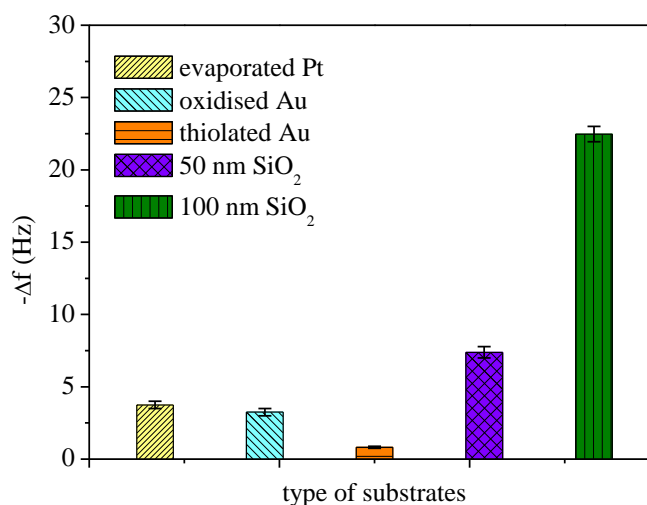


Figure 7-1 Subphase sensing with 58,300 ppm ethanol vapour.

Figure 7-1 indicates that ethanol vapour was hardly adsorbed onto the plasma oxidised bare hydrophilic quartz crystals, evaporated platinum or hydrophobic thiolated gold. In contrast, ethanol adsorbed readily onto the sputter coated SiO<sub>2</sub> film. Even greater adsorption was observed on 100 nm SiO<sub>2</sub> compared to 50 nm SiO<sub>2</sub>. As one of the target detection vapours, ethanol results in a non-negligible frequency shift on exposure to SiO<sub>2</sub> sputter coated quartz crystal.

The reason why SiO<sub>2</sub> is sensitive to ethanol vapour has not yet been determined. As mentioned in section 4.1.2, a SiO<sub>2</sub> substrate is hydrophilic. Ethanol vapour is hydrophilic as well. The mechanism of ethanol vapour and SiO<sub>2</sub> interaction may be surface reaction and binding. Because of the limited experimental data we are unable to conclude the sensitivity of SiO<sub>2</sub> to ethanol is dependent on the thickness. Nevertheless, SiO<sub>2</sub> sputter coated quartz crystals were not considered for use as the sensing film substrates.

### 7.1.2 Repeatability study on sensor response

As mentioned in section 5.3.2 a, the repeatability study was done first by measuring the crystal frequency shift results caused by film adsorption. Because of the low fundamental frequency of our working quartz (5 MHz), the frequency shift due to the small amount of lipids coated was relatively low compared to the literature where many groups use higher resonant frequencies which are beyond the working range of the Durham equipment [28] [192]. Moreover, a repeat study of this measurement condition within the day showed that there will be a precision error of about 7.9 Hz based on the reading and calculation. To make the repeatability study more reasonable, the second step of repeatability check was carried out by measuring the sensor response to ethanol vapour after the sensors were fabricated and weighed (Figure 7-2). As mentioned in section 7.1.1, because of the high sensitivity of SiO<sub>2</sub> to ethanol vapour, DLPC coated SiO<sub>2</sub> sensors were not considered for vapour sensing.

In Figure 7-2, the mean oscillation frequency shift of sensor responses on each day is shown. The response of the different types of sensor to the same vapour pressure of ethanol showed a maximum standard deviation of 6.5% for DLPC coated oxidised gold, 5.1% for DLPC coated platinum and 4.2% for DLPC coated thiolated gold. These results demonstrate good sensor response repeatability was obtained for the same sensor type (i.e. the same substrates, same sensing film and coating parameters). Comparing three different

sensor types, besides the coating solution the main difference is the coating substrates. The difference in the mean sensor response value (16.0 Hz shift for oxidised gold, 14.7 Hz shift for platinum coated crystal and 17.4 Hz shift for thiolated gold) between different sensor types might be caused by the difference in the film uniformity, its thickness and the effect of substrates response to ethanol vapour exposure. As mentioned in section 5.1.2, the sensitivity of the quartz crystal sensor is highest in its centre, and decreases towards the sensor edge. It is worth mentioning that for different substrates, even though the active area is slightly different, the most sensitive interaction area (surrounding the centre of quartz crystals) is always considered to dominate the response. Thus we conclude that in this work, spin coating has been demonstrated as a sensing film coating method with a good reproducibility i.e. well controlled quantity lipids (0.16  $\mu$ l) could be spin coated when other parameters including coating speed, lipids concentration, substrates etc. remain unchanged, whereas the uniformity depends on the substrate type and solution used.

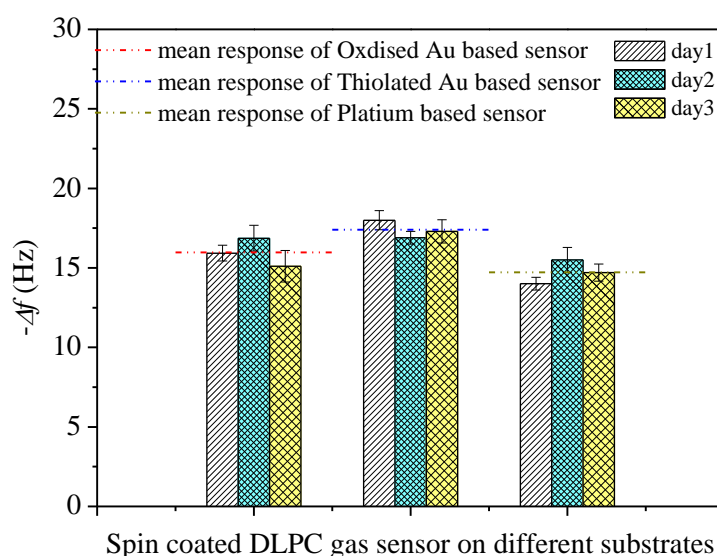


Figure 7-2 Mean frequency shift within a day obtained by applying 58,300 ppm ethanol vapour on QCM sensors spin coated with 1mg/ml DLPC (similar coating thickness for 3 different substrates was  $42.5 \pm 1.8$  Hz). The line indicates the mean response value of different sensor types during three days.

### 7.1.3 Correspondence of sensor response to film thickness on quartz crystal

The response of a sensor coated with different DLPC amounts on exposure to ethanol vapour was investigated. Figure 7-3 shows the frequency change as a function of different DLPC concentrations used for fabrication on exposure to 58,300 ppm ethanol vapour.

It has been shown that short-chain alcohols such as ethanol and methanol localise predominantly at the hydrophilic head group region of the phospholipid bilayer. Their location disturbs the natural microstructure of the lipid membrane, leading to a decrease in membrane viscosity [193]. The use of an organic solvent such as cyclohexane was also found to cause a reduction of viscosity as reported elsewhere [193]. As mentioned previously in chapter 3, the decrease of film viscosity will lead to an increase in QCM frequency. A negative frequency change means that adsorption of organic vapours caused a frequency decrease in the QCM sensor. As a result, under this experimental condition, the two multi-influences always co-existed.

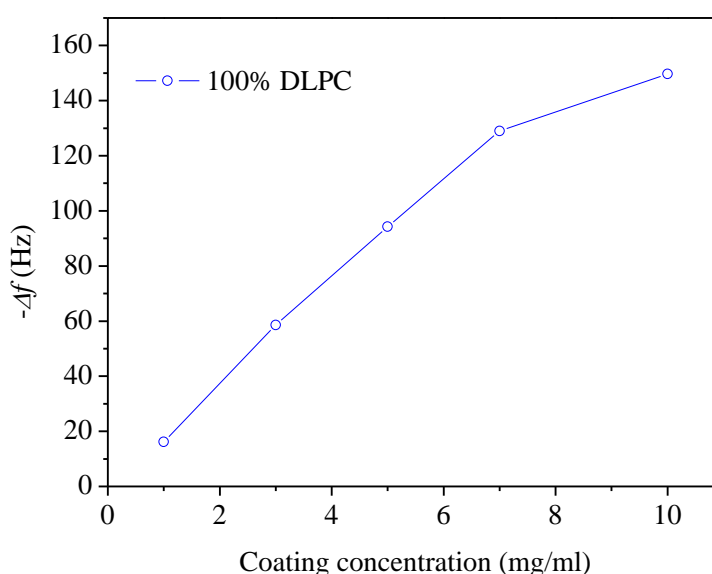


Figure 7-3 Frequency shift of QCM sensor versus different DLPC concentrations used for fabrication on exposure to 58,300 ppm ethanol vapour.

As shown in Figure 7-3, the response of DLPC coated QCM showed an increase with an increase in coated mass below  $5.85 \mu\text{g}$  (corresponding to a 331.0 Hz frequency shift,  $5845.5 \text{ ng/cm}^2$  coated DLPC, approximately film thickness of 76 nm and film density of 1.58 g/ml). This phenomenon is likely due to the adsorption of organic vapours causing a frequency decrease in the QCM sensor. Thus, the dominant factor in the vapour response of the lipid sensor has to be the film mass and thickness increase which results in a decrease in the frequency, i.e. under the experimental conditions, the viscosity effect could be ignored, and the Sauerbrey equation worked well. However, when the coating concentration was more than 7 mg/ml the curve slightly declined. This means the viscosity

influence should be taken into consideration but still can be ignored because it is not the main influence.

Overall, the response of DLPC coated QCM showed an increase with coated mass. We presume that within the working concentration range (1-10 mg/ml) the Sauerbrey equation works well, and the viscosity influence can be ignored; the vapour sensors showed a stable response based on exposure to ethanol vapours. It is worth mentioning again that we have already concluded, from the quantitative analysis of the lipid layer formed by spin coating, that when the same concentration in mg/ml of different lipid solutions was used for spin coating, similar amount of lipids could be coated. During this period of study, five sensors with different ratio of mixed DSPC/DLPC were prepared from 5 mg/ml solution, and results will be discussed in the coming section.

#### 7.1.4 Fabricated sensors

At first, the concentration of 5 mg/ml was considered (see Table 7-1). The spin coating parameters were 1500 rpm and 60 seconds. The frequency shift of sensor 1 caused by 5 mg/ml DLPC spin coating was calculated from polynomial fit based on all QCM experimental data points. All other  $\Delta f^*$  were calculated based on the mole fraction and frequency shift caused by the DLPC lipid coating in sensor 1.

Table 7-1 Sensor fabrication calibration

Sensor number	Weight fraction $\alpha$ of DSPC	Mole percentage of DSPC (%)	Calculated $\Delta f^*$ (Hz) from ratio	$\Delta f^{**}$ (Hz) from experimental linear fit	Experimental of sensor fabricated $\Delta f^{***}$ (Hz)
Sensor 1	0	0	-166.8	-166.8	-167.5
Sensor 2	0.25	21	-176.9	-178.0	-182.4
Sensor 3	0.5	44	-186.6	-189.3	-193.3
Sensor 4	0.75	70	-198.3	-200.6	-198.3
Sensor 5	1	100	-211.9	203.9	-211.1

As mentioned in section 4.4.2 and 4.4.3, highly aligned lipid sensing films on quartz crystal gold electrode were prepared by spin coating. The QCM measurement of the thickness of the deposited sensing films revealed that the approximately coating thickness

was between 38 nm and 48 nm, assuming that the film density was about 0.8 g/ml. The sensing area is approximately equal to 1.27 cm<sup>2</sup>. The fabricated sensor frequency shifts, expressing the amount of the deposited sensing materials, are shown along with their respective predicted amount in Table 7-1, where  $\Delta f^*$  is the calculated frequency shifts of each sample when the same molecules were coated. As we can see, a similar number of molecules were experimentally coated on five different sensors.

## 7.2 Sensor response

### 7.2.1 Measurement setup and procedure

All sensing experiments were carried out at room temperature (25 °C) and atmospheric pressure. Nitrogen gas was used as a carrier gas. The evaporation process of the vapours was done by bubbling. The QCM sensors were conditioned in the system for at least 1 hour prior to the exposure experiments. The liquid vapour samples were installed in the system at least 30 minutes before the measurements to allow the system to reach equilibrium.

The sample vapour was passed through the sensing chamber at a fixed constant flow rate once the stable baseline (i.e. no frequency shift) for only nitrogen gas flow had been achieved. The exposure time was chosen based on the preliminary study of the typical time responses of the sensors to different vapours, i.e. the maximum response time was taken until the frequency variations were less than 1 Hz/min for at least three successive minutes, which indicates that the maximum adsorption of the QCM sensor was obtained. The sensor chamber was always cleaned with nitrogen gas before and after each measurement.

### 7.2.2 Sensor responses

Typical real-time responses of DLPC and DSPC lipid sensors to ethanol, methanol, toluene and cyclohexane under atmospheric pressure at 25 °C are shown in Figure 7-4 (a) and (b), respectively, to show the sensors' dynamic response. Figure 7-4 (c) shows the example response pattern of a DLPC sensor (sensor 1 in Table 7-1) on exposure to step changes in the concentration of methanol vapours in the nitrogen carrier gas at room temperature (film structures referred to Figure 5-4). All other sensors showed similar real time response patterns which have not been illustrated here.

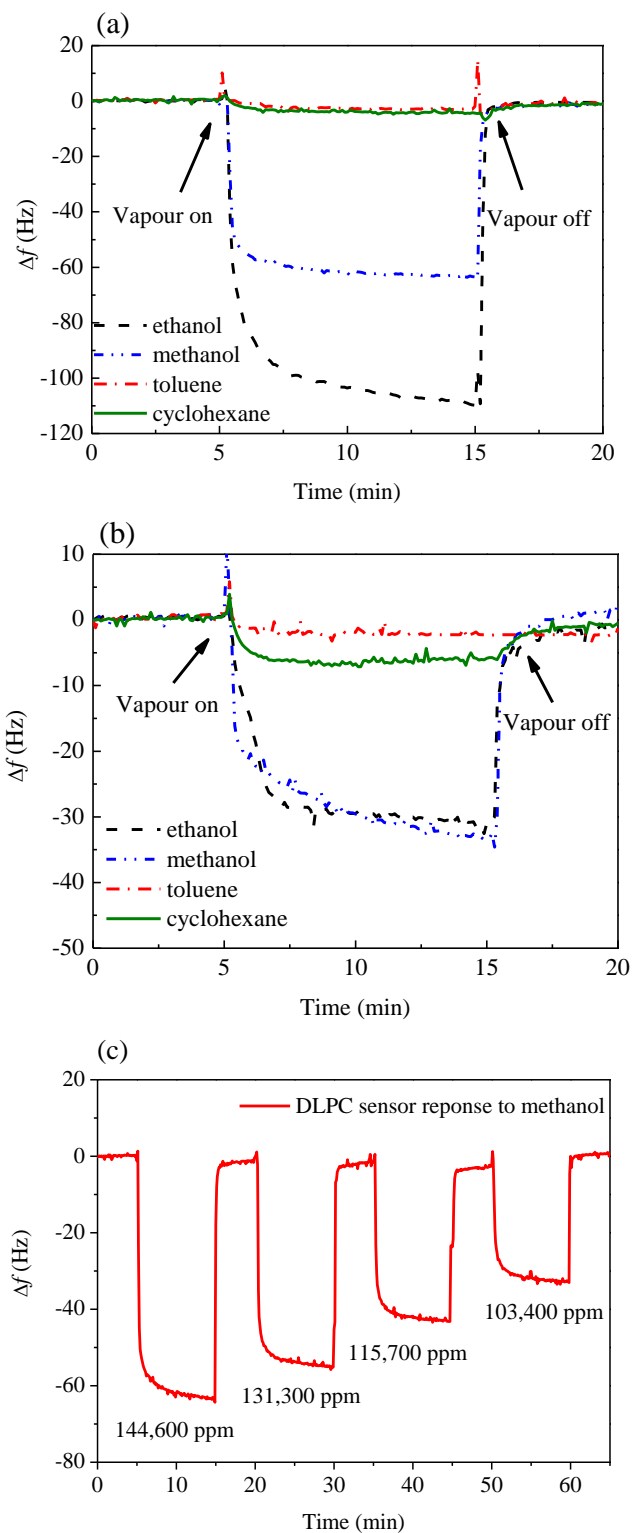


Figure 7-4 Representative real time response of (a) DLPC vapour sensor and (b) DSPC vapour sensors to alcohol (ethanol and methanol) and carbocyclic compounds (toluene and cyclohexane). (c) Frequency response of a DLPC sensor on exposure to step changes in the concentration of methanol vapours in the nitrogen carrier gas at room temperature

In Figure 7-4, the vapour flow was switched on and off at the 5 minutes and 15 minutes marks, respectively. As can be seen, the two sensors clearly responded to the vapour flow as there was a distinct wave shape occurring between the on and off times. The frequency changes, which represented the response of the QCM sensor to the mass adsorbed on the coated electrode, altered immediately with the target vapour adsorption process, and rapidly reached a steady value. After exposure, the test chamber was purged with nitrogen gas, and the vapour desorption process took place. We have confirmed that the observed responses were not the artifacts caused by the performance of the measurement system.

In these figures the frequency change  $\Delta f$  was plotted against time for different analytes. As can be seen, the time between the alcohol vapours being turned on and off with the frequency change reaching 80% of the maximum was about 40 seconds on average. The frequency recovery time was about 10 seconds for 80% de-trapping and 3 minutes for full de-trapping of vapours. The two sensors' responses intensity to toluene and cyclohexane were relatively weak. Due to this, it is hard to define and compare the precise time the two sensors took to reach their steady-state. However, it is very clear the response and recovery time was slightly increasing with the DSPC ratio contained in sensing film. Furthermore, as shown in figure 7-4 (c), the variations in the sensor response for each cycle indicate the fabricated sensor can be exposed repeatedly to the test vapour with various concentrations. A fast trapping and de-trapping response pattern was investigated during the real time sensing experiment.

The other three mixed lipids vapour sensors showed a similar response pattern. The only difference is that the weight fraction was increased of DSPC in mixed lipid films, and the sensor showed a slightly increasing time for frequency recovery on exposure to alcohol. Although it is obvious that the response curves show slightly different response patterns, excellent reversibility, negligible baseline drift and rapid response was observed in the frequency shifts, which confirmed that the sensors could be easily regenerated and could be used for continuous detection of the four vapours. The rapid response is attributed to the higher diffusion rate of vapour molecules into the relatively low viscosity lipids and this will be further mentioned and discussed in detail in Chapter 8. Besides, due to the negligible frequency shift in the baseline before and after vapour exposure, and the highly repeatable response on for the same vapour concentration (repeat exposure showed the relative standard deviation was less than 0.05%), we presume there was no coating loss

when the sensors were used for measurement, which is crucial in order to achieve a stable system. Due to the high stability of the sensor coatings, and the excellent reversibility of the sensor system, the sensors were expected to have a theoretically long life time.

It should be noted that the excellent sensor reversibility for adsorption of vapour was not found in all of the test vapours. As shown in Figure 7-5, a DLPC sensor showed an extremely slow adsorption on exposure to acetone vapour. Acetone vapour flow was switched off at the 15 minutes mark. An incomplete recovery of the frequency of a DLPC sensor was observed even after 6 hours continuous flushing of the sensor chamber with nitrogen. It was also found that once the DLPC sensor was used for detection of acetone, the response of the sensor to other vapours (such as methanol-which should exhibit a stable and reversible response) was no longer reversible, which may lead to an irreversible change in the sensor property (see Figure 7-6). It could be concluded that a DLPC sensor for the detection of acetone vapour was “one use only”. Thus acetone was not considered as a sample vapour for the rest of the experimental work.

The irreversible response of a DLPC sensor (film structure referred to in Figure 5-4 a) on exposure to acetone vapour is likely to be attributed to two possible reasons. One reason is that, on exposure to acetone, a permanent change may happen in DLPC lipid sensing film (such as the chemical structure). The other reason may be some of the acetone may permanently “stay” with the sensing membranes (either physical absorption or chemical absorption). Further discussion will be found in section 7.2.3.

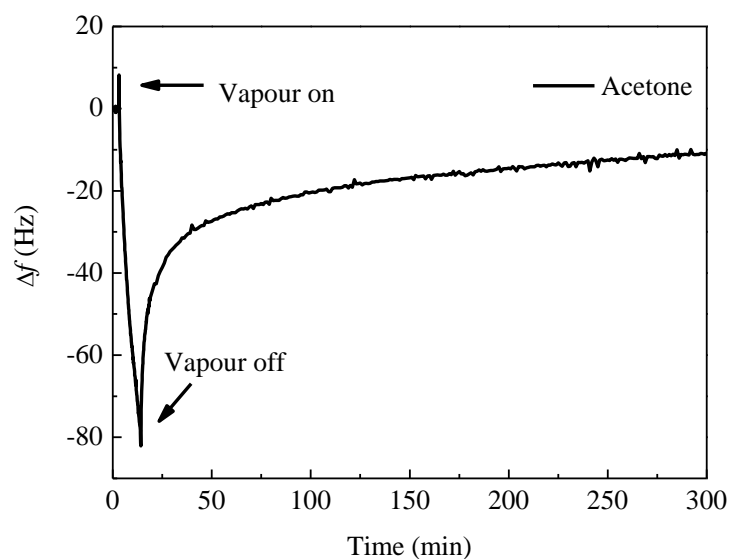


Figure 7-5 Non-recovery response of DLPC sensor on exposure to acetone vapour.

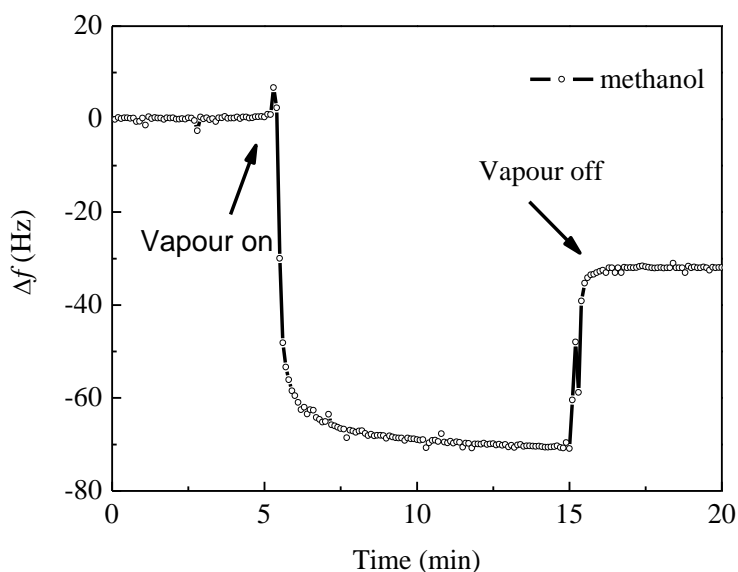


Figure 7-6 Non-recovery response of DLPC sensor on exposure to methanol vapour after being used for detection of acetone vapour.

### 7.2.3 Interaction mechanism

As mentioned in section 7.2.2, there are two types of interactions including recovery and non-recovery interactions. The proposed interaction mechanisms will be discussed here.

#### (a) Recovery sensing mechanism

Multilayer films of lipids showed repeatable response characteristics when exposed to ethanol, methanol, toluene and cyclohexane vapour, with the only differences being the sensitivity values and the selectivity properties (this will be further discussed in section 7.3). All the rapid sensor responses on exposure to vapours can be recognised by negative frequency shifts. This shift was due to vapour being trapped in the sensing film causing a change in film mass and film thickness. A schematic representation of the interaction mechanism between the lipid membranes and the vapour molecules is shown in Figure 7-7.

As shown in Figure 7-7, the proposed main reaction process of sensing includes: the formation of the first thin condensed vapour film on the surface of the lipid layer, and the diffusion of the vapour through into the underlying films causing an increase of film thickness and mass. The arrows in Figure 7-7 (b) and (c) indicate that both processes are reversible, under ideal conditions. Furthermore, due to the property of the amphiphilic lipid molecules, the hydrophilic vapours (ethanol and methanol) are more likely to condense in

the hydrophilic head of the lipids. By contrast, the hydrophobic vapours (toluene and cyclohexane) are more likely to condense in the hydrophobic tails of the lipids.

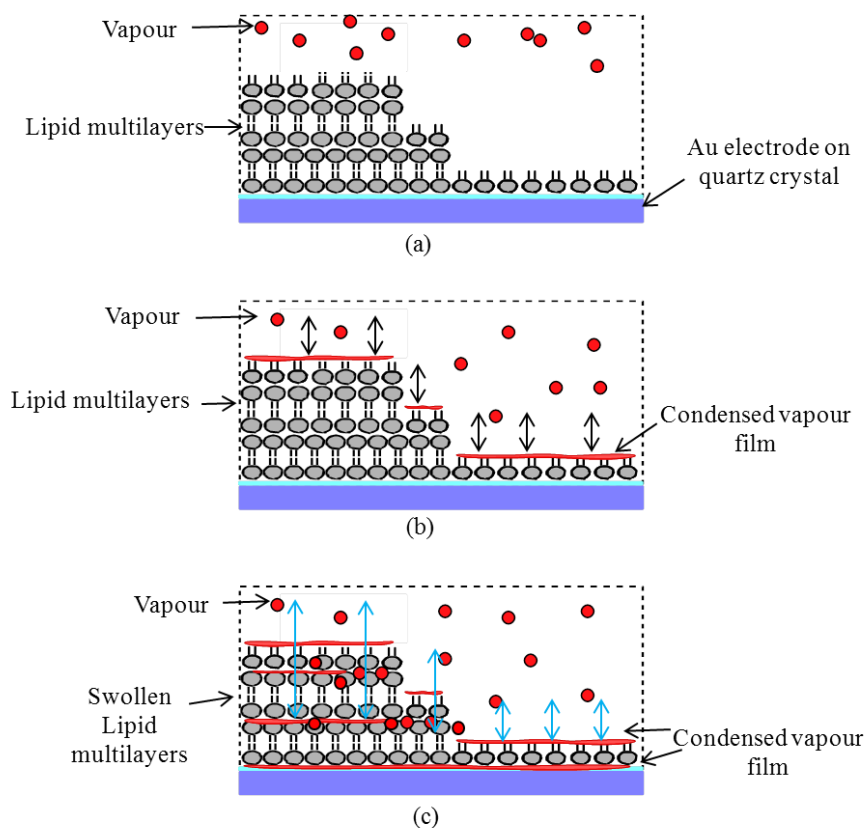


Figure 7-7 Schematic diagram illustrating the interaction mechanism between vapour molecules and sensing lipid membranes: (a) lipid membranes before reaction; (b) adsorption of condensed vapour on the surface of lipid membranes; and (c) diffusion of condensed vapour into the bulk of the lipid membranes, causing swelling, an increase of total film thickness and mass, and a decrease in membrane viscosity.

When the vapour is replaced with dry nitrogen there is a rapid drying effect of the sensing film (i.e. the loss of the vapour formed within the lipid films). This switching off of the vapour reduces the film's total mass and thickness, and therefore the frequency returns to its initial value for a particular nitrogen flow rate. Furthermore, the response and recovery time is increased with DSPC ratio contained in the sensing film. This may be because of the phase influence of the lipid film and will be further discussed in section 7.3.1. The four vapours (ethanol, methanol, toluene, and cyclohexane) took 10 seconds for 80% de-trapping and 3 minutes for full de-trapping of vapours. However, acetone vapour absorbed into the bulk of the lipid membranes took a longer time to diffuse out, and it

seems as if not all of the molecules did diffuse out within a 6 hour observation period. The possible sensing mechanism will be discussed in the coming section.

*(b) Non-recovery sensing mechanism*

As mentioned before, the DLPC sensor was “one use only” for the detection of acetone. A possible schematic representation of the reaction process is now discussed. Figure 7-8 (a) depicts the substrate before any reaction has begun. Figure 7-8 (b) shows the formation of a thin condensed vapour film and diffusion through into the lipid membrane. Figure 7-8 (c) shows that the acetone molecules partially diffuse out when the vapour is replaced with dry nitrogen. Figure 7-8 (d) depicts the changed substrate before any reaction has begun. Figure 7-8 (e) shows the formation of a condensed methanol vapour film in the lipid layer and with the existing acetone. Figure 7-8 (f) shows the partial diffusion out of the methanol when the methanol vapour was replaced with dry nitrogen.

Acetone and methanol are polar aprotic and polar protic solvents respectively. Both of them are covalent compounds. As mentioned in section 4.4.1 (c), ionic compounds are soluble in ionic solvents and covalent compounds are soluble in covalent solvents (i.e. 'like dissolves like'). There is a difference in electronegativity between hydroxyl (in methanol; hydrogen is therefore partially positive) and O=C (in acetone; oxygen is partially negative). That means hydrogen bonding is formed, and this is why methanol is soluble in acetone. If we presume some of the acetone molecules were permanently left in the sensing film, they may “capture” the extra methanol or “capture” methanol instead of the sensing film. The strong bonding between them may cause the extra molecules of methanol to remain in the sensing film. This proposed non-recovery sensing mechanism has explained the reason for the acetone response characteristic and the change of sensing pattern for methanol after the vapour sensor has been used to detect acetone vapour.

Besides the sensing mechanism, the sensor properties including sensitivity and selectivity are also important parameters which can be used to evaluate the vapour sensor. These will be discussed in the following section.

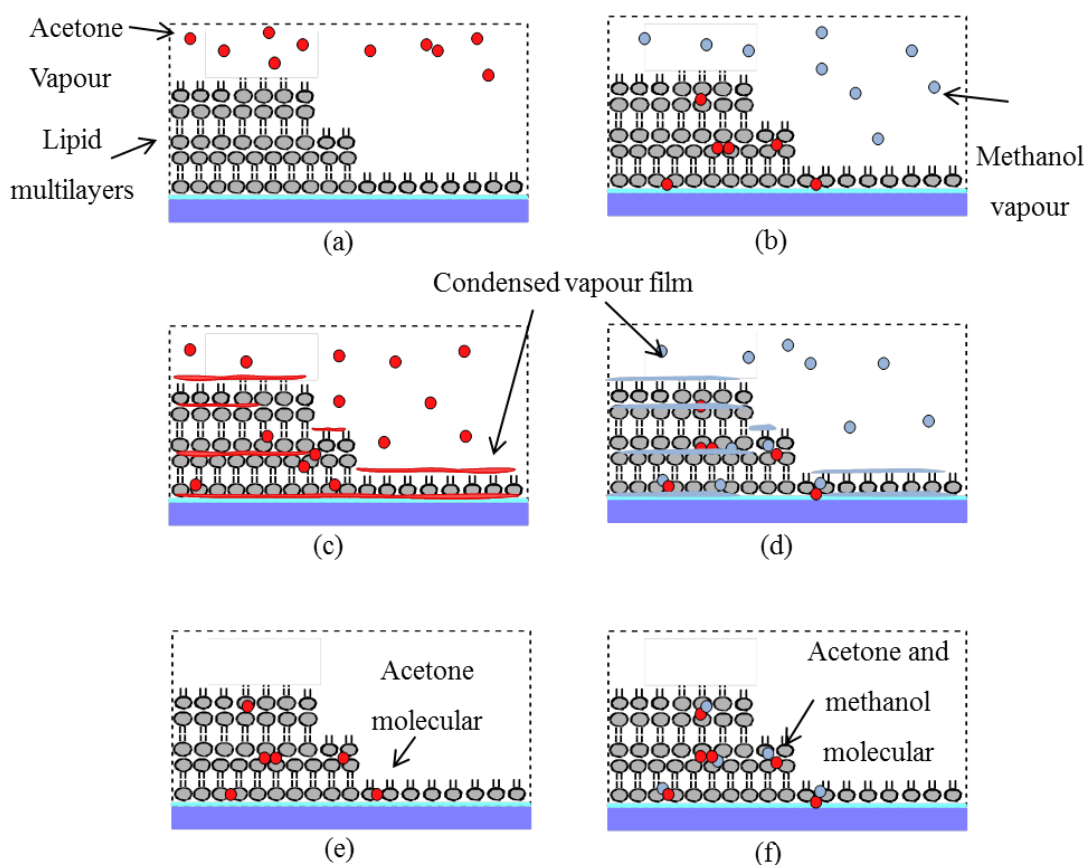


Figure 7-8 Schematic diagram illustrating the interaction between acetone vapour molecules and sensing lipid membranes: (a) lipid membrane before reaction; (b) adsorption of condensed acetone vapour and diffusion of condensed vapour into the bulk of the lipid membrane; (c) acetone molecules partially diffuse out; (d) changed sensing film before any reaction of methanol; (e) the formation of condensed methanol vapour; (f) partial diffusion out of methanol.

### 7.3 Evaluation of sensor sensitivity and selectivity

#### 7.3.1 Sensor selectivity

##### (a) Affinity of lipids to different vapours

Affinity of lipids to chemical vapours is one of the key factors in achieving the maximum sensor performance. Five fabricated phospholipid sensors were used to evaluate the selectivity of the lipid membranes. Figure 7-9 shows the sensors' responses to various saturated vapours at 20 °C. There are four responses collected for each sensor-vapour

combination. Each sensor-vapour combination was repeated at least three times within the same day. The sensor responses shown in Figure 7-9 were averaged yielding the values ( $\Delta f_n = \Delta f/C$  is the nominal frequency shift, where C is the concentration of the vapour in ppm) for particular sensors. The standard error was a measure of the sensor-vapour combination response repeatability. As mentioned section 7.2.1, the maximum responses were taken until the frequency variations were less than 1 Hz/min for at least ten successive minutes, which indicates that the maximum adsorption of the QCM sensor was obtained for all measurements.

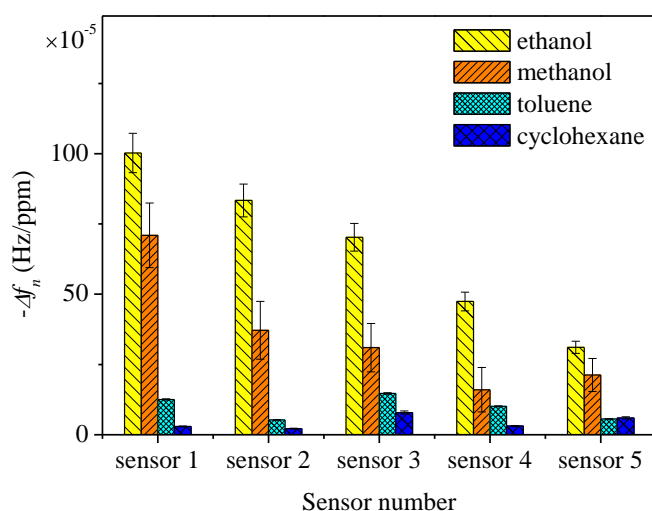


Figure 7-9 Nominal sensor response for ethanol, methanol, toluene and cyclohexane. Sensor details refer to Table 7-1

It is clear that each QCM sensor coated with a different coating material had quite different response to the same vapour. For example, when 76,200 ppm ethanol or 164,800 ppm methanol was measured, the signal intensity for each sensor decreased in sequence of sensor 1 > sensor 2 > sensor 3 > sensor 4 > sensor 5; while the array showed quite a different response pattern towards the other two vapours. However, it is quite hard to compare the signal intensity for each sensor because they are similar. On the other hand, the same sensor presented a different frequency response to the different vapours (high selectivity). It is very clear that all lipid sensors showed strong response intensities to hydrophilic alcohols, while all lipid sensors showed relatively weak response intensities to hydrophobic toluene and cyclohexane. One explanation is that the affinity of lipids to vapour could be related to the dipole moment of each vapour. It was assumed that all the lipids used for vapour sensor fabrication were polar and thus showed the greatest affinity to

vapours which were polar (i.e. ethanol and methanol) while exhibiting lower sensitivity to non-polar toluene and cyclohexane. It could be easier for vapours to be adsorbed into lipid films of similar polarity, i.e. polar vapour and polar lipid films.

*(b) Affinity of different lipids to the same vapour*

Frequency shifts of vapour sensors on exposure to a fixed concentration of different vapours are shown in Figure 7-10 (film structures referred to in Figure 5-4). This data was used as eigenvalues for data processing to compare the affinity of different lipids to the same vapour. The results shown here were five different sensor responses on exposure to ethanol and methanol. The responses of five different sensors on exposure to toluene and cyclohexane were relatively low and not clear enough to compare. Thus the responses on exposure to toluene and cyclohexane are not discussed here. To minimise the error caused by the environment, five sensors were prepared and measured on the same day. The time of exposure to vapours of ethanol and methanol was 10 minutes after a stable baseline in nitrogen flow has been held in each case for 5 minutes. The exposures were followed by recovery processes for 5 minutes.

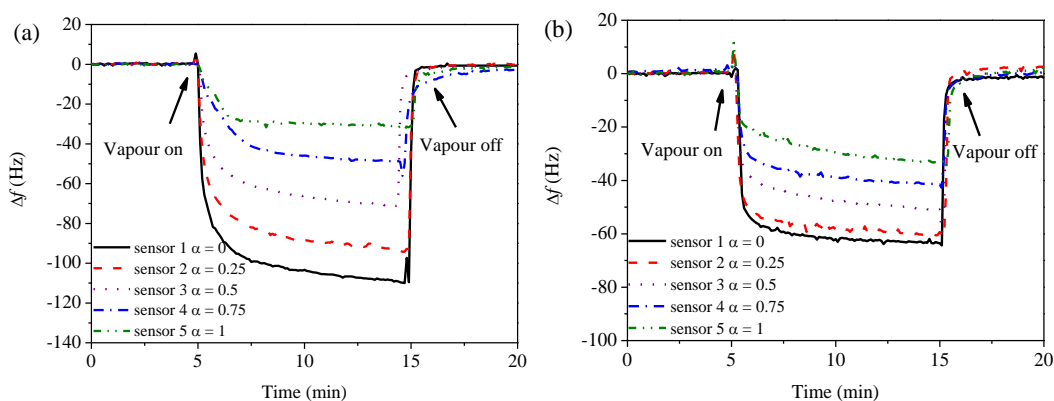


Figure 7-10 Representative real time responses of five sensors to (a) Ethanol (76,200 ppm), (b) Methanol (164,800 ppm).

Inspecting the figure, one can observe that the overall strongest response intensity on exposure to both ethanol (108.9 Hz) and methanol (63.5 Hz) was found in 100% DLPC coated vapour sensor. The weakest response intensity for both ethanol (31.7 Hz) and methanol (34.2 Hz) exposure was found in 100% DSPC coated vapour sensor. In both

cases, increasing the weight fraction of DSPC in coating samples decreased the response intensities of sensors to ethanol and methanol vapours.

Absolute maximum frequency shifts obtained from each of the crystals change due to differences (e.g. vapour pressure, physical properties) in the test vapours. Therefore, to compare the response caused by the affinity of immobilised lipids regardless of vapour concentration, the ratio of the resonant frequency shift,  $f_r$ , is defined here for normalisation [17]:

$$f_r = \frac{f_x}{f_{x_{max}}} \times 100\% \quad (7-1)$$

$f_x$  = the frequency shift corresponding to each lipid [Hz]

$f_{x_{max}}$  = the maximum frequency shift for each compound [Hz]

As mentioned in section 3.1.1, the two lipids used for film fabrication are zwitterionic phospholipids, with exactly the same hydrophilic head and glycerol linker. The only difference is the length of the hydrophobic alkyl tails. The result after normalisation is shown in Figure 7-11. The length of the acyl chain correlates with frequency shift. The acyl chain length is the average chain length calculated from the mole fraction of mixed sample lipids.

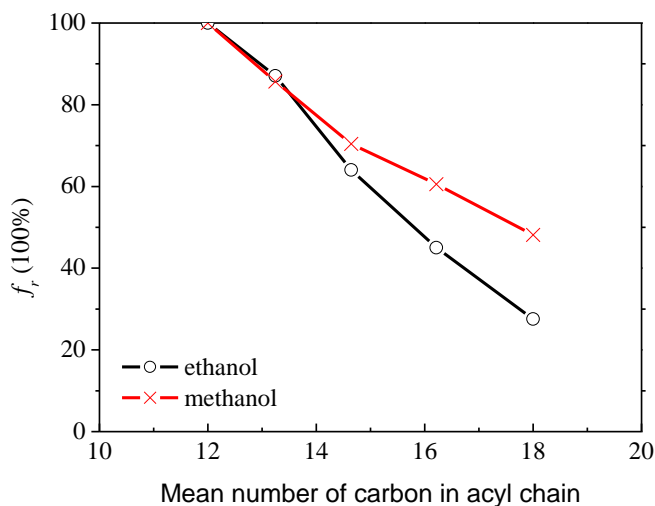


Figure 7-11 Effect of acyl chain length on frequency shift ratio ( $f_r$ ). The definition of  $f_r$  is given in the text. Frequency shifts were measured at a constant flow-rate and constant temperature.

In Figure 7-11, it is very clear that hydrophilic chemical vapour ethanol and methanol can be recognised well by lipids having shorter acyl chains, whereas lipids with longer acyl

chains showed less affinity to hydrophilic vapours. These results suggest that the sensor response is also affected by the length of the acyl chains. It is proposed, therefore, that a highly sensitive and specific chemical vapour sensor can be fabricated with regard to lipid acyl chains.

This phenomenon is likely due to the amphiphilic properties of the lipids. As mentioned section 7.1.3, short-chain alcohols such as ethanol and methanol localise predominantly at the hydrophilic head group region of the phospholipid bilayer. Thus, if the molecules of alcohol want to diffuse into the underneath layer of the lipid film to further condense onto underneath hydrophilic head groups, they need to get across the hydrophobic barrier (i.e. alky chains). It might be easier for the small molecules to reach the next layer by passing through the more fluid and shorter chains (see Figure 7-12). As a result, lipids with shorter chains showed more affinity to the hydrophilic vapours.

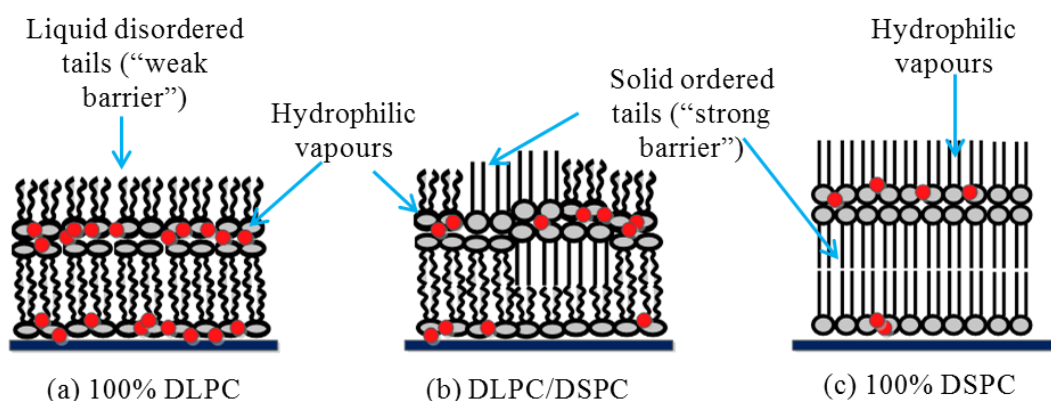


Figure 7-12 Model of ethanol or methanol vapours (a) easily diffused into the underneath layer of fluid DLPC; (b) part diffused into the underneath layer of mixed lipids (c) difficult diffusion into the underneath layer of gel phase DSPC.

The lipid film layers structure models shown in Figure 7-12 was predicted and produced from the AFM mapping study mentioned before. They show that the hydrophilic vapour molecules were easily diffused into the underneath layer of fluid DLPC while molecules were struggling to diffuse into the underneath layer of DSPC, which gives a hint of the underlying reason for the difference in response intensity and response time (vapour trapping and de-trapping) of five different sensors on exposure to hydrophilic vapours. The more vapour molecules trapped by the sensing film, the heavier the total film mass will be, and the greater the frequency shift will be (i.e. stronger response intensity here). Therefore,

the more DSPC is contained in the sensing films, the less the sensor affinity to the hydrophilic vapours and longer response time will be. This will be mentioned again in section 8.2.3.

### 7.3.2 Sensor sensitivity

The sensitivity ( $S$ ) is another important performance parameter of vapour sensor. Here, as discussed before, the fabricated sensors showed a lack of sensitivity to toluene and cyclohexane. Therefore, sensitivities of the five sensors to ethanol and methanol were evaluated.

Sensitivity can be defined in various ways depending on the measurement system. One definition is the change of response for unit change of concentration [18] [25] [73-74] [136]. Another way to obtain the sensitivities is to average the response values for particular sensors, and then subsequently normalise the averages by the amount of the deposited sensing film. Thirdly, the sensitivities can be expressed as a frequency shift due to the coating [11] [28]. The latter definition is better for the sensor system fabrication method (such as dip coating, spray coating etc.) which provide an inherent lack of quality control. The sensitivity here is defined as frequency change per unit vapour concentration change (refer to equation 7-2).

$$S = \frac{\Delta f}{\Delta C} \quad (7-2)$$

$\Delta f$  = frequency change of the QCM sensor [Hz]

$\Delta C$  = test vapour concentration difference [ppm]

Thus the sensitivities in the five sample lipids vapour sensors for ethanol and methanol vapour were calculated as the slope of the regression curves from Figure 7-13 and 7-14, respectively.

The Limit of Detection (LODs) is another important factor for sensors. It is defined as the lowest concentration of the test vapour that can be distinguished by the sensor within a stated confidence limit. It is calculated by the sensitivity of the QCM sensor, the noise level of the QCM devices and the signal-to-noise ratio, and according to the definition given by IUPAC [194] LODs is defined by a ratio shown in equation 7-3.

$$LODs = \frac{3\sigma}{S} \quad (7-3)$$

$S$  = sensitivity of the fabricated sensor [Hz/(ppm)]

$\sigma$  = noise level of the fabricated QCM sensor [Hz]

The noise level was evaluated by examining the peak-to-peak noise over a period of 8 hours. The noise level of the system was 0.9 Hz in this work. Given a criterion for a detection limit of 3 times the noise level, the system would be considered to have a system detection limit of 2.7 Hz, and taking into account the LODs of each vapour sensor.

With such methods, adsorption experiments were carried out on ethanol and methanol vapours over a wide range of concentrations under the same circumstances. Figure 7-13 and 7-14 illustrate the normalised response curve of a QCM sensor coated with five different sample lipids exposed to ethanol vapour (15,200 ppm-76,200 ppm) and methanol vapour (33,000 ppm-164,800 ppm) at different concentrations, separately.

The responses of five different sensors (film structures referred to in Figure 5-4) to more than 10 different concentrations of each vapour were investigated and recorded as shown in Figures 7-13 and 7-14, respectively. It should be noted that as the ethanol and methanol vapour concentration increased, all five vapour sensors' frequency responses were also increased. The slopes in Fig 7-13 and 7-14 indicate that the frequency changes are directly proportional to the vapour concentration for the working range. It appears that the frequency changes increase gradually with increasing vapour concentrations, and an approximately linear relationship can be obtained at different concentrations for the five different sample lipids coated vapour sensors. As discussed before, the bubbling system will give a concentration prediction error up to 15%. The higher the concentration, the greater the error will be. This might be the main reason that the regression coefficient  $R^2$  was not high (see Table 7-2). Nevertheless, it is also quite clear the sensitivities of five different sensors to ethanol and methanol are different. Thus sensitivities of five sensors were also calculated and compared using the existing data here.

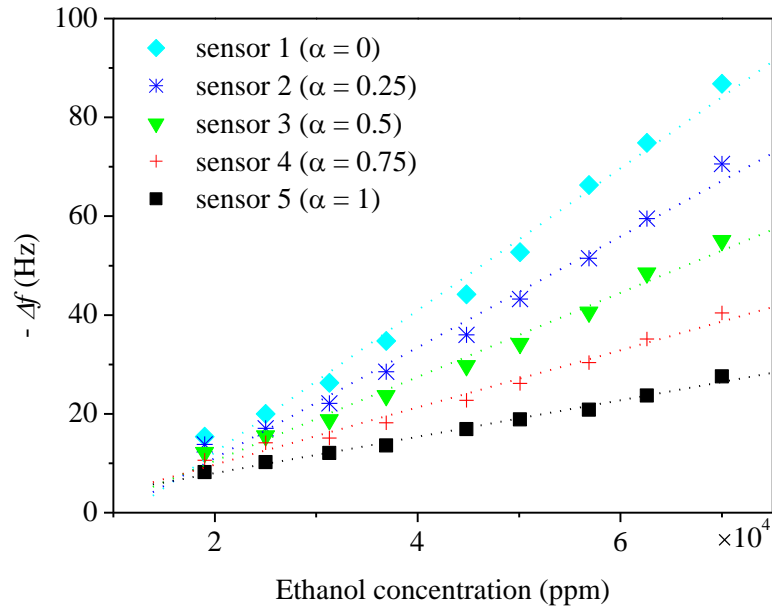


Figure 7-13 Regression curves of five sensors to ethanol. Sensor details refer to table 7-1. Lines are linear fits ( $R^2 = 0.99$ ).

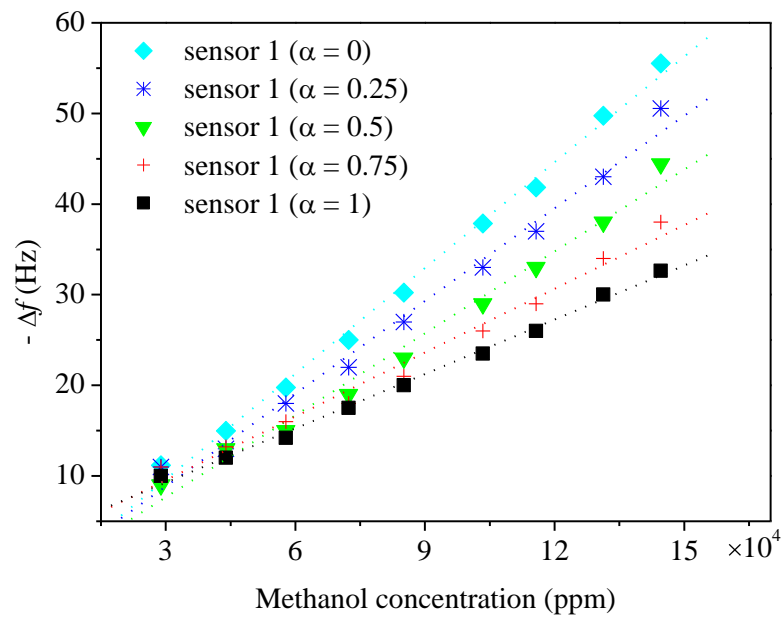


Figure 7-14 Regression curves of five sensors to methanol. Sensor details refer to table 7-1. Lines are linear fits ( $R^2 = 0.99$ ).

The comparison of the five sensors' sensitivities and LODs to ethanol and methanol are shown in Table 7-2 (a) and (b), respectively.

Table 7-2 (a) Sensitivities of five QCM sensors to ethanol

Sensor number	Weight fraction of DSPC ( $\alpha$ )	Ethanol		
		Sensitivity	Limit of Detection	Correlation coefficient
		S (Hz/ppm)	LOD (ppm)	R <sup>2</sup>
1	0	$14.4 \times 10^{-4}$	1900	0.99
2	0.25	$11.2 \times 10^{-4}$	2400	0.99
3	0.5	$8.5 \times 10^{-4}$	3200	0.99
4	0.75	$5.8 \times 10^{-4}$	4700	0.98
5	1	$3.7 \times 10^{-4}$	7300	0.99

Table 7-2 (b) Sensitivities of five QCM sensors to methanol

Sensor number	Weight fraction of DSPC ( $\alpha$ )	Methanol		
		Sensitivity	Limit of Detection	Correlation coefficient
		S (Hz/ppm)	LOD (ppm)	R <sup>2</sup>
1	0	$3.9 \times 10^{-4}$	6900	0.99
2	0.25	$3.4 \times 10^{-4}$	7800	0.99
3	0.5	$3.0 \times 10^{-4}$	8800	0.99
4	0.75	$2.3 \times 10^{-4}$	11400	0.98
5	1	$2.0 \times 10^{-4}$	13400	0.99

It is clear that the fluid DLPC coated sensor exhibits better performance on the ethanol and methanol vapour detection than other sensors by showing a higher sensitivity to both vapours. Whereas, for a DSPC coated sensor, the frequency changes did not increase significantly with the increase of the test vapour concentration. By increasing the weight fraction of the gel phase DSPC in the mixed lipid film, the sensor sensitivity to both ethanol and methanol decreases.

As discussed before, the difference in sensitivities to vapours could be attributed to the distinctness of the chemical structure and electronic properties between the lipids and the test vapour molecules. By comparing the same sensor sensitivity to ethanol and methanol, all five sensors showed greater sensitivity to ethanol vapour. The two vapours have a

similar dipole moment (1.69 for ethanol and 1.70 for methanol). Ethanol has one more alkyl chain than methanol. If we presumed the hydrophilic head of lipids would like to attract the oxhydroxyl group of the alcohols, then the hydrophobic tail may prefer to attract the carbon tail of alcohol. It seems like the extra carbon bond of ethanol has improved both the bonding and resulted in increasing the sensitivity.

Generally, compared to QCM sensors coated with other sensing materials, such as Pegylated lipids [11] [28], LB coated DPPC-AA [74] and mixed lipids [18], the studied lipid sensors have relatively low sensitivities to all vapours. This has also caused problems with obtaining accurate sensitivity and LODs to different vapours. Thus, improving the sensitivity of the sensor is quite important and will be studied and discussed in chapter 8.

### 7.3.3 Adsorption behaviour

The number of mol of coated lipid and that of trapped vapour on exposure to saturated vapour at 20 °C are compared in Table 7-3.

Table 7-3 Comparison of trapped molecule vapour amounts in different sensors

Sensor number	Lipids coated (nmol/cm <sup>2</sup> )	Ethanol trapped (nmol)	Methanol trapped (nmol)
Sensor 1	4.76	32.14	37.21
Sensor 2	4.90	24.35	33.38
Sensor 3	4.82	20.40	27.81
Sensor 4	4.73	15.00	25.63
Sensor 5	4.72	9.09	19.09

The number of vapour molecules trapped is calculated by Sauerbrey equation (referred to section 3.2.5) and the molecular weight of each sample liquid. The trapped number of vapour molecules is always more than the number of lipid molecules coated. As shown in figures 7-13 and 7-14, in the case of alcohols, the frequency change increases significantly with increase of concentration. In other words, at high concentration, the surface of the coated crystal never saturated with vapour molecules. As discussed before, both ethanol and methanol have strong electron attracting groups, and so their adsorbed vapour molecules can subsequently interact with further analyte on the vapour phase. In this experiment condition, as the alcohol vapour concentration increases, more vapour molecules are adsorbed on the vapour sensor by interacting with molecules previously

captured on the surface to form multilayers. Figure 7-15 gives a schematic representation of the proposed model bonding behaviour between lipids and ethanol vapours.

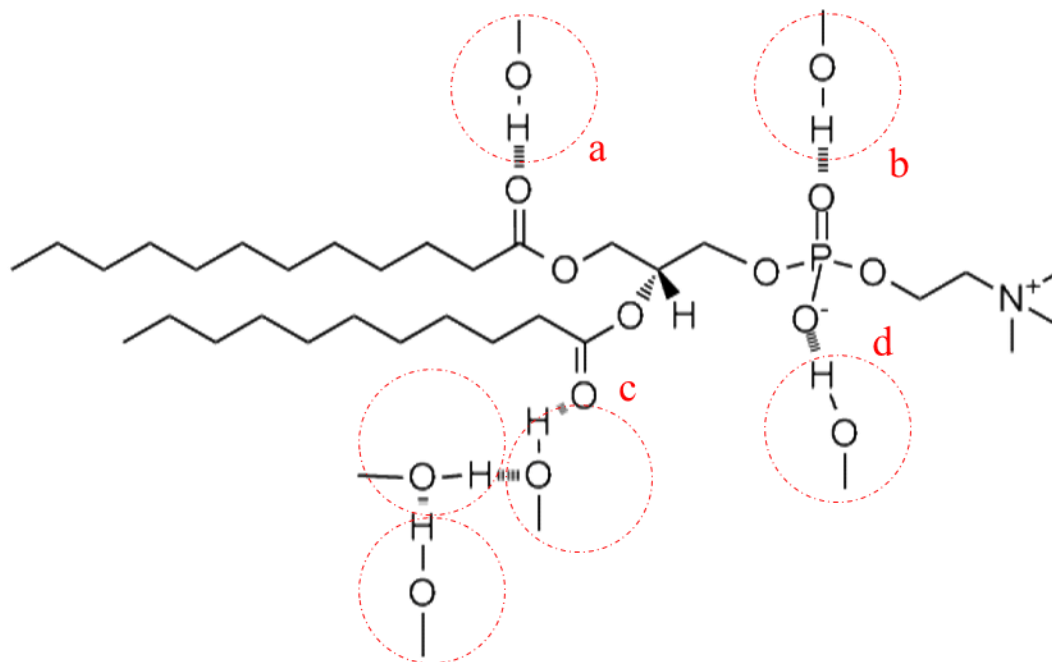


Figure 7-15 Schematic representation of the formation of multilayer adsorption of ethanol onto DLPC coated sensor, where a, b, c and d indicate the four possible bonding positions of the vapour molecules. Red circles indicate each single ethanol molecule vapour may be located when adsorption happened.

There are four possible hydrogen bonding sites at the head group of the lipid. The electromagnetic attractive interaction also exists between ethanol vapour molecules and is indicated in Figure 7-15 location c.

#### 7.4 Evaluation of sensor useful life

A critical issue in a successful sensor is the device's useful life, because the substitution of sensors increases the cost of any detection system. Five fabricated vapour sensors were analysed by ethanol vapour over a period of 4 months. Figure 7-16 illustrates the response loss (%) of each sensor with time. Sensor response loss (%) is defined as the ratio between the drop in response with time and the first sensor response.

All sensors reduced their frequency response with time and they did not reach a stable value. Four months later, the mean value of QCM response loss for five sensors was 26%,

with the highest one for sensor 5 (32%) and the lowest value for sensor 4 (18%). Sensor 1 and 4 showed a response loss lower than the mean one, but sensors 2, 3 and 5 showed higher values than the mean one. These results suggest that QCM sensors proposed in this study were relatively stable within 2 months' time, and a DSPC ( $\alpha=1$ ) coated QCM sensor is less stable compared to the other four sensors.

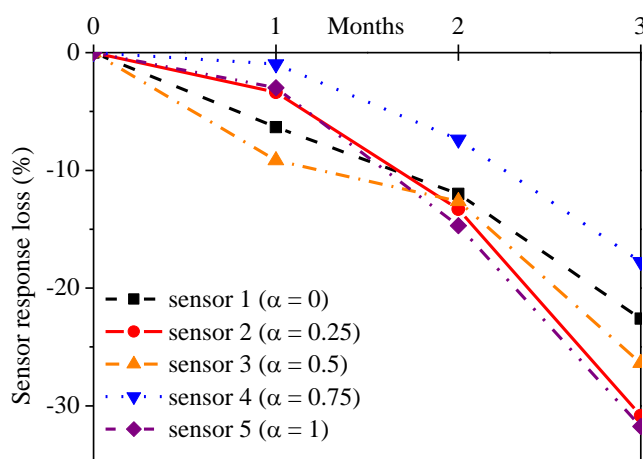


Figure 7-16 Response loss (%) of sensors with time.

There are two possible reasons for sensor response loss. The first reason might be the lipid molecular loss. As sensors were reused, the lipid molecules may be un-immobilised from the quartz crystal surface during handling, causing a sensor response loss. The second reason of sensor response loss might be lipid recrystallisation. The best storage temperature of both DLPC and DSPC lipids is  $-20\text{ }^{\circ}\text{C}$ . After the sensors were fabricated, they were kept and stored at room temperature and have the chance to be exposed to contamination in air which may speed up the lipid “deterioration”. The five sensors were treated to model the progress of the lipid recrystallisation. Figure 7-17 illustrates the response loss (%) of each sensor with treating stages.

All sensors reduced their frequency response with increase of treatment times and they did not reach a stable value. After three treatments, the mean value of QCM response loss for five sensors was 61%, with the highest one for sensor 1 (67%) and the lowest value for sensor 2 (56%). Sensors 2, 3 and 4 showed a response loss lower than the mean value, but sensors 1 and 5 showed higher values than the mean one. These results suggest that QCM sensors proposed in this study were relatively stable for 6 hours treatment at  $30\text{ }^{\circ}\text{C}$ . When

the sensors were placed at a high temperature for several hours, the sensor response loss was obvious. The idea of heating the sensors is to try to model “speed up” progress of sensor response capacity change in several months of use. During three months of use, the lipids have a chance of drying out, recrystallising, oxidation or even further degradation to other compounds. It has been reported the oxidation was promoted by heat, but restricted by humidity. Here, the sensing lipid deterioration promotion happened via heat treatment [195].

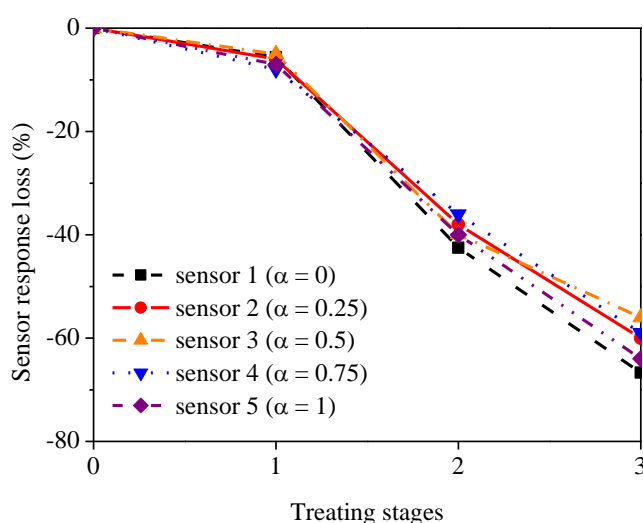


Figure 7-17 Response loss (%) of sensors with treating stages. Stage 1 is to heat the five sensors up to 30 °C for 6 hours; stage 2 is to heat the five sensors up to 60 °C for 2 hours; stage 3 is to heat the five sensors up to 60 °C for 2 hours.

As argued above, there may be lipid loss during handling in three months’ use. The sensors were not used quite often and the baseline frequency does not shift a lot each time before experiment starts. As a result, the material loss is not a major reason for the sensors’ capacity reducing. The the largest contributor to the sensors’ capacity reducing would be the lipid deterioration. It indicates the best environment for storing the sensors is at a relative high humidity, low temperature and under vacuum.

## 7.5 Summary

Five different lipid sensors were fabricated by the spin coating method on QCM. A water-wettable gold electrode was used as the main working subphase. The concentration used for fabrication was 5 mg/ml. The properties of five sensors and the sensing

mechanism were evaluated. An excellent reversibility for adsorption of vapour was found in ethanol, methanol, toluene and cyclohexane vapours except acetone. Lipid sensors showed the stronger response intensity to alcohol than to toluene and cyclohexane. As increasing the weight fraction of DSPC in coated lipids film, the sensor response intensity and sensitivities to ethanol and methanol decreased. Lipids with shorter acyl chains showed more affinity to hydrophilic vapours. These results suggest that the sensor response is affected not only by the hydrophilic groups of phospholipids, but also by the length of the acyl chains. Furthermore, all sensors were relatively stable within two months' time after preparation. The main reason to cause the sensors' capacity reduction would be the lipid deterioration. It indicates the best environment for storing the sensors is at relative high humidity, low temperature and vacuum.

The sensitivity of the vapour sensors prepared was low, and so the main effort will be made to improve the sensors' sensitivity and will be further discussed in the next chapter.

# Chapter 8 Results and discussion: increase of sensitivity

A vapour sensor was successfully constructed by immobilising DLPC, DSPC or DLPC/DSPC mixed lipids on a QCM surface. The interaction mechanism between the lipids (i.e. DLPC or DSPC) and the vapour molecules has been discussed in detail in chapter 7. The potential of using DLPC and DSPC to fabricate a rapid response and reusable vapour sensor has been demonstrated. Five sensors (Table 7-1) have been prepared and studied. These sensors are better for hydrophilic alcohols and showed a lack of affinity to hydrophobic vapours. The occupational exposure limits (OELs) for hazardous substances at work recommend a maximum long term limit of 8 hours continuous exposure to ethanol, methanol, cyclohexane and toluene are 1000 ppm, 200 ppm, 100 ppm and 50 ppm, respectively. Comparing the limit of detection for the previously prepared sensors (Table 7-2), all sensors showed relatively weak response intensity to all vapours. Thus, improving the sensor's sensitivity is a priority. This chapter examines the sensitivity improvement of QCM vapour sensor by increasing the concentration of lipids and changes to the film property using cholesterol.

## 8.1 Improving sensitivity

There are several ways which could be considered to improve the sensors' sensitivities: these include increasing the sensitivity of the transducer itself by using high fundamental frequency quartz crystals; changing the properties of the sensing film by increasing the thickness of the film; and adding cholesterol. A change to the film phase was the main way to improve the sensor sensitivity which will be investigated and discussed in this chapter.

## 8.2 Optimization of film thickness

### 8.2.1 Testing of high concentration DLPC and DSPC lipid sensors

DLPC and DSPC solutions with different concentrations, including 1, 3, 5, 7 and 10 mg/ml, were prepared for spin coating in Chapter 7. Investigations including a repeatability study, and film weighing were carried out by using solutions with a concentration less than 10 mg/ml. Results indicate that spin coating is a reliable process which guarantees applying a reproducible amount of lipid onto a QCM surface. A strong linear relationship between the fabricated lipid amount and the concentration of the solution used for spin coating were found. In other words, the sensing film thickness can be controlled via the concentration of the solution used for spin coating. When the same mg/ml concentration of DLPC, DSPC or two lipid mixture solutions is used for spin coating, a similar number of lipid molecules could be applied on the QCM substrate under our experiment conditions.

Based on these results, high concentration lipid solutions were prepared for thick film fabrication. The original solution was prepared based on the solubility of each lipid to chloroform (data offered by Avanti Polar Lipids, Inc.). The DLPC solution was prepared to be 100 mg/ml and diluted to the target concentrations: 10, 13, 15, 20, 30, 40, 50 and 100 mg/ml. The DSPC solution was prepared to be 60 mg/ml and diluted to the target concentrations: 10, 15, 20, 30 and 50 mg/ml. Frequency shifts due to lipid adsorptions were measured each time after coating. The DLPC and DSPC film growth can conveniently be characterised in terms of the film thickness obtained as an average from the frequency shifts. Figure 8-1 shows the mean oscillation frequency shift  $-\Delta f_{\text{lipid}}$  plotted versus the coating concentration  $C_{\text{coat}}$ . The standard error of the lipid coating amount is equal to or larger than 16.6 Hz. It is effectively a measure of the sensor-to-sensor response due to coating reproducibility (i.e. the standard deviation), separately. For better clarity, here, we define the concentration used for spin coating to be “low concentration” when it is less than 10 mg/ml and “high concentration” when it is equal or greater than 10 mg/ml. For both high concentrations of DLPC and DSPC lipids deposited by spin coating, an approximate a proportional relationship was found and shown in equation 8-1.

$$-\Delta f_{\text{lipid}} = \alpha_{\text{lipid}} \times C_{\text{coat}} \quad (8-1)$$

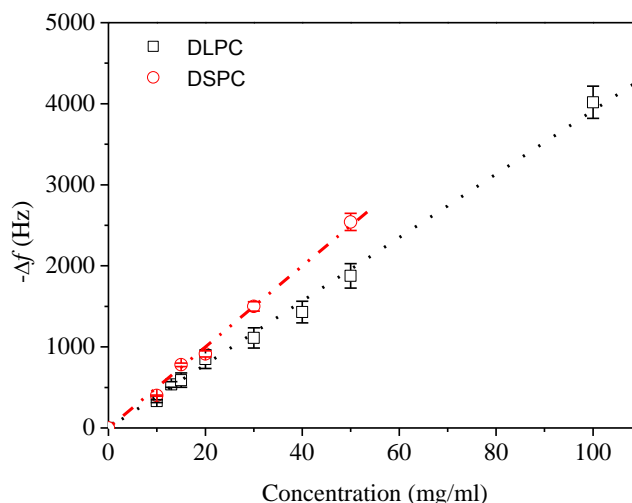


Figure 8-1 Concentration plots of the mean of the frequency shift generated from QCM measurements. Data displayed for dry DLPC and DSPC films. Lines are linear fits ( $R^2 = 0.99$ )

This relationship is in agreement with our previous results when a low concentration was used for spin coating (equation 5-1). The only difference is the proportionality constant. For samples prepared from a high concentration solution, the proportionality constant (coating constant,  $\alpha_{lipid-high}$ ) was found to be 41.7 Hz/(mg/ml) for DLPC and 50.0 Hz/(mg/ml) for DSPC. The comparison of low concentration experimental coating constant and the calculated coating constant is shown in Table 8-1.

Table 8-1 Comparison of proportionality constant

Weight fraction of DSPC	Mole percentage of DSPC (%)	Low concentration $\alpha_{lipid}^*$ [Hz/(mg·ml <sup>-1</sup> )]	High concentration $\alpha_{lipid-high}$ [Hz/(mg·ml <sup>-1</sup> )]
$\alpha = 0$	0	32.8	41.7
$\alpha = 1$	100	40.2	50.0

The experimental measurement coating constant for DLPC is used to work out the calculated coating constant of DSPC based on the presumption that the same number of DLPC and DSPC molecules were coated on the substrate. That is, the calculated coating constant for DSPC is determined based on the experimental results of DLPC. If we believe the experimental coating constant of DLPC is 41.7 Hz/(mg/ml), then when the same amount of DSPC be coated the coating constant of which will be 50.0 Hz/(mg/ml). By comparing the experimental coating constant of DSPC with the calculated one, it indicates the experimental results are still in good agreement with our previous conclusion, i.e. when

the same concentration solution in g/ml was used for spin coating, a similar number of lipid molecules could be coated on the substrate. The coating constant is different for low and high concentration lipids. This difference can be mainly attributed to the different experimental conditions. The lipid solution used for sensor spin coating was prepared on different days and with a different initial concentration. There will be an error during these experimental procedures. Nevertheless, these results are in good agreement that a similar amount of DLPC and DSPC lipids were coated with the same concentration lipid solution in mg/ml that was used for spin coating.

The standard deviation of the thickness distribution for DLPC and DSPC are quite similar and the value of the deviation increase with the spin coating concentration. Even so, the repeat study showed an acceptable sensor response difference while on exposure to the same vapour pressure vapour (maximum frequency shift difference about one fifth of the frequency shift caused by vapour exposure).

### 8.2.2 Correspondence of sensor response to film thickness on quartz crystal

The film thickness optimisation was carried out by investigating different amounts of DLPC or DSPC coated on the 5 MHz QCM surface. Figure 8-2 illustrates the frequency change as a function of coated lipid molecule number when exposed to 76,200 ppm ethanol vapour. The response of DLPC coated QCM showed an increase with coated mass below 6.9  $\mu\text{g}$  (corresponding to a film thickness of about 84 nm).

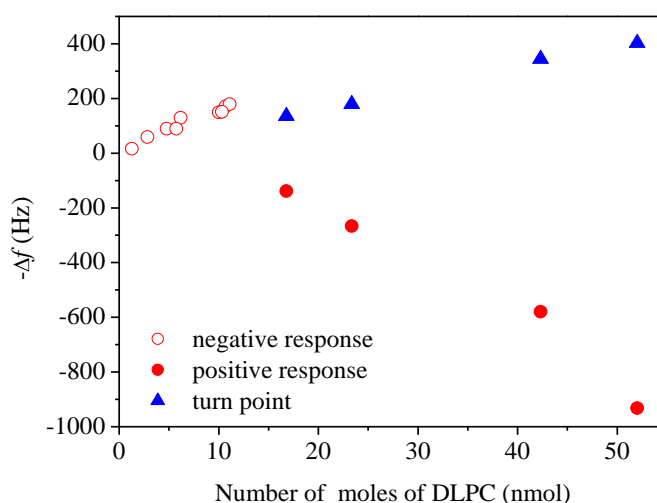


Figure 8-2 Frequency change of QCM sensor versus different number of moles of DLPC on exposure to 76,200 ppm ethanol vapour.

A negative frequency change means that adsorption of organic vapours caused a frequency decrease in the QCM sensor. However, the response declined when the coating concentration was more than 10 mg/ml (corresponding to about -220 Hz frequency shift, 3885.2 ng/cm<sup>2</sup> coated DLPC, 50.6 nm). The frequency shift may be attributed to the three possible effects. The first, perhaps obvious, is the mass increase in the film resulting in a decrease in the QCM frequency. However, two other competing effects are: a viscosity decrease resulting in an increase in the QCM frequency [71] [110] and an uneven loading of the crystal causing only part of the crystal to stop oscillating. For thin films (the concentration of solution used for coating was less than 7 mg/ml here), the latter effects (i.e. viscosity effect and uneven loading effect) can be ignored and the Sauerbrey equation works well. With thick DLPC films, the viscosity decrease becomes the dominant factor to influence the QCM performance, leading to a response which is opposite to that of conventional QCM devices which are based on the detection of mass loadings. The adsorption of organic vapours to the DLPC films resulted in a positive frequency shift. Accordingly, when the DLPC is too thick, we cannot rationalise the vapour response results based on the equation originally derived by Sauerbrey. Normally, on exposure to saturated ethanol vapour, the frequency of the quartz crystal will start to decrease at the beginning. At one point the frequency will start to increase. The final equilibrium is normally reached after about 5 minutes. The lowest points here are named as “turn points”. The thicker the film is, the lower the turn point will be. These points are also marked on the figure 8-4 in the red circle.

The positive response has been previously reported and utilised as a sensing mechanism for vapour sensing of ionic liquids by other groups [71] [110]. However, no study has been done on lipid based QCM sensors to the best of the author’s knowledge. More details will be discussed in section 8.2.3. To minimise the influence of viscosity on the sensor response, a concentration of 10 mg/ml is well suited for the spin coating of single phase DLPC lipids. Similar work has been undertaken on DSPC lipids in order to optimise the film thickness. Figure 8-3 illustrates the frequency change as a function of coated DSPC or DLPC molecule number when exposed to 76,200 ppm ethanol vapour.

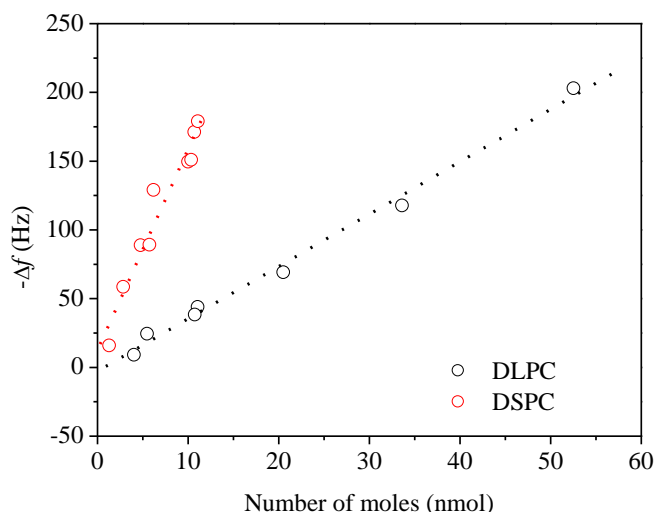


Figure 8-3 Comparison of the optimisation of the DSPC and DLPC sensor response versus a different number of moles on exposure to 76,200 ppm ethanol vapour. Lines are linear fits ( $R^2 = 0.99$ ).

Different from the DLPC results, DSPC showed a relative stable negative response on exposure to saturated ethanol vapour even when the DSPC concentration used for spin coating had reached a high level (50 mg/ml). A good linear relationship was found between coated number of moles of DSPC and the frequency response on exposure to ethanol vapour ( $R^2=0.99$ ). It indicates that the response of DSPC coated QCM still showed an increase with an increase in coated mass when it is below 41.5  $\mu\text{g}$ . The main driving force of frequency shift is still the mass loading and the Sauerbrey equation is holding well. The stable response of the DSPC coated QCM sensor makes a high concentration spin coated DSPC sensor a good potential candidate sensor for highly sensitive vapour detection. However, a negative aspect of this sensor is the slower vapour adsorption speed with thicker films.

### 8.2.3 Typical response of high concentration DLPC and DSPC single phase sensors

#### (a) DLPC sensor

The typical real-time responses of thick DLPC film coated QCM vapour sensors (film structures referred to in Figure 5-4) to ethanol vapour under atmosphere at 25 °C (i.e. 76,200 ppm) are shown in Figure 8-4 (a). Different concentrations used for spin coating are indicated by different colours in this figure. The corresponding concentrations of DLPC solution used for spin coating are also shown. The variations in the sensor response for the

first, second and further exposures of the DLPC sensor (prepared from spin coated 40 mg/ml DLPC solution) to different concentrations of ethanol is shown in Figure 8-4 (b). In each cycle, the sensor was exposed to a given concentration of ethanol for 10 minutes and then flushed with nitrogen for 5 minutes.

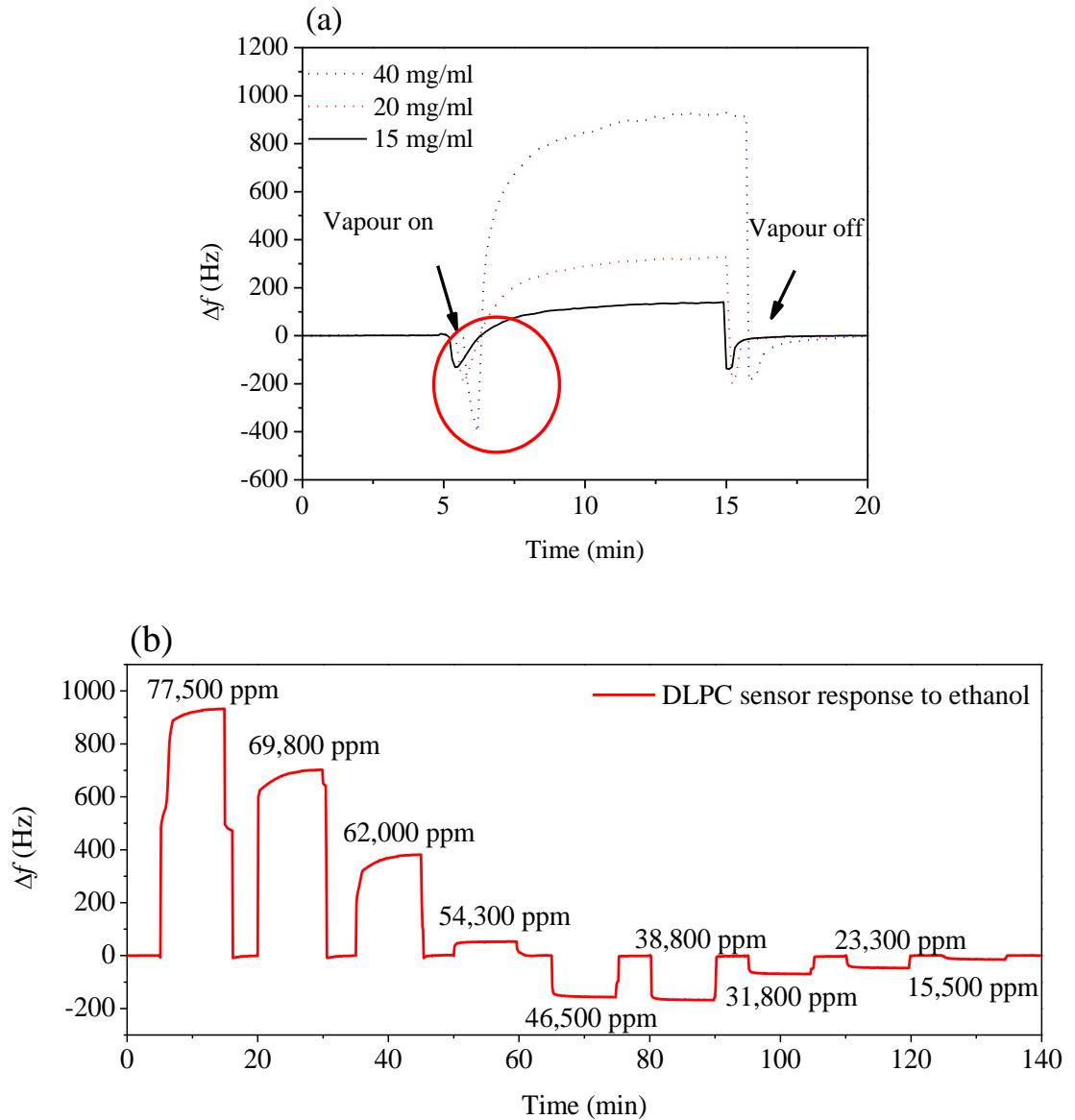


Figure 8-4 (a) Typical response of different thickness DLPC film sensors with 76,200 ppm ethanol vapour (“turn points” mentioned in section 8.2.2 are shown in the red circle) and (b) frequency response pattern of a DLPC sensor (spin coated from 40 mg/ml solution) on exposure to step changes in the concentration of ethanol vapours in the nitrogen carrier gas at room temperature.

After stabilisation for at least five minutes, the sensors were exposed to saturated ethanol vapour for ten minutes. The three sensors clearly responded to the sample vapour and always fully recovered after each exposure. The solubility equilibrium of organic vapours in DLPC lipids was normally reached within five minutes. However, on exposure to the ethanol vapour, the frequency decreased for a few seconds, and finally reached equilibrium at a higher frequency (frequency increased compared to the initial stable baseline. This is related to the viscosity decrease of DLPC upon dissolution of solute molecules [71] [196-197].

Furthermore, Figure 8-4 (b) clearly shows one example of a typical real-time response pattern of the DLPC sensor with both positive and negative response on exposure to different concentrations of ethanol vapour (also referred to in figure 8-5). A fast trapping (about 30 seconds) and de-trapping (about 30 seconds) response pattern was identified during the sensing experiments. Frequency shifts of QCM devices result from a comprehensive change in the physicochemical properties of a surrounding medium. In addition to the change of film density on the QCM electrode, the variation of viscosity of a surrounding medium also gives rise to a frequency shift of the resonator [71]. From the real-time response of these sensors on exposure to ethanol vapour, the ethanol molecules were adsorbed by the DLPC film, resulting in the decrease of the quartz crystal frequency. When enough vapour has been adsorbed by the film, the positive frequency shift caused by viscosity change cannot be ignored, and finally results in an increase of the quartz crystal frequency. Excellent sensor reversibility indicates that the positive frequency shift was not caused by the loss of sensing film mass.

A positive frequency shift was observed with a thick ( $> 81$  nm) DLPC film based QCM sensor on exposure to both saturated ethanol vapour and methanol vapour. Figure 8-5 and 8-6 illustrate the normalised response curve of a QCM sensor coated with  $32.2 \mu\text{g}$  DLPC film (corresponding to about  $392.8$  nm) exposed to ethanol vapour (15,200 ppm-76,200 ppm) and methanol vapour (33,000 ppm-164,800 ppm) at different concentrations, separately.

As the ethanol and methanol vapour concentration increases, the sensor response first becomes more negative, and then less negative until finally it increases positively. The

slopes in Figures 8-5 and 8-6 also indicate that the frequency changes were influenced by the mass loading and viscosity decreasing.

Membrane viscosity is a key parameter in cell physiology, cell function and cell signalling [193]. Alcohols are excellent well explored examples which have the effect of membrane viscosity-reducing [198-199]. As mentioned section 7.1.3, the short-chain alcohols localise predominantly at the hydrophilic head group region of the phospholipid bilayer. Their location disturbs the natural microstructure of the lipid membrane leading to the decrease in membranes' viscosity [193]. Kanazawa and Gordon [200] derived an equation which expresses the frequency shift ( $\Delta f$ ) of the quartz crystal in contact with a fluid and the decay length of the shear wave ( $\delta$ ).

$$\Delta f = -f_0^{3/2}(\eta_L \rho_L / \pi \mu_Q \rho_Q)^{1/2} \quad (8-2)$$

$$\delta = (\eta_L / \pi f_0 \rho_L)^{1/2} \quad (8-3)$$

$f_0$  = oscillation frequency of the bare crystal [Hz]

$\eta_L$  = absolute viscosity of the liquid [N·sec/m<sup>2</sup>]

$\rho_L$  = absolute density of the liquid [kg/m<sup>3</sup>]

$\mu_Q$  = elastic modulus of the quartz [g/cm/sec]

$\rho_Q$  = density of the quartz [kg/m<sup>3</sup>]

$\delta$  = decay length of the shear wave [cm]

In general, the dissolution of the alcohol vapours in lipid membranes can induce changes in many physical properties of the lipid membranes. As mentioned section 7.1.3, there are two factors that are relevant to our present discussion, which are the change in viscosity and the change of mass upon addition of organic solvents. Under these experimental conditions, the viscosity of the DLPC lipid greatly decreased after the addition of low-viscosity solvents, whereas the mass of the membranes was significantly increased with the addition of the solvents. Figures 8-5 and 8-6 indicate that for both ethanol and methanol vapours, at relatively low concentration, the effect on the frequency of increasing mass is more dominant than that of viscosity, while at relatively high vapour concentration, the reduction of viscosity is more pronounced than that of mass. This phenomenon results in the frequency shift starting as negative and increase of positive with an increasing as the vapour concentration.

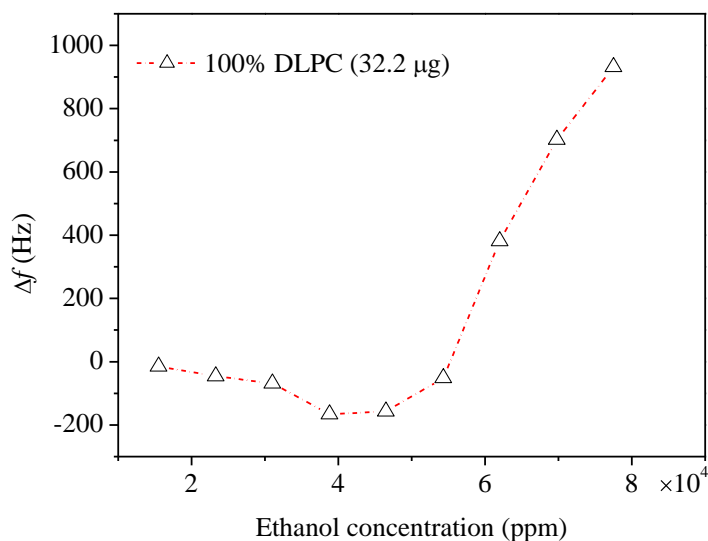


Figure 8-5 DLPC (32.2  $\mu\text{g}$ ) sensor response on exposure to different concentrations of ethanol vapour.

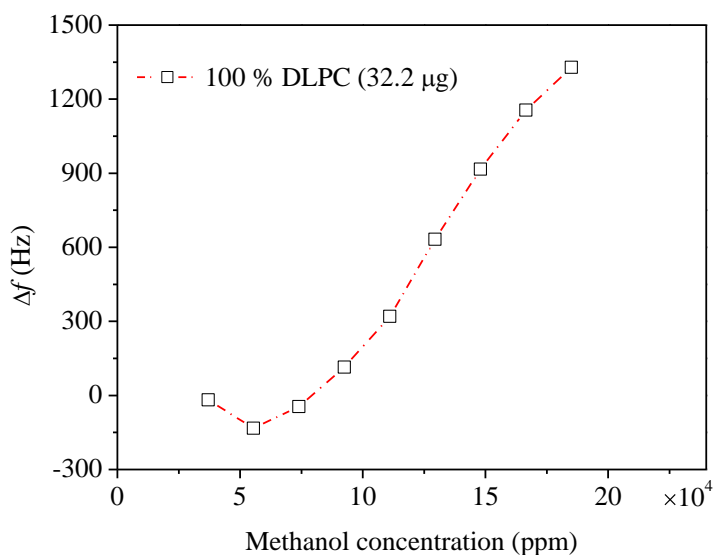


Figure 8-6 DLPC (32.2  $\mu\text{g}$ ) sensor response on exposure to different concentrations of methanol vapour.

On first inspection, the relatively large positive frequency shifts observed with DLPC make the lipid a good candidate for highly sensitive QCM vapour sensors. However, the origin of the strong dependence of viscosity on the solvent concentration in DLPC lipids is not completely understood [71]. Furthermore, under different experimental condition (temperature, humidity etc.), the complex influences may make the frequency shift quantitative analysis more complex. As a result, the maximum concentration considered for a single phase DLPC vapour sensor is 10 mg/ml, below which the fabricated sensor

will give a stable negative frequency response on exposure to high concentration alcohol vapours.

*(b) DSPC sensor*

The typical real-time response of thick DSPC film coated QCM vapour sensors (film structure referred to in Figure 5-4 b) to ethanol vapour under atmosphere at 25 °C (i.e. 76,200 ppm) is shown in Figure 8-7. The concentration used for spin coating is also indicated in this figure along with the corresponding coated DSPC mass.

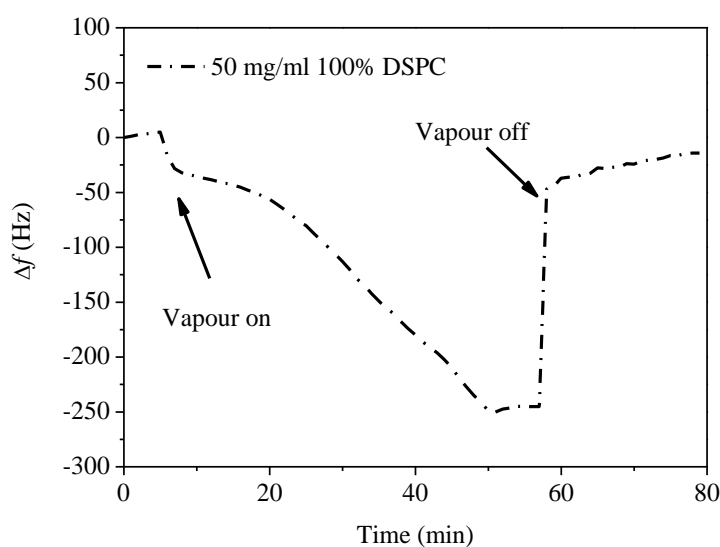


Figure 8-7 Typical response of DSPC films sense with 76,200 ppm ethanol vapour.

Good reversibility for adsorption of vapour in the coated materials and slow response was observed in Figure 8-7, which also confirmed that the thick DSPC film coated sensor could be easily regenerated and used for continuous measurement. For the DSPC sensor, the time between the alcohol vapours being turned on and the frequency change reaching 80% of the maximum was about 30 minutes on average. Clearly, the DSPC vapour sensor exhibited a fairly slow response, negligible baseline drift and good albeit slow reversibility for alcohol vapour. The single phase DSPC vapour sensor response time to alcohol is much longer compared to DLPC sensor and DSPC/DLPC sensor. As discussed in section 7.3.1, the DSPC single phase sensor took the longest time to reach frequency equilibrium and the longest time to recover which was caused by the gel phase of the lipids. Furthermore, the time for frequency equilibrium became even longer as the films coated on the crystal became thicker.

If we do not consider the unit thickness response of the DSPC vapour sensors, a high concentration DSPC gas sensor showed the relatively largest and most negative stable response towards ethanol vapours which indicates that the DSPC lipid would be a good candidate for high sensitivity vapour sensor fabrication, with the only disadvantage being the slow response.

The slow adsorption may be caused by the property of the DSPC lipid itself. At room temperature, the DSPC membrane is in a gel phase. The slow response is attributed to the slower diffusion rate of vapour molecules in the relatively high viscosity of DSPC lipids compared to DLPC lipids. As a result, changing the lipid phase would be an option to increase the response speed and this will be further discussed later.

### 8.3 Sensor sensitivity improvement by increase film thickness

#### 8.3.1 Sample sensor preparation

Based on the optimisation of the film thickness results, the improvement of five sensor (5 mg/ml) sensitivity was achieved by increasing the concentration used for spin coating. Five sensors were prepared for comparing with the five sensors discussed in chapter 7 (refer to Table 7-1). The sensors were fabricated by the spin coating method at 1500 rpm for 60 seconds. The comparison of old and new sensors are shown in Table 8-2. A similar amount of lipids was coated on the five different sensors.

Table 8-2 Sensor list

Sensor 1		Sensor 2		Sensor 3		Sensor 4		Sensor 5		n/a	
mg/ml	$\alpha$	mg/ml	$\alpha$								
5	0	5	0.25	5	0.5	5	0.75	5	1	n/a	n/a
Sensor 1*		Sensor 2*		Sensor 3*		Sensor 4*		Sensor 5*		Sensor 6	
mg/ml	$\alpha$	mg/ml	$\alpha$								
10	0	10	0.25	10	0.5	10	0.75	10	1	50	1

The improved sensitivity sensors are sensor 1\*, sensor 2\*, sensor 3\*, sensor 4\* and sensor 5\*. The only difference between the two groups of sensors is the concentration used for spin coating. The frequency shift caused by spin coating is shown and compared with

the five sensors prepared before in Table 8-3. The sensor weighing results indicate that the coated molecule number of the sensors in group 2 has almost doubled.

Table 8-3 Comparison of sensor fabrication

Sensor group	Sensor number	Weight fraction $\alpha$ of DSPC	Mole percentage of DSPC (%)	Concentration (mg/ml)	Experimental $\Delta f^{***}$ (Hz)	Mass ( $\mu\text{g}/\text{cm}^2/\text{Hz}$ )
1	Sensor 1	0	0	5	-167.5	3.0
	Sensor 2	0.25	21	5	-182.4	3.2
	Sensor 3	0.5	44	5	-193.3	3.4
	Sensor 4	0.75	70	5	-198.3	3.5
	Sensor 5	1	100	5	-211.1	3.7
2	Sensor 1*	0	0	10	-420.0	7.4
	Sensor 2*	0.25	21	10	-449.0	7.9
	Sensor 3*	0.5	44	10	-452.6	8.0
	Sensor 4*	0.75	70	10	-460.0	8.1
	Sensor 5*	1	100	10	-493.5	8.7
3	Sensor 6	1	100	50	-2345.0	41.4

### 8.3.2 Evaluation of sensors' sensitivity and selectivity

Figures 8-8 and 8-9 illustrate the normalised response curve of a QCM sensor (film structures refer to Figure 5-4) coated with five different sample lipids exposed to ethanol vapour (14,300 ppm-68,600 ppm) and methanol vapour (9,800 ppm-164,800 ppm) at different concentrations, separately. The comparison of the five sensors' sensitivities and LODs to ethanol and methanol are shown in Tables 8-4 and 8-5, respectively. The real time response patterns of sensors (refer to Table 8-3, group 2 and 3) on exposure to step changes in the concentration of vapours are similar as those (refer to Figure 7-4 c) of sensors prepared from 5 mg/ml lipid solution (refer to Table 7-1). The only difference is the response intensity.

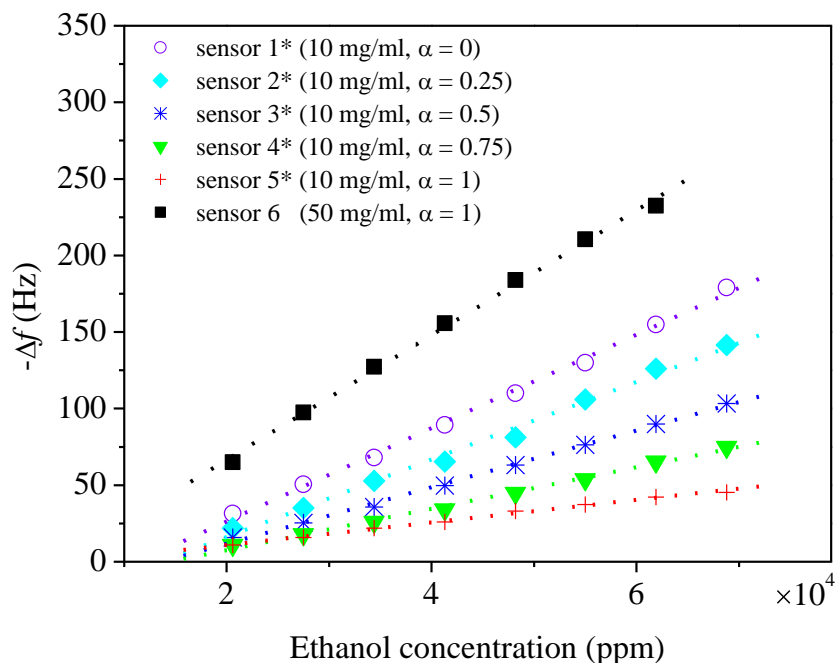


Figure 8-8 Regression curves of sensor 1\*, sensor 2\*, sensor 3\*, sensor 4\*, and sensor 5\* to ethanol, where  $\alpha$  is the weight fraction of DSPC.

Table 8-4 Sensitivity improvement of sensor response to ethanol by increased concentration

Sensor number	Concentration used for coating (mg/ml)	Weight fraction of DSPC ( $\alpha$ )	Ethanol		
			Sensitivity	Limit of Detection	Correlation coefficient
			S (Hz/ppm)	LOD (ppm)	R <sup>2</sup>
1	5	0	$14.4 \times 10^{-4}$	1900	0.99
1*	10	0	$30.5 \times 10^{-4}$	900	0.99
2	5	0.25	$11.2 \times 10^{-4}$	2400	0.99
2*	10	0.25	$25.4 \times 10^{-4}$	1100	0.99
3	5	0.5	$8.5 \times 10^{-4}$	3200	0.99
3*	10	.5	$18.5 \times 10^{-4}$	1500	0.99
4	5	0.75	$5.8 \times 10^{-4}$	4700	0.98
4*	10	0.75	$13.5 \times 10^{-4}$	2100	0.99
5	5	1	$3.7 \times 10^{-4}$	7300	0.99
5*	10	1	$7.4 \times 10^{-4}$	3700	0.99
6	50	1	$33.6 \times 10^{-4}$	1100	0.99

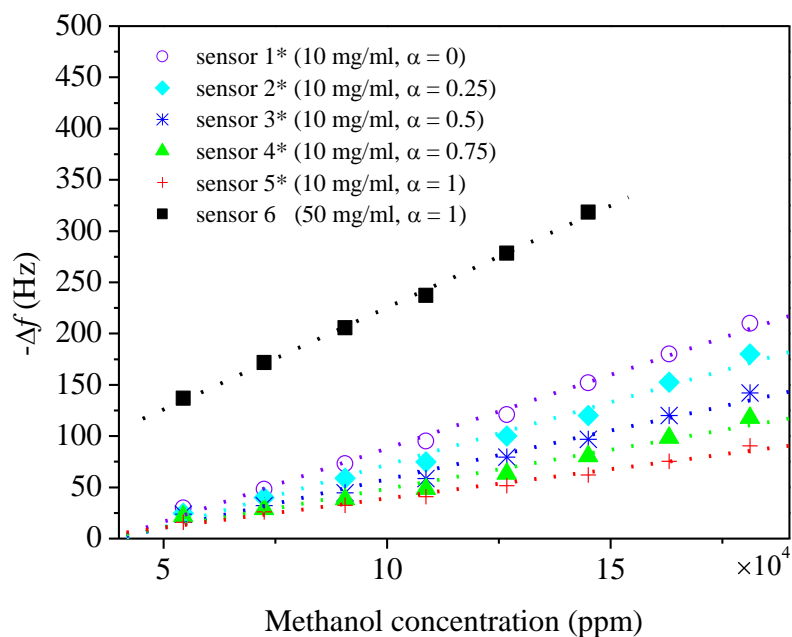


Figure 8-9 Regression curves of sensor 1\*, sensor 2\*, sensor 3\*, sensor 4\*, and sensor 5\* to methanol, where  $\alpha$  is the weight fraction of DSPC.

Table 8-5 Sensitivity improvement of sensor response to methanol by increased concentration

Sensor number	Concentration used for coating (mg/ml)	Weight fraction of DSPC ( $\alpha$ )	Methanol		
			Sensitivity	Limit of Detection	Correlation coefficient
			S (Hz/ppm)	LOD (ppm)	R <sup>2</sup>
1	5	0	$3.9 \times 10^{-4}$	6900	0.99
1*	10	0	$14.3 \times 10^{-4}$	1900	0.99
2	5	0.25	$3.4 \times 10^{-4}$	7800	0.99
2*	10	0.25	$12.2 \times 10^{-4}$	2200	0.99
3	5	0.5	$3.0 \times 10^{-4}$	8800	0.99
3*	10	0.5	$9.5 \times 10^{-4}$	2800	0.98
4	5	0.75	$2.3 \times 10^{-4}$	11400	0.98
4*	10	0.75	$7.6 \times 10^{-4}$	3500	0.97
5	5	1	$2.0 \times 10^{-4}$	13400	0.99
5*	10	1	$5.7 \times 10^{-4}$	4700	0.98
6	50	1	$19.9 \times 10^{-4}$	1300	0.99

The responses of five different sensors to 8 different concentrations of each vapour were investigated and recorded as shown in Figures 8-8 and 8-9, respectively. The same response behaviour was found in group 2 and 1 sensors (sensor details refer to Table 8-3), in that as the ethanol and methanol vapour concentration increased, all five QCM vapour sensors' frequency responses were also increased. The slopes in Figures 8-8 and 8-9

indicate that the frequency changes are directly proportional to the vapour concentration for the working range. It appears that the frequency changes increase gradually with increasing vapour concentrations and an approximately linear relationship can be obtained at different concentrations for the five different sample lipid coated vapour sensors.

The sensors' sensing behaviours in group 2 were the same as the behaviours in group 1. The fluid DLPC coated sensor exhibits better performance with ethanol and methanol vapour detection than other sensors by showing a higher sensitivity to both vapours. Whereas, for the DSPC coated sensor, the frequency changes did not increase significantly with the increase of the test vapour concentration. By increasing the weight fraction of the gel phase DSPC, the sensor sensitivity to both ethanol and methanol decreases.

In Tables 8-4 and 8-5, the sensitivity changes of the lipid based sensors are also compared. If the same lipid (mixed lipids) coated QCM sensors in groups 1 and 2 were compared, almost all five sensors' sensitivities have doubled. These results were expected as the average coated lipid amount has doubled. As discussed before, the sensing mechanism for sensors in both groups 1 and 2 is the simple mass increase leading to a frequency decrease. The five sensors' sensitivities to ethanol and methanol vapours were improved by increasing the sensing film thickness. It also appears that the sensitivities are decreasing and the LODs are increasing with an increase in the weight fraction of DSPC in the DSPC/DLPC film.

It should be noticed that, another high concentration DSPC sensor (group 3, sensor 6, 50 mg/ml spin coated 100% DSPC) was also prepared. Figures 8-8, 8-9 and Tables 8-4, 8-5 clearly indicate that the highest sensitivity to ethanol and methanol vapours was obtained in sensor 6 whereas the responses of all the sensors to hydrophobic vapours were still not so clear, which will not be discussed here. The sensitivity of sensor 6 to ethanol is about 11 times higher than the sensor 5 (the lowest sensitivity sensor to ethanol from group 1); and the sensitivity of sensor 6 to methanol is about 14 times higher than the sensor 5 (the lowest sensitivity sensor to methanol from group 1). The high sensitivity of sensor 6 to ethanol and methanol make sensor 6 a good candidate for preparing a high sensitivity sensor. There are still some shortcomings which need to be optimised.

There are several ways to increase the fluidity of the lipid bilayers which may, in turn, lead to potential increase of the adsorption speed and the maximum amount of the vapours into the sensing films, discussed later.

### 8.3.3 Sensor selectivity: effect of acyl chain length on sensor response

The selectivity of the lipid-based sensor to four chemical vapours is shown in Figure 8-10. It indicates the affinity of five high concentration spin coated sensors in group 2 and 50 mg/ml DSPC spin coated sensor 6 in group 3 response to various saturated vapours at 25 °C.

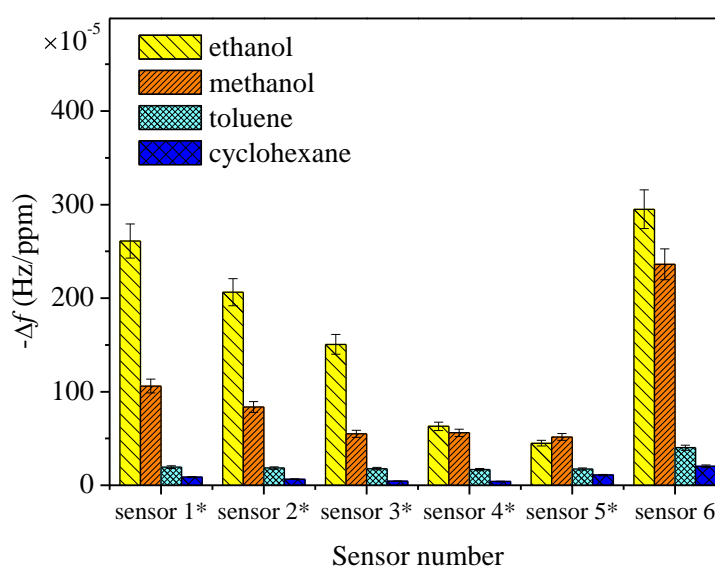


Figure 8-10 Six sensors affinity comparison to 4 different vapours.

There are four responses collected for each sensor-vapour combination. Each sensor-vapour combination was repeated at least three times within the same day. The sensor responses shown in Figure 8-10 were averaged, yielding the values for particular sensors (i.e.  $\Delta f_n = \Delta f/C$  is the nominal frequency shift, where C is the concentration of the vapour). The standard error was a measure of the sensor-vapour combination response repeatability (i.e. about 7% for all sensors).

Similar to the low concentration coated QCM sensor, each high concentration lipid coated QCM sensor had a quite different response for the same vapour. It is still clear that all of the lipid sensors showed a strong response intensity to hydrophilic alcohols.

However, all lipid sensors showed a relatively weak response intensity to hydrophobic toluene and cyclohexane. It is still hard to compare the response of different sensors to hydrophobic vapours because the frequency shifts are too small. Whereas, the response of different sensors to hydrophilic vapours is very clear: when 68,600 ppm ethanol or 145,000 ppm methanol was measured, the signal intensity for each sensor decreased in sequence of sensor 6 > sensor 1\* > sensor 2\* > sensor 3\* > sensor 4\* > sensor 5\*. The reason for the response intensity difference was caused by the phase difference of the lipid sensing films. The sensing films were prepared from liquid phase DLPC and gel phase DSPC. The “stronger” barrier provided by gel phase DSPC will make it difficult for the hydrophilic vapour molecules to reach the layers under the films. As a result, the more gel phase DSPC contained in the sensing film, the weaker response intensity and slower adsorption speed will be.

Overall, the optimisation of sensing film thickness results showed a high concentration DSPC solution coated QCM sensor is a good candidate for preparing a highly sensitive vapour sensor. Efforts will be made to modify the film to optimise flexibility and improve the response speed.

#### **8.4 Optimization of DSPC/cholesterol film flexibility**

There are several ways to increase the fluidity of the lipid bilayers which may lead to potential increase of the adsorption speed and the maximum amount of the vapours diffusing into the sensing films. One such way could be to add cholesterol to DSPC lipid. It has been reported that, the fluidity of the lipid bilayers of the cells is known to be affected by cholesterol located in the cell membrane, as well as by the chemical properties of the lipid acyl chains [201]. A second approach is to add a small amount of fluid DLPC, which will be further discussed later.

##### **8.4.1 Effect of cholesterol on DSPC sensor response**

The mixed lipid solutions were prepared so that the volume ratio of 50 mg/ml cholesterol to 50 mg/ml DSPC was in the range 0-40% and 100%. Quartz crystals were modified by these solutions separately by the spin coating method. Ethanol, methanol, toluene and cyclohexane were used as analytes. All the DSPC/cholesterol sensors prepared

are shown in Table 8-6. Figure 8-11 shows the effect of cholesterol on the adsorption of alcohols (Figure 8-11 a) and hydrophobic vapours (Figure 8-11 b) by the membranes.

Table 8-6 DSPC/cholesterol sensor list

Sensor number	volume fraction to DSPC( $\alpha^*$ and $\alpha^{**}$ )		Concentration (mg/ml)		
	Cholesterol ( $\alpha^*$ )	DLPC ( $\alpha^{**}$ )	Cholesterol	DLPC	DSPC
6	0	0	50	n/a	50
7	0.05	0	50	n/a	50
8	0.1	0	50	n/a	50
9	0.15	0	50	n/a	50
10	0.2	0	50	n/a	50
11	0.3	0	50	n/a	50
12	0.4	0	50	n/a	50
13	1	0	50	n/a	50

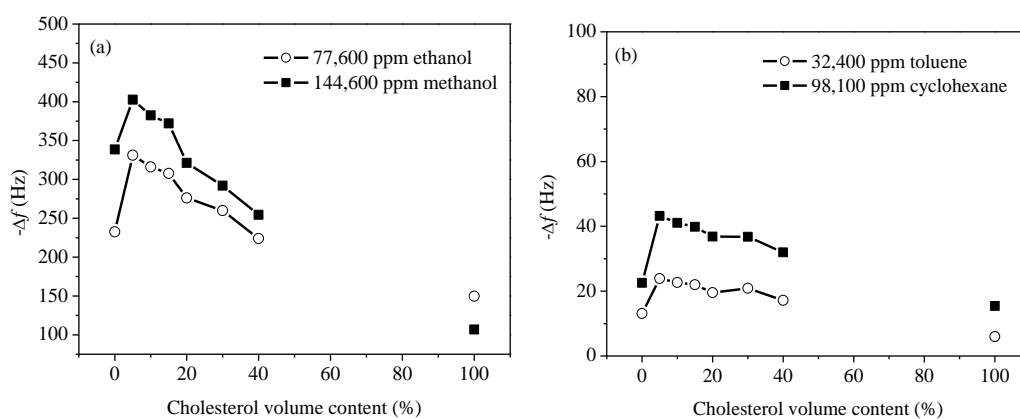


Figure 8-11 Correlation between cholesterol content and frequency shift.

The frequency shifts increased with the cholesterol concentration. The maximum response was obtained when 5%-10% cholesterol to DSPC solution was co-immobilised on quartz crystals, whereas the frequency shift decreased when more than 10% cholesterol was used. This suggests that a moderate concentration of cholesterol is useful to improve the sensitivity of the sensors. The 100% 50 mg/ml cholesterol was also prepared for comparison. Different response intensity and response type to DSPC/cholesterol and DSPC based sensors were investigated while the same concentration vapours were exposed. The sensor response was quite reproducible with a relative standard deviation of 7%.

#### 8.4.2 Typical response of cholesterol and cholesterol modified DSPC sensors

Typical real-time responses of cholesterol sensor to ethanol, vapour under atmosphere at 25 °C are shown in Figure 8-12.

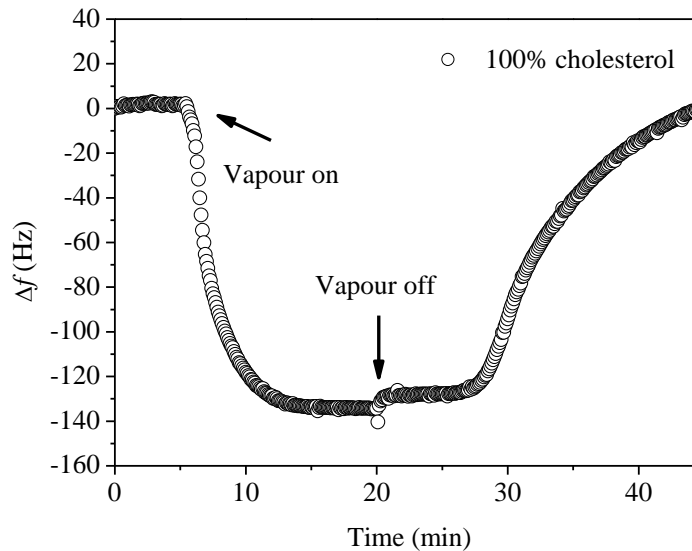


Figure 8-12 Typical response of 100% 50 mg/ml cholesterol to 68,600 ppm ethanol vapour.

In this figure, the starting and stopping of the vapour flow occurred at 5 minutes and 20 minutes, respectively. The cholesterol sensor responded to the presented vapour. Similar to the DLPC sensor, the frequency altered almost immediately with exposure to the vapour, and rapidly reached a steady value. The difference is that after the test chamber was purged with nitrogen gas, the vapour desorption process did not take place immediately, which means a delayed recovery was observed. The delayed recovery time and the total frequency recovery time for cholesterol sensor were about 8 minutes and 20 minutes, respectively. It is obvious that the response curves show excellent reversibility, and negligible baseline drift, but with a slow recovery.

Typical real-time responses of the DSPC/cholesterol sensor to ethanol vapour under atmosphere at 25 °C are shown in Figure 8-13, where the flow was started and stopped at 5 minutes and 10 minutes, respectively. The DSPC/cholesterol sensor clearly responded to the vapour. The frequency altered almost immediately with the vapour adsorption process, and rapidly reached a steady value. After the test chamber was purged with nitrogen gas, the vapour desorption took place almost immediately. It is obvious that these transient responses curves show excellent reversibility, negligible baseline drift and rapid adsorption, and recovery can be seen in Figure 8-13. The real time response patterns of sensors (referred to in Table 8-6) on exposure to step changes in the concentration of

vapours are similar as those (refer to Figure 7-4 c) of sensors prepared from 5 mg/ml lipid solution (referred to in Table 7-1). The only difference is the response intensity.

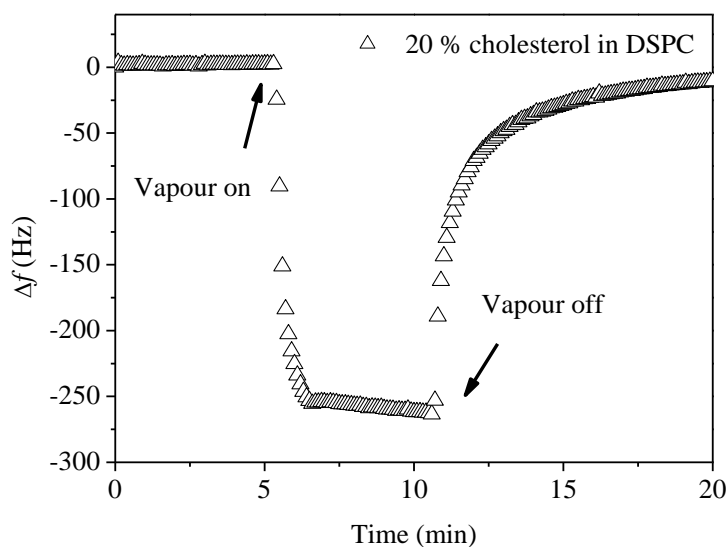


Figure 8-13 Typical response of 20% 50 mg/ml DSPC/cholesterol to 68,600 ppm ethanol vapour.

This typical response is not only different from the typical response of the single phase high concentration DSPC vapour sensor, but also different from the typical response of the single phase high concentration cholesterol solution prepared vapour sensor. It is very clear, with the addition of cholesterol, that the rate of ethanol vapour adsorption into DSPC has been improved. On the other hand, the sensor also recovered quickly after vapour flow was switched off. It is a completely different response behaviour when compared to the single phase cholesterol sensor. This indicates it is not a simple combination of two responses. Therefore, the DSPC/cholesterol mixed film property is different from single phase DSPC lipid and single phase cholesterol. This will be further discussed in section 8.5.3.

### 8.4.3 Evaluation of sensors sensitivity and selectivity

The comparison of seven sensors' sensitivity and limit of detection to ethanol, methanol, cyclohexane and toluene are shown in tables 8-7, 8-8, 8-9 and 8-10 (film structure referred to in Figure 8-20), respectively.

Table 8-7 Sensitivity improvement to ethanol by adding cholesterol

Sensor number	Concentration used for coating (mg/ml)	volume fraction to DSPC		Ethanol		
		Cholesterol ( $\alpha^*$ )	DLPC ( $\alpha^{**}$ )	Sensitivity (Hz/ppm)	Limit of Detection (ppm)	Correlation coefficient $R^2$
7	50	0.05	0	$46.7 \times 10^{-4}$	600	0.99
8	50	0.1	0	$47.0 \times 10^{-4}$	600	0.99
9	50	0.15	0	$44.3 \times 10^{-4}$	600	0.99
10	50	0.2	0	$41.7 \times 10^{-4}$	900	0.99
11	50	0.3	0	$36.1 \times 10^{-4}$	700	0.99
12	50	0.4	0	$33.6 \times 10^{-4}$	1100	0.99

Table 8-8 Sensitivity improvement to methanol by adding cholesterol

Sensor number	Concentration used for coating (mg/ml)	volume fraction of Cholesterol to DSPC		Methanol		
		Cholesterol ( $\alpha^*$ )	DLPC ( $\alpha^{**}$ )	Sensitivity (Hz/ppm)	Limit of Detection (ppm)	Correlation coefficient $R^2$
7	50	0.05	0	$28.3 \times 10^{-4}$	1000	0.99
8	50	0.1	0	$26.9 \times 10^{-4}$	1000	0.99
9	50	0.15	0	$13.5 \times 10^{-4}$	1000	0.99
10	50	0.2	0	$22.3 \times 10^{-4}$	1000	0.99
11	50	0.3	0	$19.7 \times 10^{-4}$	1400	0.99
12	50	0.4	0	$18.3 \times 10^{-4}$	1500	0.99

Table 8-9 Sensitivity improvement to cyclohexane by adding cholesterol

Sensor number	Concentration used for coating (mg/ml)	volume fraction of Cholesterol to DSPC		Cyclohexane		
		Cholesterol ( $\alpha^*$ )	DLPC ( $\alpha^{**}$ )	Sensitivity (Hz/ppm)	Limit of Detection (ppm)	Correlation coefficient $R^2$
7	50	0.05	0	$6.5 \times 10^{-4}$	4100	0.98
8	50	0.1	0	$6.5 \times 10^{-4}$	4200	0.98
9	50	0.15	0	$5.9 \times 10^{-4}$	4400	0.98
10	50	0.2	0	$4.0 \times 10^{-4}$	6600	0.95
11	50	0.3	0	$4.5 \times 10^{-4}$	5800	0.99
12	50	0.4	0	$3.1 \times 10^{-4}$	8600	0.99

Table 8-10 Sensitivity improvement to toluene by adding cholesterol

Sensor number	Concentration used for coating (mg/ml)	volume fraction of Cholesterol to DSPC		Toluene		
		Cholesterol ( $\alpha^*$ )	DLPC ( $\alpha^{**}$ )	Sensitivity (Hz/ppm)	Limit of Detection (ppm)	Correlation coefficient $R^2$
6	50	0	0	$2.9 \times 10^{-4}$	9000	0.99
7	50	0.05	0	$8.6 \times 10^{-4}$	3100	0.99
8	50	0.1	0	$7.9 \times 10^{-4}$	3300	0.99
9	50	0.15	0	$6.3 \times 10^{-4}$	4200	0.99
10	50	0.2	0	$4.9 \times 10^{-4}$	5400	0.99
11	50	0.3	0	$7.0 \times 10^{-4}$	3800	0.94
12	50	0.4	0	$5.0 \times 10^{-4}$	5300	0.95

By inspecting the tables, one can observe that the sensitivity improvement is similar for ethanol, methanol, cyclohexane and toluene. It is clear that for all the vapours it might be generalised that the DSPC/cholesterol sensor sensitivities increased with the cholesterol concentration. The best sensitivity to the four vapours was obtained when 5-10% cholesterol to DSPC solution was co-immobilised on quartz crystals. The results showed the apparent effect of cholesterol on the adsorption of alcohols and hydrophobic vapours by the membranes. The sensitivity to hydrophilic alcohol has been raised about one third when comparing the best responding sensor (sensor 7 and sensor 8) to the DSPC sensor. The sensitivity of sensor 8 to hydrophobic vapours is about 2 to 3 times greater than sensor 8. The length of the DSPC hydrophobic chain influences directly the membrane permeability and consequently the sorption properties. The sensitivities of DSPC sensors to four vapours were improved by adding a 10% volume ratio of cholesterol. The proposed mechanism of sensitivity improvement will be further discussed in section 8.5.3.

### 8.5 Optimization of DSPC/DLPC/cholesterol film flexibility

As discussed in chapter 5, the mixed DSPC/DLPC lipids film structure is relatively unstable compared to DSPC. Normally in a real plasma membrane various phospholipids exist at the same time. There is a hint of a flip-flop process in DSPC molecules with the existence of DLPC. Mixed DLPC/DSPC sensors have already been investigated. The sensor response of the mixed DLPC and DSPC lipids is a combination of single lipid coated sensors. It seems that even if there is a flip-flop of DSPC lipid molecules happening in the mixed multilayer membrane structure, it does not efficiently improve the response intensity of the vapour sensors on exposure to different vapours. The cholesterol was added to the high concentration solution of mixed lipids. The three mixed lipids were spin coated

on the gold electrode of the quartz crystal and investigated. The results were discussed in this section.

Considering the complex mechanism of DLPC lipid based sensor in this working concentration range, the total concentration of DLPC lipid used for preparing vapour sensors should be controlled within 10 mg/ml. If the mixed lipids are considered, then the total concentration of DLPC in the lipid mixture should be controlled. Besides, the maximum response was obtained when 5%-10% cholesterol to DSPC solution was co-immobilised on quartz crystals. As result, 10% DLPC and 10% cholesterol to DSPC solution was considered for three spin coated lipids. The DSPC/cholesterol sensors and DLPC/DSPC/cholesterol sensor prepared are shown in Table 8-11.

Table 8-11 Cholesterol Sensor list

Sensor number	volume fraction to DSPC( $\alpha^*$ and $\alpha^{**}$ )		Concentration (mg/ml)		
	Cholesterol ( $\alpha^*$ )	DLPC ( $\alpha^{**}$ )	Cholesterol	DLPC	DSPC
6	0	0	50	n/a	50
8	0.1	0	50	n/a	50
14	0	0.1	n/a	50	50
15	0.1	0.1	50	50	50

Based on the optimisation of the film thickness results and optimisation the volume ratio of 50 mg/ml cholesterol to 50 mg/ml DSPC, the improvement of sensor (50 mg/ml) sensitivity is achieved by adding 10% DLPC and 10% cholesterol to 50 mg/ml DSPC solution used for spin coating. All sensors prepared for vapour sensing during this period of study were listed in Table 8-11. All sensors were fabricated by the spin coating method at 1500 rpm for 60 seconds. The sensor spin coating with three mixed lipids was still quite reproducible with a relative standard deviation of 8%.

### 8.5.1 Effect of cholesterol on DSPC/DLPC sensor response

The results showed the apparent effect of cholesterol and cholesterol/DLPC on the adsorption of alcohols (Figure 8-14 a) and hydrophobic vapours (Figure 8-14 b) by the membranes.

The frequency shifts increased with an increase in the cholesterol concentration. Maximum response was obtained when 5-10% cholesterol to DSPC solution was co-immobilised on quartz crystals, whereas the frequency shift decreased when more than 10% cholesterol was used. As a comparison, the red marks indicate the response intensity

of the DSPC/DLPC/cholesterol sensor to four different vapours. This suggests that a moderate concentration of cholesterol is useful to improve the sensitivity of the DLPC/DSPC sensors, and improved significantly the sensor response intensity to hydrophobic vapours compared to DSPC/cholesterol sensors. The sensor response was quite reproducible with a relative standard deviation of 7%.

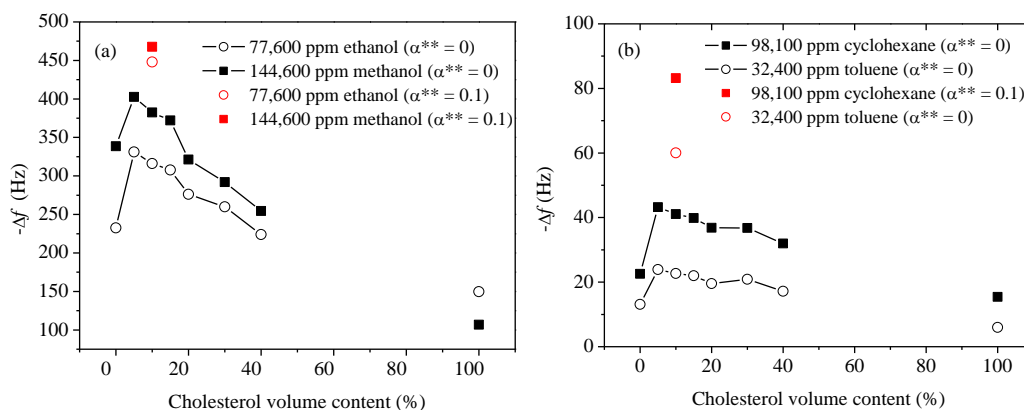


Figure 8-14 Correlation between cholesterol content and frequency shift, where  $\alpha^{**}$  is the volume fraction of DLPC to DSPC solution.

### 8.5.2 Sensor sensitivity and selectivity

The responses of sensors (film structures referred to in Figure 8-20) to different concentrations of ethanol vapour (15,200 ppm-68,600 ppm), methanol vapour (33,000 ppm-148,400 ppm), toluene vapour (14,500 ppm-32,600 ppm) and cyclohexane vapour (50,200 ppm-125,700 ppm) were investigated and recorded as shown in Figure 8-15 (a-d), respectively. The real time response patterns of sensor (referred to in Table 8-11) on exposure to step changes in the concentration of vapours are similar as those (refer to Figure 7-4 c) of sensors prepared from 5 mg/ml lipid solution (referred to in Table 7-1). The only difference is the response intensity.

As ethanol, methanol, toluene and cyclohexane vapour concentration increased, all vapour sensors' frequency responses also increased. The slopes in Figure 8-15 indicate that the frequency changes are directly proportional to the vapour concentration for the working range. It appears that the frequency changes increased gradually with increasing vapour concentrations, and approximately linear relationships can be obtained at different concentrations for the three mixed lipid coated vapour sensors. Not surprisingly, sensor 6

and sensor 15 showed a similar sensitivity as only 10% of DLPC was added to DSPC. Furthermore, sensor 15 showed a more rapid response compared to sensor 6 on exposure to different vapours (figures not shown here). It is also quite clear the sensitivities of sensor 15 to ethanol and methanol are different and in good agreement with previous findings. Furthermore, sensor 15 clearly responded to toluene and cyclohexane vapours.

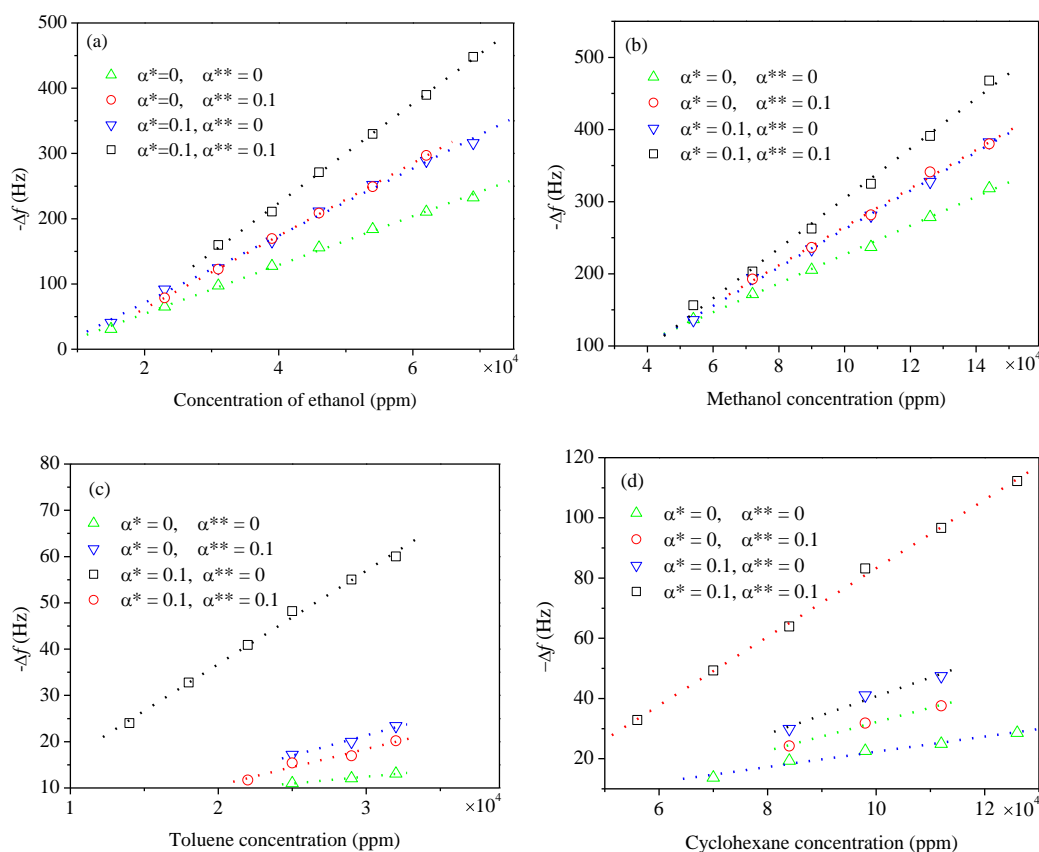


Figure 8-15 Regression curves of sensors to (a) ethanol (b) methanol (c) toluene and (d) cyclohexane. Sensor details refer to table 8-11, where  $\alpha^*$  is the volume percentage of cholesterol in sample solution and  $\alpha^{**}$  is the volume percentage of DLPC in sample solution.

The comparison of sensitivities and LODs of sensors listed in Table 8-11 to ethanol, methanol, toluene and cyclohexane vapour are shown in Table 8-12. The sensing behaviour of sensor 15 is the same as the behaviours of other DSPC/cholesterol sensors. Generally, the sensitivity of sensor 15 to all vapours is increased. It should be noticed that, the sensitivity of sensor 15 to hydrophobic vapours is significantly increased. Figure 8-16 illustrates the sensitivities of 9 types of sensors to four vapours. Figure 8-16 and Table 8-12 clearly indicate that the highest sensitivity to four vapours was obtained in sensor 15. The

sensitivity of sensor 15 to ethanol is about 0.5 times higher than the sensor 8; and the sensitivity of sensor 15 to hydrophobic vapours is about 2 times higher than the sensor 8.

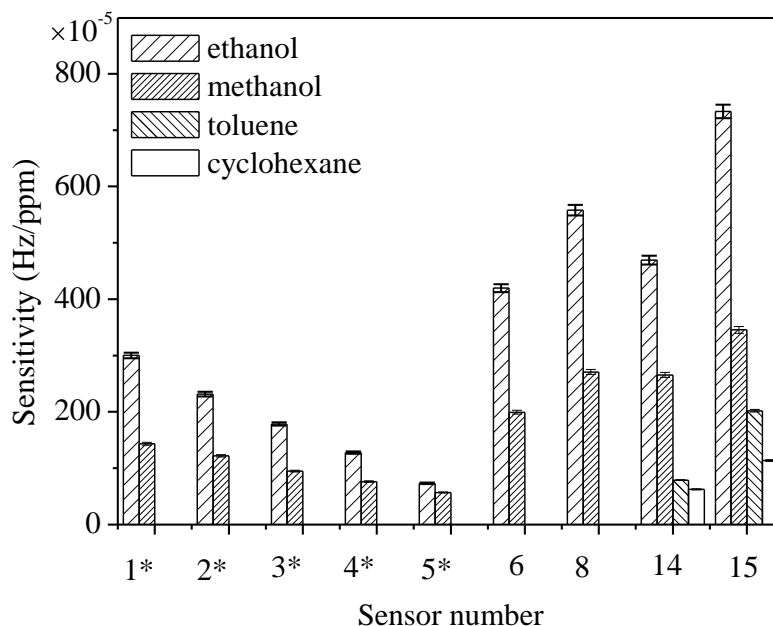


Figure 8-16 Sensitivities of 9 types of sensors to four vapours. Sensor details refer to Table 9-2, 8-3 and 8-11. The standard error was a measure of the sensor-to-sensor response reproducibility.

The results showed the apparent effect of cholesterol on the adsorption of alcohols and hydrophobic vapours by the mixed lipid membranes. The three lipids mixed sensor exhibited the best performance on all four vapours, that is, excellent reversibility, a negligible baseline drift and a rapid response. In this case, it is very clear the performance and response pattern of the mixed lipid based sensor is not a combined performance of the two lipids. This suggests that a moderate concentration of cholesterol together with the fluid lipid is more useful at improving the sensitivity of the sensors. The proposed sensing mechanism of sensitivity improvement will be further discussed in the coming section.

The selectivity of lipid based sensors with/without cholesterol and DLPC/cholesterol to four chemical vapours is shown in Figure 8-17. It indicates the sensitivity improvement is making progress from five high concentrations spin coated DSPC/DLPC sensor in group 2, DSPC/cholesterol sensors in group 3 and 50 mg/ml DLPC/DSPC/cholesterol spin coated sensor 15 responses to various saturated vapours at 25 °C.

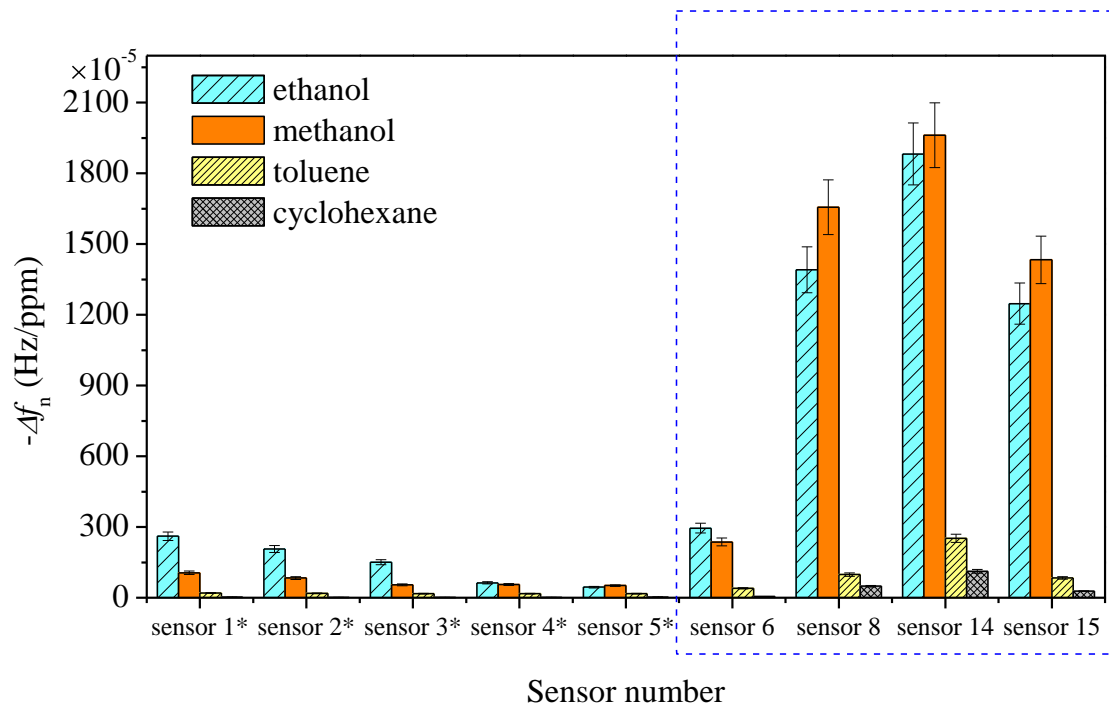


Figure 8-17 Response intensities of nine types of sensors to different vapours. The sensor number details can be found in Table 8-2 and Table 8-11. The four sensors in the blue rectangle are the sensitivity improved sensors compared to figure 7-9.

Table 8-12 Sensitivity improvement to ethanol, methanol, toluene and cyclohexane vapours

Sensor number	Coating concentration (mg/ml)	volume fraction to DSPC		Ethanol		Methanol		Cyclohexane		Toluene	
				Sensitivity	LOD	Sensitivity	LOD	Sensitivity	LOD	Sensitivity	LOD
		Cholesterol ( $\alpha^*$ )	DLPC ( $\alpha^{**}$ )	S (Hz/ppm)	(ppm)						
<b>6</b>	50	0	0	$33.6 \times 10^{-4}$	1100	$20.0 \times 10^{-4}$	1300	n/a	n/a	n/a	n/a
<b>8</b>	50	0.1	0	$47.0 \times 10^{-4}$	600	$26.6 \times 10^{-4}$	1000	$6.3 \times 10^{-4}$	4200	$7.9 \times 10^{-4}$	3300
<b>14</b>	50	0	0.1	$55.8 \times 10^{-4}$	500	$27.1 \times 10^{-4}$	1000	n/a	n/a	n/a	n/a
<b>15</b>	50	0.1	0.1	$73.3 \times 10^{-4}$	400	$34.6 \times 10^{-4}$	800	$11.4 \times 10^{-4}$	2300	$20.2 \times 10^{-4}$	1300

As mentioned in section 7.1.2, there are four responses collected for each sensor-vapour combination. Each sensor-vapour combination was repeated at least three times within the same day. The sensor responses shown in Figure 8-17 were nominal averaged yielding the values for particular sensors. The standard error was a measure of the sensor-vapour combination response repeatability (i.e. about 7% for all sensors).

It is still very clear that all lipid sensors showed strong response intensities to hydrophilic alcohols, while all lipid sensors showed relatively weak response intensities to hydrophobic toluene and cyclohexane. It is still possible to compare the response of sensors 15 intensity to other sensors intensities to hydrophobic vapours. While the sensor 15 response intensity to hydrophilic and hydrophobic vapours showed the best performance, the possible mechanism of sensitivity improvement will be discussed in the coming section.

### 8.5.3 Mechanism of sensitivity improvement and interaction mechanism

The lipid bilayer of many cell membranes is not only composed exclusively of phospholipids, but also contains cholesterol and glycolipids. Cholesterol is abundant in cell membranes and maintains the integrity of the cell membrane. Molecule for molecule, cholesterol can make up a different percentage of the cell membrane. For example, eucaryotic plasma membranes contain especially large amounts of cholesterol (up to one molecule for every mixture of different phospholipids molecule), while bacterial plasma membranes are often composed of one main type of phospholipid and contain no cholesterol [202].

The chemical structure of cholesterol is shown in Figure 8-18. Since it is smaller and weighs less than other molecules in the cell membrane, it makes up a lesser proportion of the cell membranes' mass.

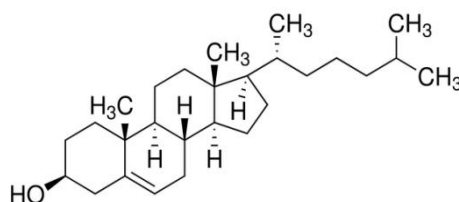


Figure 8-18 The chemical structure of cholesterol.

As shown in Figure 8-18, cholesterol is an amphipathic molecule which contains a hydrophilic and a hydrophobic portion. Cholesterol's hydroxyl (OH) group aligns with the phosphate heads of the phospholipids. The model structures of mixed DSPC and cholesterol are shown in Figure 8-19.

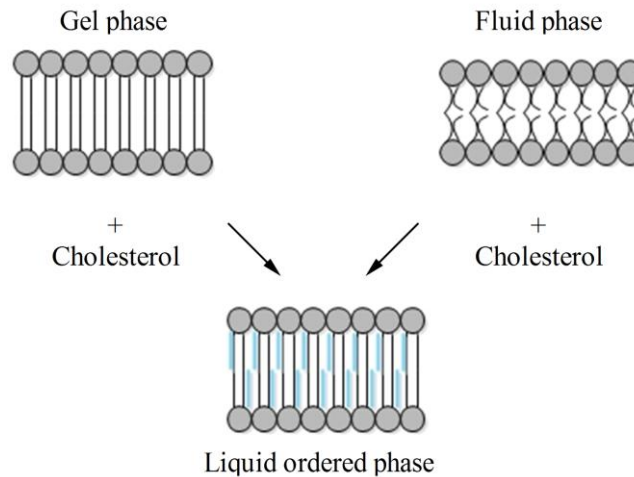


Figure 8-19 Phase behaviour of phospholipids, including gel, fluid and liquid ordered phases formed via mixing with cholesterol.

Cholesterol molecules orient themselves in the bilayer with their hydroxyl groups close to the polar head groups of the phospholipid molecules. Because of the way cholesterol is shaped, their rigid, platelike steroid rings (the four hydrocarbon rings in between the hydroxyl group and the hydrocarbon "tail") interact with and partly immobilise those regions of the hydrocarbon chains closest to the polar head groups [202].

The cholesterol molecules enhance the permeability-barrier properties of the lipid bilayer. In the plasma membranes, cholesterol helps to slightly immobilise the outer surface of the membrane and make it less soluble to very small water-soluble molecules that could otherwise pass through more easily by decreasing the mobility of the first few  $\text{CH}_2$  groups of the hydrocarbon chains of the phospholipid molecules. It also makes the lipid bilayer less deformable in this region and thereby decreases the permeability of the bilayer to small water-soluble molecules. In addition, it also helps maintain the fluidity of cell membranes by preventing the hydrocarbon chains from coming together and crystallising, it inhibits possible phase transitions. Without cholesterol, cell membranes would be too fluid, not firm enough, and too permeable to some molecules. Cholesterol adds firmness and integrity to the plasma membrane and prevents it from becoming overly

fluid, it also helps maintain its fluidity. Cholesterol helps separate the phospholipids so that the fatty acid chains cannot come together and crystallise. Therefore, cholesterol helps prevent extremes-whether too fluid, or too firm-in the consistency of the cell membrane.

Under working conditions, DSPC as a type of phospholipid can, for well orientated multilayer membrane structures, be piles of bilayers similar to plasma membranes. Under dry conditions, the main role of the cholesterol is to prevent the crystallisation of the acyl chains by fitting in between them. The higher the cholesterol content in a lipid bilayer, the more fluid the bilayer becomes. Cholesterol inserted in the membrane plays a role of a “spacer”, which tends to reduce the hydrophobic interaction between acyl chains of the lipids. Moreover, cholesterol itself has little influence on the hydrophilic groups of the lipids [17]. Thus, by incorporating cholesterol into the lipid solution and allowing the films' fluidity to be enhanced, an effective adsorption of chemical vapours is expected. Cholesterol makes the lipid layer more fluid which could be why the cholesterol helps to increase the sensor response intensity by adding it to DSPC lipids. Furthermore, it was also noticed that the frequency shift of the sensors decreased when more than 10-15% cholesterol was used (see Figure 8-11). This might be because cholesterol may fail to maintain the membrane structure when cholesterol in DSPC was more than 10-15%, resulting in a poor sensor response.

In order to confirm the assumption, lipids with cholesterol (see Table 8-13) were spin coated on a template stripped gold substrate; the surface structures of the film with cholesterol were studied by AFM and compared with the surface structures of the film without cholesterol. Spin coated phospholipid multilayer films were imaged using an AFM setup in tapping mode at room temperature (25 °C), using standard silicon nitride cantilevers with nominal force constant of 40 N/m and a resonance frequency in air of 300 kHz for all scans [152]. The tapping mode amplitude set point was 1 mV with a scan rate at 1 Hz. In this experiment, three sample solutions were prepared in chloroform. The mixed solutions were prepared so that the volume ratio of 0.5 mg/ml cholesterol to 0.5 mg/ml phospholipid (either DSPC or DLPC) was 10%. The details of three sample solutions were listed in Table 8-13 including three sample solutions prepared before (refer to section 5.2.1 b). All samples were spin coated on a template stripped gold substrate for 1 minute at 1500 rpm.

Table 8-13 Details of cholesterol/phospholipid sample solutions and phospholipid solution prepared for spin coating, where  $\alpha$  is the volume ratio of DSPC solution,  $\alpha^*$  is the volume ratio of cholesterol and  $\alpha^{**}$  is the volume ratio of DLPC solution.

Measurement number	Sample details			Concentration (mg/ml)			Measurement temperature (°C)
	$\alpha$	$\alpha^*$	$\alpha^{**}$	Cholesterol	DLPC	DSPC	
1	0	0	1	0.5	0.5	0.5	25 °C
2	0.5	0	0.5	0.5	0.5	0.5	25 °C
3	1	0	0	0.5	0.5	0.5	25 °C
4	0	0.1	0.9	0.5	0.5	0.5	25 °C
5	0.45	0.1	0.45	0.5	0.5	0.5	25 °C
6	0.9	0.1	0	0.5	0.5	0.5	25 °C

Figure 8-20 illustrates the AFM topography images and corresponding phase images of DLPC, DLPC/DSPC and DSPC films with and without cholesterol in air. All sample details refer to Table 8-13.

With cholesterol, membrane lipids are expected to be in a liquid ordered phase. The phase is formed by the interaction of phospholipid with cholesterol. In a moderate tapping mode AFM image, the phase shift of the harder part becomes larger than that of the softer part; the difference in the stiffness of each area can also be deduced from the phase angle of the phase image. Considering the two different lipids, a hard gel-phase DSPC and soft fluid DLPC will have different a stiffness and viscoelastic response to the cantilever motion which will give rise to a contrast difference in the phase image [172-173].

Comparing the phase images of the same content films with and without cholesterol; it is quite clear that with cholesterol, the phase of the films has been changed significantly. The onset is clearly seen where the sample films without cholesterol (Figure 8-20 d, e and f) exhibit a few dark areas corresponding to the different domain phases which exist within the same sample. In the DLPC/DSPC sample films (Figure 8-20 b and e), a hard gel phase DSPC domain and soft fluid phase DLPC domain will have a different stiffness and viscoelastic response to the cantilever motion which will give rise to a contrast difference in the phase image, i.e. the phase separation [172-173]. However, in DLPC or DSPC single phase sample films (Figure 8-20 d and f), the phase separation was exist, corresponding to areas where the complex multilayers were allocated. It was reported that this is characterised by a high degree of acyl chain order associated with lateral diffusion properties close to those determined for lipids in the liquid-crystalline or fluid phase where the acyl chains are kinked and loosely packed [203]. The measured AFM phase shift may be caused by the aggregation of lipid molecules in the thick multilayers resulting in

mechanically tougher films compared to the upper films. Recrystallisation in some part of the films could also be one reason for the phase shift. These may be reflected in a lower sensitivity of the sensor. The phase images corresponding to films contain cholesterol (Figure 8-20 j, k and l) contain basically no contrast except at the boundary lines of the lipid layers. The absence of contrast in extended areas is a clear sign that the substrate is completely covered by lipids with continuous single phase films, and none of the holes in the lipid layers extend all the way to the substrate. Comparing the rms amplitude of the phase images of the same phospholipid content, all phase images of the films with cholesterol have lower rms amplitudes than without. Furthermore, comparing the surface structure of the same phospholipid content film with and without cholesterol, it is quite clear that films with cholesterol are more likely to show connection of larger domains, resulting in the formation of a lipid-ordered network. Overall, the phase shift is reduced; the phospholipid gel and fluid phase changes were caused by cholesterol, resulting in the formation of continuous single liquid ordered phase films has been confirmed.

Film structure stability was investigated during a one hour AFM investigation on the first day of preparation and an extra AFM investigation on the fifth day of preparation. AFM images of the sample film structure changes with respect to time are shown in Figure 8-21 (a-d). Figure 8-21 (a-c) show the structure stability of lipid films with cholesterol while Figure 8-21 (d) shows the structures stability of lipid films without cholesterol. The root mean squared surface roughness of the height and the rms amplitude of phase ( $R_q$ ) of each sample are indicated on the corner of each image.

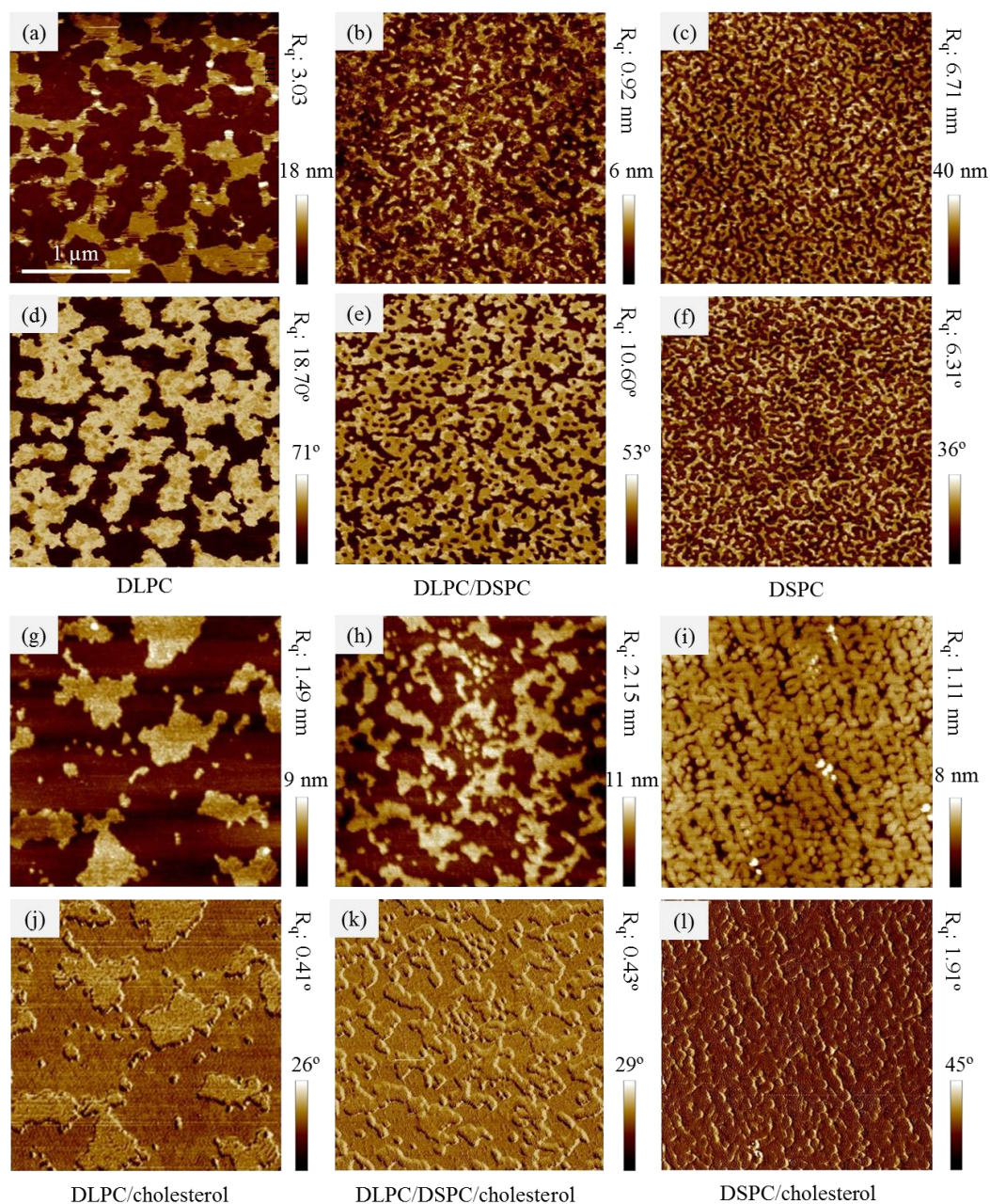


Figure 8-20 Tapping mode AFM imaging of spin coated lipid films in air with all images covering  $2.5 \times 2.5 \mu\text{m}^2$ . Images in parts a, b, c, g, h and i are topographical maps whereas parts d, e, f, j, k and l show the corresponding phase images. Lipid sample for spin-coating were DLPC multilayer films without (a and d, sample 1) and with (g and j, sample 4) cholesterol; DLPC/DSPC multilayer films without (b and e, sample 2) and with (h and k, sample 5) cholesterol; DSPC multilayer films without (c and f, sample 3) and with (i and l, sample 6) cholesterol. The corresponding  $R_q$  and  $z$  scale were indicated on the top right corner of each image. Scale bar:  $1 \mu\text{m}$ . All samples refer to table 8-13.

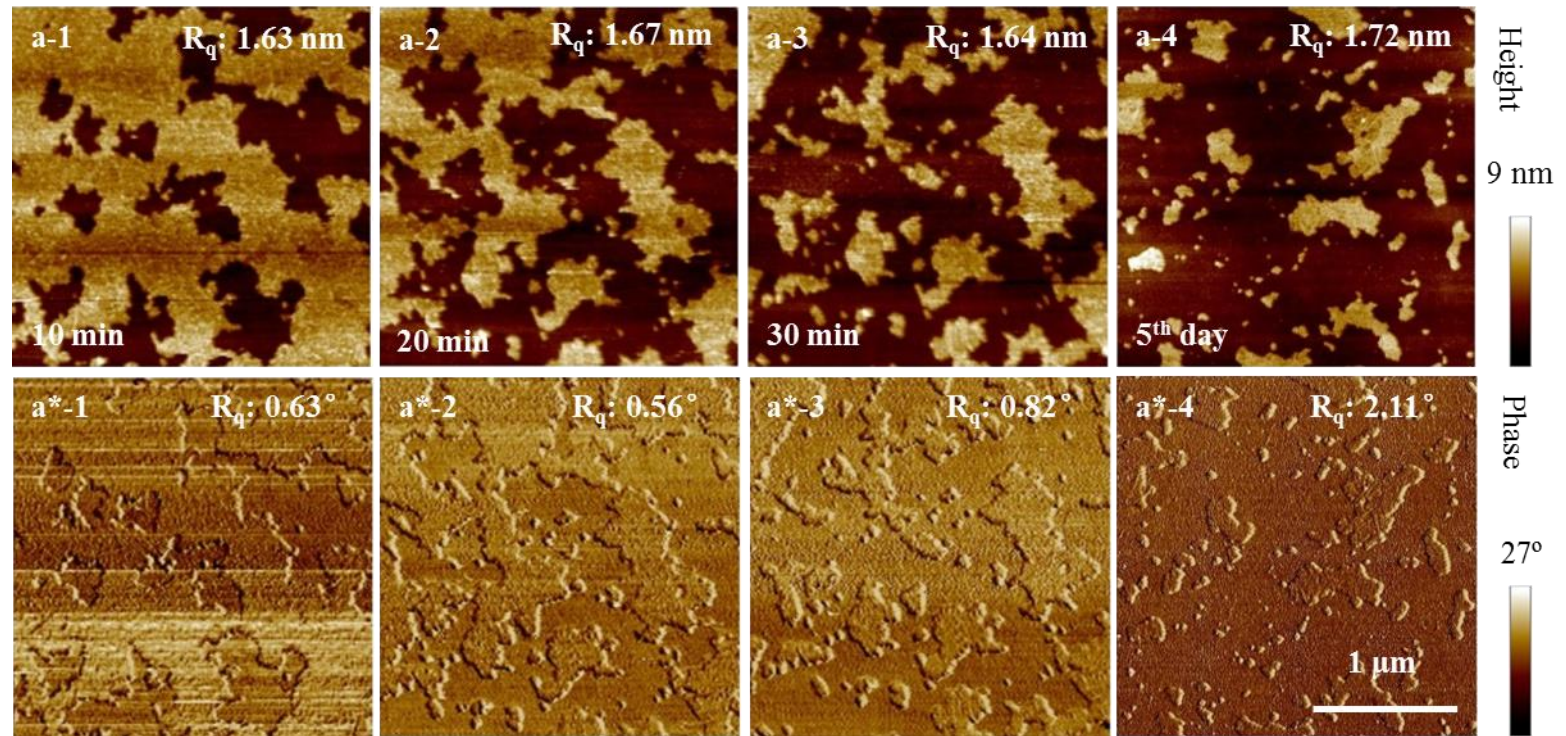


Figure 8-21 (a)  $2.5 \times 2.5 \mu\text{m}^2$  tapping mode AFM images of spin coated lipid films in air. Height images of DLPC films with cholesterol (sample 4 refer to table 8-13) for the continuous first (a-1), the second (a-2), the third scan (a-3) on the first day and the fourth scan (a-4) on the fifth day after preparation. The corresponding  $2.5 \times 2.5 \mu\text{m}^2$  phase images for the first (a\*-1), the second (a\*-2), the third (a\*-3) and the fourth scan (a\*-4). The  $R_q$  is indicated on the top right corner of each image.

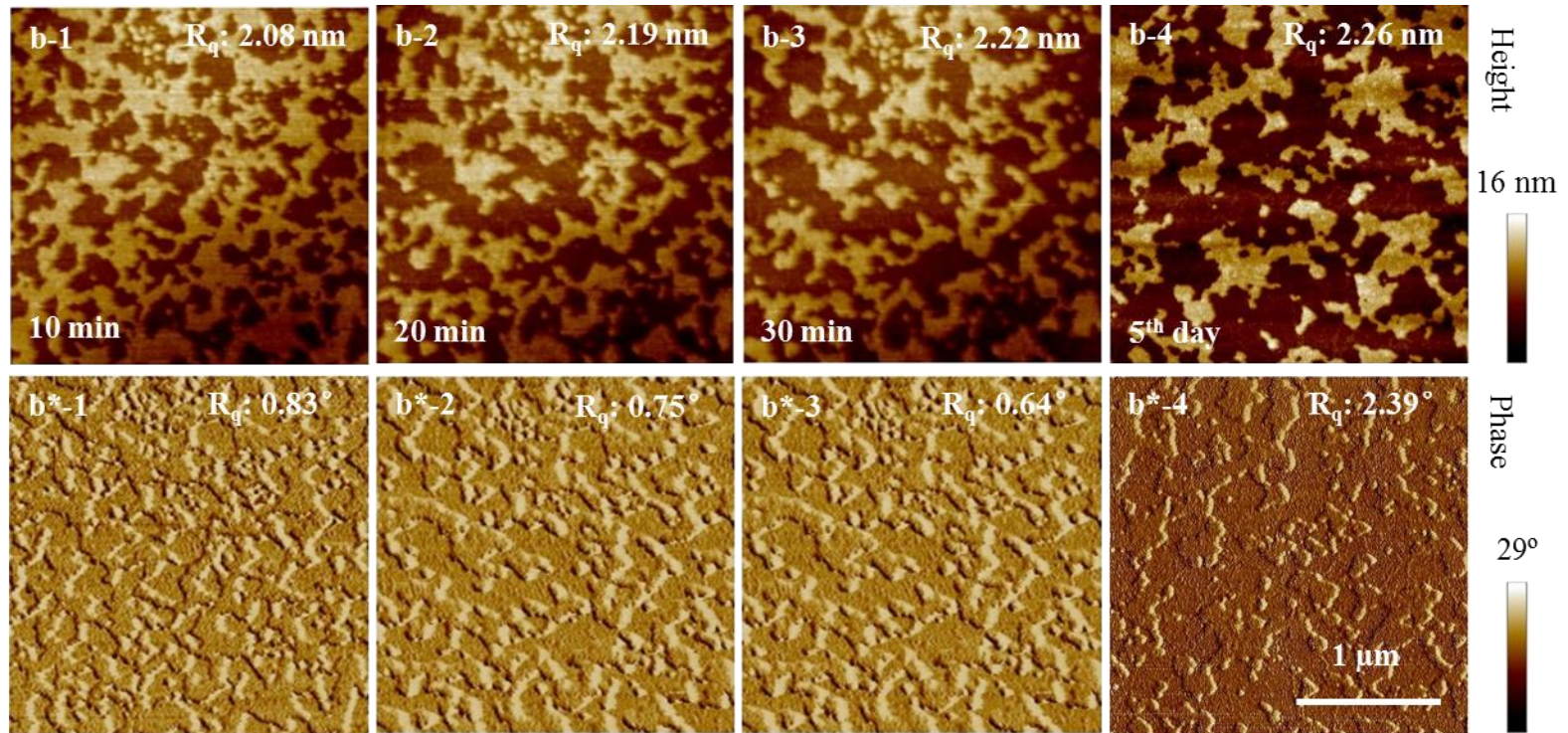


Figure 8-21 (b)  $2.5 \times 2.5 \mu\text{m}^2$  tapping mode AFM images of spin coated lipid films in air. Height images of 1:1 DLPC:DSPC films with cholesterol (sample 5 refer to table 8-13) for the continuous first (b-1), the second (b-2), the third scan (b-3) on the first day and the fourth scan (b-4) on the fifth day after preparation. The corresponding  $2.5 \times 2.5 \mu\text{m}^2$  phase images for the first (b\*-1), the second (b\*-2), the third (b\*-3) and the fourth scan (b\*-4). The  $R_q$  is indicated on the top right corner of each image.

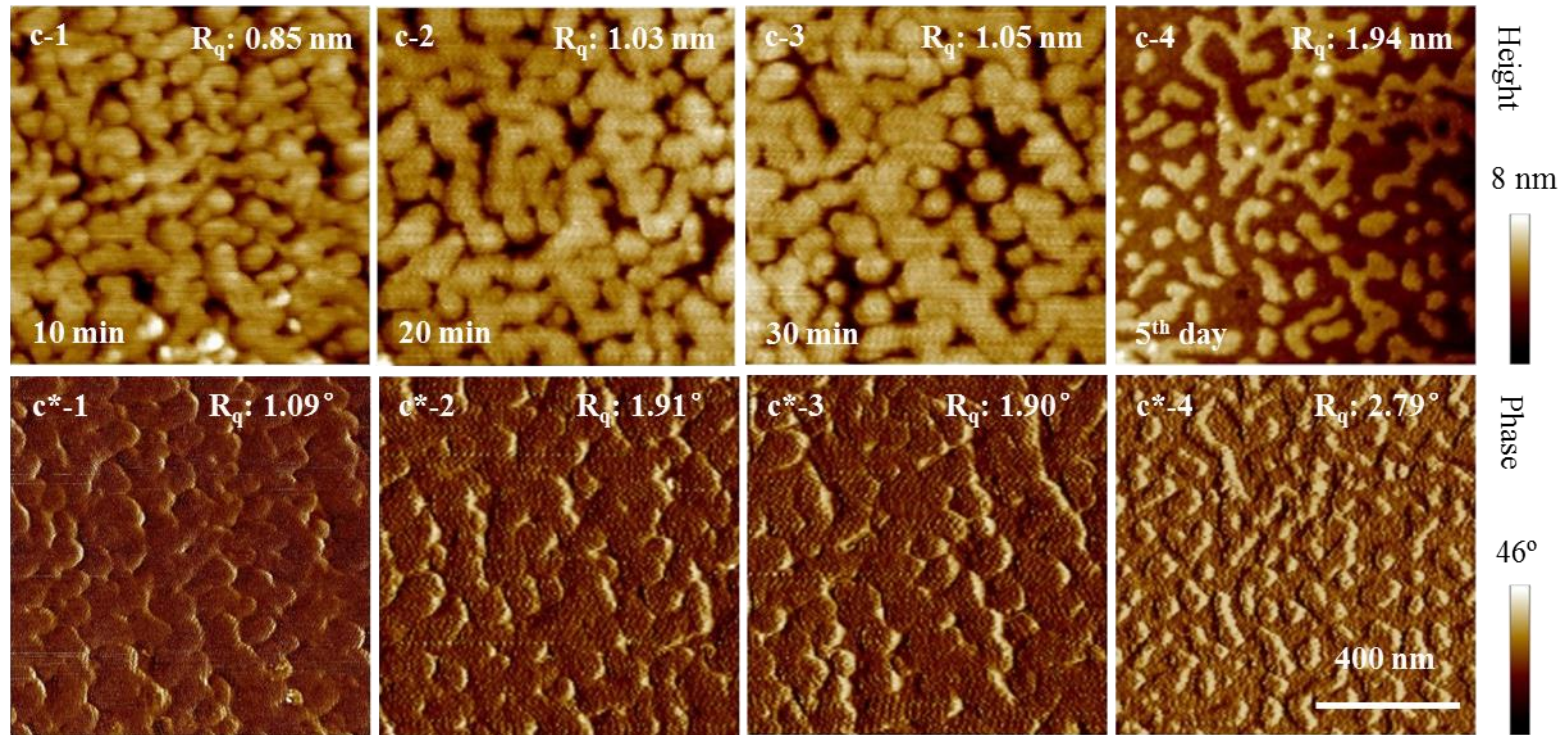


Figure 8-21 (c)  $1 \times 1 \mu\text{m}^2$  tapping mode AFM images of spin coated lipid films in air. Height images of DSPC films with cholesterol (sample 6 refer to table 8-13) for the continuous first (c-1), the second (c-2), the third scan (c-3) on the first day and the fourth scan (c-4) on the fifth day after preparation. The corresponding  $1 \times 1 \mu\text{m}^2$  phase images for the first (c\*-1), the second (c\*-2), the third (c\*-3) and the fourth scan (c\*-4). The  $R_q$  is indicated on the top right corner of each image.

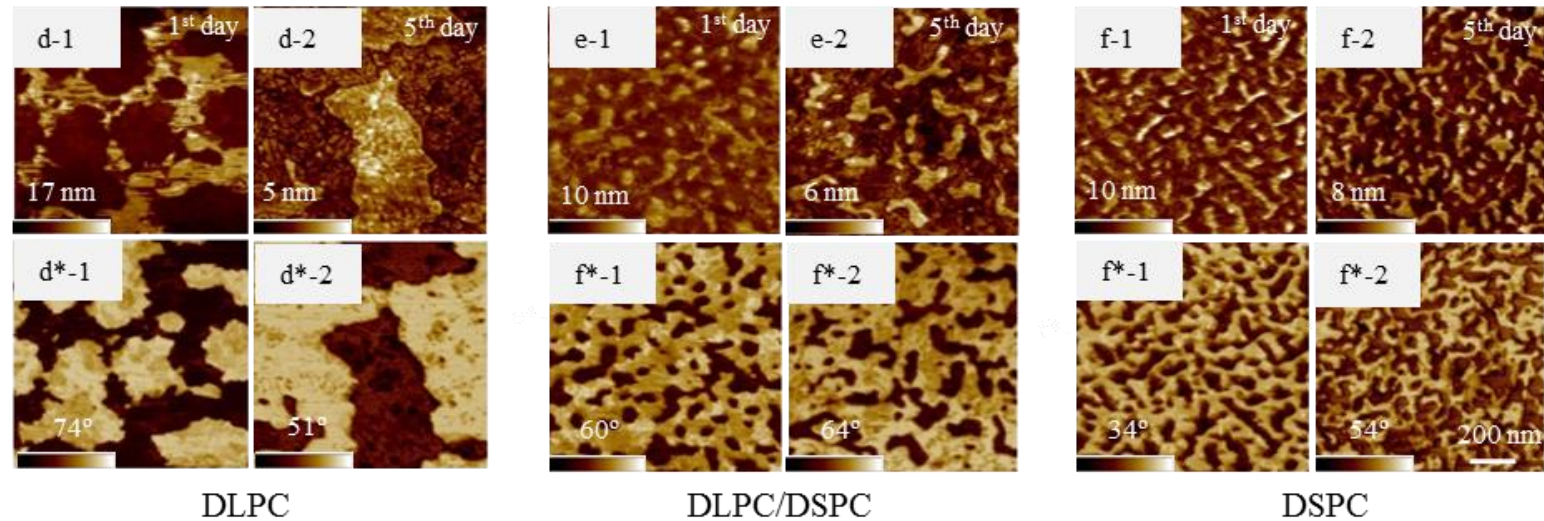


Figure 8-21 (d)  $1 \times 1 \mu\text{m}^2$  tapping mode AFM images of spin coated lipid films without cholesterol in air. Height images of DLPC films (sample 1 refer to table 8-13) scanned on the first (d-1) and fifth day (d-2) of preparation, the corresponding DLPC phase images for the first (d\*-1) and the fifth day (d\*-2). Height images of DSPC/DLPC films (sample 2 refer to table 8-13) scanned on the first (e-1) and the fifth day (e-2) of preparation, the corresponding phase images of DSPC/DLPC phase images for the first (e\*-1) and the fifth day (e\*-2); Height images of DSPC films (sample 3 refer to table 8-13) scanned on the first (f-1) and the fifth day (f-2) of preparation, the corresponding phase images for the first (f\*-1) and the fifth day (f\*-2). The  $R_q$  of each sample is indicated on to top right corner of each image.

As shown in Figure 8-21, all structures of lipid films with and without cholesterol changed with time after preparation. The structures of the DSPC, DSPC/DLPC and DSPC lipid films without cholesterol were relatively stable on the first day of preparation and these structural changes happened during five days' drying. Different from samples without cholesterol, the main changes of films with cholesterol happened during the 3 hours scanning on the first day of preparation. While few structural changes were found for DSPC/cholesterol on the first day during the scanning, the main changes were found when AFM investigation was carried out on the fifth day after preparation. All phase images remain unchanged. Overall, comparing the stability of the film with and without cholesterol, all films with cholesterol were less stable. Changes were also found in DSPC/cholesterol films even though it is slower than that found in DLPC/cholesterol and DLPC/DSPC/cholesterol films. We believe that, with the existence of cholesterol, the film phase changes to increase the films' fluidity. The AFM images were scanned under tapping mode.

Furthermore, we believe that the sensor sensitivity is improved by increasing the films' fluidity due to the effect of DLPC in DSPC/cholesterol mixed solution. During the film mapping, DSPC lipid was noticed to possibly flip-flop from the proximal leaflet to the distal leaflet during the conversion process. Symmetric DSPC domains and complex multilayer mixed lipids were unstable and converted, through the lipid flip-flop to the stable asymmetric distribution. In comparison, single phase DSPC coated film was relatively more stable. We assume that with the existence of DLPC, a possible "route" was opened for DSPC to move. Even though only DSPC and DLPC were mixed, the response intensity of this sensor type is just a combined response of the two lipids as the phase of the two. With cholesterol, the DSPC lipids will form a liquid ordered phase which will significantly increase the fluidity of the film and then result in the increase of the sensor response intensity. In the sensor coated with cholesterol/DSPC/DLPC, the extra DLPC has made this optimisation "route" work more efficiently as the phase of the mixed film has been changed. Thus the response intensity of sensor coated with cholesterol/DSPC/DLPC to four vapours showed the best performance.

Overall, all this evidence from AFM results has confirmed the cholesterol mechanism assumption discussed previously. Cholesterol has changed the phase of the film and made

all the films more fluid which prevents film crystallisation, and enables the sample vapours to reach the underneath of the multilayer films more readily, resulting in the improvement of the sensitivity of the vapour sensors.

## 8.6 Sensors' useful life

The number 15 sensor lifetime when exposed to all four sample vapours was checked. Sensor response loss (%) is also defined as the ratio between the drop in response with time and the first sensor response. Ethanol, methanol, toluene and cyclohexane sample vapours have been analysed by the 1:1:8 Cholesterol: DLPC: DSPC vapour sensors once each 1 month. The response loss (%) of each sensor with time is illustrated in Figure 8-22.

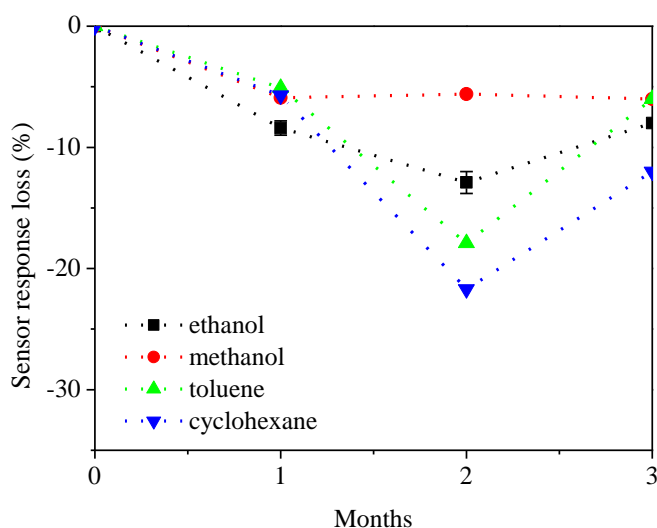


Figure 8-22 Response loss (%) of sensor 15 with time.

Sensor 15 slightly reduced its frequency response with time to all four sample vapours. Four months later, the mean value of QCM response loss for sensor 15 to four sample vapours was 8%, with the highest one for cyclohexane (12%) and the lowest value for methanol (6%). Sensor 15 showed a response loss much lower than the sensors coated with cholesterol free lipid films. This is possibly because cholesterol has also helped the lipid films to keep the same stable phase (i.e. delay the degradation). Results show that the sensors proposed in this study were relatively stable within a 3 month time period.

## 8.7 Oil vapour sensing

Besides the test vapours introduced in the experiments before, there are other vapours which the fabricated sensor could be used to detect. This section will give an application example of oil vapour sensing.

A vacuum pump is a device which has been widely used in engineering, chemistry, physics and biology fields. It removes vapour molecules from a sealed volume in order to create a partial vacuum space.

Mineral oil (vapour created is hydrophobic organic vapour), normally colourless and odourless, is a light mixture of alkanes in the  $C_{15}$  to  $C_{40}$  range from a mineral source. It is essential for vacuum pump to work normally. Because of the working principle of a vacuum pump, during its operation, mineral oil vapour will be generated at the same time. This vapour can diffuse back to the vacuum chamber and deposit inside it, including on any sample in preparation. This is clearly undesirable. It is then important to detect the oil vapour in advance. The real time oil vapour detection by sensor 15 (refer to Table 8-11) is illustrated in Figure 8-23. Sensor 15 was chosen because of its best sensitivity.

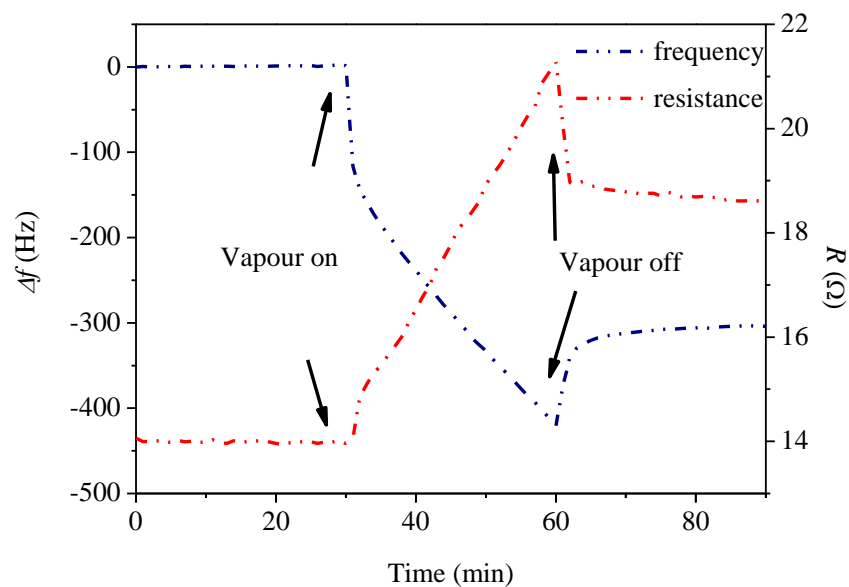


Figure 8-23 Real time detection of oil vapour.

During the operation of the vacuum pump, significant noise will be generated at the same time. Before connect the sensing chamber to the oil vapour pipe, N<sub>2</sub> gas was flowed through the chamber at a constant rate of 100 ml/min. A stable baseline was achieved after more than 3 hours under the constant flow of carrier gas and the noise. After that, the sensor was exposed to oil vapour at the same constant flow rate (i.e. 100 ml/min). From Figure 8-25, it is very clear that sensor 15 responded to oil vapour with a slow adsorption and partial recovery behaviour. No equilibrium has been achieved within 30 minutes exposure. The slow adsorption may be caused by large vapour molecules struggling to break through the physical bonding of the hydrophilic head and even the hydrophobic tails to underneath layers.

The vacuum pump will normally produce fully saturated oil vapour during the working procedure. The evaluation of the exact vapour concentration is not essential because the work aim to detect the existence of oil vapour and protect the pipe from blocking. Furthermore, this response also indicates the sensor for detection of oil vapour is “one use only”. Nevertheless, based on the sensing material used (lipids), quartz crystal used (5 MHz AT cut, £ 25 each) and the fabrication process used (spin coating), the fabrication of cost effective sensor for oil vapour detection has also been demonstrated.

## 8.8 Summary

In this section, the response behaviour of high concentration DLPC and DSPC lipids was studied. DLPC was found to show a fast but positive response on exposure to 25 °C saturated ethanol vapour when films were thicker than 51 nm. This phenomenon was reported to be caused by a decrease in the film viscosity. DSPC showed a slow but stable negative response on exposure to 25 °C saturated ethanol vapour.

Efforts were made to increase the sensor sensitivity and improve the sensor performance. Firstly, five high concentration sensors in group 2 were fabricated and investigated as a comparison of the same type of sensors in group 1. Results showed that increasing the film thickness within a certain range was an effective way to improve the sensor sensitivity. Secondly, the cholesterol was added to 50 mg/ml DSPC lipids to increase the film fluid. DLPC was also considered to be a good way to improve the film flexibility. Finally, it was found that, by incorporating 10% cholesterol and 10% DLPC in volume ratio into the 50 mg/ml DSPC lipid solution and allowing the mixture to form a sensing membrane,

enhanced fluidity can be expected, resulting in effective adsorption of chemical vapours. Cholesterol makes the mixed lipid layer more fluid, which could be why the cholesterol helps to increase the sensor response intensity. These assumptions have been confirmed by AFM studies. The application of sensor 15 to detection of oil vapour has also been demonstrated.

# Chapter 9 Conclusions and future work

This chapter contains conclusions from the whole thesis, including suggestions for future work.

## 9.1 Initial aims

The initial aim of this study was to produce artificial membrane based vapour sensors which incorporate mechanisms present in the sensor system.

This work investigates the development of a vapour sensor that might be useful for environmental protection, healthcare and engineering industry pump oil vapour detection. The sensor was based on a Quartz Crystal Microbalance (QCM), with a sensitivity and selectivity which can be used in the detection volatile organic compounds (VOCs) which may be harmful to people. A summary review of vapour sensing techniques is given, leading to the choice of exploiting a simple, low cost, high-resolution mass sensing technique-QCM to fabricate lipids based vapour sensor. Both hydrophilic and hydrophobic vapours have been introduced in the sensing experiments.

## 9.2 Results

The combination of the technique of QCM with lipid films has produced a successful vapour sensor. Several different lipids type based sensors were used on the same experimental QCM design including 1, 2-dilauroyl-*sn*-glycero-3-phosphocholine (DLPC), 1, 2-dioctadecanoyl-*sn*-glycero-3-phosphocholine (DSPC), cholesterol and their mixtures. A spin coating method was used throughout the sensor fabrication. Though the system was able to discriminate ethanol, methanol, toluene and cyclohexane vapour, the large vapour

concentrations were needed (normally more than 1000 ppm for all vapours). All sensors were exposed to four different vapours, and thus their responses were analysed. Efforts were made to understand the sensing mechanism of the lipid based QCM vapour sensor and the ways to improve the sensitivity of those sensors.

The physical properties of the single and multiphase lipid formed membranes were investigated in great detail. AFM was introduced for topography analysis and QCM was introduced for quantitative analysis of the lipid films.

The AFM studies reveal that the thickness of the DSPC bilayer is 5.8 nm, while the thickness of the inverted DLPC bilayer is 4.3 nm in air under our experimental conditions. The orientation of the lipid multilayer have been presented as the hydrophilic heads of lipids is in contact with the hydrophilic gold electrode surface on quartz crystal with hydrophobic heads residing on top. The lipid multilayer is stacks of well orientated hydrophilic to hydrophilic and hydrophobic to hydrophobic unilamellar layers residing on top. Finally, the surface of the membranes ends with a final mono layer with its hydrophobic alkyl chains on top of the remaining layers. The fluid phase DLPC was relatively more unstable than mixed DSPC/DLPC and single phase DSPC lipids. With the existence of DLPC, gel phase DSPC was able to flip-flop over the leaflet of the lipid membrane. Mixed films were more likely to form a final uniform structure.

The QCM studies reveal that DLPC, DSPC, DLPC/DSPC and DLPC/DSPC/cholesterol mixtures have been successfully coated on the quartz crystals. Sensor construction process repeatability studies on DLPC showed a good repeatable coating process and guaranteed application of a reproducible amount of coating material onto a quartz crystal resonator. The average thickness, density (mass per cubic metre) and total mass were increasing proportionally with the concentration of the coating solution. It was found when a fixed concentration in mg/ml of different lipid solution was used for spin coating, a repeatable amount of lipids could be coated.

The average film thickness is approximately proportional to the coating concentration with a constant of proportionality of 4.3 nm/mM and 7.3 nm/mM for DLPC and DSPC, respectively. The root-mean-square roughness of the dry films is also approximately proportional to concentration. The results from the AFM and QCM trials have led to the

development of a controllable process for the fabrication similar molecule amount of the single and mixed lipid membranes based vapour sensors.

The DLPC, DLPC/DSPC ( $\alpha = 0.25, 0.5$  and  $0.75$ ;  $\alpha$  is the weight fraction of DSPC), DSPC lipid based sensors (10 mg/ml lipid in chloroform, 1500 rpm, 60 seconds) were individually exposed to concentrations of ethanol (15,200 ppm-68,600 ppm), methanol (33,000 ppm-148,400 ppm), toluene (14,500 ppm-32,600 ppm) and cyclohexane (50,200 ppm-125,700 ppm). The response of each film when exposed to ethanol, methanol, toluene and cyclohexane vapours was recorded. The excellent sensor reversibility for adsorption of vapour was found in ethanol, methanol, toluene and cyclohexane vapours. The results show that hydrophilic compounds could be recognised efficiently by lipids having shorter alkyl chains i.e. DLPC or DLPC/DSPC mixtures with more DLPC, whereas lipids with longer alkyl chains showed affinity to more hydrophobic vapours i.e. DSPC or DLPC/DSPC mixtures with more DLPC. Furthermore, lipid sensors showed the higher response intensity to alcohol than to toluene and cyclohexane. From a comparison of the three DLPC/DSPC based vapour sensors, by increasing the weight fraction of DSPC in the coated lipids film, the sensor response intensity and sensitivities to ethanol and methanol decreased.

All the rapid sensor responses, including sensor number 1\*-5\* (refer to Table 8-2), on exposure to vapours can be recognised by a negative frequency shifts. The vapour sensing results indicated that the shift is due to vapour being trapped in the sensing film causing a change in film mass, thickness and viscosity. Under our experimental conditions, the viscosity effect could be ignored. Due to the property of the amphiphilic lipid molecules, the hydrophilic vapours (ethanol and methanol) are more likely to condense in the hydrophilic head of the lipids. By contrast, the hydrophobic vapours (toluene and cyclohexane) are more likely to condense in the hydrophobic tails of the lipids. Spin coated multilayer lipid films were relatively stable, with some degradation in response for vapours after a period of 3 months from fabrication. The response times of each vapour were similar, with turn on and off times of about 5 minutes and full recovery achieved within about 5 minutes. DSPC based sensor showed a longer response time compared to DLPC based sensor to all vapours.

Cholesterol, which not only helps to slightly immobilise the outer surface of the membrane but also makes the lipid bilayer less deformable, was used to improve the lipid based sensors' sensitivities. The vapour sensing results indicated that a moderate concentration of cholesterol is useful to improve the sensitivity of the DLPC/DSPC sensors and even significantly improved the sensor response intensity to hydrophobic vapours compared to DSPC/cholesterol sensors. The best sensing behaviour (that is, excellent reversibility, negligible baseline drift and rapid response) and sensitivity was achieved in sensor 15 (50 mg/ml DLPC/DSPC/cholesterol-1:1:8 in volume ratio). The limit of detection of sensor 15 to ethanol is 400 ppm to ethanol, 800 ppm to methanol, 1300 ppm to toluene and 2300 ppm to cyclohexane, separately. With cholesterol, the DLPC/DSPC lipids formed a liquid ordered phase which significantly increased the fluid of the film and then resulted in the increase of the sensor response intensity. In sensor 15, cholesterol was incorporated into the lipid film. It enhanced the fluidity of the lipid membrane and resulted in improving the adsorption of chemical vapours. Extra amount of DLPC in the DSPC/cholesterol sensor has made the "route" work more efficiently, as the phase of the mixed film has been changed. Thus the response intensity of sensor 15 to four vapours showed the best performance.

### 9.3 Limitations and future work

The fundamental results presented in this work show that lipid films and QCM can be used as a vapour sensor. Though the lipids were responsive to each vapour, the magnitude of response in some cases was small. This problem was partially overcome by modifying the lipid films to optimise the film thickness and improve the film fluidity. The sensor immobility and response mechanism are always under consideration when optimising the film thickness. Moreover, several suggestions related to future development are also discussed. Increasing the fundamental frequency could be an option which may significantly increase the sensitivity of the sensors.

The linear relationship between the mass adsorbed to a QCM device and the resonance frequency discovered by Sauerbrey can be described with the equation shown below

$$\Delta f = -\frac{2nf^2}{\sqrt{\mu_q \times \rho_q}} \frac{\Delta M}{A} \quad (3-4)$$

Thus, it is very clear that, by increasing the fundamental crystal resonance frequency, the frequency shift based on per unit mass load could also increase.

In this work, the vapour sensing mechanism of lipids has been examined in detail yet the true nature of the interaction between the vapour and DLPC/DSPC/cholesterol film is still unknown. Experiments such as AFM force measurement, Raman spectroscopy, could be undertaken to determine the films' mechanical properties.

To discriminate between different vapours and overcome some shortcomings of QCM itself to create a practical device, it is necessary to obtain some extra information from the vapour sensing data. Vapour sensing arrays with a different transducer such as SAW, SPR could be considered. The adsorption of the vapour could be monitored by different transduction methods, such as changes in wavelength, mass, conductivity and so on. The combination of these data could then be used to discriminate between different vapours and may be suitable for different requirements of detection.

---

## References

- [1] K. Toko, *Biomimetic sensor technology*, Cambridge: Cambridge University Press, 2000.
- [2] EH40/2002 occupational exposure limits 2002 : containing the list of maximum exposure limits and occupational exposure standards for use with the Control of Substances Hazardous to Health Regulations 1999, London: Great Britain, Health and Safety Executive, 2002.
- [3] K. Toko, "Odor sensors," in *Biomimetic sensor technology*, Cambridge, Cambridge university press, 2000, p. 92.
- [4] H. Ebato, C. A. Gentry, J. N. Herron, W. Muller, Y. Okahata, H. Ringsdorf and P. A. Suci, "Investigation of Specific Binding of Antifluorescein Antibody and Fab to Fluorescein Lipids in Langmuir-Blodgett Deposited Films Using Quartz-Crystal Microbalance Methodology," *Analytical Chemistry*, vol. 66, no. 10, pp. 1683-1689, 1994.
- [5] E. Sackmann, "Supported membranes: Scientific and practical applications," *Science*, vol. 271, no. 5245, pp. 43-48, 1996.
- [6] R. Tampe, C. Dietrich, S. Gritsch, G. Elender and L. Schmitt, "Biofunctionalized membranes on solid surfaces," in *Nanofabrication and biosystems : integrating materials science, engineering and biology*, Cambridge, Cambridge University press, 1996, pp. 201-221.
- [7] K. Toko, "measurement of taste of foods," in *biomimetic sensortechnology*, Cambridge, Cambridge University Press, 2000, pp. 149-165.
- [8] K. Toko, "Quality control of foods," in *Biomimetic sensor technology*, Cambridge, Cambridge University Press, 2000, pp. 165-172.
- [9] K. Toko, "Suppression of bitterness," in *Biomimetic sensor technology*, Cambridge, Cambridge University Press, 2000, pp. 172-177.
- [10] R. M. White, "A Sensor Classification Scheme," *Ieee Transactions on Ultrasonics Ferroelectrics and Frequency Control*, vol. 34, no. 2, pp. 124-126, 1987.

- 
- [11] B. Wyszynski, P. Somboon and T. Nakamoto, "Pegylated lipids as coatings for QCM odor-sensors," *Sensors and Actuators B-Chemical*, vol. 121, no. 2, pp. 538-544, 2007.
- [12] A. D. Belchi, N. Rothpfeffer, J. Pelegri-Sebastia, J. Chilo, D. G. Rodriguez and T. Sogorb, "Sensor characterization for multisensor odor-discrimination system," *Sensors and Actuators a-Physical*, vol. 191, pp. 68-72, 2012.
- [13] S. Omatu, H. Araki, T. Fujinaka, M. Yoshioka and H. Nakazumi, "Mixed Odor Classification for QCM Sensor Data by Neural Networks," *Distributed Computing and Artificial Intelligence*, vol. 151, pp. 1-8, 2012.
- [14] M. Habara, C. Hong, H. Ikezaki and K. Toko, "Study of sweet-sensitive taste sensor with lipid/polymer membranes," *Rare Metal Materials and Engineering*, vol. 35, pp. 71-74, 2006.
- [15] Y. Tahara, K. Nakashi, K. Ji, A. Ikeda and K. Toko, "Development of a Portable Taste Sensor with a Lipid/Polymer Membrane," *Sensors*, vol. 13, no. 1, pp. 1076-1084, 2013.
- [16] G. H. Hui, S. S. Mi and S. P. Deng, "Sweet and bitter tastants specific detection by the taste cell-based sensor," *Biosensors & Bioelectronics*, vol. 35, no. 1, pp. 429-438, 2012.
- [17] K. Yano, H. Yoshitake, U. T. Bornscheuer, R. D. Schmid, K. Ikebukuro, K. Yokoyama, Y. Masuda and I. Karube, "Development of a chemical vapor sensor using piezoelectric quartz crystals with coated unusual lipids," *Analytica Chimica Acta*, vol. 340, no. 1-3, pp. 41-48, 1997.
- [18] S. Ichinohe, . H. Tanaka and Y. Kanno, "Gas sensing by AT-cut quartz crystal oscillator coated with mixed-lipid film," *Sensors and Actuators B-Chemical*, vol. 123, no. 1, pp. 306-312, 2007.
- [19] X. Liu, S. T. Cheng, H. Liu, S. Hu, D. Q. Zhang and H. S. Ning, "A Survey on Gas Sensing Technology," *Sensors*, vol. 12, no. 7, pp. 9635-9665, 2012.
- [20] C. Hagleitner, D. Lange, A. Hierlemann, O. Brand and H. Baltes, "CMOS single-chip gas detection system comprising capacitive, calorimetric and mass-sensitive microsensors," *Ieee Journal of Solid-State Circuits*, vol. 37, no. 22, pp. 1867-1878, 2002.

- [21] K. Persaud and P. Pelosi, *Sensors and Sensory Systems for an electronic Nose*, vol. 212, P. N. Bartlett and J. W. Gardner, Eds., London and New York: Springer Netherlands, 1992.
- [22] A. G. Shrivastava, R. G. Bavane and A. M. Mahajan, "Electronic nose: A toxic gas sensor by polyaniline thin film conducting polymer," *Proceedings of the 2007 International Workshop on the Physics of Semiconductor Devices: Iwpsd-2007*, pp. 621-623, 2007.
- [23] J. W. Gardner and P. N. Bartlett, "Design of conducting polymer gas sensors: Modeling and experiment," *Synthetic Metals*, vol. 57, no. 1, pp. 3665-3670, 1993.
- [24] L. F. B. L. Pontes, J. E. G. de Souza, A. Galembeck and C. P. de Melo, "Gas sensor based on montmorillonite/polypyrrole composites prepared by in situ polymerization in aqueous medium," *Sensors and Actuators B-Chemical*, vol. 177, pp. 1115-1121, 2013.
- [25] J. Huang, Y. D. Jiang, X. S. Du and J. Bi, "A new siloxane polymer for chemical vapor sensor," *Sensors and Actuators B-Chemical*, vol. 146, no. 1, pp. 388-394, 2010.
- [26] Z. Q. Wu, X. D. Chen, S. B. Zhu, Z. W. Zhou, Y. Yao, W. Quan and B. Liu, "Enhanced sensitivity of ammonia sensor using graphene/polyaniline nanocomposite," *Sensors and Actuators B-Chemical*, vol. 178, pp. 485-493, 2013.
- [27] M. F. Mabrook, C. Pearson and M. C. Petty, "Inkjet-Printed Polymer Films for the Detection of Organic Vapors," *IEEE sensors journal*, vol. 6, no. 6, pp. 1435-1444, 2006.
- [28] B. Wyszynski, P. Somboon and T. Nakamoto, "Chemisorbed PEGylated lipopolymers as sensing film supports for QCM odor sensors," *Sensors and Actuators B-Chemical*, vol. 130, no. 2, pp. 857-863, 2008.
- [29] B. Wyszynski, D. Kim and T. Nakamoto, "Stabilization of coating for QCM odor sensors with liquid GC materials supported by lipopolymers and lipids," *Sensors and Actuators B-Chemical*, vol. 179, pp. 81-86, 2013.
- [30] L. Yang, R. W. Zhang, D. Staiculescu, C. P. Wong and M. M. Tentzeris, "A Novel Conformal RFID-Enabled Module Utilizing Inkjet-Printed Antennas and Carbon Nanotubes for Gas-Detection Applications," *Ieee Antennas and Wireless*

- Propagation Letters*, vol. 8, pp. 653-656, 2009.
- [31] S. J. Kim, "The Effect on the Gas Selectivity of CNT-Based Gas Sensors by Binder in SWNT/Silane Sol Solution," *Ieee Sensors Journal*, vol. 10, no. 1, pp. 173-177, 2010.
- [32] W. Ding, R. Hayashi, J. Suehiro, K. Imasaka and M. Hara, "Observation of dynamic behavior of PD-generated SF<sub>6</sub> decompositions using carbon nanotube gas sensor," *2005 Annual Report Conference on Electrical Insulation and Dielectric Phenomena*, pp. 561-564, 2005.
- [33] N. Koyama and K. Kurihara, "Effect of Odorants on Lipid Monolayers from Bovine Olfactory Epithelium," *Nature*, vol. 236, no. 5347, pp. 402-404, 1972.
- [34] K. Kurihara, K. Yoshii and M. Kashiwayanagi, "Transduction Mechanisms in Chemoreception," *Comparative Biochemistry and Physiology a-Physiology*, vol. 85, no. 1, pp. 1-22, 1986.
- [35] S. S. Nielsen, "Introduction to Food Analysis," *Food Analysis, Fourth Edition*, 2010.
- [36] E. Fahy, S. Subramaniam, H. A. Brown, C. K. Glass, A. H. Merrill, R. C. Murphy, C. R. H. Raetz, D. W. Russell, Y. Seyama, W. Shaw, T. Shimizu, F. Spener, G. van Meer, M. S. VanNieuwenhze, S. H. White, J. L. Witztum and E. A. Dennis, "A comprehensive classification system for lipids," *Journal of Lipid Research*, vol. 46, no. 5, pp. 839-861, 2005.
- [37] B. A. Cornell, V. L. B. BraachMaksvytis, L. G. King, P. D. J. Osman, B. Raguse, L. Wiczorek and R. J. Pace, "A biosensor that uses ion-channel switches," *Nature*, vol. 387, no. 6633, pp. 580-583, 1997.
- [38] I. Reviakine, W. Bergsma-Schutter and A. Brisson, "Growth of protein 2-d crystals on supported planar lipid bilayers imaged in situ by AFM," *Journal of Structural Biology*, vol. 121, no. 3, pp. 356-362, 1998.
- [39] L. A. Kung, L. Kam, J. S. Hovis and S. G. Boxer, "Patterning hybrid surfaces of proteins and supported lipid bilayers," *Langmuir*, vol. 16, no. 17, pp. 6773-6776, 2000.
- [40] Z. B. Zhou, Q. H. Wu and C. C. Liu, "Microfabricated Thin-Film Microelectrode for Amperometric Determination of Co<sub>2</sub> in the Gas-Phase," *Sensors and Actuators*

- B-Chemical*, vol. 21, no. 2, pp. 101-108, 1994.
- [41] M. Josowicz, J. Janata, K. Ashley and S. Pons, "Electrochemical and Ultraviolet Visible Spectroelectrochemical Investigation of Selectivity of Potentiometric Gas Sensors Based on Polypyrrole," *Analytical Chemistry*, vol. 59, no. 2, pp. 253-258, 1987.
- [42] I. Eisele, T. Doll and M. Burgmair, "Low power gas detection with FET sensors," *Sensors and Actuators B-Chemical*, vol. 78, no. 1-3, pp. 19-25, 2001.
- [43] K. J. Albert, N. S. Lewis, C. L. Schauer, G. A. Sotzing, S. E. Stitzel, T. P. Vaid and D. R. Walt, "Cross-reactive chemical sensor arrays," *Chemical Reviews*, vol. 100, no. 7, pp. 2595-2626, 2000.
- [44] E. L. Kalman, A. Lofvendahl, E. Winqvist and I. Lundstrom, "Classification of complex gas mixtures from automotive leather using an electronic nose," *Analytica Chimica Acta*, vol. 403, no. 1-2, pp. 31-38, 2000.
- [45] T. C. Pearce, *Handbook of machine olfaction : electronic nose technology*, Weinheim: Wiley-VCH, 2003.
- [46] S. S. Park, H. X. Zheng and J. D. Mackenzie, "Ethanol Gas-Sensing Properties of  $\text{SnO}_2$ -Based Thin-Film Sensors Prepared by the Sol-Gel Process," *Materials Letters*, vol. 17, no. 6, pp. 346-352, 1993.
- [47] H. Steffes, C. Imawan, F. Solzbacher and E. Obermeier, "Enhancement of  $\text{NO}_2$  sensing properties of  $\text{In}_2\text{O}_3$ -based thin films using an Au or Ti surface modification," *Sensors and Actuators B-Chemical*, vol. 78, no. 1-3, pp. 106-112, 2001.
- [48] E. Schaller, J. O. Bosset and F. Escher, "Electronic noses' and their application to food," *Food Science and Technology-Lebensmittel-Wissenschaft & Technologie*, vol. 31, no. 4, pp. 305-316, 1998.
- [49] A. Galdikas, A. Mironas and A. Setkus, "Copper-Doping Level Effect on Sensitivity and Selectivity of Tin Oxide Thin-Film Gas Sensor," *Sensors and Actuators B-Chemical*, vol. 26, no. 1-3, pp. 29-32, 1995.
- [50] G. Behr and W. Fliegel, "Electrical-Properties and Improvement of the Gas Sensitivity in Multiple-Doped  $\text{SnO}_2$ ," *Sensors and Actuators B-Chemical*, vol. 26, no. 1-3, pp. 33-37, 1995.

- [51] M. Saha, A. Banerjee, A. K. Halder, J. Mondal, A. Sen and H. S. Maiti, "Effect of alumina addition on methane sensitivity of tin dioxide thick films," *Sensors and Actuators B-Chemical*, vol. 79, no. 2-3, pp. 192-195, 2001.
- [52] S. C. George and S. Thomas, "Transport phenomena through polymeric systems," *Progress in Polymer Science*, vol. 26, no. 6, pp. 985-1017, 2001.
- [53] J. H. Chen, H. Iwata, N. Tsubokawa, Y. Maekawa and M. Yoshida, "Novel vapor sensor from polymer-grafted carbon black: effects of heat-treatment and gamma-ray radiation-treatment on the response of sensor material in cyclohexane vapor," *Polymer*, vol. 43, no. 8, pp. 2201-2206, 2002.
- [54] A. C. Partridge, M. L. Jansen and W. M. Arnold, "Conducting polymer based sensor," *Materials Science & Engineering C-Biomimetic and Supramolecular Systems*, vol. 12, no. 1-2, pp. 37-42, 2000.
- [55] J. Webster, *The measurement, instrumentation and sensors handbook*, Boca Raton: CRC Press, 1999, pp. 32-113.
- [56] J. Janata and R. Huber, *Solid state chemical sensors*, Orlando [Fla.]: Academic Press, 1985, pp. 197-203.
- [57] A. Elia, C. Di Franco, P. M. Lugara and G. Scamarcio, "Photoacoustic spectroscopy with quantum cascade lasers for trace gas detection," *Sensors*, vol. 6, no. 10, pp. 1411-1419, 2006.
- [58] P. Tardy, J. R. Coulon, C. Lucat and F. Menil, "Dynamic thermal conductivity sensor for gas detection," *Sensors and Actuators B-Chemical*, vol. 98, no. 1, pp. 63-68, 2004.
- [59] A. Loui, S. Elhadj, D. J. Sirbuly, S. K. McCall, B. R. Hart and T. V. Ratto, "An analytic model of thermal drift in piezoresistive microcantilever sensors," *Journal of Applied Physics*, vol. 107, no. 5, 2010.
- [60] J. Clark, "absorption spectra - the Beer-Lambert Law," 2007. [Online]. Available: <http://www.chemguide.co.uk/analysis/uvvisible/beerlambert.html>. [Accessed 06 04 2014].
- [61] T. C. Bond, G. D. Cole, L. L. Goddard and E. M. Behymer, "Photonic MEMS for NIR in-situ gas detection and identification," *2007 Ieee Sensors*, Vols. 1-3, pp. 1368-1371, 2007.

- [62] H. M. Zheng, "Experiment Study of continuous emission monitoring system based on Differential Optical Absorption Spectroscopy," *2008 International Workshop on Education Technology and Training and 2008 International Workshop on Geoscience and Remote Sensing*, vol. 1, pp. 175-177, 2009.
- [63] C. Charlton, B. Temelkuran, G. Dellemann and B. Mizaikoff, "Midinfrared sensors meet nanotechnology: Trace gas sensing with quantum cascade lasers inside photonic band-gap hollow waveguides," *Applied Physics Letters*, vol. 86, no. 19, 2005.
- [64] K. Liu, T. G. Liu, J. F. Jiang, G. D. Peng, H. X. Zhang, D. G. Jia, Y. Wang, W. C. Jing and Y. M. Zhang, "Investigation of Wavelength Modulation and Wavelength Sweep Techniques in Intracavity Fiber Laser for Gas Detection," *Journal of Lightwave Technology*, vol. 29, no. 1, pp. 15-21, 2011.
- [65] K. Arshak, E. Moore, G. Lyons, J. Harris and S. Clifford, "A review of gas sensors employed in electronic nose applications," *sensor review*, vol. 24, no. 2, pp. 181 - 198, 2004.
- [66] E. D. McNaghten, A. M. Parkes, B. C. Griffiths, A. I. Whitehouse and S. Palanco, "Detection of trace concentrations of helium and argon in gas mixtures by laser-induced breakdown spectroscopy," *Spectrochimica Acta Part B-Atomic Spectroscopy*, vol. 64, no. 10, pp. 1111-1118, 2009.
- [67] V. Arunajatesan, B. Subramaniam, K. W. Hutchenson and F. E. Herkes, "In situ FTIR investigations of reverse water gas shift reaction activity at supercritical conditions," *Chemical Engineering Science*, vol. 62, no. 18-20, pp. 5062-5069, 2007.
- [68] H. T. Nagle, R. GutierrezOsuna and S. S. Schiffman, "The how and why of electronic noses," *Ieee Spectrum*, vol. 35, no. 11, pp. 22-31, 1998.
- [69] Z. P. Khlebarov, A. I. Stoyanova and D. I. Topalova, "Surface Acoustic-Wave Gas Sensors," *Sensors and Actuators B-Chemical*, vol. 8, no. 1, pp. 33-40, 1992.
- [70] G. Sauerbrey, "The use of quartz oscillators for weighing thin layers and for microweighing," *Phys.*, vol. 155, no. 2, pp. 206-222, 1959.
- [71] C. D. Liang, C. Y. Yuan, R. J. Warmack, C. E. Barnes and S. Dai, "Ionic liquids: A new class of sensing materials for detection of organic vapors based on the use of a

- quartz crystal microbalance,” *Analytical Chemistry*, vol. 74, no. 9, pp. 2172-2176, 2002.
- [72] M. E. Escuderos, S. Sanchez and A. Jimenez, “Quartz Crystal Microbalance (QCM) sensor arrays selection for olive oil sensory evaluation,” *Food Chemistry*, vol. 124, no. 3, pp. 857-862, 2011.
- [73] X. C. Zhou, L. Zhong, S. F. Y. Li, S. C. Ng and H. S. O. Chan, “Organic vapour sensors based on quartz crystal microbalance coated with self-assembled monolayers,” *Sensors and Actuators B-Chemical*, vol. 42, no. 1, pp. 59-65, 1997.
- [74] F. D. Cui, X. X. Cai, J. H. Han, Z. H. He, H. Z. Zhu and G. P. Feng, “Lipid LB films for room temperature ethanol gas assay,” *Sensors and Actuators B-Chemical*, vol. 45, no. 3, pp. 229-232, 1997.
- [75] G. R. Dai, “A study of the sensing properties of thin film sensor to trimethylamine,” *Sensors and Actuators B-Chemical*, vol. 53, no. 1-2, pp. 8-12, 1998.
- [76] T. A. Dickinson, J. White, J. S. Kauer and D. R. Walt, “Current trends in 'artificial-nose' technology,” *Trends in Biotechnology*, vol. 16, no. 6, pp. 250-258, 1998.
- [77] M. Penza, G. Cassano, F. Tortorella and G. Zaccaria, “Classification of food, beverages and perfumes by WO<sub>3</sub> thin-film sensors array and pattern recognition techniques,” *Sensors and Actuators B-Chemical*, vol. 73, no. 1, pp. 76-87, 2001.
- [78] D. C. Dyer and J. W. Gardner, “High-precision intelligent interface for a hybrid electronic nose,” *Sensors and Actuators a-Physical*, vol. 62, no. 1-3, pp. 724-728, 1997.
- [79] F. Schedin, A. K. Geim, S. V. Morozov, E. W. Hill, P. Blake, M. I. Katsnelson and K. S. Novoselov, “Detection of individual gas molecules adsorbed on graphene,” *Nature Materials*, vol. 6, no. 9, pp. 652-655, 2007.
- [80] S. Kulinyi, D. Brandszajsz, H. Amine, M. Adam, P. Furjes, I. Barsony and C. Ducso, “Olfactory detection of methane, propane, butane and hexane using conventional transmitter norms,” *Sensors and Actuators B-Chemical*, vol. 111, pp. 286-292, 2005.
- [81] C. Caucheteur, M. Debliquy, D. Lahem and P. Megret, “Catalytic fiber Bragg grating sensor for hydrogen leak detection in air,” *Ieee Photonics Technology*

- Letters*, vol. 20, no. 1-4, pp. 96-98, 2008.
- [82] Z. Jin, Y. X. Su and Y. X. Duan, "Development of a polyaniline-based optical ammonia sensor," *Sensors and Actuators B-Chemical*, vol. 72, no. 1, pp. 75-79, 2001.
- [83] M. P. Goertz, B. L. Stottrup, J. E. Houston and X. Y. Zhu, "Nanomechanical Contrasts of Gel and Fluid Phase Supported Lipid Bilayers," *Journal of Physical Chemistry B*, vol. 113, no. 27, pp. 9335-9339, 2009.
- [84] T. E. Thompson and T. W. Tillack, "Organization of Glycosphingolipids in Bilayers and Plasma-Membranes of Mammalian-Cells," *Annual Review of Biophysics and Biophysical Chemistry*, vol. 14, pp. 361-386, 1985.
- [85] D. A. Brown and E. London, "Structure and origin of ordered lipid domains in biological membranes," *Journal of Membrane Biology*, vol. 164, no. 2, pp. 103-114, 1998.
- [86] A. E. McKiernan, T. V. Ratto and M. L. Longo, "Domain growth, shapes, and topology in cationic lipid bilayers on mica by fluorescence and atomic force microscopy," *Biophysical Journal*, vol. 79, no. 5, pp. 2605-2615, 2000.
- [87] R. P. Richter and A. R. Brisson, "Following the formation of supported lipid bilayers on mica: A study combining AFM, QCM-D, and ellipsometry," *Biophysical Journal*, vol. 88, no. 5, pp. 3422-3433, Biophysical Journal 2005.
- [88] R. Richter, A. Mukhopadhyay and A. Brisson, "Pathways of lipid vesicle deposition on solid surfaces: A combined QCM-D and AFM study," *Biophysical Journal*, vol. 85, no. 5, pp. 3035-3047, 2003.
- [89] R. P. Richter, R. Berat and A. R. Brisson, "Formation of solid-supported lipid bilayers: An integrated view," *Langmuir*, vol. 22, no. 8, pp. 3497-3505, 2006.
- [90] B. P. Stehrer, H. Gruber, R. Schwodiauer, I. M. Graz and S. Bauer, "High Frequency QCM Flow Cell with Enhanced Accuracy for Liquid and Biochemical Sensing," *Proceedings of the Eurosensors Xxiii Conference*, vol. 1, no. 1, pp. 1507-1510, 2009.
- [91] L. Srisombat, A. C. Jamison and T. R. Lee, "Stability: A key issue for self-assembled monolayers on gold as thin-film coatings and nanoparticle protectants," *Colloids and Surfaces a-Physicochemical and Engineering Aspects*, vol. 390, no.

- 1-3, pp. 1-19, 2011.
- [92] J. T. Woodward, M. L. Walker, C. W. Meuse, D. J. Vanderah, G. E. Poirier and A. L. Plant, "Effect of an oxidized gold substrate on alkanethiol self-assembly," *Langmuir*, vol. 16, no. 2, pp. 5347-5353, 2000.
- [93] V. Prachayasittikul, C. Isarankura-Na-Ayudhya, L. Hilterhaus, A. Hinz, T. Tantimongcolwat and H. J. Galla, "Interaction analysis of chimeric metal-binding green fluorescent protein and artificial solid-supported lipid membrane by quartz crystal microbalance and atomic force microscopy," *Biochemical and Biophysical Research Communications*, vol. 327, no. 1, pp. 174-182, 2005.
- [94] H. Ron, S. Matlis and I. Rubinstein, "Self-assembled monolayers on oxidized metals. 2. Gold surface oxidative pretreatment, monolayer properties, and depression formation," *Langmuir*, vol. 14, no. 5, pp. 1116-1121, 1998.
- [95] K. Hermansson, U. Lindberg, B. Hok and G. Palmskog, "Wetting properties of silicon surfaces," *IEEE*, pp. 193-195, 1991.
- [96] H. C. Berg, *Random walks in biology*, Princeton ; Guildford: Princeton University Press, 1993.
- [97] A. Bruce, *Molecular biology of the cell*, New York: Garland Science, 2002.
- [98] S. J. Singer and G. L. Nicolson, "Fluid Mosaic Model of Structure of Cell-Membranes," *Science*, vol. 175, no. 4023, pp. 720-731, 1972.
- [99] D. A. Brown and E. London, "Structure of detergent-resistant membrane domains: Does phase separation occur in biological membranes?," *Biochemical and Biophysical Research Communications*, vol. 240, no. 1, pp. 1-7, 1997.
- [100] K. Simons and E. Ikonen, "Functional rafts in cell membranes," *Nature*, vol. 387, no. 6633, pp. 569-572, 1997.
- [101] J. Hwang, L. A. Gheber, L. Margolis and M. Edidin, "Domains in cell plasma membranes investigated by near-field scanning optical microscopy," *Biophysical Journal*, vol. 74, no. 5, pp. 2184-2190, 1998.
- [102] A. C. Simonsen and L. A. Bagatolli, "Structure of spin-coated lipid films and domain formation in supported membranes formed by hydration," *Langmuir*, vol. 20, no. 22, pp. 9720-9728, 2004.
- [103] A. Manbachi and R. S. C. Cobbold, "Development and application of piezoelectric

- materials for ultrasound generation and detection,” *Ultrasound*, vol. 19, no. 4, pp. 187-196, 2011.
- [104] G. Lippman, “Principe de la conservation de l’électricité,” *Annales de chimie et de physique*, vol. 24, no. 145, pp. 381-394, 1881.
- [105] Jacques and P. Curie, “Contractions et dilatations produites par des tensions dans les cristaux hémihédres à faces inclinées,” *Comptes rendus hebdomadaires des séances de l’Académie des sciences*, vol. 93, pp. 1137-1140, 1881.
- [106] D. A. Skoog, F. J. Holler and S. R. Crouch, “chapter 1 introduction,” in *Principles of Instrumental Analysis*, Pacific Grove, Calif., Brooks/Cole ; London : Thomson Learning [distributor], 2007.
- [107] S. R. P. Inc., “Hydrothermal Growth of Quartz-Technical Brief,” September 1999. [Online]. Available: [http://www.sawyerllc.com/Tech%20Brief/Quartz\\_growth\\_tech\\_brief.pdf](http://www.sawyerllc.com/Tech%20Brief/Quartz_growth_tech_brief.pdf). [Accessed Febuary 2014].
- [108] C. Lu and A. W. Czanderna, *Applications of piezoelectric quartz crystal microbalances*, Amsterdam ; Oxford: Elsevier, 1984.
- [109] J. Cartright, “Choosing an AT or SC cut for OCXOs,” Connor winfield, October 2008. [Online]. Available: [http://www.conwin.com/pdfs/at\\_or\\_sc\\_for\\_ocxo.pdf](http://www.conwin.com/pdfs/at_or_sc_for_ocxo.pdf). [Accessed 4 June 2013].
- [110] T. Schafer, F. Di Francesco and R. Fuoco, “Ionic liquids as selective depositions on quartz crystal microbalances for artificial olfactory systems- a feasibility study,” *Microchemical Journal*, vol. 85, no. 1, pp. 52-56, 2007.
- [111] C. A. Keller and B. Kasemo, “Surface specific kinetics of lipid vesicle adsorption measured with a quartz crystal microbalance,” *Biophysical Journal*, vol. 75, no. 3, pp. 1397-1402, 1998.
- [112] E. Reimhult, F. Hook and B. Kasemo, “Vesicle adsorption on SiO<sub>2</sub> and TiO<sub>2</sub>: Dependence on vesicle size,” *Journal of Chemical Physics*, vol. 117, no. 16, pp. 7401-7404, 2002.
- [113] R. P. Richter and A. Brisson, “QCM-D on mica for parallel QCM-D-AFM studies,” *Langmuir*, vol. 20, no. 11, pp. 4609-4613, 2004.
- [114] C. S. Lu and O. Lewis, “Investigation of Film-Thickness Determination by

- Oscillating Quartz Resonators with Large Mass Load,” *Journal of Applied Physics*, vol. 43, no. 11, pp. 4385-4390, 1972.
- [115] D. R. Denison, “Linearity of a Heavily Loaded Quartz Crystal Microbalance,” *Journal of Vacuum Science & Technology*, vol. 10, no. 1, pp. 126-129, 1973.
- [116] K. H. Behrndt, “Long-Term Operation of Crystal Oscillators in Thin-Film Deposition,” *Journal of Vacuum Science & Technology*, vol. 8, no. 5, p. 622, 1971.
- [117] Q. sense, “The QCM-D principle,” Q sense, [Online]. Available: <http://www.q-sense.com/the-qcm-d-principle>. [Accessed 4 June 2013].
- [118] W. Chen, A. Y. Fadeev, M. C. Hsieh, D. Oner, J. Youngblood and T. J. McCarthy, “Ultrahydrophobic and ultralyophobic surfaces: Some comments and examples,” *Langmuir*, vol. 15, no. 10, pp. 3395-3399, 1999.
- [119] D. Oner and T. J. McCarthy, “Ultrahydrophobic surfaces. Effects of topography length scales on wettability,” *Langmuir*, vol. 16, no. 20, pp. 7777-7782, 2000.
- [120] S. Semal, T. D. Blake, V. Geskin, M. J. de Ruijter, G. Castelein and J. De Coninck, “Influence of surface roughness on wetting dynamics,” *Langmuir*, vol. 15, no. 25, pp. 8765-8770, 1999.
- [121] M. Voue and J. De Coninck, “Spreading and wetting at the microscopic scale: Recent developments and perspectives,” *Acta Materialia*, vol. 48, no. 18-19, pp. 4405-4417, 2000.
- [122] R. D. Hazlett, “Fractal Applications - Wettability and Contact-Angle,” *Journal of Colloid and Interface Science*, vol. 137, no. 2, pp. 527-533, 1990.
- [123] A. Krozer and M. Rodahl, “X-ray photoemission spectroscopy study of UV/ozone oxidation of Au under ultrahigh vacuum conditions,” *Journal of Vacuum Science & Technology a-Vacuum Surfaces and Films*, vol. 15, no. 3, pp. 1704-1709, 1997.
- [124] C. Bryce and D. Berk, “Kinetics of GaAs dissolution in H<sub>2</sub>O<sub>2</sub>-NH<sub>4</sub>OH-H<sub>2</sub>O solutions,” *Industrial & Engineering Chemistry Research*, vol. 35, no. 12, pp. 4464-4470, 1996.
- [125] J. M. Delarios, C. R. Helms, D. B. Kao and B. E. Deal, “Effect of Silicon Surface Cleaning Procedures on Oxidation-Kinetics and Surface-Chemistry,” *Applied Surface Science*, vol. 30, no. 1-4, pp. 17-24, 1987.
- [126] A. Ulman, “Formation and structure of self-assembled monolayers,” *Chemical*

- Reviews*, vol. 96, no. 4, pp. 1533-1554, 1996.
- [127] D. Behn, S. Bosk, H. Hoffmeister, A. Janshoff, R. Witzgall and C. Steinem, "Quantifying the interaction of the C-terminal regions of polycystin-2 and polycystin-1 attached to a lipid bilayer by means of QCM," *Biophysical Chemistry*, vol. 150, no. 1-3, pp. 47-53, 2010.
- [128] D. J. Kim, R. Pitchimani, D. E. Snow and L. J. Hope-Weeks, "A simple method for the removal of thiols on gold surfaces using an NH<sub>4</sub>OH-H<sub>2</sub>O<sub>2</sub>-H<sub>2</sub>O solution," *scanning*, vol. 30, no. 2, pp. 118-122, 2008.
- [129] T. Mori, T. Motonaga and Y. Okahata, "Cast films of lipid-coated enzymes as selective sensors for disaccharides," *Colloids and Surfaces a-Physicochemical and Engineering Aspects*, vol. 146, no. 1-3, pp. 387-395, 1999.
- [130] S. Munoz-Aguirre, T. Nakamoto and T. Moriizumi, "Study of deposition of gas sensing films on quartz crystal microbalance using an ultrasonic atomizer," *Sensors and Actuators B-Chemical*, vol. 105, no. 2, pp. 144-149, 2005.
- [131] M. Menke, S. Kunneke and A. Janshoff, "Lateral organization of G(M1) in phase-separated monolayers visualized by scanning force microscopy," *European Biophysics Journal with Biophysics Letters*, vol. 31, no. 4, pp. 317-322, 2002.
- [132] A. Ulman, *ultrathin organic films*, San Diego: Academic Press, 1991.
- [133] V. Vie, N. Van Mau, E. Lesniewska, J. P. Goudonnet, F. Heitz and C. Le Grimellec, "Distribution of ganglioside G(M1) between two-component, two-phase phosphatidylcholine monolayers," *Langmuir*, vol. 14, no. 16, pp. 4574-4583, 1998.
- [134] H. A. Rinia, R. A. Demel, J. P. J. M. van der Eerden and B. de Kruijff, "Blistering of Langmuir-Blodgett bilayers containing anionic phospholipids as observed by atomic force microscopy," *Biophysical Journal*, vol. 77, no. 3, pp. 1683-1693, 1999.
- [135] P. E. Milhiet, C. Domec, M. C. Giocondi, N. Van Mau, F. Heitz and C. Le Grimellec, "Domain formation in models of the renal brush border membrane outer leaflet," *Biophysical Journal*, vol. 81, no. 1, pp. 547-555, 2001.
- [136] A. K. M. S. Islam, Z. Ismail, M. N. Ahmad, B. Saad, A. R. Othman, A. Y. M. Shakaff, A. Daud and Z. Ishak, "Transient parameters of a coated quartz-crystal microbalance sensor for the detection of volatile organic compounds (VOCs),"

- Sensors and Actuators B-Chemical*, vol. 109, no. 2, pp. 238-243, 2005.
- [137] U. Stahl, M. Rapp and T. Wessa, "Adhesives: a new class of polymer coatings for surface acoustic wave sensors for fast and reliable process control applications," *Analytica Chimica Acta*, vol. 450, no. 1-2, pp. 27-36, 2001.
- [138] D. W. Schubert and T. Dunkel, "Spin coating from a molecular point of view: its concentration regimes, influence of molar mass and distribution," *Materials Research Innovations*, vol. 7, no. 5, pp. 314-321, 2003.
- [139] M. E. Escuderos, S. Sanchez and A. Jimenez, "Virgin olive oil sensory evaluation by an artificial olfactory system, based on Quartz Crystal Microbalance (QCM) sensors," *Sensors and Actuators B-Chemical*, vol. 147, no. 1, pp. 159-164, 2010.
- [140] M. M. B. Nielsen and A. C. Simonsen, "Imaging Ellipsometry of Spin-Coated Membranes: Mapping of Multilamellar Films, Hydrated Membranes, and Fluid Domains," *Langmuir*, vol. 29, no. 5, pp. 1525-1532, 2013.
- [141] A. Dols-Perez, L. Fumagalli, A. C. Simonsen and G. Gomila, "Ultrathin Spin-Coated Dioleoylphosphatidylcholine Lipid Layers in Dry Conditions: A Combined Atomic Force Microscopy and Nanomechanical Study," *Langmuir*, vol. 27, no. 21, pp. 13165-13172, 2011.
- [142] T. L. Richardson and E. Lokensgard, "Dip coating," in *Industrial Plastics: Theory and Applications 4th edition*, United states of America, Thomson Delma learning, 2004, p. 292.
- [143] M. S. Freund and N. S. Lewis, "A Chemically Diverse Conducting Polymer-Based Electronic Nose," *Proceedings of the National Academy of Sciences of the United States of America*, vol. 92, no. 7, pp. 2652-2656, 1995.
- [144] M. Petty and W. Barlow, "Film deposition," in *Langmuir-Blodgett Films*, New York, A Division of Plenum, 1990, p. 116.
- [145] U. Mennicke and T. Salditt, "Preparation of solid-supported lipid bilayers by spin-coating," *Langmuir*, vol. 18, no. 21, pp. 8172-8177, 2002.
- [146] S. Hamakawa, L. Li, A. Li and E. Iglesia, "Synthesis and hydrogen permeation properties of membranes based on dense SrCe<sub>0.95</sub>Yb<sub>0.05</sub>O<sub>3</sub>-alpha thin films," *Solid State Ionics*, vol. 148, no. 1-2, pp. 71-81, 2002.
- [147] T. L. Richardson and E. Lokensgard, "sary coating," in *Industrial Plastics:*

- Theory and Applications 4th edition*, United states of America, Thomson Delma learning, 2004, p. 293.
- [148] R. C. Jaeger, "Film Deposition," in *Introduction to microelectronic fabrication*, Upper Saddle River. N.J., Prentice Hall ; London : Pearson Education, 2002.
- [149] S. M. Sze, *Semiconductor devices, physics and technology*, New York ; [Chichester]: Wiley, 2001.
- [150] W. H. Tao and C. H. Tsai, "H<sub>2</sub>S sensing properties of noble metal doped WO<sub>3</sub> thin film sensor fabricated by micromachining," *Sensors and Actuators B-Chemical*, vol. 81, no. 2-3, pp. 237-247, 2002.
- [151] A. P. I. Inc., "preparation of liposomes," Avanti Polar lipids Inc., 6 June 2013. [Online]. Available: [http://avantilipids.com/index.php?option=com\\_content&view=article&id=1384&Itemid=372](http://avantilipids.com/index.php?option=com_content&view=article&id=1384&Itemid=372). [Accessed 6 June 2013].
- [152] T. V. Ratto and M. L. Longo, "Obstructed diffusion in phase-separated supported lipid bilayers: A combined atomic force microscopy and fluorescence recovery after photobleaching approach," *Biophysical Journal*, vol. 83, no. 6, pp. 3380-3392, 2002.
- [153] C. C. R. o. C. University, "fabrication and process," CEPSR Clean Room of Columbia University, 6 June 2013. [Online]. Available: <http://www.clean.cise.columbia.edu/process/spintheory.pdf>. [Accessed 6 June 2013].
- [154] K. L. Williamson, *Macroscale and microscale organic experiments*, Lexington, Mass.: D.C. Heath, 1994.
- [155] C. controls, "Dielectric Constant Values," Clipper controls, 6 June 2013. [Online]. Available: <http://www.clippercontrols.com/pages/Dielectric-Constant-Values.html>. [Accessed 6 June 2013].
- [156] Z. Salamon, D. Huang, W. A. Cramer and G. Tollin, "Coupled plasmon-waveguide resonance spectroscopy studies of the cytochrome b(6)f/plastocyanin system in supported lipid bilayer membranes," *Biophysical Journal*, vol. 75, no. 4, pp. 1874-1885, 1998.
- [157] C. A. Keller, K. Glasmastar, V. P. Zhdanov and B. Kasemo, "Formation of

- supported membranes from vesicles,” *Physical Review Letters*, vol. 84, no. 23, pp. 5443-5446, 2000.
- [158] C. Steinem, A. Janshoff, W. P. Ulrich, M. Sieber and H. J. Galla, “Impedance analysis of supported lipid bilayer membranes: A scrutiny of different preparation techniques,” *Biochimica Et Biophysica Acta-Biomembranes*, vol. 1279, no. 2, pp. 169-180, 1996.
- [159] P. Nollert, H. Kiefer and F. Jahnig, “Lipid Vesicle Adsorption Versus Formation of Planar Bilayers on Solid-Surfaces,” *Biophysical Journal*, vol. 69, no. 4, pp. 1447-1455, 1995.
- [160] J. M. Johnson, T. Ha, S. Chu and S. G. Boxer, “Early steps of supported bilayer formation probed by single vesicle fluorescence assays,” *Biophysical Journal*, vol. 83, no. 6, pp. 3371-3379, 2002.
- [161] M. Benes, D. Billy, W. T. Hermens and M. Hof, “Muscovite (mica) allows the characterisation of supported Bilayers by ellipsometry and confocal fluorescence correlation spectroscopy,” *Biological Chemistry*, vol. 383, no. 2, pp. 337-341, 2002.
- [162] T. Oguchi, K. Sakai, H. Sakai and M. Abe, “DSPC/DLPC Mixed Films Supported on Silica: A QCM-D and Friction Force Study,” *Journal of Oleo Science*, vol. 60, no. 4, pp. 177-183, 2011.
- [163] A. Kunze, M. Zach, S. Svedhem and B. Kasemo, “Electrodeless QCM-D for lipid bilayer applications,” *Biosensors & Bioelectronics*, vol. 26, no. 5, pp. 1833-1838, 2011.
- [164] I. Reviakine and A. Brisson, “Formation of supported phospholipid bilayers from unilamellar vesicles investigated by atomic force microscopy,” *Langmuir*, vol. 16, no. 4, pp. 1806-1815, 2000.
- [165] X. M. Liang, G. Z. Mao and K. Y. S. Ng, “Probing small unilamellar EggPC vesicles on mica surface by atomic force microscopy,” *Colloids and Surfaces B-Biointerfaces*, vol. 34, no. 1, pp. 41-51, 2004.
- [166] S. Morandat and K. El Kirat, “Exploring the Properties and Interactions of Supported Lipid Bilayers on the Nanoscale by Atomic Force Microscopy,” *Microscopy: Science, Technology, Applications and Education*, pp. 1925-1939,

- 2010.
- [167] P. J. Eaton and P. West, *Atomic force microscopy*, Oxford: Oxford University Press, 2010.
- [168] Q. Zhong, D. Inness, K. Kjoller and V. B. Elings, "Fractured Polymer Silica Fiber Surface Studied by Tapping Mode Atomic-Force Microscopy," *Surface Science*, vol. 290, no. 1-2, pp. L688-L692, 1993.
- [169] S. N. Magonov, V. Elings and M. H. Whangbo, "Phase imaging and stiffness in tapping-mode atomic force microscopy," *Surface Science*, vol. 375, no. 2-3, pp. L385-L391, 1997.
- [170] B. Pignataro, C. Steinem, H. J. Galla, H. Fuchs and A. Janshoff, "Specific adhesion of vesicles monitored by scanning force microscopy and quartz crystal microbalance," *Biophysical Journal*, vol. 78, no. 1, pp. 487-498, 2000.
- [171] W. C. Lin, C. D. Blanchette, T. V. Ratto and M. L. Longo, "Lipid asymmetry in DLPC/DSPC-supported lipid bilayers: A combined AFM and fluorescence microscopy study," *Biophysical Journal*, vol. 90, no. 1, pp. 228-237, 2006.
- [172] J. Tamayo and R. Garcia, "Deformation, contact time, and phase contrast in tapping mode scanning force microscopy," *Langmuir*, vol. 16, no. 18, pp. 4430-4435, 1996.
- [173] R. Garcia and R. Perez, "Dynamic atomic force microscopy methods," *Surface Science Reports*, vol. 47, no. 68, pp. 197-301, 2002.
- [174] T. Smith, "The Hydrophilic Nature of a Clean Gold Surface," *Journal of Colloid and Interface Science*, vol. 75, no. 1, pp. 51-55, 1980.
- [175] G. L. Gaines, "On the Water Wettability of Gold," *Journal of Colloid and Interface Science*, vol. 79, no. 1, pp. 295-295, 1981.
- [176] D. L. Garcia-Gonzalez and R. Aparicio, "Detection of vinegary defect in virgin olive oils by metal oxide sensors," *Journal of Agricultural and Food Chemistry*, vol. 50, no. 7, pp. 1809-1814, 2002.
- [177] A. C. Simonsen, U. B. Jensen and P. L. Hansen, "Hydrolysis of fluid supported membrane islands by phospholipase A(2): Time-lapse imaging and kinetic analysis," *Journal of Colloid and Interface Science*, vol. 301, no. 1, pp. 107-115, 2006.

- [178] L. Perino-Gallice, G. Fragneto, U. Mennicke, T. Salditt and F. Rieutord, "Dewetting of solid-supported multilamellar lipid layers," *European Physical Journal E*, vol. 8, no. 3, pp. 275-282, 2002.
- [179] G. O. Nelson, *Gas Mixtures: Preparation and Control*, Chelsea: Lewis publishers, 1992.
- [180] J. Namiesnik, "Generation of Standard Gaseous-Mixtures," *Journal of Chromatography*, vol. 300, no. 1, pp. 79-108, 1984.
- [181] R. S. Barratt, "The Preparation of Standard Gas-Mixtures - a Review," *Analyst*, vol. 106, no. 1265, pp. 817-849, 1981.
- [182] S. Tumbiolo, L. Vincent, J. F. Gal and P. C. Maria, "Thermogravimetric calibration of permeation tubes used for the preparation of gas standards for air pollution analysis," *Analyst*, vol. 130, no. 10, pp. 1369-1374, 2005.
- [183] J. M. Mckelvey and H. E. Hoelscher, "Apparatus for Preparation of Very Dilute Gas Mixtures," *Analytical Chemistry*, vol. 29, no. 1, pp. 123-123, 1957.
- [184] A. Naganowska-Nowak, P. Konieczka, A. Przyjazny and J. Namiesnik, "Development of techniques of generation of gaseous standard mixtures," *Critical Reviews in Analytical Chemistry*, vol. 35, no. 1, pp. 31-55, 2005.
- [185] R. J. Huang and T. Hoffmann, "Diffusion technique for the generation of gaseous halogen standards," *Journal of Chromatography A*, vol. 1217, no. 13, pp. 2065-2069, 2010.
- [186] G. O. Nelson, "diffusion method," in *gas mixtures: preparation and control*, Boca Ratan, Fla., U.S.A., Lewis Publishers, 1992, pp. 137-146.
- [187] T. Nakamoto, Y. Suzuki and T. Moriizumi, "Study of VHF-band QCM gas sensor," *Sensors and Actuators B-Chemical*, vol. 84, no. 2-3, pp. 98-105, 2002.
- [188] W. M. Haynes and D. R. Lide, *CRC handbook of chemistry and physics : a ready-reference book of chemical and physical data*, London: Taylor & Francis, 2011.
- [189] F. W. Sears and G. L. Salinger, *Thermodynamics, kinetic theory and statistical thermodynamics*. 3rd ed, Reading, Mass., etc.: Addison-Wesley, 1975.
- [190] R. H. Perry, D. W. Green and J. O. Maloney, *Perry's chemical engineers' handbook*, London: McGraw-Hill, 1984.

- [191] R. Weast, CRC handbook of chemistry and physics, Boca Rato: Boca Raton : CRC Press, 1988.
- [192] T. Emadi, C. Shafai, M. Freund, D. Thomson, D. Jayasz and N. Whitex, "Development of a Polymer-based Gas Sensor Humidity and CO<sub>2</sub> Sensitivity," in *Microsystems and Nanoelectronics Research Conference, 2009. MNRC 2009. 2nd*, Ottawa, ON, Canada, 13-14 Oct. 2009.
- [193] M. E. Nipper, S. Majd, M. Mayer, J. C. M. Lee, E. A. Theodorakis and M. A. Haidekker, "Characterization of changes in the viscosity of lipid membranes with the molecular rotor FCVJ," *Biochimica Et Biophysica Acta-Biomembranes*, vol. 1778, no. 4, pp. 1148-1153, 2008.
- [194] G. Long and J. Winefordner, "Limit of Detection A Closer Look at the IUPAC Definition," *analytical chemistry*, vol. 55, no. 07, pp. 712A-724A, 1983.
- [195] X. Y. Lin, J. Wu, R. B. Zhu, P. Chen, G. W. Huang, Y. Li, N. H. Ye, B. H. Huang, Y. P. Lai, H. Zhang, W. Y. Lin, J. J. Lin, Z. B. Wang, H. Zhang and R. G. Ruan, "California Almond Shelf Life: Lipid Deterioration During Storage," *Journal of Food Science*, vol. 77, no. 6, pp. C583-C593, 2012.
- [196] J. M. Zhang, W. Z. Wu, T. Jiang, H. X. Gao, Z. M. Liu, J. He and B. X. Han, "Conductivities and viscosities of the ionic liquid [bmim][PF<sub>6</sub>] plus water plus ethanol and [bmim][PF<sub>6</sub>] plus water plus acetone ternary mixtures," *Journal of Chemical and Engineering Data*, vol. 48, no. 5, pp. 1315-1317, 2003.
- [197] S. Pandey, K. A. Fletcher, S. N. Baker and G. A. Baker, "Correlation between the fluorescent response of microfluidity probes and the water content and viscosity of ionic liquid and water mixtures," *Analyst*, vol. 7, no. 569-573, p. 129, 2004.
- [198] D. B. Goldstein, "the effects of drugs on membrane fluidity," *Annual Review of Pharmacology and Toxicology*, vol. 24, pp. 43-64, 1984.
- [199] R. A. Harris and F. Schroeder, "Ethanol and the Physical-Properties of Brain Membranes - Fluorescence Studies," *Molecular Pharmacology*, vol. 20, no. 1, pp. 128-137, 1981.
- [200] K. K. Kanazawa and J. G. Gordon, "The Oscillation Frequency of a Quartz Resonator in Contact with a Liquid," *Analytica Chimica Acta*, vol. 175, no. 9, pp. 99-105, 1985.

- [201] R. A. Demel and B. Dekruyff, "Function of Sterols in Membranes," *Biochimica Et Biophysica Acta*, vol. 457, no. 2, pp. 109-132, 1976.
- [202] B. Alberts, in *Molecular biology of the cell: 4th edition*, New York, Garland Science, 2002, p. 588.
- [203] M. Giocondi, D. Yamamoto, E. Lesniewska, P. Milhiet, T. Ando and C. L. Grimellec, "Surface topography of embrane domains," *Biochimica et Biophysica Acta*, pp. 703-718, 2010.
- [204] I. Avati polar lipids, "Avati polar lipids," Avati polar lipids, Inc., 29 03 2014. [Online]. Available: <http://avantilipids.com>. [Accessed 29 03 2014].